ISSN 1997-308X
eISSN 2412-8767

ИЗВЕСТИЯ ВУЗОВ
ПОРОШКОВАЯ МЕТАЛЛУРГИЯ И ФУНКЦИОНАЛЬНЫЕ ПОКРЫТИЯ

POWDER METALLURGY AND FUNCTIONAL COATINGS

2024
Том 18 № 1
Vol. 18 No. 1
powder.misis.ru

ISSN 1997-308X
eISSN 2412-8767

POWDER METALLURGY AND FUNCTIONAL COATINGS

Scientific and Technical Journal
Founded in 2007
Four issues per year

2024
Vol. 18 No. 1
Том 18 № 1

ИЗВЕСТИЯ ВУЗОВ ПОРОШКОВАЯ МЕТАЛЛУРГИЯ И ФУНКЦИОНАЛЬНЫЕ ПОКРЫТИЯ

Научно-технический журнал
Основан в 2007 г.
Выходит 4 раза в год

POWDER METALLURGY AND FUNCTIONAL COATINGS

ISSN 1997-308X
eISSN 2412-8767

SCIENTIFIC AND TECHNICAL JOURNAL
FOUNDED IN 2007
SIX ISSUES PER YEAR

http://powder.misis.ru

Founder:

National University of Science and Technology "MISIS"
Address: 4 bld. 1 Leninskiy Prosp., Moscow 119049, Russian Federation
http://www.misis.ru

Journal is included into the List of peer-reviewed scientific publications recommended by the Highest Attestation Commission of the Ministry of Education and Science of the Russian Federation for publishing the results of doctoral and candidate dissertations.
Abstracting/Indexing: Scopus, Russian Science Citation Index (RSCI), Ulrich's Periodicals Directory, VINITI Database (Abstract Journal).

Certificate of registration **No. FS77-27955** (12.04.2007)
Re-registration **PI No. FS77-79230** (25.09.2020)

Signed print 20.02.2024. Format 60×90 1/8
Offset paper No. 1. Digital printing. Quires 11.75
Order 19161. Free price
Printed in the printing house of the MISIS Publish House
4 bld. 1 Leninskiy Prosp., Moscow, 119049 Russian Federation
Phone/fax: +7 (499) 236-76-17

ИЗВЕСТИЯ ВУЗОВ
ПОРОШКОВАЯ МЕТАЛЛУРГИЯ
И ФУНКЦИОНАЛЬНЫЕ ПОКРЫТИЯ

НАУЧНО-ТЕХНИЧЕСКИЙ ЖУРНАЛ
ОСНОВАН В 2007 Г.
ВЫХОДИТ 6 РАЗ В ГОД

http://powder.misis.ru

ISSN 1997-308X
eISSN 2412-8767

Учредитель:

ФГАОУ ВО Национальный исследовательский технологический университет «МИСИС»
Адрес: 119049, Москва, Ленинский пр-т, 4, стр. 1
https://www.misis.ru

Журнал включен в Перечень рецензируемых научных изданий, рекомендованных ВАК Минобрнауки РФ для публикации результатов диссертаций на соискание ученых степеней.
Журнал включен в базы данных: Scopus, Russian Science Citation Index (RSCI), Ulrich's Periodicals Directory, РИНЦ, БД/РЖ ВИНИТИ.

Редакция журнала

Адрес: 119049, Москва,
Ленинский пр-т, 4, стр. 1. НИТУ МИСИС

Тел.: +7 (495) 638-45-35. ***Эл. почта:*** izv.vuz@misis.ru

Свидетельство о регистрации № **ФС77-27955** от 12.04.2007 г.
Перерегистрация 25.09.2020 г. **ПИ № ФС77-79230**

Ведущий редактор: А.А. Кудинова
Выпускающий редактор: О.В. Соснина
Дизайн и верстка: В.В. Расенець

Подписано в печать 20.02.2024. Формат 60×90 $^1/_8$
Бум. офсетная № 1. Печать цифровая. Усл. печ. л. 11,75
Заказ 19161. Цена свободная
Отпечатано в типографии Издательского Дома МИСИС
119049, г. Москва, Ленинский пр-т, 4, стр. 1
Тел./факс: +7 (499) 236-76-17

Contents

Содержание

Materials and Coatings Fabricated Using the Additive Manufacturing Technologies

Материалы и покрытия, получаемые методами аддитивных технологий

The 20th International Scientific Conference on "Modern Materials, Advanced Manufacturing Technologies, and Associated Equipment"

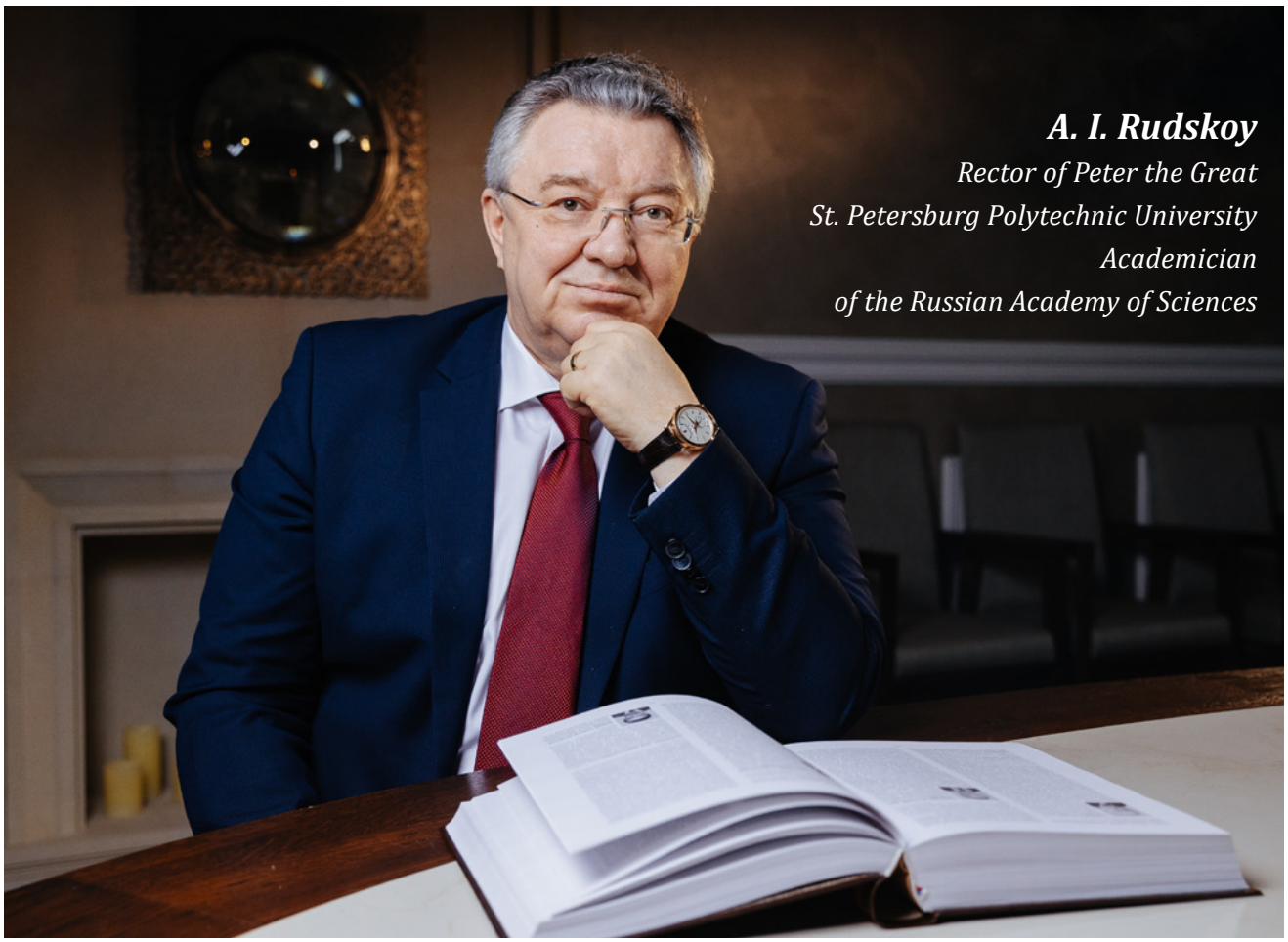

From June 30th to July 2nd, 2023, the 20th International Scientific Conference titled "Modern Materials, Advanced Manufacturing Technologies, and Associated Equipment" was held at Peter the Great St. Petersburg Polytechnic University. This conference coincided with the celebration of the 300th anniversary of the Russian Academy of Sciences and the 125th anniversary of the establishment of Peter the Great St. Petersburg Polytechnic University. The co-organizers of the conference included the Ministry of Science and Higher Education of the Russian Federation, the Russian Academy of Sciences (Department of Chemistry and Materials Science), the National Academy of Sciences of the Republic of Belarus (Department of Physical-Technical Sciences), the State Corporation "Rosatom", and Peter the Great St. Petersburg Polytechnic University.

Prominent representatives from the Russian Academy of Sciences, higher education, and industry deliberated and analyzed a wide array of findings reflecting contemporary trends in the advancement of materials science and cutting-edge manufacturing technologies. Special emphasis was placed on the latest advancements in the production of new metallic, ceramic, and composite materials, as well as the design of technological equipment.

Participants of the conference highlighted the unprecedented technological breakthroughs currently underway, propelled by the adoption of pioneering technologies and a diverse range of materials within the industrial sphere, thus ensuring the requisite standards of performance for high-tech products. It is unsurprising that among the conference speakers were representatives from various industrial enterprises.

This journal issue presents articles derived from the conference materials.

Materials and Coatings Fabricated Using the Additive Manufacturing Technologies
Материалы и покрытия, получаемые методами аддитивных технологий

UDC 669.018.58
https://doi.org/10.17073/1997-308X-2024-1-6-19

Review article
Обзорная статья

Exploring 3D printing with magnetic materials: Types, applications, progress, and challenges

G. A. Konov, A. K. Mazeeva, D. V. Masaylo,
N. G. Razumov, A. A. Popovich

Peter the Great St. Petersburg Polytechnic University
29 Polytekhnicheskaya Str., St. Petersburg 195251, Russian Federation

mazeevaalina@gmail.com

Abstract. 3D printing, also known as additive manufacturing (AM), represents a rapidly evolving technological field capable of creating distinctive products with nearly any irregular shape, often unattainable using traditional techniques. Currently, the focus in 3D printing extends beyond polymer and metal structural materials, garnering increased attention towards functional materials. This review conducts an analysis of published data concerning the 3D printing of magnetic materials. The paper provides a concise overview of key AM technologies, encompassing vat photopolymerization, selective laser sintering, binder jetting, fused deposition modeling, direct ink writing, electron beam melting, directed energy deposition and laser powder bed fusion. Additionally, it covers magnetic materials currently utilized in AM, including hard magnetic Nd–Fe–B and Sm–Co alloys, hard and soft magnetic ferrites, and soft magnetic alloys such as permalloys and electrical steels. Presently, materials produced through 3D printing exhibit properties that often fall short compared to their counterparts fabricated using conventional methods. However, the distinct advantages of 3D printing, such as the fabrication of intricately shaped individual parts and reduced material wastage, are noteworthy. Efforts are underway to enhance the material properties. In specific instances, such as the application of metal-polymer composites, the magnetic properties of 3D-printed products generally align with those of traditional analogs. The review further delves into the primary fields where 3D printing of magnetic products finds application. Notably, it highlights promising areas, including the production of responsive soft robots with increased freedom of movement and magnets featuring optimized topology for generating highly homogeneous magnetic fields. Furthermore, the paper addresses the key challenges associated with 3D printing of magnetic products, offering potential approaches to mitigate them.

Keywords: 3D printing, additive manufacturing, additive technologies, magnetic materials

Acknowledgements: This work was supported by the Russian Science Foundation (grant No. 23-13-00305).

For citation: Konov G.A., Mazeeva A.K., Masaylo D.V., Razumov N.G., Popovich A.A. Exploring 3D printing with magnetic materials: Types, applications, progress, and challenges. *Powder Metallurgy and Functional Coatings*. 2024;18(1):6–19. https://doi.org/10.17073/1997-308X-2024-1-6-19

Обзор 3D-печати изделий из магнитных материалов: виды, применение, достижения и проблемы

Г. А. Конов, А. К. Мазеева, Д. В. Масайло,
Н. Г. Разумов, А. А. Попович

Санкт-Петербургский политехнический университет Петра Великого
Россия, 195251, г. Санкт-Петербург, ул. Политехническая, 29

mazeevaalina@gmail.com

Аннотация. 3D-печать, или аддитивное производство (АП), – это активно развивающаяся область техники, позволяющая изготавливать уникальные изделия практически любой сложной формы, которую зачастую невозможно получить традиционными технологиями. В настоящее время помимо работ с изделиями из полимерных и металлических конструкционных материалов востребованной также становится 3D-печать изделий из функциональных материалов. В данном обзоре представлен

анализ литературных данных по 3D-печати изделий из магнитных материалов. Кратко рассмотрены основные технологии АП – фотополимеризация в ванне, селективное лазерное спекание, струйное нанесение связующего, моделирование методом наплавления, прямое написание чернилами, электронно-лучевая плавка, прямой подвод энергии и материала, синтез на подложке с помощью лазера, а также используемые в АП магнитные материалы – магнитотвердые сплавы Nd–Fe–B и Sm–Co, магнитотвердые и магнитомягкие ферриты, магнитомягкие сплавы типа пермаллоев и электротехнических сталей. Показано, что на данный момент материалы, изготовленные методами 3D-печати, пока уступают по своим свойствам аналогичным материалам, полученным более традиционными методами, однако основные преимущества 3D-печати – создание единичных изделий сложной формы и сокращение отходов материала, при этом ведутся работы по улучшению комплекса свойств. В некоторых случаях, например при использовании металл-полимерных композиций, магнитные характеристики 3D-изделий из них в целом уже сопоставимы с традиционными аналогами. В обзоре приведены основные направления применения 3D-печати магнитных изделий – в частности, показано, что весьма перспективно изготовление мягких роботов с быстрым откликом и высокой степенью свободы, а также магнитов с оптимизированной топологией, позволяющих генерировать магнитное поле с высокой степенью однородности. Также представлены основные проблемы 3D-печати магнитных изделий и возможные способы их решения.

Ключевые слова: 3D-печать, аддитивное производство, аддитивные технологии, магнитные материалы

Благодарности: Данная работа была выполнена при поддержке Российского научного фонда (грант № 23-13-00305).

Для цитирования: Конов Г.А., Мазеева А.К., Масайло Д.В., Разумов Н.Г., Попович А.А. Обзор 3D-печати изделий из магнитных материалов: виды, применение, достижения и проблемы. *Известия вузов. Порошковая металлургия и функциональные покрытия*. 2024;18(1):6–19. https://doi.org/10.17073/1997-308X-2024-1-6-19

Introduction

Magnetic materials are capable of generating their own magnetic fields and are widely used in various electrical devices [1–3], such as generators, transformers, magnetic recording systems, and other units with specific geometries and architectures. Traditional methods for manufacturing such products are limited to simple shapes, requiring expensive tools and sophisticated post-processing. This pushes up the costs of low-volume production of unique items and leads to considerable waste. Consequently, an increasing number of studies are devoted to the development of new technologies, including 3D printing.

3D printing enables the creation of arbitrarily-shaped structures with complex geometries using a variety of materials, including polymers [4; 5], metals [6–8], ceramics [9–11], composites [12–14], etc. This technology allows for reduced production time, lowered costs, controlled shapes, printing with multiple materials, and the production of structures that were previously impossible to obtain using traditional methods. The capabilities of 3D printing technology offer tremendous opportunities for manufacturing magnetic materials with irregular shapes, simultaneously reducing waste and enabling the creation of unique products unattainable through traditional methods. Further studies on materials and processes are required to fully explore the potential of 3D printing in manufacturing magnetic materials.

The aim of this paper is to review published works pertaining to the additive manufacturing of magnetic materials. It will specifically explore the 3D printing technologies employed for this purpose, the application scope of materials produced through this method, the potential and accomplishments of additive technologies in this domain, and finally, it will address current challenges and the prospects for their resolution.

1. 3D printing technologies for manufacturing magnetic materials

A variety of technologies and materials are employed in the additive manufacturing of magnetic materials using 3D printing. Some of these techniques are discussed below.

Vat photopolimerization [15; 16] (Fig. 1, *a*) is a 3D printing technology that uses liquid polymers as initial materials along with a laser, projector, or liquid crystal display as a radiation source.

Stereolithography apparatus (SLA) technology operates by using a laser to illuminate photopolymer resin in the printer vat through point-by-point scanning. The laser beam targets the vat's bottom and, via mirror galvanometers, illuminates specific regions based on the developed 3D computer model of the product. This process forms a cured layer corresponding to the specified cross-section of the model. The platform then rises by the thickness of one layer, and the procedure repeats until the product is fully printed.

Digital light processing (DLP) technology [17] employs projectors to solidify photopolymer resin into three-dimensional objects. It simultaneously exposes the entire resin layer to optical range radiation, curing the entire layer with a single exposure, eliminating the need for scanning procedures. Digital micromirror devices (DMD), consisting of thousands of micro-

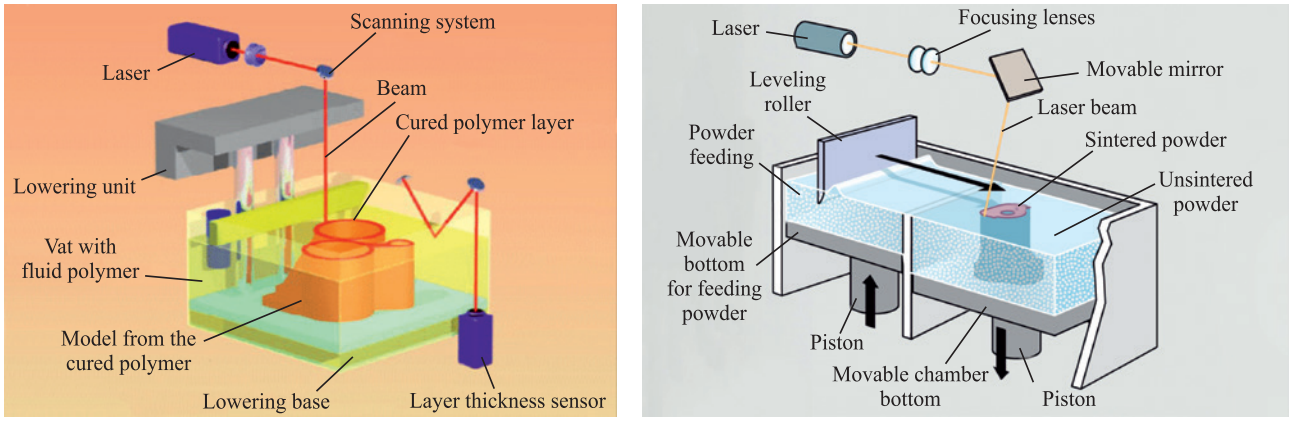

a *b*

Fig. 1. Vat photopolymerization method [21] (***a***) and SLS method [22] (***b***)

Рис. 1. Метод фотополимеризации в ванне [21] (***a***) и метод СЛС [22] (***b***)

mirrors, control the reflection of light onto the resin surface, allowing the creation of images using pixels and voxels similar to conventional 2D or 3D cameras.

Photopolymerization can also be accomplished using a liquid crystal display (LCD) [18–20]. LCD printers, unlike the projection method, lack mirrors and instead employ powerful LCD panels. LEDs shine light onto the model, with the LCD panel blocking light in regions where photopolymer solidification is not needed. Only the necessary regions permit light to pass through onto the finished part. This approach simplifies the printing process, eliminating the need for mirrors or galvanometers. DLP and LCD technologies expedite the printing process, although the achievable level of detail is slightly lower compared to SLA.

Vat photopolymerization is known for its high accuracy and excellent feature detail, making it a preferred choice for manufacturing small complex parts, prototypes, and models. In this method, magnetic materials are obtained using magnetic fluid or ink.

Selective laser sintering (SLS) [15; 12–24] (Fig. 1, *b*) is a method that employs a laser to sinter powder. Unlike the vat photopolymerization method, SLS uses powders from specialized reservoir instead of liquid materials. The laser sinters the powder, forming a solid surface that corresponds to the specified cross-section based on the pre-designed 3D model. In the manufacturing of magnetic products via the SLS method, magnetic powders are used as the feedstock materials.

Binder jetting (BJ) [25–29] (Fig. 2, *a*) is an additive manufacturing process that involves depositing a liquid binder onto a layer of powder to selectively bind its particles. The powder layer is then densified,

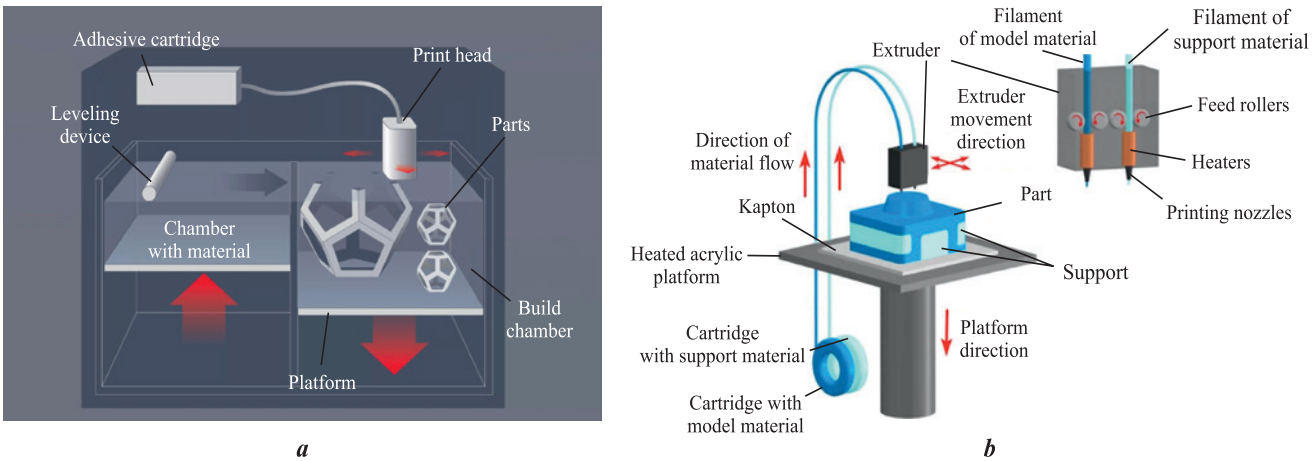

a *b*

Fig. 2. BJ method [33] (***a***) and FDM method [34] (***b***)

Рис. 2. Методы BJ [33] (***a***) и FDM [34] (***b***)

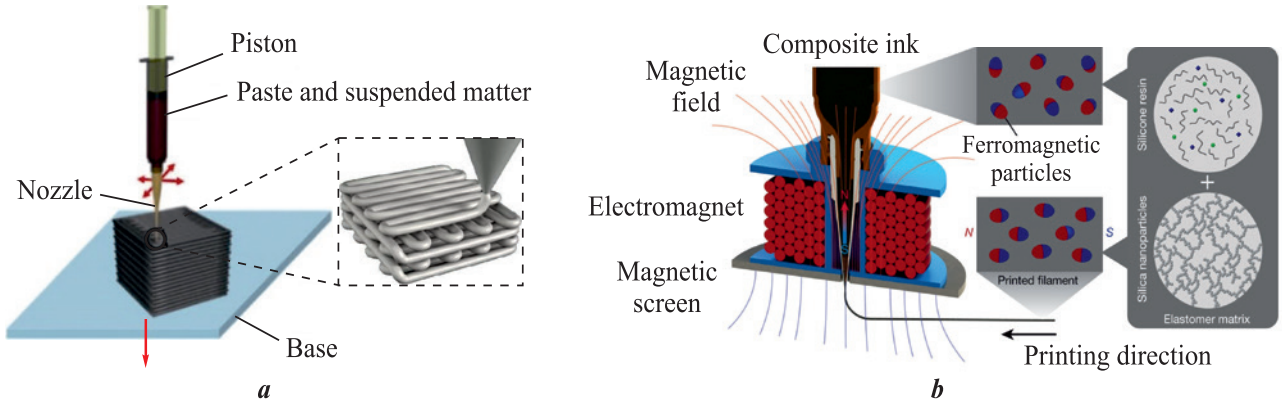

Fig. 3. DIW technique [32] (***a***) and magnetic field-assisted DIW technique [32] (***b***)

Рис. 3. Технология DIW [32] (***a***) и технология DIW с приложенным магнитным полем [32] (***b***)

and the process is repeated layer by layer until the part is fully fabricated. The unbound powder is removed, leaving the fabricated part behind. In order to print magnet materials by this method, magnetic particles are mixed with a binder during the printing process.

Fused deposition modeling (FDM) [29; 30] (Fig. 2, *b*) is a type of 3D printing based on depositing plastic material, usually thermoplastic polymers, onto existing layers. The filament is fed into a heated nozzle where it melts and is deposited onto the assembly platform in the exact order determined by the 3D model, thus creating layers of material that cool and solidify to form a part of the desired shape. Special composite filaments containing magnetic particles are used to manufacture magnetic materials.

Direct ink writing (DIW) [31; 32] (Fig. 3) represents one of the 3D printing techniques capable of producing intricate structures with exceptional accuracy and detailed features. The DIW method utilizes materials in the form of liquid paste (Fig. 3, *a*), that is subsequently solidified during post-printing. The solidification occurs either through water evaporation, in the case of a water-based binder, or via polymerization induced by exposure to high temperatures around 100 °C or a UV source. Various methodologies exist for governing the shape and properties of the printed materials, one of which involves the application of a magnetic field (Fig. 3, *b*). Employing a magnetic field allows for the deliberate orientation of material particles, enhancing magnetic properties and facilitating precise control over the shape of the printed products.

Electron beam melting (EBM) (Fig. 4, *a*) [25; 32; 35; 36] is a printing method that utilizes an electron beam to fuse metal powders into a three-dimensional part. In the EBM process, an electron beam is generated within a vacuum chamber and directed at the powder

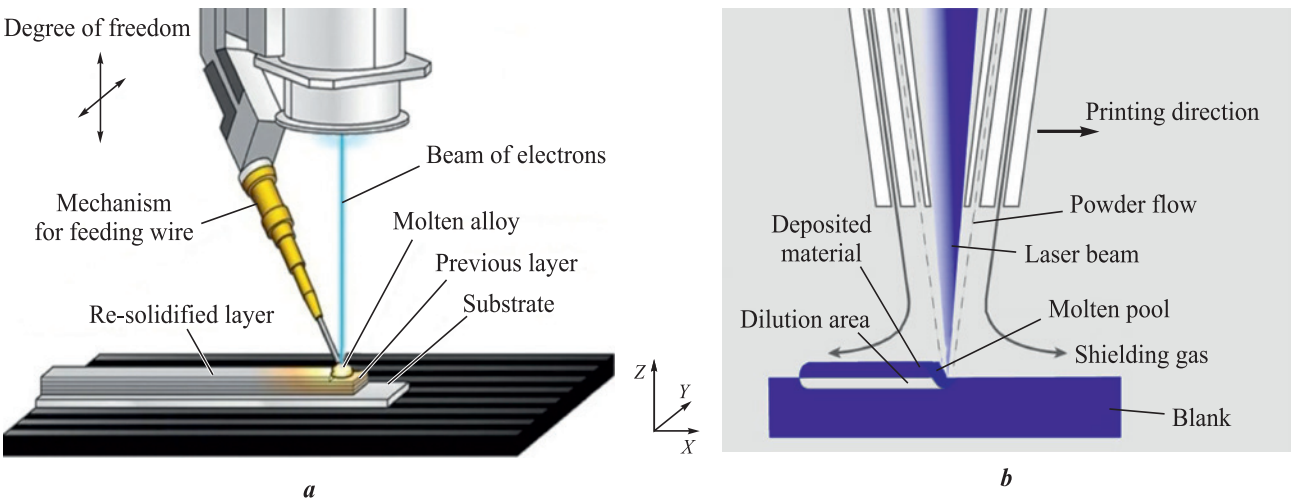

Fig. 4. EBM method [37] (***a***) and DED method [38] (***b***)

Рис. 4. Методы EBM [37] (***a***) и DED [38] (***b***)

bed, causing the powder to melt. Metal parts are fabricated using this method. Powders containing magnetic particles are employed to create magnetic materials.

Directed energy deposition (DED) (Fig. 4, *b*) [32; 39; 40] is a printing method that employs a laser or plasma to fuse metal powders and create three-dimensional parts. In the DED process, the material is heated until it begins to melt, and its controlled flow is fused with the layer below. This printing method is well-suited for fabricating parts made of metal and ceramics. In order to produce magnetic materials using this method, powders containing magnetic particles are used as feedstock materials.

Laser powder bed fusion (L-PBF) [15; 22; 32] (Fig. 5) is a technique similar to the SLS method. However, in this case, the laser is not utilized for sintering but for powder melting.

2. Overview of magnetic materials in additive manufacturing

Magnetic materials [42; 43] are commonly classified into two groups: hard and soft magnetic materials. This classification depends on the material's coercive force (H_c). Soft magnetic materials possess a coercive force lower than 4 kA/m, whereas hard magnetic materials have a coercive force higher than 4 kA/m. Soft magnetic materials are often employed in manufacturing transformer cores, magnetic shields, microwave devices, and so on, while hard magnetic materials find application in producing permanent magnets, various sensors, an so on.

2.1. Soft magnetic materials

Soft magnetic materials [42–44] possess the ability to magnetize and demagnetize easily. They exhibit low coercive force (H_c), resulting in lower losses associated with magnetization reversal. These materials are well-suited for applications requiring rapid changes in magnetic fields. Additionally, soft magnetic materials should often possess high saturation induction (B_s) and high magnetic permeability, even at high frequencies. They find usage in diverse devices such as electric motors [45; 46], transformers [47; 48], magnetic sensors [49], and magnetic shields [50; 51].

Permalloys [52; 53] constitute a group of iron- and nickel-based alloys with high magnetic permeability. They serve as the foundation for numerous parts in electrical equipment. Permalloys have widespread industrial applications, including the production of motors, generators, inductors, transformers, and other devices. Due to their magnetic properties, permalloys can be effectively employed in 3D printing to fabricate intricate magnetic structures. For example, in [52], 3D printing with L-PBF was utilized to directly manufacture permalloy magnetic shields based on Ni–Fe fiber-optic gyroscopes in spacecraft. Comparative evaluations of the soft magnetic properties of printed Ni–15Fe–5Mo permalloy, with and without annealing, demonstrated similarity to traditionally processed permalloy parts, indicating the feasibility and applicability of the L-PBF method.

Fe–Si electrical steels (with varying proportions of iron and silicon, e.g., 6.9 % Si) [54] exhibit high magnetic permeability, low coercive force, and high

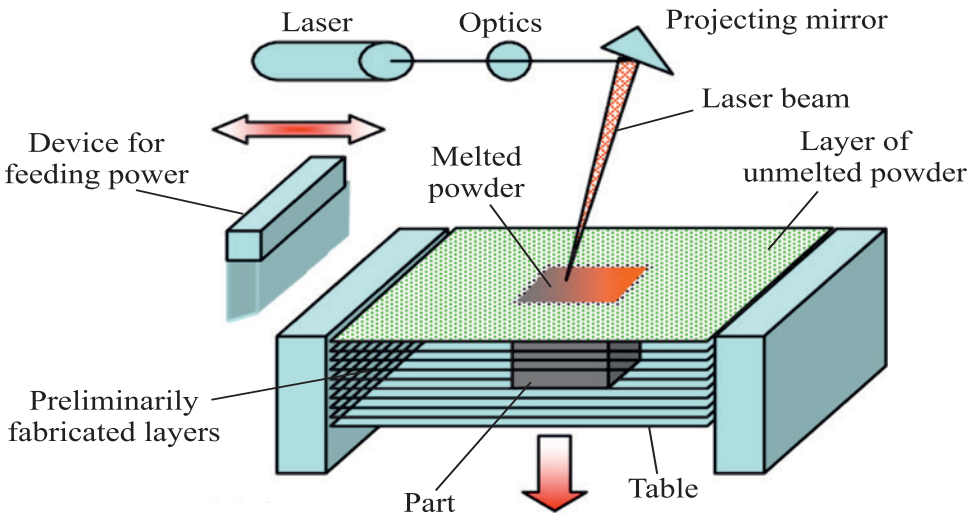

Fig. 5. L-PBF technique [41]

Рис. 5. Метод L-PBF [41]

electrical conductivity. These characteristics make them suitable for diverse fields such as electronics, automotive, and microelectronics. The L-PBF method in additive manufacturing can produce magnetic components like toroids, transformer cores, magnetic conductors, and other elements using these alloys [54].

Soft magnetic ferrites (such as $NiFe_2O_4$, Fe_3O_4, Ni–Zn and Ni–Zn–Cu ferrites) are used in manufacturing transformer cores, elements of microwave devices, and as magnetic fillers for producing soft robots and manipulators.

2.2. Hard magnetic materials

Hard magnetic materials [32; 55–59] retain a strong magnetic field even without an external magnetic force and are commonly used in manufacturing permanent magnets. These materials are challenging to magnetize but can retain their magnetization after the external magnetic field is removed. Essential characteristics for such materials include high values of H_c, B_r and maximum magnetic energy product $(BH)_{max}$. They find applications in producing items requiring a constant strong magnetic field, such as motors, generators, magnetic storage devices, and various sensor types. Common materials utilized for fabricating permanent magnets include alloys based on the Nd–Fe–B and Sm–Co systems, along with hard magnetic ferrites.

Nd–Fe–B magnets [60–62] are known for their exceptional magnetic performance and possess a high energy density, enabling the generation of intense magnetic fields. These magnets are highly sought after in electronics, electromechanics, and medical equipment. Conventionally, magnets based on the Nd–Fe–B system are manufactured by sintering a blank pressed from initial powder, followed by infiltration with a low-fusible alloy based on the Pr–Cu system to enhance coercivity. In [63], the authors proposed applying the L-PBF method to a mixture of Nd–Fe–B powder and eutectic alloy powder $(Pr_{0.5}Nd_{0.5})_3(Cu_{0.25}Co_{0.75})$ to obtain a magnet with $Nd_2Fe_{14}B$ magnetic grains and a non-magnetic intergrain layer in a single manufacturing operation.

However, a distinctive feature of 3D printing using metallic materials, especially Nd–Fe–B magnetic alloys, is porosity. This arises due to both insufficient injected radiation energy causing lack-of-fusion zones and excessive energy leading to intense metal evaporation in the laser beam zone. By varying laser power and scanning speed using L-PBF technology, the authors [64] identified optimal modes to ensure the stability of the Nd–Fe–B-based alloy melting process and obtain high-quality fused track for competitive permanent magnet fabrication.

The Nd–Fe–B-based magnets produced by metallic 3D printing methods are also prone to cracking and brittleness. In [65], the double scanning method was proposed, involving scanning each layer twice – initially with full laser power and then with half the power. This approach, involving partial remelting of the already deposited layer, resulted in denser samples with fewer defects in the form of pores and cracks, thus preventing their destruction when separated from the substrate.

Polymer-bonded magnets [66; 67] consist of polymers infused with magnetic particles, typically ferrites (such as $SrFe_{12}O_{19}$, $BaFe_{12}O_{19}$, $CoFe_2O_4$). While they possess lower energy compared to traditional sintered iron, nickel, or cobalt-based magnets, polymer-bonded magnets serve purposes where a lightweight and flexible magnetic solution is required. Moreover, they are relatively cost-effective and easy to manufacture. The utilization of 3D printing for producing ferrite-based magnets offers numerous advantages. It allows the creation of magnets in diverse sizes, shapes, and intricate geometries that might be inaccessible via traditional methods.

A prevalent technique for fabricating ferrite-based magnets using 3D printing involves extruding the material while applying an external magnetic field. During this process, molten plastic is dispensed through a nozzle onto a special platform, and an external magnetic field – created using a permanent magnet or a current-carrying coil – is directed at the composite of polymer and magnetic particles. This field aligns the magnetic particles in the polymer, resulting in an anisotropic magnet when the polymer cools and solidifies.

These magnets find widespread applications in work surfaces, storage devices, magnetic toys, and can even be customized into specific shapes like logos.

Currently, polymer-bonded magnets [68–70] are gaining attention in industries due to their comparable magnetic properties (in contrast to traditional pressing and injection molding methods), mold flexibility, low cost, and acceptable mechanical properties [71; 72].

The manufacturing of magnets has shifted from traditional pressing and injection molding techniques to the widespread utilization of 3D printing methods. An illustrative instance is the application of the BJ method, used to 3D print isotropic magnets based on polymer-bonded Nd–Fe–B. These magnets were shaped using initial materials of approximately 70 μm particles [26]. Upon completion of the printing process,

the resulting green model underwent curing at temperatures ranging from 100 to 150 °C. Subsequently, the surface underwent infiltration with urethane resin, achieving a magnet density of 3.47 g/cm^3. This density corresponds to 46 vol. % of the Nd–Fe–B density (7.6 g/cm^3). It's noteworthy that the residual induction of the magnet samples produced by binder jetting, reaching approximately 0.3 T, aligns closely with residual induction values of 0.5 and 0.65 T typically achieved in standard isotropic magnets through conventional pressing and injection molding methods [26]. Furthermore, this approach enables precise control of the magnetic characteristics during the printing process, leading to maximum efficiency gains.

Sm–Co magnets [73] possess notably high coercive properties, trailing only behind NdFeB-based magnets in terms of their characteristics. They prove advantageous in 3D printing applications, particularly in scenarios requiring high-temperature resistance. These magnets, based on the Sm–Co system, often consist of multiple components, incorporating elements such as Fe, Cu, and Zr. Notably, they exhibit a high energy density, exceptional temperature stability, and resilience to mechanical stresses. These distinctive traits render Sm–Co magnets indispensable across various industrial fields, spanning from medical devices to electronics and the automotive industry.

However, the conventional manufacturing process for Sm–Co magnets is notably expensive and labor-intensive, thereby posing challenges for smaller manufacturers to affordably engage in production. This issue finds a potential solution through the application of 3D printing technology. Employing 3D printing for the fabrication of Sm–Co magnets offers a significant advantage in cost reduction, particularly when producing magnets in smaller batches.

Despite its numerous advantages, utilizing 3D printing techniques like L-PBF for fabricating Sm–Co magnets presents certain drawbacks. Notably, the magnets produced through this method often exhibit relatively low mechanical strength, potentially limiting their application in specific sectors, particularly within aviation and marine transportation industries. Nevertheless, the realm of 3D printing Sm–Co alloys holds immense promise and signifies a compelling avenue for the future development of magnetic material production. The prospect of reduced manufacturing costs while maintaining quality and productivity, alongside the capacity to fabricate more intricate products, positions the 3D printing of Sm–Co magnets as a prospective mainstream industrial method [74].

Hard ferrites [75; 76], also referred to as ceramic or ferrite magnets, represent a class of permanent magnets composed of iron oxide and ceramics ($BaFe_{12}O_{19}$, $SrFe_{12}O_{19}$, $MnZnFe_2O_4$) [77].

Despite their relatively modest magnetic properties, hard ferrite ceramic materials boast exceptional resistance to corrosion and mechanical impacts, rendering them the most cost-effective type of magnetic materials available. They are widely utilized in manufacturing of electronic devices, magnetic systems, motors, transformers, and various other equipment.

Typically, the production process for hard ferrite ceramic materials involves blending corresponding powders, subjecting them to pressure, and subsequent sintering at elevated temperatures. However, with the advent and advancement of 3D printing technologies, ferritic components can now be fabricated using innovative methods such as the DIW technique [77]. This technological approach allows for the adjustment of their magnetic properties by varying the ratio of magnetic iron oxide and incorporating additional magnetic metals.

While hard ferrite ceramic materials possess inferior magnetic properties compared to other types of magnets such as Nd–Fe–B and Sm–Co, their superior stability and versatility make them a compelling option for a diverse array of applications across various fields.

3. Application scope of 3D printing with magnetic materials

3D printing has transformed the manufacturing industry, facilitating the creation of intricate shapes and designs previously unattainable through conventional manufacturing methods. When combined with magnetic materials, 3D printing technology opens doors to a wide array of innovative products.

3.1. Magnetic sensors

Magnetic materials find extensive use in the production of sensors. These sensors serve various purposes, including determining the position of moving objects, measuring the speed of rotating objects, and detecting the presence of metal objects. Utilization of 3D printing technology allows for the production of sensors with intricate shapes and precise dimensions, customizable to meet specific requirements. Certain applications, such as medical diagnostics, necessitate irregularly shaped sensors, enabling insertion into the body

to monitor indicators such as temperature, blood pressure, and blood oxygen levels. Magnetic sensors can be manufactured using FDM technology [68; 78; 79].

3.2. Magnetic drives

Magnetic drives utilize the interaction between magnetic fields and magnetic materials to generate motion. They find widespread applications, particularly in robotics, automation, and the automotive industry. 3D printing technologies such as SLA and FDM [80; 81] enable the production of intricately designed magnetic drives [82], tailored to specific requirements. Magnetic drives created through 3D printing exhibit advanced features [83] and enhanced efficiency compared to their traditional counterparts. For instance, a publication [83] details the printing of a magnet with optimized topology via the FDM process. This production method offers advantages such as rapid and cost-effective fabrication, increased distortion power factor, and high power output. Optimizing the magnet's topology allows for the creation of magnets generating a homogeneous magnetic field, crucial in applications such as nuclear magnetic resonance, magnetometers, sensors, and magnetic traps, among others. Additive technologies, particularly FDM, enable the replication of a pre-designed computer 3D model with remarkable accuracy.

3.3. Soft robots

Soft drives and robots represent a significant advancement in human-machine interaction, offering unrestricted movement due to their pliable nature [84]. Unlike conventional rigid robots, soft robots typically utilize gels [85; 86], elastomers [87], and other flexible materials, allowing them to adapt to their surroundings [88]. Furthermore, integrating magnetic particles into the polymer matrix [89; 90] or applying magnetic coatings onto polymer frameworks [91; 92] enables these soft robots to function within magnetic fields. However, achieving multiple functionalities without intricate geometry remains challenging [93; 94]. 3D printing plays a pivotal role in producing complex designs using multiple materials. For example, studies detailed in papers [95; 96] highlight the creation of a soft worm-like robot through SLA technology. This robot, comprised of composites involving magnetic particles and polymer, demonstrates both linear and rotational motion (see Fig. 6) [95]. This magnetically driven robot shows promise, particularly in controlled medicine delivery [32].

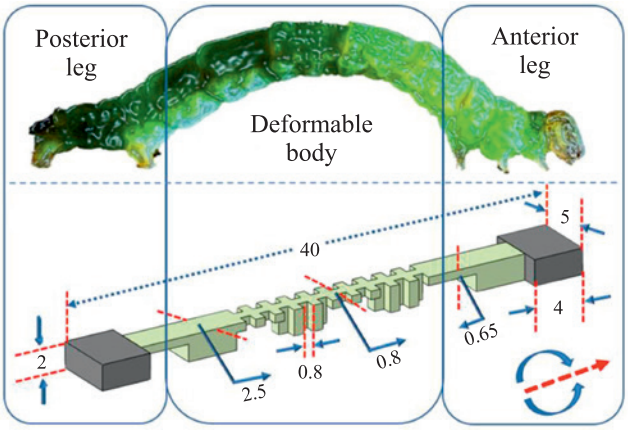

Fig. 6. Soft robot structure [95]

Рис. 6. Конструкция мягкого робота [95]

The evolution of 3D printing technologies has expanded horizons for manufacturing magnetic materials and related products. The ability to fabricate parts with advanced features and increased efficiency, owing to complex shapes and high accuracy, showcases the potential of 3D printing in this field. Magnetic materials produced via 3D printing find applications across various sectors – from sensors and drives to medical devices and data storage systems. As 3D printing continues to advance, more innovative uses of magnetic materials are anticipated in the future.

4. Prospects for the development of 3D printing with magnetic materials

While modern 3D printing offers numerous advantages, certain inherent features pose challenges in creating magnetic materials. The key current issues and potential solutions associated with 3D printing of magnetic materials are listed below [32].

4.1. Low magnetic properties

3D-printed magnetic materials often exhibit lower magnetic properties compared to traditionally manufactured ones. This discrepancy arises due to the inherent porosity in materials produced through 3D printing, resulting in slightly reduced material density and subsequently lower magnetic performance.

One potential solution involves the development of improved magnetic powders and further optimization of technological parameters in the 3D printing process.

4.2. Limited accuracy

Another characteristic challenge in 3D printing magnetic materials is the limited accuracy of the printing process. Despite significant advancements in accuracy and surface quality, 3D printing still falls short compared to traditional methods like CNC machining. This limitation becomes critical when intricate micro-sized parts from magnetic materials are necessary. Minor alterations in the geometry of a printed part can substantially impact the material's magnetic properties, potentially restricting its utility in specific applications.

Selecting a 3D printing method based on desired surface quality and detail, with minimal post-processing, could mitigate this issue to some extent.

4.3. Requirements for post-processing

A notable challenge in 3D printing magnetic materials is the necessity for post-processing to attain the desired magnetic properties. This often involves subsequent heat treatments and mechanical adjustments, particularly for enhancing surface quality. However, it's worth noting that traditional methods also frequently require substantial post-processing.

4.4. Limited scalability

One of the significant unresolved challenges in 3D printing magnetic materials pertains to the limited scalability of the process. Despite its flexibility and customization capabilities, 3D printing is currently unable to match the scale or speed of traditional manufacturing technologies.

While 3D printing excels in small batch production and prototyping, it might not be suitable for large-scale manufacturing due to its restricted scalability. Additionally, the limited range of available materials and the need for post-processing can further hinder the scalability of 3D printing for magnetic materials. Nonetheless, emerging technologies like *Big Area Additive Manufacturing* (BAAM) and *Wire Arc Additive Manufacturing* (WAAM) [97] are starting to enable the printing of virtually unlimited sizes, potentially addressing this limitation [97].

Conclusion

In conclusion, the utilization of 3D printing for magnetic materials holds the potential to transform numerous industries by facilitating the creation of intricate designs with complex geometries previously unachievable through conventional manufacturing methods. The combination of 3D printing with magnetism integration presents remarkable possibilities for manipulating and controlling soft robots and drives, particularly in highly demanding environments such as targeted medicine delivery within the body. Nevertheless, several challenges currently impede the seamless implementation of 3D printing for magnetic materials, including lower magnetic properties, limited printing accuracy, post-processing requirements, and scalability limitations. Despite these obstacles, the advancement of 3D printing technology for magnetic materials remains an extremely promising area of research. Overcoming these challenges could unlock even greater opportunities in the future, fostering innovation and opening doors to new applications and advancements across various industries.

References / Список литературы

1. Gutfleisch O., Willard M.A., Brück E., Chen C.H., Sankar S.G., P. Liu J. Magnetic materials and devices for the 21st century: Stronger, lighter, and more energy efficient. *Advanced Materials*. 2011;23(7):821–842. https://doi.org/10.1002/adma.201002180
2. Jang S.M., Seo H.J., Park Y.S., Park H.Il, Choi J.Y. Design and electromagnetic field characteristic analysis of 1.5 kW small scale wind power generator for substitution of Nd–Fe–B to ferrite permanent magnet. *IEEE Transactions on Magnetics*. 2012;48(11):2933–2936. http://doi.org/10.1109/TMAG.2012.2203111
3. Zhao W., Lipo T.A., Kwon B.Il. Comparative study on novel dual stator radial flux and axial flux permanent magnet motors with ferrite magnets for traction application. *IEEE Transactions on Magnetics*. 2014;50(11):8104404. http://doi.org/10.1109/TMAG.2014.2329506
4. Mao Y., Yu K., Isakov M.S., Wu J., Dunn M.L., Qi H.J. Sequential self-folding structures by 3D printed digital shape memory polymers. *Scietific Reports*. 2015;5:13616. http://doi.org/10.1038/srep13616
5. Yuk H., Lu B., Lin S., Qu K., Xu J., Luo J., Zhao X. 3D printing of conducting polymers. *Nature Communications*. 2020;11:1604. http://doi.org/10.1038/s41467-020-15316-7
6. Kanyilmaz A., Demir A.G., Chierici M., Berto F., Gardner L., Kandukuri S. Y., Kassabian P., Kinoshita T., Laurenti A., Paoletti I., Plessis A., Razavi N. Role of metal 3D printing to increase quality and resource-efficiency in the construction sector. *Additive Manufacturing*. 2022;50: 102541. http://doi.org/10.1016/j.addma.2021.102541
7. Velásquez-García L.F., Kornbluth Y. Biomedical applications of metal 3D printing. *Annual Review of Biomedical Engineering*. 2021;23:307–338. http://doi.org/10.1146/annurev-bioeng-082020-032402
8. Geng S., Luo Q., Liu K., Li Y., Hou Y., Long W. Research status and prospect of FDM metal 3D printing. Case stu-

dies in construction. *Materials*. 2023;18:e01952. http://doi.org/10.15980/j.tzzz.2023.02.004

9. Chen Zh., Li Z., Li J., Liu Ch., Lao Ch., Fu Y., Liu Ch., Li Y., Wang P., He Y. 3D printing of ceramics: A review. *Journal of the European Ceramic Society*. 2019;39(4):661–687. http://doi.org/10.1016/j.jeurceramsoc.2018.11.013
10. Du X., Fu S., Zhu Y. 3D printing of ceramic-based scaffolds for bone tissue engineering: An overview. *Journal of Materials Chemistry B*. 2018;6:4397–4412. http://doi.org/10.1039/c8tb00677f
11. Ly M., Spinelli S., Hays S., Zhu D. 3D printing of ceramic biomaterials. *Engineered Regeneration*. 2022;3(1):41–52. http://doi.org/10.1016/j.engreg.2022.01.006
12. Kokkinis D., Schaffner M., Studart A.R. Multimaterial magnetically assisted 3D printing of composite materials. *Nature Communication*. 2015;6:8643. http://doi.org/10.1038/ncomms9643
13. Saran O.S., Reddy A.P., Chaturya L., Kumar M.P. 3D printing of composite materials: A short review. *Materials Today Proceeding*. 2022;64(1):615–619. http://doi.org/10.1016/j.matpr.2022.05.144
14. Yuan C., Wang F., Qi B., Ding Z., Rosen D.W., Ge Q. 3D printing of multi-material composites with tunable shape memory behavior. *Materials and Design*. 2020;193: 108785. http://doi.org/10.1016/j.matdes.2020.108785
15. Kafle A., Luis E., Silwal R., Pan H.M., Shrestha P.L., Bastola A.K. 3D/4D printing of polymers: Fused deposition modelling (FDM), selective laser sintering (SLS), and stereolithography (SLA). *Polymers*. 2021; 13(18):3101. http://doi.org/10.3390/polym13183101
16. Peterson E. What is stereolithography? | 3D printing. URL: https://www.livescience.com/38190-stereolithography.html (accessed: 26.06.2023).
17. Chaudhary R., Fabbri P., Leoni E., Mazzanti F., Akbari R., Antonini C. Additive manufacturing by digital light processing: A review. *Progress in Additive Manufacturing*. 2023;8:331–351. https://doi.org/10.1007/s40964-022-00336-0
18. Quan H., Zhang T., Xu H., Luo S., Nie J., Zhu X. Photo-curing 3D printing technique and its challenges. *Bioactive Materials*. 2020;5:110–115. https://doi.org/10.1016/j.bioactmat.2019.12.003
19. Saitta L., Tosto C., Pergolizzi E., Patti A., Cicala G. Liquid crystal display (LCD) printing: A novel system for polymer hybrids printing. *Macromolecular Symposia*. 2021;395:1–3. https://doi.org/10.1002/masy.202000254
20. Tsolakis I.A., Papaioannou W., Papadopoulou E., Dalampira M., Tsolakis A.I. Comparison in terms of accuracy between DLP and LCD printing technology for dental model printing. *Dentistry Journal*. 2022;10:181. https://doi.org/10.3390/dj10100181
21. Stereolithography (vectorial printing). URL: http://www.mcp.by/technology/?id=1 (accessed: 26.06.2023). (In Russ.).

    Стереолитография (векторная печать). URL: http://www.mcp.by/technology/?id=1 (дата обращения: 26.06.2023).
22. Efremov D.V., Gerasimova A.A. Production of Fe–Cr–Co-based magnets by selective laser sintering. *Steel in Translation*. 2021;51:688–692. http://doi.org/10.3103/S0967091221100028

    Ефремов Д.Б., Герасимова А.А. Получение магнитов из материала системы Fe–Cr–Co методами селективного лазерного спекания. *Известия вузов. Черная металлургия*. 2021;64(10):721–727. https://doi.org/10.17073/0368-0797-2021-10-721-727
23. Han W., Kong L., Xu M. Advances in selective laser sintering of polymers. *International Journal of Extreme Manufacturing*. 2022;4:042002. http://doi.org/10.1088/2631-7990/ac9096
24. Maltseva V.E., Andreev S.V., Neznakhin D.S., Urzhumtsev A.N., Selezneva N.V., Volegov A.S. The magnetic properties of a NdFeB permanent magnets prepared by selective laser sintering. *Physics of Metals and Metallography*. 2022;123(8):740–745. http://doi.org/10.1134/S0031918X2208004X

    Мальцева В.Е., Андреев С.В., Незнахин Д.С., Уржумцев А.Н., Селезнева Н.В., Волегов А.С. Магнитные свойства постоянных магнитов NdFeB, изготовленных методом селективного лазерного спекания. *Физика металлов и металловедение*. 2022;123(8):789–795.
25. Gokuldoss P.K., Kolla S., Eckert J. Additive manufacturing processes: Selective laser melting, electron beam melting and binder jetting-selection guidelines. *Materials*. 2017;10(6):672. http://doi.org/10.3390/ma10060672
26. Paranthaman M.P., Shafer C.S., Elliott A.M., Siddel D.H., McGuire M.A., Springfield R.M., Martin J., Fredette R., Ormerod J. Binder jetting: A novel NdFeB bonded magnet fabrication process. *JOM*. 2016;68(7):1978–1982. http://doi.org/10.1007/s11837-016-1883-4
27. Shakor P., Chu S.H., Puzatova A., Dini E. Review of binder jetting 3D printing in the construction industry. *Progress in Additive Manufacturing*. 2022;7:643–669. http://doi.org/10.1007/s40964-021-00252-9
28. Ziaee M., Crane N.B. Binder jetting: A review of process, materials, and methods. *Additive Manufacturing*. 2019;28: 781–801. http://doi.org/10.1016/j.addma.2019.05.031
29. Chatzipirpiridis G., Gervasoni S., Fischer C., Ergeneman O., Pellicer E., Nelson B.J., Pané S. 3D printing of thermoplastic-bonded soft- and hard-magnetic composites: Magnetically tuneable architectures and functional devices. *Advanced Intelligent Systems*. 2019;1(6):1900069. http://doi.org/10.1002/aisy.201900069
30. Ziemann S.J., Fischer N.A., Lu J., Lee T.J., Ennis M., Höft T.A., Nelson-Cheeseman B. Hard magnetic elastomers incorporating magnetic annealing and soft magnetic particulate for fused deposition modeling. *AIP Advances*. 2022;12:115305. http://doi.org/10.1063/5.0119669
31. Wan X., Luo L., Liu Y., Leng J. Direct ink writing based 4D printing of materials and their applications. *Advanced Science*. 2020;7(16):2001000. http://doi.org/10.1002/advs.202001000
32. Wei X., Jin M.L., Yang H., Wang X.X., Long Y.Z., Chen Z. Advances in 3D printing of magnetic materials: Fabrication, properties, and their applications. *Journal of Advanced Ceramics*. 2022;11(5):665–701. http://doi.org/10.1007/s40145-022-0567-5
33. Ozerov A. What is Binder Jetting and how to fabricate a mold within twenty-four hours. URL: https://blog.iqb.ru/binder-jetting/ (accessed: 26.06.2023). (In Russ.).

Озеров А. Что такое Binder Jetting и как изготовить литейную форму за сутки. URL: https://blog.iqb.ru/binder-jetting/ (дата обращения: 26.06.2023).

34. Technologies. Digital laboratory FABLAB. URL: https://fablab.vvsu.ru/about/technologies/ (accessed: 26.06.2023). (In Russ.).

Технологии. Цифровая лаборатория FABLAB. URL: https://fablab.vvsu.ru/about/technologies/ (дата обращения: 26.06.2023).

35. Körner C. Additive manufacturing of metallic components by selective electron beam melting – A review. *International Materials Reviews*. 2016;61:361–377. http://doi.org/10.1080/09506608.2016.1176289

36. Radulov I.A., Popov V.V.Jr., Koptyug A., Maccari F., Kovalevsky A., Essel S., Gassmann J., Skokov K.P., Bamberger M. Production of net-shape Mn–Al permanent magnets by electron beam melting. *Additive Manufacturing*. 2019;30:100787. http://doi.org/10.1016/j.addma.2019.100787

37. Additive fabrication of products from metals and alloys by an electron beam: Direct deposition of energy and material to the melting zone (part 2). URL: https://additiv-tech.ru/publications/additivnoe-formoobrazovanie-izdeliy-iz-metallov-i-splavov-puchkom-elektronov-pryamaya (accessed: 26.06.2023). (In Russ.).

Аддитивное формообразование изделий из металлов и сплавов пучком электронов: Прямая подача энергии и материала в зону плавления (часть 2). URL: https://additiv-tech.ru/publications/additivnoe-formoobrazovanie-izdeliy-iz-metallov-i-splavov-puchkom-elektronov-pryamaya (дата обращения: 26.06.2023).

38. What is 3D printing – 3D Printer for sale. URL: http://d3dprinter.com/docs/3d-printting-document/what-is-3d-printing/ (accessed: 26.06.2023).

39. Jinoop A.N., Paul C.P., Bindra K.S. Laser assisted direct energy deposition of Hastelloy-X. *Optics and Laser Technology*. 2019;109:14–19. http://doi.org/10.1016/j.optlastec.2018.07.037

40. Sun K., Li F., Rong C., Zuo L. Direct energy deposition applied to soft magnetic material additive manufacturing. *Journal of Manufacturing Processes*. 2022;84:162–173. http://doi.org/10.1016/j.jmapro.2022.10.004

41. Mumtaz K.A., Erasenthiran P., Hopkinson N. High density selective laser melting of Waspaloy®. *Journal of Materials Processing Technology*. 2007;195(1–3):77–87. https://doi.org/10.1016/j.jmatprotec.2007.04.117

42. Chaudhary V., Mantri S.A., Ramanujan R.V., Banerjee R. Additive manufacturing of magnetic materials. *Progress in Materials Science*. 2020;114:100688. http://doi.org/10.1016/j.pmatsci.2020.100688

43. Périgo E.A., Jacimovic J., Ferré F.G., Scherf L.M. Additive manufacturing of magnetic materials. *Additive Manufacturing*. 2019;30:100870. http://doi.org/10.1016/j.addma.2019.100870

44. Goll D., Schuller D., Martinek G., Kunert T., Schurr J., Sinz C., Schubert T., Bernthaler T., Riegel H., Schneider G. Additive manufacturing of soft magnetic materials and components. *Additive Manufacturing*. 2019;27:428–439. http://doi.org/10.1016/j.addma.2019.02.021

45. Lin D., Yang F., Gong D., Li R. Bio-inspired magnetic-driven folded diaphragm for biomimetic robot. *Nature Communications*. 2023;14:163. http://doi.org/10.1038/s41467-023-35905-6

46. Wang D., Wang J., Shen Z., Jiang Ch., Zou J., Dong L., Fang N.X., Gu G. Soft actuators and robots enabled by additive manufacturing. *Annual Review of Control, Robotics, and Autonomous Systems*. 2023;6:31–63. http://doi.org/10.1146/annurev-control-061022-012035

47. Hu X., Liang Z., Li Q., Hu S., Qu S. Experimental study on the magnetic permeability of inclusion filled soft polymeric composite for soft-core transformer applications. *Polymer Testing*. 2022;106:107430. http://doi.org/10.1016/j.polymertesting.2021.107430

48. Ram B.S., Paul A.K., Kulkarni S.V. Soft magnetic materials and their applications in transformers. *Journal of Magnetism and Magnetic Materials*. 2021;537:168210. http://doi.org/10.1016/j.jmmm.2021.168210

49. Tan E.L., Pereles B.D., Shao R., Ong J., Ong K.G. A wireless, passive strain sensor based on the harmonic response of magnetically soft materials. *Smart Materials and Structures*. 2008;17:025015. http://doi.org/10.1088/0964-1726/17/2/025015

50. Ahmad H.S., Hussain T., Nawab Y., Salamat S. Effect of dielectric and magnetic nanofillers on electromagnetic interference shielding effectiveness of carbon/epoxy composites. *Journal of Composite Materials*. 2022;56(1):69–82. http://doi.org/10.1177/00219983211052615

51. Gurusiddesh M., Madhu B.J., Shankaramurthy G.J. Structural, dielectric, magnetic and electromagnetic interference shielding investigations of polyaniline decorated $Co_{0.5}Ni_{0.5}Fe_2O_4$ nanoferrites. *Journal of Material Science: Materials in Electronics*. 2018;29(4):3502–3509. http://doi.org/10.1007/s10854-017-8285-4

52. Li B., Zhang L., Fu W., Xu H. General investigations on manufacturing quality of permalloy via selective laser melting for 3D printing of customized magnetic shields. *JOM*. 2020;72(8):2834–2844. http://doi.org/10.1007/s11837-019-03979-7

53. Yang J., Zhu Q., Wang Z., Xiong F., Li Q., Yang F., Li R., Ge X., Wang M. Effects of metallurgical defects on magnetic properties of SLM NiFeMo permalloy. *Materials Characterization*. 2023;197:112672. http://doi.org/10.1016/j.matchar.2023.112672

54. Garibaldi M., Ashcroft I., Simonelli M., Hague R. Metallurgy of high-silicon steel parts produced using Selective Laser Melting. *Acta Materialia*. 2016;110:207–216. http://doi.org/10.1016/j.actamat.2016.03.037

55. Coey J.M.D. Hard magnetic materials: A perspective. *IEEE Transactions on Magnetics*. 2011;47(12):4671–4681. http://doi.org/10.1109/TMAG.2011.2166975

56. Gorelikov E.S., Tarasov V.P., Kutepov A.V., Osipenkova A.A. The influence of gallium and copper on the corrosion properties of magnetically hard materials of the Nd–Fe–B system. *Tsvetnye Metally*. 2018;7:12–16. (In Russ.). http://doi.org/10.17580/tsm.2018.07.02

Гореликов Е.С., Тарасов В.П., Кутепов А.В., Осипенкова А.А. Влияние галлия и меди на коррозионные свойства магнитотвердых материалов системы Nd–Fe–B. *Цветные металлы*. 2018;7:12–16.

57. Manaf A., Buckley R.A., Davies H.A. New nanocrystalline high-remanence Nd–Fe–B alloys by rapid solidification. *Journal of Magnetism and Magnetic Materials*. 1993;128(3):302–306. http://doi.org/10.1016/0304-8853(93)90475-H

58. Li D., Pan D., Li Sh., Zhang Zh. Recent developments of rare-earth-free hard-magnetic materials. *Science China: Physics, Mechanics and Astronomy*. 2016;59(1):617501. http://doi.org/10.1007/s11433-015-5760-x

59. Coey J.M.D. Perspective and prospects for rare earth permanent magnets. *Engineering*. 2020;6:119–131. https://doi.org/10.1016/j.eng.2018.11.034

60. Huber C., Mitteramskogler G., Goertler M., Teliban V., Groenefeld M., Suess D. Additive manufactured isotropic NdFeB magnets by stereolithography, fused filament fabrication, and selective laser sintering. *Materials*. 2020;13:1916. http://doi.org/10.3390/ma13081916

61. Jacimovic J., Christen T., Dénervaud E. Self-organized giant magnetic structures via additive manufacturing in NdFeB permanent magnets. *Additive Manufacturing*. 2020;34:101288. http://doi.org/10.1016/j.addma.2020.101288

62. Pigliaru L., Paleari L., Bragaglia M., Nanni F., Ghidini T., Rinaldi M. Poly-ether-ether-ketone – Neodymium-iron-boron bonded permanent magnets via fused filament fabrication. *Synthetic Metals*. 2021;279:116857. http://doi.org/10.1016/j.synthmet.2021.116857

63. Volegov A.S., Andreev S.V., Selezneva N.V., Ryzhikhin I.A., Kudrevatykh N. V., Mädler L., Okulov I.V. Additive manufacturing of heavy rare earth free high-coercivity permanent magnets. *Acta Materialia*. 2020;188:733–739. https://doi.org/10.1016/j.actamat.2020.02.058

64. Pelevin I.A., Ozherelkov D.Y., Chernyshikhin S.V., Nalivaiko A.Y., Gromov A.A., Chzhan V.B., Terekhin E.A., Tereshina I.S. Selective laser melting of Nd–Fe–B: Single track study. *Materials Letters*. 2022;315:131947. https://doi.org/10.1016/j.matlet.2022.131947

65. Pelevin I.A., Terekhin E.A., Ozherelkov D.Y., Tereshina I.S., Karpenkov D.Y., Bochkanov F.Y., Chernyshikhin S.V., Nalivaiko A.Y., Gromov A.A. New scanning strategy approach for laser powder bed fusion of Nd–Fe–B hard magnetic material. *Metals*. 2023;13:1084. https://doi.org/10.3390/met13061084

66. Kume M., Hayashi M., Yamamoto M., Kawamura K., Ihara K. Heat resistant plastic magnets. *IEEE Transactions on Magnetics*. 2005;41(10):3895–3897.

67. Osawa Z., Kawauchi K. Effect of polymer matrices on magnetic properties of plastic magnets. *Journal of Materials Science*. 1988;23:2637–2644. http://doi.org/10.1007/BF01111926

68. Huber C., Abert C., Bruckner F., Groenefeld M., Schuschnigg S., Teliban I., Vogler C., Wautischer G., Windl R., Suess D. 3D printing of polymer-bonded rare-earth magnets with a variable magnetic compound fraction for a predefined stray field. *Scientific Reports*. 2017;7(1):9419. http://doi.org/10.1038/s41598-017-09864-0

69. Rösel U., Drummer D. Possibilities in recycling magnetic materials in applications of polymer-bonded magnets. *Magnetism*. 2022;2(3):251–270. http://doi.org/10.3390/magnetism2030019

70. Shen A., Peng X., Bailey C.P., Dardona S., Ma A.W.K. 3D printing of polymer-bonded magnets from highly concentrated, plate-like particle suspensions. *Materials and Design*. 2019;183:108133. http://doi.org/10.1016/j.matdes.2019.108133

71. Ormerod J., Constantinides S. Bonded permanent magnets: Current status and future opportunities (invited). *Journal of Applied Physics*. 1997;81(8):4818–4820. http://doi.org/10.1063/1.365471

72. Zhai F., Sun A., Yuan D., Wang J., Wu S., Volinsky A., Wang Z. Epoxy resin effect on anisotropic Nd–Fe–B rubber-bonded magnets performance. *Journal of Alloys and Compounds*. 2011;509(3):687–690. http://doi.org/10.1016/j.jallcom.2010.09.210

73. Kirchmayr H.R. Permanent magnets and hard magnetic materials. *Journal of Physics D: Applied Physics*. 1996;29(11): 2763–2778. http://doi.org/10.1088/0022-3727/29/11/007

74. Olano A., Ren J., Zhang G., Tang H., Zhang T., Li J. Improvements in miniaturized Hall Thrusters by use of high-temperature SmCo magnets and additive manufacturing techniques. *IOP Conference Series: Materials Science and Engineering*. 2019;576(1):012002. http://doi.org/10.1088/1757-899X/576/1/012002

75. Amirov A., Omelyanchik A., Murzin D., Kolesnikova V., Vorontsov S., Musov I., Musov Kh., Khashirova S., Rodionova V. 3D printing of PLA/magnetic ferrite composites: Effect of filler particles on magnetic properties of filament. *Processes*. 2022;10(11):2412. http://doi.org/10.3390/pr10112412

76. Hu Y., Zou B., Xing H., Liu J., Chen Q., Wang X., Li L. Preparation of Mn–Zn ferrite ceramic using stereolithography 3D printing technology. *Ceramics International*. 2022;48(5):6923–6932. http://doi.org/10.1016/j.ceramint.2021.11.248

77. Peng E., Wei X., Herng T.S., Garbe U., Yu D., Ding J. Ferrite-based soft and hard magnetic structures by extrusion free-forming. *RSC Advances*. 2017;7(43):27128–27138. http://doi.org/10.1039/c7ra03251j

78. Khatri B., Lappe K., Noetzel D., Pursche K., Hanemann T. A 3D-printable polymer-metal soft-magnetic functional composite-development and characterization. *Materials*. 2018;11(2):189. http://doi.org/10.3390/ma11020189

79. Zhang C., Li X., Jiang L., Tang D., Xu H., Zhao P., Fu J., Zhou Q., Chen Y. 3D printing of functional magnetic materials: From design to applications. *Advanced Functional Materials*. 2021;31(34):2102777. http://doi.org/10.1002/adfm.202102777

80. Lazarus N., Bedair S.S., Smith G.L. Creating 3D printed magnetic devices with ferrofluids and liquid metals. *Additive Manufacturing*. 2019;26:15–21. http://doi.org/10.1016/j.addma.2018.12.012

81. Sochol R.D., Sweet E., Glick C.C., Wu S.-Y., Yang Ch., Restaino M., Lin L. 3D printed microfluidics and microelectronics. *Microelectronic Engineering*. 2018;189: 52–68. http://doi.org/10.1016/j.mee.2017.12.010

82. Kang Y.G., Lee K.M., Choi G. Rapid prototyping of three-phase AC machine drive system with subtractive and additive manufacturing. *Energies*. 2023;16(5):2266. http://doi.org/10.3390/en16052266

83. Wang Z., Huber C., Hu J., He J., Suess D., Wang S.X. An electrodynamic energy harvester with a 3D printed magnet and optimized topology. *Applied Physics Letters*. 2019;114:013902. http://doi.org/10.1063/1.5074123
84. Truby R.L., Lewis J.A. Printing soft matter in three dimensions. *Nature*. 2016;540:371–378. http://doi.org/10.1038/nature21003
85. Ionov L. Biomimetic hydrogel-based actuating systems. *Advanced Functional Materials*. 2013;23(36):4555–4570. http://doi.org/10.1002/adfm.201203692
86. Tabatabaei S.N., Lapointe J., Martel S. Shrinkable hydrogel-based magnetic microrobots for interventions in the vascular network. *Advanced Robotics*. 2011;25(8): 1049–1067. https://doi.org/10.1163/016918611X568648
87. Suzumori K. Elastic materials producing compliant robots. *Robotics and Autonomous Systems*. 1996;18(1-2):135–140. http://doi.org/10.1016/0921-8890(95)00078-X
88. Rus D.,Tolley M.T. Design, fabrication and control of soft robots. *Nature*. 2015;521(7553):467–475. http://doi.org/10.1038/nature14543
89. Kim J., Chung S.E., Choi S.E., Lee H., Kim J., Kwon S. Programming magnetic anisotropy in polymeric microactuators. *Nature Materials*. 2011;10(10):747–752. http://doi.org/10.1038/nmat3090
90. Kim J., Lee H., Kim J., Kim H., Kwon S. Programming structural color and magnetic anisotropy in polymer composite micrustructure for novel biosystems. In: *2013 Transducers & Eurosensors XXVII: The 17th International conference on solid-state sensors, actuators microsystems (TRANSDUCERS & EUROSENSORS XXVII)* (16–20 June 2013). Barcelona: IEEE, 2013. Vol. 1. P. 1543–1548. http://doi.org/10.1109/Transducers.2013.6627076
91. Jiang D., Liu S., Tang W. Fabrication and manipulation of non-spherical particles in microfluidic channels: A review. *Micromachines*. 2022;13(10):1659. http://doi.org/10.3390/mi13101659
92. Zhu T., Cheng R., Sheppard G. R., Locklin J., Mao L. Magnetic-field-assisted fabrication and manipulation of non-spherical polymer particles in ferrofluid-based droplet microfluidics. *Langmuir*. 2015;31(31):8531–8534. http://doi.org/10.1021/acs.langmuir.5b02097
93. Diller E., Sitti M. Three-dimensional programmable assembly by untethered magnetic robotic micro-grippers. *Advanced Functional Materials*. 2014;24(28):4397–4404 http://doi.org/10.1002/adfm.201400275
94. Hu W., Lum G.Z., Mastrangeli M., Sitti M. Small-scale soft-bodied robot with multimodal locomotion. *Nature*. 2018;554(7690):81–85. http://doi.org/10.1038/nature25443
95. Joyee E.B., Pan Y. Multi-material additive manufacturing of functional soft robot. *Procedia Manufacturing*. 2019;34:566–573. http://doi.org/10.1016/j.promfg.2019.06.221
96. Joyee E.B., Pan Y. A fully three-dimensional printed inchworm-inspired soft robot with magnetic actuation. *Soft Robotics*. 2019;6(3):333–345. http://doi.org/10.1089/soro.2018.0082
97. Hasanov S., Alkunte S., Rajeshirke M., Gupta A., Huseynov O., Fidan I., Alifui-Segbaya F., Rennie A. Review on additive manufacturing of multi-material parts: Progress and challenges. *Journal of Manufacturing and Materials Processing*. 2022;6(1):4. http://doi.org/10.3390/jmmp6010004

Information about the Authors

Gleb A. Konov – Laboratory Assistant of the Russian-Chinese Research Laboratory for functional materials at Peter the Great St. Petersburg Polytechnic University (SPbPU)
ORCID: 0009-0009-3782-3901
E-mail: 071133gleb@mail.ru

Alina K. Mazeeva – Cand. Sci. (Eng.), Associate Professor at Research and Educational Center "Structural and functional materials", SPbPU
ORCID: 0000-0002-8980-0869
E-mail: mazeevaalina@gmail.com

Dmitry V. Masaylo – Cand. Sci. (Eng.), Associate Professor at Research and Educational Center "Structural and functional materials", SPbPU
ORCID: 0000-0001-5516-9848
E-mail: dmasaylo@gmail.com

Nikolay G. Razumov – Cand. Sci. (Eng.), Associate Professor at Research and Educational Center "Structural and functional materials", SPbPU
ORCID: 0000-0002-7147-6239
E-mail: n.razumov@inbox.ru

Anatoly A. Popovich – Dr. Sci. (Eng.), Professor, Director of the Institute of Machinery, Materials and Transport, SPbPU
ORCID: 0000-0002-5974-6654
E-mail: popovicha@mail.ru

Сведения об авторах

Глеб Александрович Конов – лаборант российско-китайской научно-исследовательской лаборатории «Функциональные материалы» Санкт-Петербургского политехнического университета Петра Великого (СПбПУ)
ORCID: 0009-0009-3782-3901
E-mail: 071133gleb@mail.ru

Алина Константиновна Мазеева – к.т.н., доцент научно-образовательного центра «Конструкционные и функциональные материалы» СПбПУ
ORCID: 0000-0002-8980-0869
E-mail: mazeevaalina@gmail.com

Дмитрий Валерьевич Масайло – к.т.н., доцент научно-образовательного центра «Конструкционные и функциональные материалы» СПбПУ
ORCID: 0000-0001-5516-9848
E-mail: dmasaylo@gmail.com

Николай Геннадьевич Разумов – к.т.н., доцент научно-образовательного центра «Конструкционные и функциональные материалы» СПбПУ
ORCID: 0000-0002-7147-6239
E-mail: n.razumov@inbox.ru

Анатолий Анатольевич Попович – д.т.н., проф., директор Института машиностроения, материалов и транспорта СПбПУ
ORCID: 0000-0002-5974-6654
E-mail: popovicha@mail.ru

Contribution of the Authors

G. A. Konov – contributed to data processing and manuscript writing.
A. K. Mazeeva – conceptualized the idea, determed the purpose and objectives of the work, and participated in the discussion of the results.
D. V. Masaylo – conducted searches for published data and summarized them.
N. G. Razumov – conducted critical literature analysis, participated in the discussion of the results, and drew conclusions from the study.
A. A. Popovich – conducted critical analysis of the manuscript, added technical corrections, participated in the discussion of the results, and drew conclusions from the study.

Вклад авторов

Г. А. Конов – обработка данных, подготовка текста статьи.

А. К. Мазеева – концептуализация идеи, определение цели работы и ее задач, участие в обсуждении результатов.

Д. В. Масайло – поиск опубликованных данных и их обобщение.
Н. Г. Разумов – критический анализ литературы, участие в обсуждении результатов, формулировка выводов исследования.
А. А. Попович – критический анализ текста статьи с внесением технических правок, участие в обсуждении результатов, формулировка выводов исследования.

Received 28.06.2023
Revised 31.10.2023
Accepted 03.11.2023

Статья поступила 28.06.2023 г.
Доработана 31.10.2023 г.
Принята к публикации 03.11.2023 г.

Materials and Coatings Fabricated Using the Additive Manufacturing Technologies
Материалы и покрытия, получаемые методами аддитивных технологий

UDC 621.763

https://doi.org/10.17073/1997-308X-2024-1-20-30

Review article
Обзорная статья

Additive manufacturing of continuous fibre reinforced polymer composites using industrial robots: A review

A. V. Sotov, **A. I. Zaytsev**, **A. E. Abdrahmanova**, **A. A. Popovich**

Peter the Great St. Petersburg Polytechnic University
29 Polytekhnicheskaya Str., St. Petersburg 195251, Russian Federation

sotovanton@yandex.ru

Abstract. In recent years, the mechanical engineering sector has undergone significant changes due to the creation and expanding application of new technologies and materials capable of radically improving the quality of manufactured products, the entire structure and production conditions. Such technologies include additive manufacturing capable of creating products from advanced materials such as continuous reinforced polymer composites. Furthermore, the integration of additive manufacturing with industrial robots offers new opportunities to create spatially reinforced composites with a directed internal structure, obtained by the orderly arrangement of continuous fibres. This review analyzes the currently available technologies for 3D printing spatially reinforced polymer composites with the addition of continuous fibers using industrial robots. The review presents the main advanced companies supplying off-the-shelf commercial systems and presents the successful experience of using these systems in the production of reinforced parts.

Keywords: additive manufacturing, polymer composites, continuous fibres, spatially reinforced composites, industrial robots

Acknowledgements: This study was carried out under the grant of Russian Science Foundation No. 23-79-30004, https://rscf.ru/en/project/23-79-30004/.

For citation: Sotov A.V., Zaytsev A.I., Abdrahmanova A.E., Popovich A.A. Additive manufacturing of continuous fibre reinforced polymer composites using industrial robots: A review. *Powder Metallurgy and Functional Coatings*. 2024;18(1):20–30. https://doi.org/10.17073/1997-308X-2024-1-20-30

Аддитивное производство непрерывно армированных полимерных композитов с использованием промышленных роботов: Обзор

А. В. Сотов, **А. И. Зайцев**, **А. Э. Абдрахманова**, **А. А. Попович**

Санкт-Петербургский политехнический университет Петра Великого
Россия, 195251, г. Санкт-Петербург, ул. Политехническая, 29

sotovanton@yandex.ru

Аннотация. В последние годы в машиностроительном комплексе происходят значительные изменения, связанные с созданием и расширяющимся применением новых технологий и материалов, способных коренным образом улучшить качественные показатели выпускаемых изделий, всю структуру и условия производства. К таким технологиям относятся технологии аддитивного производства, с помощью которых возможно изготовление изделий из передовых материалов – к ним относятся непрерывно армированные полимерные композиты. В свою очередь, интеграция аддитивных технологий с промышленными роботами открывает новые возможности создания пространственно армированных композитов с направленной внутренней структурой, получаемой за счет упорядоченного расположения непрерывных волокон. В данном обзоре проведен анализ существующих на сегодняшний день технологий 3D-печати пространственно армированных полимерных компози-

ционных материалов с добавлением непрерывных волокон на базе промышленных роботов-манипуляторов. Представлены основные передовые компании, поставляющие готовые коммерческие системы, рассмотрен опыт успешного использования данных систем при изготовлении армированных деталей.

Ключевые слова: аддитивное производство, полимерные композиционные материалы, непрерывные волокна, пространственно армированные композиты, промышленные роботы

Благодарности: Исследование выполнено за счет гранта Российского научного фонда № 23-79-30004, https://rscf.ru/project/23-79-30004/.

Для цитирования: Сотов А.В., Зайцев А.И., Абдрахманова А.Э., Попович А.А. Аддитивное производство непрерывно армированных полимерных композитов с использованием промышленных роботов: Обзор. *Известия вузов. Порошковая металлургия и функциональные покрытия*. 2024;18(1):20–30. https://doi.org/10.17073/1997-308X-2024-1-20-30

Introduction

Additive manufacturing (AM) constitutes a swiftly expanding market, attaining significance in the shift towards advanced industrial production. Previously, emphasis predominantly centered on the 3D printing of metal [1–5] and polymer materials [6–9]. However, there exists a burgeoning interest in more intricate applications and innovative material types, commonly referred to as modern or advanced materials. These materials hold potential for implementation across five distinct categories [10]: technical ceramics (oxides, carbides) [11; 12], polymers (such as the PAEK family encompassing PEEK and PEKK) [13; 14], metals (refractory metals like tungsten and molybdenum) [15; 16], 4D materials (materials exhibiting shape memory) [17–20], and composites, specifically polymer composite materials (PCMs) featuring continuous fibers [21; 22].

Presently, traditional PCM production, primarily conducted using woven fiber sheets and thermosetting resins, stands as one of the labor-intensive and costly manufacturing processes [23]. Nonetheless, composites persist as one of the swiftest growing and rapidly evolving industrial segments in the global market. The anticipation is that AM technologies will assume a pivotal role in this evolution, given the array of emerging commercially available technologies and processes.

Recently, VoxelMatters (UK), a company specializing in market research and analytics within the AM industry, unveiled a comprehensive map showcasing technologies and existing companies offering commercial systems for implementing 3D printing processes [24]. This map provides users with insights into the spectrum of extant 3D printing technologies and the evolving landscape of AM across various materials, notably polymer composites. Employees at VoxelMatters [25] highlight that among all material families, polymer composites reinforced with fibers-specifically continuous fibers-possess distinctive properties and advantages. They underscore that leveraging 3D printing technology will augment the utilization of these materials, enabling more efficient, cost-effective, and expedited manufacturing of parts with a unique combination of final functional properties.

There are currently companies offering desktop systems designed for 3D printing of continuous fiber PCM. However, utilizing these 3D printers for PCM manufacturing presents several disadvantages, the primary one being the limitation of fiber placement solely within the plane of the construction platform [26]. This limitation significantly impacts product design and creation since the highest mechanical properties are attained when load application aligns with the direction of reinforcement. This drawback restricts the production of a broad range of parts that experience loads not confined to the same plane. To address these limitations and other issues inherent in desktop 3D printers, specialized equipment is being developed based on industrial robotic manipulators. This approach introduces fresh possibilities and sets new benchmarks for PCM manufacturing. Key advantages include a larger working area facilitated by robotic arms compared to desktop 3D printers, along with the capability to fabricate spatially reinforced polymer composite products. This is made feasible due to the increased degrees of freedom afforded by robot manipulators. Detailed insights into the intricacies of producing such products and materials, encompassing aspects like tool path planning, kinematics, robot collision avoidance, and technological constraints encountered during the printing process, are extensively described in papers.

This review focuses on examining the present-day technologies for 3D printing of spatially reinforced PCM with added continuous fibers through industrial robotic manipulators. It highlights leading advanced companies providing readily available commercial systems and assesses the successful utilization of these systems in producing reinforced parts.

Existing technology of 3D printing for continuously reinforced PCM

The evolution of 3D printing technologies for continuously reinforced PCM has been steady yet notably

swift, resulting in the emergence of various terms and methodologies. Researchers at the Technical University of Munich have endeavored to establish a conceptual framework for standardizing 3D printing processes involving continuously reinforced PCM. The intricacy of this endeavor largely stems from the idiosyncrasies inherent in the execution of printing processes adopted by different companies [29]. Nevertheless, contemporary trends indicate a movement toward categorizing these processes based on the methodologies used for supplying reinforcing and matrix materials to the printing head and their deposition during the part-building process. Fig. 1 provides an overview of the current implementation schemes and identifies companies offering commercial systems for PCM 3D printing incorporating continuous fibers.

It is evident that there are presently five distinct approaches employed in the realization of the robotic 3D printing process for continuously reinforced PCMs using commercially available equipment. Below, a summary of the primary accomplishments attained thus far for each of these schemes is outlined.

1. *In situ* impregnation

The core principle of this technology involves the *in situ* impregnation of continuous dry fiber within the extrusion head of the printer using specialized thermosetting or thermoplastic polymer materials. This is followed by material extrusion through a nozzle and subsequent curing. Among the key companies employing the *in situ* impregnation process via industrial robotic manipulators are Continuous Composites (USA) [33], Orbital Composites (USA) [34], and Moi Composites (Italy) [35]. Predominantly, carbon and basalt fibers serve as the primary reinforcing materials, while less commonly used options include glass fiber and natural fibers.

Continuous Composites, established in 2015, has pioneered a patented 3D printing technology termed *Continuous Fiber 3D Printing* (CF3D). This technique involves the *in situ* impregnation of continuous dry fiber with a specialized fast-curing thermoset resin. As the material is extruded through the nozzle, it undergoes instant curing facilitated by a UV light source. According to the company's reports [36], the utilization of an industrial robot enables material deposition in any direction, optimizing the orientation of reinforcing fibers based on the specific design requirements of the manufactured part. Continuous Composites' patented CF3D technology can be employed with gantry robots or industrial robots, providing flexibility in manufacturing. Utilizing a 6-axis robot from Comau, the company has successfully fabricated intricate parts and components, including a carbon fiber aircraft wing spar element (Fig. 2, *b*).

Continuous Composites employs both structural fibers (such as carbon, glass-filled, and Kevlar) and functional fibers (including optical and metallic fibers) as reinforcing materials. The choice of the matrix polymer material is predicated on mechanical properties, heat transfer characteristics, and environmental resilience, aligning with the operational requisites of the intended product.

The successful application of CF3D technology has extended to several university research laboratories [37–40]. In one study [40], the researchers show-

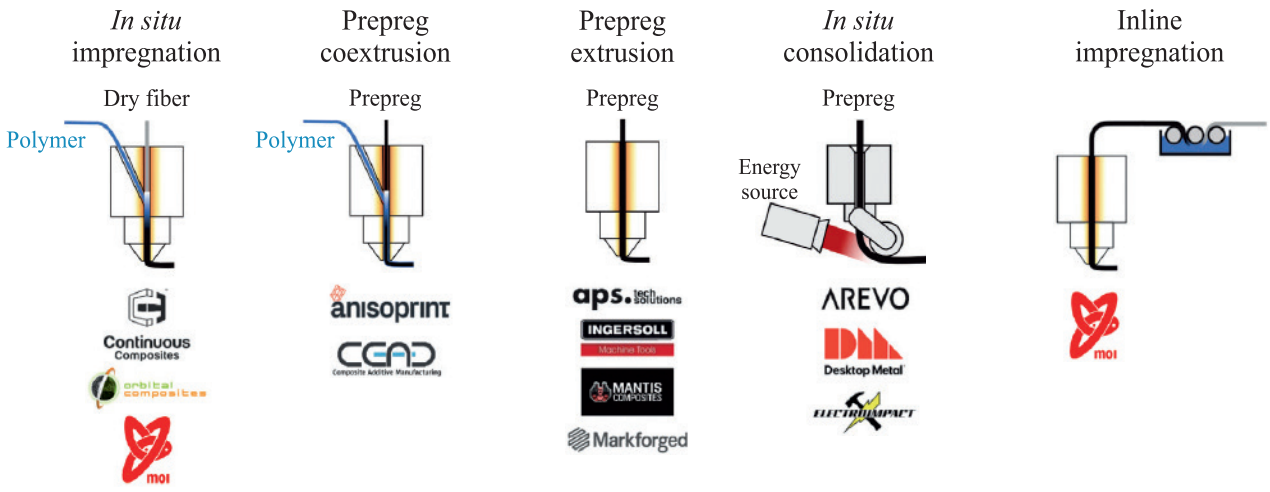

Fig. 1. Processes classification and basic 3D printing companies of continuous fiber reinforced PCM based on an industrial robot [32]

Рис. 1. Схемы реализации процесса и основные компании по 3D-печати непрерывно армированных ПКМ на базе промышленного робота [32]

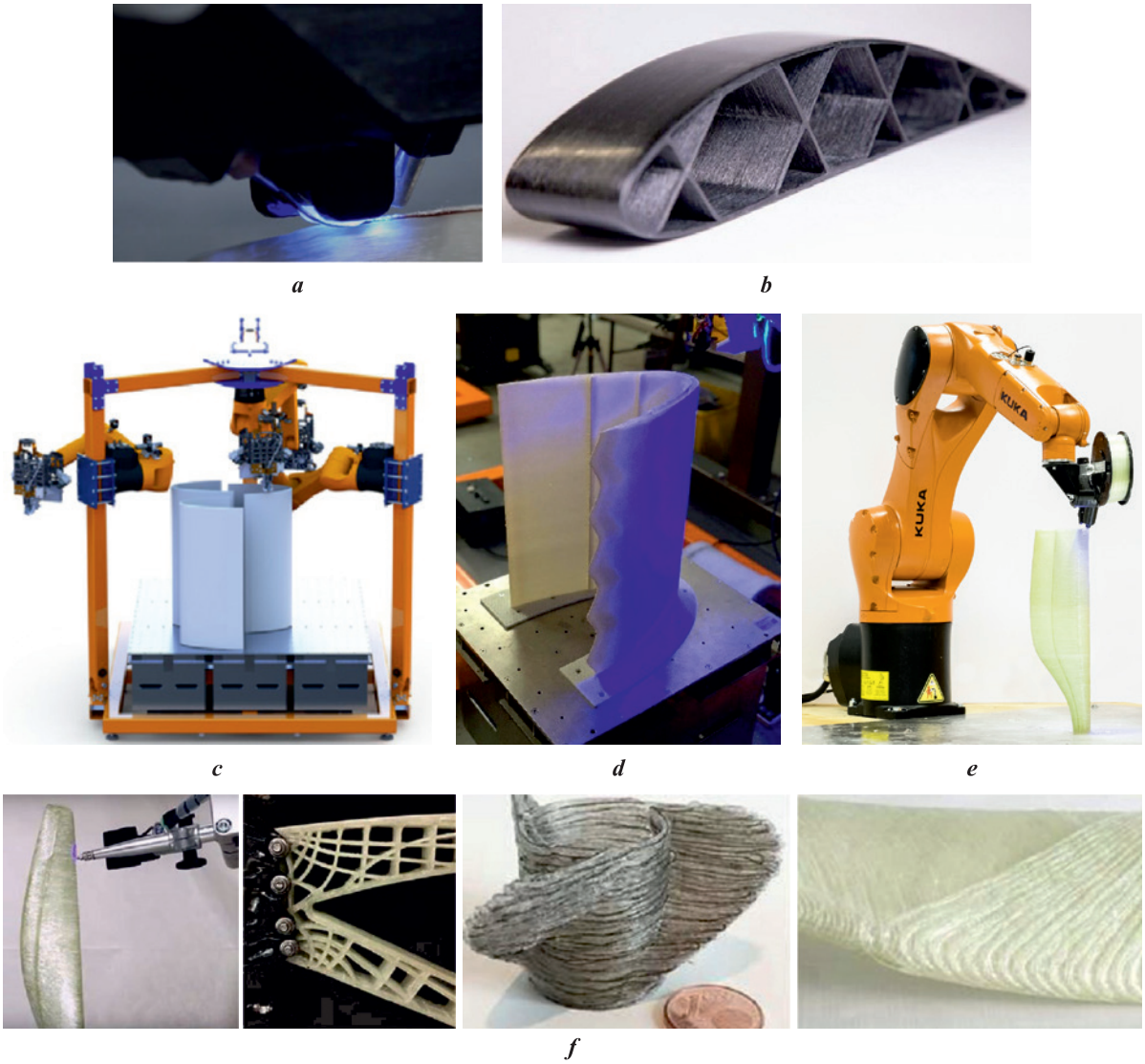

Fig. 2. Examples of the use of 3D printing of PCM by various companies

a, ***b*** – robot-based 3D printing of PCM from "Continuous Composites" (***a***) and carbon fibre aircraft wing spar element for "Lockheed Martin" (***b***) [33];
c, ***d*** – "Orbital S" 3D printer from "Orbital Composites" (***c***) and leading-edge protector for a wind turbine blade (***d***) [34];
e, ***f*** – "Kuka" robotic printing system from "Moi Composites" (***e***) and continuous fibre reinforced complex-shape parts (***f***) [35]

Рис. 2. Примеры использования 3D-печати ПКМ различными компаниями

a, ***b*** – роботизированная 3D-печать от компании «Continuous Composites» (***a***) и элемент лонжерона крыла самолета из углеродного волокна для компании «Lockheed Martin» (***b***) [33]; ***c***, ***d*** – 3D-принтер модели «Orbital S» от компании «Orbital Composites» (***c***) и защита передней кромки для лопасти ветряной установки (***d***) [34]; ***e***, ***f*** – роботизированная система печати на основе робота «Kuka» от компании «Moi Composites» (***e***) и примеры изготовления сложнопрофильных конструкций, армированных непрерывными волокнами (***f***) [35]

cased their investigations into the mechanical properties of PCMs manufactured using CF3D technology via the Comau industrial robotic arm. They examined samples fabricated from high-temperature thermosetting acrylic polymer GF-2, combined with high-strength carbon fiber T-1100 at a volume fraction of 41.5 %. The resulting samples exhibited a Young's modulus of 122 GPa and a tensile strength of 1599 MPa, constituting 89 % (137 GPa) and 55 % (2926 MPa) of the theoretical values, respectively. The authors [40] underscored that these results are notably high within the realm of additive manufacturing, highlighting the promising potential of CF3D technology for manufacturing PCM parts.

Established in 2014, Orbital Composites initially carved its niche in 3D printing components tailored for space applications. Presently, the company is pioneering its proprietary 3D printing technology, entailing the *in situ* impregnation of continuous dry fiber with thermoplastic polymer material, subsequently compacted using a roller. The manufacturer currently offers three distinct types of 3D printers based on industrial robots:

"Orbital e-" – a 6-axis robot geared towards educational and research endeavors, featuring a 1.2×1.2 m building platform capable of printing with high-temperature thermoplastics; "Orbital S" is an industrial-class robot with a unique manipulator movement system, enabling flexible attachment points. This facilitates the printing of large parts from multiple angles (Fig. 2, *c*); "Orbital F" is a container-type 3D printer for producing substantial composite structures of large dimensions.

The 3D printers developed by Orbital Composites possess the capability to heat the nozzle to temperatures surpassing 500 °C. This functionality enables printing with a wide spectrum of matrix materials, encompassing all prevailing low-temperature thermoplastics, in addition to high-temperature materials like PEEK, PEKK, and others.

Founded in 2018 at the Polytechnic University of Milan, Moi Composites has pioneered a 3D printing technology named Continuous Fiber Manufacturing (CFM) for continuously reinforced PCM. This technology involves impregnation utilizing epoxy resin, vinyl ester, and acrylic in conjunction with continuous glass, carbon, basalt, and other fibers (Fig. 2, *e*). Besides manufacturing 3D printers, the company produces 3D printing tool heads capable of integration with any 4-axis CNC machines, offering a flexible and scalable printing solution.

Moi Composites uses various thermosetting matrix materials, including epoxy resin, complex vinyl esters, and acrylic compositions. Continuous glass, carbon, and basalt fibers are employed as reinforcing components. The company is currently developing aramid and natural fibers. The company emphasises the use of acrylic materials for architectural details due to their transparency and the absence of a need for temperature during curing/post-curing. Materials based on complex vinyl esters are employed for marine components, whereas epoxy resin-based materials are favoured for the oil and gas as well as aerospace sectors.

2. Prepreg coextrusion

The underlying principle of this technology involves the coextrusion of a composite comprising preformed prepreg containing continuous fibers along with the addition of a thermoplastic element to facilitate adhesion to the matrix material. Key companies employing the prepreg coextrusion process utilizing robotic manipulators include Anisoprint (Luxembourg) [41] and CEAD (the Netherlands) [42].

Anisoprint, established in 2015, has innovated its own *Continuous Fiber Coextrusion* (CFC) 3D printing technology, employing two nozzles for matrix and reinforcing materials. The reinforcement nozzle comprises two distinct spools: one holding a tow of continuous fibers impregnated with thermoset, while the other contains a thermoplastic filament to enhance adhesion between the reinforcement and the matrix. Both are fed into a single extruder. This configuration of the process enables precise control over the volumetric ratio of fibers, while the utilization of a robot permits the establishment of intricate curvilinear trajectories during the 3D printing process (Fig. 3, *a*). The resulting manufactured parts constitute PCM structures comprising thermoset and thermoplastic polymers, interwoven with continuous fibers.

Several low-temperature thermoplastics like PC, PLA, TPU, PETG, and PA can function effectively as matrix materials. Reinforcement can be achieved using prepregs containing continuous fibers of carbon, glass, aramid, basalt, and boron.

It is noteworthy that, the robotic prepreg coextrusion technology developed by Anisoprint has found extensive application across various industries [43–48]. In a study by the authors of [48], the focus was on investigating the 3D printing of conformal paths using industrial robots to create shell structures composed of PCM through coextrusion technology. The primary stages of the study involved the development of the production system, trajectory planning for conformal paths, and performance testing. The equipment utilized in the study comprised a Universal Robots UR10e robot equipped with a coextrusion head, along with an Anisoprint Composer A4 desktop 3D printer. During the research, three samples were fabricated (Fig. 4): the first sample was produced using 3-axis Composer A4 equipment; in the second sample, the conical part was also crafted on a 3D printer, while the stiffeners were generated by a robotic system; the third sample was manufactured using a conformal method with the robotic system. The part produced conformally using the robotic system exhibited a compressive strength and stiffness that were 258.6 % and 134.9 % higher, respectively, compared to parts created using a 3D printer with three degrees of freedom.

The CEAD company, established in 2014, specializes in manufacturing large-scale robotic 3D printers and is known for developing its proprietary technology known as "Continuous Fiber Additive Manufacturing" (CFAM). This patented technology involves a print head that integrates continuous fibers with molten thermoplastic granules (Fig. 3, *b*, *c*).

3. Prepreg extrusion

The technology involves the extrusion of a composite prepreg impregnated with a thermoplastic polymer and embedded with continuous fibers. One notable com-

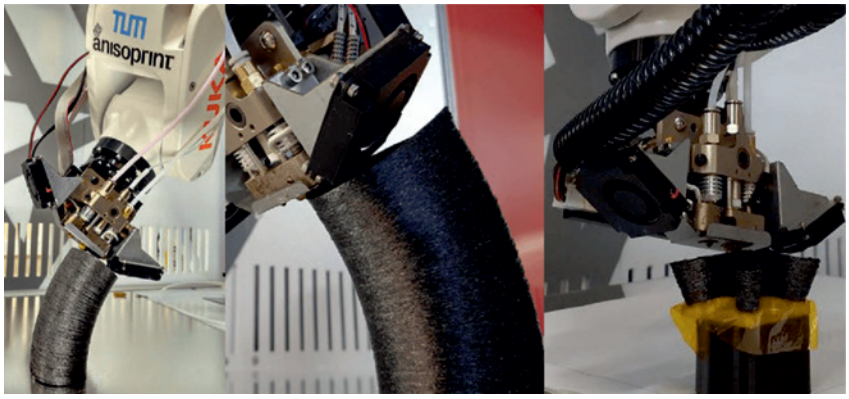

a

b *c*

Fig. 3. Continuous fibre co-extrusion 3D printer based on the Kuka industrial robot from "Anisoprint" (***a***) [44], CEAD's 36 m "Mega II" 3D printer for "Al Seer Marine" (***b***) and composite tooling for boat building (***c***) [42]

Рис. 3. 3D-принтер с коэкструзией непрерывных волокон на базе промышленного робота «Kuka» от компании «Anisoprint» (***a***) [44], 36-метровый 3D-принтер «Mega II» для морской компании «Al Seer Marine» от компании CEAD (***b***) и композитная оснастка для изготовления лодок (***c***) [42]

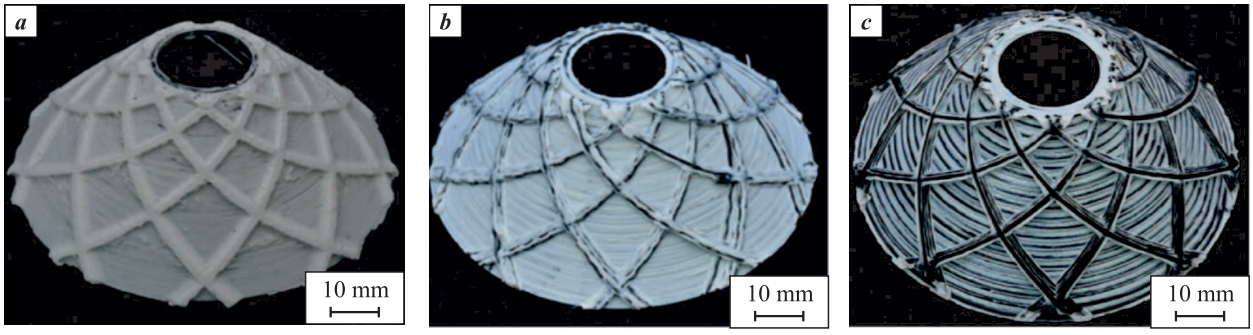

Fig. 4. Sample obtained on 3-axis equipment sample (***a***); sample produced using 3D printer and robotic system (***b***); sample produced conformally by robotic system (***c***) [48]

Рис. 4. Образец, полученный на 3-осевом оборудовании (***a***); образец, изготовленный с использованием 3D-принтера и роботизированной установки (***b***); образец, созданный конформным способом роботизированной системой (***c***) [48]

mercial entity utilizing prepreg extrusion technology alongside industrial robotic manipulators is Ingersoll Machine Tools (USA) [49].

Founded in 1891, Ingersoll Machine Tools became a part of the Camozzi Group Corporation (Italy) in 2003. The company primarily specializes in the manufacturing of precision machines for metalworking, 3D printing, and automated fiber placement. Since 2015, the company has expanded its presence in the AM domain, currently offering five commercially available solutions, including MasterPrint Linear, MasterPrint 3X, and MasterPrint 5X. These machines are designed as large-scale 3D printers tailored for printing large-format PCM. Furthermore, the company presents two additional solutions grounded on industrial robotic arms specifically dedicated to 3D printing continuously reinforced PCM: "MasterPrint Robotic" and "MasterPrint Continuous Filament" (Fig. 5).

4. *In situ* consolidation

In situ consolidation technology, also referred to as automated fiber placement, entails the passage of fiber in prepreg form through a nozzle and subsequent heating with an added heat source directly at the outlet. In the realm of equipment manufacturers, there are companies providing desktop solutions, whereas the primary manufacturer utilizing industrial robots in this domain is the prominent company Electroimpact (USA) [50].

Established in 1986, Electroimpact employs robotic systems for 3D printing through *Automated Fiber Placement* (AFP) technology. The company's developed technology merges the AFP method with FDM 3D printing [51]. This innovative approach involves printing a mold using the FDM method from a soluble polymer material. Continuous fibers are then laid in the form of a narrow ribbon on the mold's surface by heating and sealing using a roller pre-impregnated with synthetic resin non-metallic fibers via the AFP method. After fiber placement, the polymer mold is dissolved. Electroimpact's developments encompass SCRAM (*Scalable Composite Robotic Additive Manufacturing*), a 6-axis machine that combines AFP technology with FDM 3D printing [52].

Continuous fiber tape serves as the reinforcing material, pressed using a specialized roller during installation. The matrix materials primarily comprise thermoplastic polymers from the PAEK family (such as PEEK, PEKK, etc.), alongside nylon and other low-temperature thermoplastics like PA12, ABS, and others. Besides thermoplastics as matrix components, the printing technology also involves the utilization of water-soluble thermoplastics for producing temporary equipment. Fig. 6 showcases a 3D printer from the SCRAM series and a product exemplifying continuously reinforced PCM.

5. Inline impregnation

Inline impregnation technology represents a hybrid process amalgamating the benefits of both conventional and additive manufacturing. In this method, composite fibers are prepared using conventional impregnation processes and subsequently applied to the build platform through a nozzle. As of now, "Moi Composites" (Italy) the company previously mentioned, stands as one of the representatives pioneering this technology.

Conclusions

This review presents an in-depth analysis of existing additive technologies and equipment utilized in the manufacturing of continuously reinforced PCM employing industrial robotic manipulators. It underscores the exceptional relevance and promise of this research domain, particularly in introducing spatially reinforced PCM imbued with distinctive properties for producing components in aviation, marine, nuclear, and other industrial sectors. The technologies discussed in the review are actively employed in the production of large-scale structural components, lightweight and durable aircraft parts, and composite equipment. Beyond structural applications, the utilization of robotic systems opens doors to creating shape-memory polymer

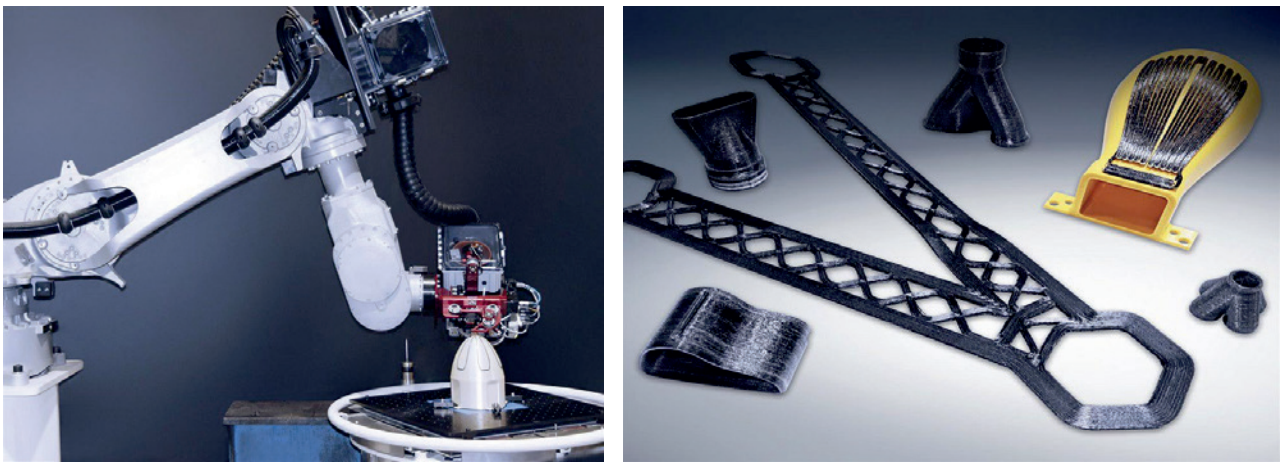

a ***b***

Fig. 5. 3D printing of PCM based on an industrial robot from "Ingersoll Machine Tools" (***a***) and examples of manufactured continuous fiber products (***b***) [49]

Рис. 5. 3D-печать ПКМ на базе промышленного робота-манипулятора от компании «Ingersoll Machine Tools» (***a***) и примеры изготовленных изделий из непрерывного волокна (***b***) [49]

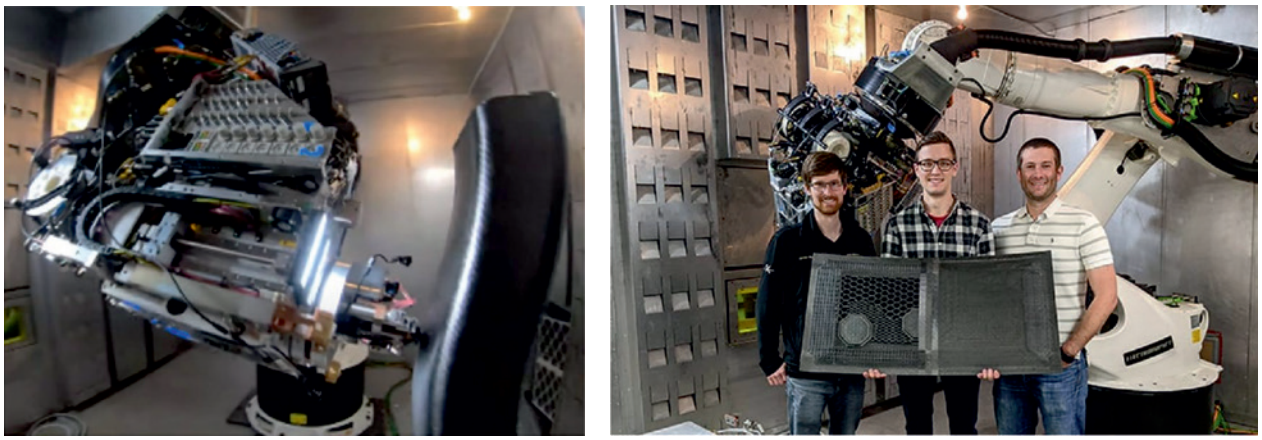

a ***b***

Fig. 6. SCRAM 3D printer in the process of applying fibres to a water-soluble tooling (***a***) and a compartment door element printed from continuously reinforced PCM (***b***) [50]

Рис. 6. 3D-принтер SCRAM в процессе нанесения волокон на водорастворимую оснастку (***a***) и элемент двери отсека, напечатанный из непрерывно армированного ПКМ (***b***) [50]

4D materials for intelligent structures. These structures offer controllable attributes, such as deployable hinge structures for solar panels and mirror antennas in space applications, reconfigurable antenna devices capable of altering directional patterns during operation, and intelligent metamaterial designs with adaptive dynamic characteristics for energy absorption and noise suppression across various frequency bands.

Significantly, the use of industrial robots offers increased degrees of freedom, enabling the fabrication of materials with an ordered arrangement of continuous fibers. This ability facilitates the formation of a directed internal structure in products, accounting for material property anisotropy. The creation of an ordered, directional structure via robotic 3D printing using continuous fibers achieves optimal reinforcing effects, aligning with the operational requirements of the final product. Despite the notable advancements, it's evident from the literature analysis that the development of spatially reinforced PCMs using industrial robots remains an underexplored yet promising research area. The rapid evolution of the additive technology market and its distinctive capabilities in product shaping highlight the immense potential of this field. A key objective in advancing AM within this research domain is the standardization of manufacturing processes for continuously reinforced PCMs using industrial robotic manipulators, with the ultimate aim of deploying these technologies across diverse industries.

Список литературы / References

1. Sefene E.M. State-of-the-art of selective laser melting process: A comprehensive review. *Journal of Manufacturing Systems*. 2022;63:250–274. https://doi.org/10.1016/j.jmsy.2022.04.002
2. Yerubayeva A., Shehab E., Ali M.H. Recent advances and application of Selective Laser Melting (SLM) technology in the aerospace industry. In: *AIP Conference Proceedings* (25 April 2022). AIP Publishing LLC, 2022. Vol. 2470. No. 1. P. 030002. https://doi.org/10.1063/5.0080173
3. Sotov A.V., Agapovichev A.V., Smelov V.G., Kokareva V.V., Zenina M.V. Investigation of the Ni–Co–Cr alloy microstructure for the manufacturing of combustion chamber GTE by selective laser melting. *International Journal of Advanced Manufacturing Technology*. 2019;101:3047–3053. https://doi.org/10.1007/s00170-018-3166-4
4. Ahmed N. Direct metal fabrication in rapid prototyping: A review. *Journal of Manufacturing Processes*. 2019;42:167–191. https://doi.org/10.1016/j.jmapro.2019.05.001
5. Svetlizky D., Das M., Zheng B., Vyatskikh A.L., Bose S., Bandyopadhyay A., Schoenung J.M., Lavernia E.J., Eliaz N. Directed energy deposition (DED) additive manufacturing: Physical characteristics, defects, challenges and applications. *Materials Today*. 2021;49:271–295. https://doi.org/10.1016/j.mattod.2021.03.020
6. Tan L.J., Zhu W., Zhou K. Recent progress on polymer materials for additive manufacturing. *Advanced Functional Materials*. 2020;30(43):2003062. https://doi.org/10.1002/adfm.202003062
7. Saleh Alghamdi S., John S., Roy Choudhury N., Dutta N.K. Additive manufacturing of polymer materials: Progress, promise and challenges. *Polymers*. 2021;13(5):753. https://doi.org/10.3390/polym13050753
8. Gao X., Qi S., Kuang X., Su Y., Li J., Wang D. Fused filament fabrication of polymer materials: A review of interlayer bond. *Additive Manufacturing*. 2021;37:101658. https://doi.org/10.1016/j.addma.2020.101658
9. Szymczyk-Ziółkowska P., Łabowska M.B., Detyna J., Michalak I., Gruber P. A review of fabrication polymer scaffolds for biomedical applications using additive manu-

facturing techniques. *Biocybernetics and Biomedical Engineering*. 2020;40(2):624–638. https://doi.org/10.1016/j.bbe.2020.01.015

10. At the fringe of the fringe of manufacturing. URL: https://www.voxelmatters.com/wp-content/uploads/2020/04/3dpbm-publishes-Advanced-Materials-am-focus-2020-ebook.pdf.pdf (accessed: 20.06.2023)
11. Shuai X., Zeng Y., Li P., Chen J. Fabrication of fine and complex lattice structure Al_2O_3 ceramic by digital light processing 3D printing technology. *Journal of Materials Science*. 2020;55:6771–6782. https://doi.org/10.1007/s10853-020-04503-y
12. Polozov I., Razumov N., Masaylo D., Silin A., Lebedeva Y., Popovich A. Fabrication of silicon carbide fiber-reinforced silicon carbide matrix composites using binder jetting additive manufacturing from irregularly-shaped and spherical powders. *Materials*. 2020;13(7):1766. https://doi.org/10.3390/ma13071766
13. Cicala G., Latteri A., Del Curto B., Lo Russo A., Recca G., Farè S. Engineering thermoplastics for additive manufacturing: A critical perspective with experimental evidence to support functional applications. *Journal of Applied Biomaterials & Functional Materials*. 2017;15(1):10–18. https://doi.org/10.5301/jabfm.5000343
14. Francis J.N., Banerjee I., Chugh A., Singh J. Additive manufacturing of polyetheretherketone and its composites: A review. *Polymer Composites*. 2022;43(9):5802–5919. https://doi.org/10.1002/pc.26961
15. Padmakumar M. Additive manufacturing of tungsten carbide hardmetal parts by selective laser melting (SLM), selective laser sintering (SLS) and binder jet 3D printing (BJ3DP) techniques. *Lasers Manufacturing and Materials Processing*. 2020;7(3):338–371. https://doi.org/10.1007/s40516-020-00124-0
16. Talignani A., Seede R., Whitt A., Zheng S., Ye J., Karaman I., Kirka M.M., Kato Y., Wang Y.M. A review on additive manufacturing of refractory tungsten and tungsten alloys. *Additive Manufacturing*. 2022;103009. https://doi.org/10.1016/j.addma.2022.103009
17. Sotov A., Kantyukov A., Popovich A., Sufiiarov V. A review on additive manufacturing of functional gradient piezoceramic. *Micromachines*. 2022;13(7):1129. https://doi.org/10.3390/mi13071129
18. Sufiiarov V., Kantyukov A., Popovich A., Sotov A. Structure and properties of barium titanate lead-free piezoceramic manufactured by binder jetting process. *Materials*. 2021;14(16):4419. https://doi.org/10.3390/ma14164419
19. Garces I.T., Ayranci C. Advances in additive manufacturing of shape memory polymer composites. *Rapid Prototyping Journal*. 2021;27(2):379–398. https://doi.org/10.1108/RPJ-07-2020-0174
20. Sabahi N., Chen W., Wang C.H., Kruzic J.J., Li X. A review on additive manufacturing of shape-memory materials for biomedical applications. *JOM*. 2020;72(3):1229–1253. https://doi.org/10.1007/s11837-020-04013-x
21. Liu G., Xiong Y., Zhou L. Additive manufacturing of continuous fiber reinforced polymer composites: Design opportunities and novel applications. *Composites Communications*. 2021;27:100907. https://doi.org/10.1016/j.coco.2021.100907
22. Goh G.D., Yap Y.L., Agarwala S., Yeong W.Y. Recent progress in additive manufacturing of fiber reinforced polymer composite. *Advanced Materials Technologies*. 2019;4(1):1800271. https://doi.org/10.1002/admt.201800271
23. Frketic J., Dickens T., Ramakrishnan S. Automated manufacturing and processing of fiber-reinforced polymer (FRP) composites: An additive review of contemporary and modern techniques for advanced materials manufacturing. *Additive Manufacturing*. 2017;14:69–86. https://doi.org/10.1016/j.addma.2017.01.003
24. Map of additive manufacturing technologies. URL: https://www.voxelmatters.com/wp-content/uploads/2019/06/3dpbm-Map-of-Additive-Manufacturing-Technologies-and-Companies-1.svg (accessed: 20.06.2023).
25. Sher D. The new map of composites additive manufacturing technologies. URL: https://www.voxelmatters.com/why-a-map-of-composites-additive-manufacturing-technologies-and-companies-matters-now/ (accessed: 20.06.2023).
26. Li H., Li Z., Wang N., Peng Y., Jiang Z., Zhang Q. Improving the mechanical properties of CCFRPLA by enhancing the interface binding energy and strengthening the anti-separation ability of a PLA matrix. *Polymers*. 2023;15(11):2554. https://doi.org/10.3390/polym15112554
27. Shah A. Emerging trends in robotic aided additive manufacturing. *Materials Today: Proceedings*. 2022;62:7231–7237. https://doi.org/10.1016/j.matpr.2022.03.680
28. Fry N.R., Richardson R.C., Boyle J.H. Robotic additive manufacturing system for dynamic build orientations. *Rapid prototyping journal*. 2020;26(4):659–667. https://doi.org/10.1108/RPJ-09-2019-0243
29. Bhatt P.M., Kulkarni A., Malhan R.K., Shah B.C., Yoon Y.J., Gupta S.K. Automated planning for robotic multi-resolution additive manufacturing. *Journal of Computing and Information Science in Engineering*. 2022; 22(2):021006. https://doi.org/10.1115/1.4052083
30. Lettori J., Raffaeli R., Bilancia P., Peruzzini M., Pellicciari M. A review of geometry representation and processing methods for cartesian and multiaxial robot-based additive manufacturing. *International Journal of Advanced Manufacturing Technology*. 2022;123(11-12):3767–3794. https://doi.org/10.3390/app11114825
31. Yao Y., Zhang Y., Aburaia M., Lackner M. 3D printing of objects with continuous spatial paths by a multi-axis robotic FFF platform. *Applied Sciences*. 2021;11(11):4825. https://doi.org/10.3390/app11114825
32. Ginger G. The evolution of additive composites. URL: https://www.compositesworld.com/articles/the-evolution-of-additive-composites (accessed: 20.06.2023).
33. Continuous composites. URL: https://www.continuous-composites.com/technology (accessed: 21.06.2023).
34. Orbital composites. URL: https://www.orbitalcomposites.com (accessed: 21.06.2023).
35. Moi composites. URL: https://www.moi.am (accessed: 21.06.2023).
36. Davide Sher. Continuous composites demonstrate CF3D continuous fiber composite AM. URL: https://www.voxelmatters.com/continuous-composites-demonstrate-future-continuous-fiber-composite/ (accessed: 21.06.2023).

37. Parmar H., Khan T., Tucci F., Umer R., Carlone P. Advanced robotics and additive manufacturing of composites: towards a new era in Industry 4.0. *Materials and Manufacturing Processes*. 2022;37(5):483–517. https://doi.org/10.1080/10426914.2020.1866195

38. Furmansti J., Abbott A., Tandon G.P., Flores M., Barnett P., Salviato M., Baur J., Butcher D. Challenges in additively manufactured thermoset continuously reinforced composites. In: *Proceedings for the American Society for Composites – Thirty Seventh Technical Conference 2022* (19–21 September 2022). The University of Arizona, Tucson, Arizona, USA. http://dx.doi.org/10.12783/asc37/36427

39. Baur J.W., Abbott A.C., Tandon G.P., Stranberg N.A., Alvarado T.B. Mechanical properties of additively printed, continuous carbon fiber reinforced, thermosetting composites. In: *SAMPE 2022 Conference and Exhibition* (Charlotte, USA, 23–26 May 2022). Soc. for the Advancement of Material and Process Engineering, 2022.

40. Baur J.W., Abbott A.C., Barnett P.R., Tandon G.P., Furmanski J., Stranberg N.A., Alvarado T.B. Mechanical properties of additively printed, UV cured, continuous fiber unidirectional composites for multifunctional applications. *Journal of Composite Materials*. 2023;57(4):865–882. https://doi.org/10.1177/00219983221146264

41. Anisoprint. URL: https://anisoprint.com (accessed: 21.06.2023).

42. CEAD. URL: https://ceadgroup.com (accessed: 21.06.2023).

43. De Backer W., Bergs A.P., Van Tooren M.J. Multi-axis multi-material fused filament fabrication with continuous fiber reinforcement. In: *AIAA/ASCE/AHS/ASC Structures, Structural Dynamics, and Materials Conference 2018*. P. 0091. https://doi.org/10.2514/6.2018-0091

44. Azarov A.V., Kolesnikov V.A., Khaziev A.R. Development of equipment for composite 3D printing of structural elements for aerospace applications. In: *IOP Conference Series: Materials Science and Engineering. ACST 2019* (Moscow, 20–21 November 2019). IOP Publishing, 2020. Vol. 934. No. 1. P. 012049. https://doi.org/10.1088/1757-899X/934/1/012049

45. Kallai Z., Dammann M., Schueppstuhl T. Operation and experimental evaluation of a 12-axis robot-based setup used for 3D-printing. In: *ISR 2020: 52th International Symposium on Robotics* (9 December 2020). Berlin: VDE Verlag, 2020. P. 1–9.

46. Fernandes R.R., Van de Werken N., Koirala P., Yap T., Tamijani A.Y., Tehrani M. Experimental investigation of additively manufactured continuous fiber reinforced composite parts with optimized topology and fiber paths. *Additive Manufacturing*. 2021;44:102056. https://doi.org/10.1016/j.addma.2021.102056

44. Zhang G., Wang Y., Qiu W., Dong K., Xiong Y. Geometric characteristics of single bead fabricated by continuous fiber reinforced polymer composite additive manufacturing. *Materials Today: Proceedings*. 2022;70:431–437. https://doi.org/10.1016/j.matpr.2022.09.361

48. Zhang G., Wang Y., Chen Z., Xu X., Dong K., Xiong Y. Robot-assisted conformal additive manufacturing for continuous fibre-reinforced grid-stiffened shell structures. *Virtual and Physical Prototyping*. 2023;18(1):e2203695. https://doi.org/10.1080/17452759.2023.2203695

49. Ingersoll machine tools. URL: https://en.machinetools.camozzi.com (accessed: 22.06.2023).

50. Electroimpact. URL: https://www.electroimpact.com (accessed: 21.06.2023).

51. Jeff Sloan. Electroimpact launches plug-and-play AFP system. URL: https://www.compositesworld.com/products/electroimpact-launches-plug-and-play-afp-system (accessed: 21.06.2023).

52. Ginger G. Electroimpact's 6-axis continuous fiber 3D printer, one part of future multi-functional manufacturing cell. URL: https://www.compositesworld.com/news/electroimpacts-6-axis-continuous-fiber-3d-printer-one-part-of-future-multi-functional-manufacturing-cell (accessed: 21.06.2023).

Information about the Authors

Anton. V. Sotov – Cand. Sci. (Eng.), Leading Researcher of the Laboratory "Material design and additive manufacturing", Peter the Great St. Petersburg Polytechnic University (SPbPU)
ORCID: 0000-0002-7303-5912
E-mail: sotovanton@yandex.ru

Alexander I. Zaytsev – Engineer of the Russian-Chinese Research Laboratory "Functional materials", SPbPU
ORCID: 0000-0002-3138-8365
E-mail: zajtsev_ai2@spbstu.ru

Anna E. Abdrahmanova – Engineer of the Laboratory "Material design and additive manufacturing", SPbPU
ORCID: 0009-0003-4494-7300
E-mail: abdrahmanova.an@yandex.ru

Anatoly A. Popovich – Dr. Sci. (Eng.), Professor, Director of the Institute of Machinery, Materials, and Transport, SPbPU
ORCID: 0000-0002-5974-6654
E-mail: director@immet.spbstu.ru

Сведения об авторах

Антон Владимирович Сотов – к.т.н., ведущий научный сотрудник лаборатории «Дизайн материалов и аддитивного производства» Санкт-Петербургского политехнического университета Петра Великого (СПбПУ)
ORCID: 0000-0002-7303-5912
E-mail: sotovanton@yandex.ru

Александр Ильич Зайцев – инженер российско-китайской научно-исследовательской лаборатории «Функциональные материалы» СПбПУ
ORCID: 0000-0002-3138-8365
E-mail: zajtsev_ai2@spbstu.ru

Анна Эдуардовна Абдрахманова – инженер лаборатории «Дизайн материалов и аддитивного производства» СПбПУ
ORCID: 0009-0003-4494-7300
E-mail: abdrahmanova.an@yandex.ru

Анатолий Анатольевич Попович – д.т.н., проф., директор Института машиностроения, материалов и транспорта СПбПУ
ORCID: 0000-0002-5974-6654
E-mail: director@immet.spbstu.ru

Contribution of the Authors

A. V. Sotov – formation of the main concept, search and analysis of the literature, formulation of the conclusions.
A. I. Zaytsev – search and analysis of the literature, writing the text.

A. E. Abdrahmanova – correction of the text, formulation of the conclusions.
A. A. Popovich – scientific guidance, objective formalization, formation of the main concept.

Вклад авторов

А. В. Сотов – формирование основной концепции, поиск и анализ литературы, формулировка выводов.
А. И. Зайцев – поиск и анализ литературы, подготовка текста статьи.
А. Э. Абдрахманова – корректировка текста, формулировка выводов.
А. А. Попович – научное руководство, формализация задачи, формирование основной концепции.

Received 27.06.2023
Revised 24.08.2023
Accepted 29.08.2023

Статья поступила 27.06.2023 г.
Доработана 24.08.2023 г.
Принята к публикации 29.08.2023 г.

Materials and Coatings Fabricated Using the Additive Manufacturing Technologies
Материалы и покрытия, получаемые методами аддитивных технологий

UDC 621.762

https://doi.org/10.17073/1997-308X-2024-1-31-39

Research article
Научная статья

Influence of copper on the microstructure and mechanical properties of titanium ortho-alloy produced by selective laser melting

I. A. Polozov, V. V. Sokolova, A. M. Gracheva, A. A. Popovich

Peter the Great St. Petersburg Polytechnic University
29 Polytekhnicheskaya Str., St. Petersburg 195251, Russian Federation

polozov_ia@spbstu.ru

Abstract. This study explores an intermetallic orthorhombic titanium alloy produced by incorporating varying copper concentrations ranging from 0 to 6 wt. % through in-situ doping during selective laser melting (SLM) fabrication, coupled with simultaneous substrate preheating. The investigation delves into the influence of copper introduction on grain refinement within the primary B2/β-phase and subsequent alterations in mechanical properties. Through *X*-ray diffraction analysis and scanning electron microscopy, the microstructure characterized by the presence of the B2/β-phase and orthorhombic phase precipitates was identified. Additionally, the detection of a minor quantity of the α_2-Ti_3Al-phase was noted, with its proportion increasing proportionally with the augmentation of copper content. Differential scanning calorimetry revealed a shift in the phase transformation temperatures towards higher temperatures and a constricted α_2-Ti_3Al + B2/β + Ti_2AlNb region, attributed to the inclusion of copper. The addition of copper, up to 6 wt. %, resulted in the softening and embrittlement of the orthorhombic alloy, forming a fine-grained microstructure with an average grain size of 8.3 μm. Energy dispersive *X*-ray spectroscopy confirmed the presence of an intermetallic O-phase along the grain boundaries, contributing to a 12 % increase in hardness compared to the orthorhombic alloy without copper after SLM with substrate heating at 850 °C. An alloy containing 4 wt. % copper exhibited superior plastic properties and a tensile strength of 1080 MPa, comparable to the strength of the orthorhombic alloy obtained via SLM followed by hot isostatic pressing.

Keywords: orthorhombic alloy, additive manufacturing, aviation alloys, doping, *in situ* doping

Acknowledgements: The research is supported by the grant awarded by the Russian Science Foundation No. 23-79-30004, https://rscf.ru/project/23-79-30004/.

For citation: Polozov I.A., Sokolova V.V., Gracheva A.M., Popovich A.A. Influence of copper on the microstructure and mechanical properties of titanium ortho-alloy produced by selective laser melting. *Powder Metallurgy and Functional Coatings*. 2024; 18(1):31–39. https://doi.org/10.17073/1997-308X-2024-1-31-39

Влияние меди на микроструктуру и механические свойства титанового орто-сплава, изготовленного методом селективного лазерного плавления

И. А. Полозов, В. В. Соколова, А. М. Грачева, А. А. Попович

Санкт-Петербургский политехнический университет Петра Великого
Россия, 195251, г. Санкт-Петербург, ул. Политехническая, 29

polozov_ia@spbstu.ru

Аннотация. Проведено исследование интерметаллидного орторомбического титанового сплава, полученного методом селективного лазерного плавления (СЛП) с добавлением меди в количестве от 0 до 6 мас. % с помощью *in situ* легирования в процессе изготовления с использованием подогрева подложки от 300 до 850 °С. Показано, что введение меди в сплав способствовало измельчению зерна первичной B2/β-фазы и изменению механических свойств. В результате рентгеноструктурного анализа и сканирующей микроскопии была выявлена микроструктура, состоящая из B2/β-фазы с выделениями орторомбической фазы. Также в образцах прослеживается наличие небольшого количества α_2-Ti_3Al-фазы, количество которой увеличивается с повышением содержания меди в сплаве. Методом дифференциальной сканирующей калометрии установлено, что добавление меди приводит к смещению температур фазовых превращений в область более высоких температур и сужает область α_2-Ti_3Al + B2/β + Ti_2AlNb. Введение меди до 6 мас. % обуславливает разупрочнение и охрупчивание орторомбического сплава с формированием мелкозернистой микроструктуры, средний размер зерна которой составил 8,3 мкм. Результаты энергодисперсионной рентгеновской спектроскопии показали наличие на границах зерен интерметаллидной О-фазы, что способствовало увеличению твердости на 12 % в сравнении с орторомбическим сплавом без добавления меди после СЛП с подогревом подложки при 850 °С. Наилучшие пластические свойства проявил сплав с содержанием меди 4 мас. % при пределе прочности 1080 МПа, что сопоставимо со значением прочности орто-сплава, полученного методом СЛП после горячего изостатического прессования.

Ключевые слова: орторомбический сплав, аддитивное производство, авиационные сплавы, легирование, *in situ* легирование

Благодарности: Исследование выполнено за счет гранта Российского научного фонда № 23-79-30004, https://rscf.ru/project/23-79-30004/.

Для цитирования: Полозов И.А., Соколова В.В., Грачева А.М., Попович А.А. Влияние меди на микроструктуру и механические свойства титанового орто-сплава, изготовленного методом селективного лазерного плавления. *Известия вузов. Порошковая металлургия и функциональные покрытия*. 2024;18(1):32–39. https://doi.org/10.17073/1997-308X-2024-1-31-39

Introduction

Titanium aluminide-based intermetallic alloys have garnered significant attention among researchers as potential heat-resistant materials to replace nickel alloys in automotive and aerospace industries. Among these, orthorhombic titanium alloys stand out due to their exceptional heat and creep resistance, attributed to the presence of the orthorhombic intermetallic Ti_2AlNb [1]. However, the existence of this intermetallic phase poses challenges in fabricating products using traditional methods [2–4].

Modern orthorhombic titanium aluminide alloys surpass previous generations based on the Ti_3Al intermetallic compound in various aspects. It is widely acknowledged that incorporating β-isomorphous dopants such as Mo, V, Ta, and especially Nb, into titanium aluminide-based alloys has enhanced their creep and strength properties at elevated temperatures [5–7]. Copper doping has been employed to combat the embrittlement of titanium alloys at lower temperatures while improving their strength characteristics [8]. Previous studies indicate that resulting eutectics in such alloys contain the Ti_2Cu intermetallic compound, acting as a strengthening agent [9; 10]. The addition of copper also aids in reducing temperature gradients during the laser molding process in a powder bath tank, promoting the formation of equiaxed eutectoid grains in binary alloys due to the solutal undercooling effect [11; 12]. Despite copper's positive impact on enhancing thermal conductivity and heat resistance, the divergence in melting temperatures among components heightens the risk of gas pore and crack formation [13].

The intermetallic casting of titanium alloys demands strict adherence to specific fabrication conditions, including a high-quality surface for casting molds, elevated temperatures, and a protective atmosphere to prevent defect formation [14]. These alloys possess higher brittleness and reduced machinability, leading to labor-intensive and costly machining processes [15; 16]. Consequently, there is relevance in exploring additive technologies (AT) for manufacturing products from

intermetallic titanium alloys [17; 18]. the application of At in producing intermetallic alloys often leads to crack formation and involves significantly higher cooling rates compared to casting processes. This discrepancy contributes to the generation of substantial thermal stresses [13]. To mitigate thermal stress in selective laser melting (SLM) technology, controlling temperature conditions during crystallization becomes essential. Studies have demonstrated that the production of defect-free intermetallic samples necessitates additional high-temperature substrate preheating during SLM [19]. It has been observed that heating the substrate above 800 °C is necessary to achieve defect-free samples from Ti_2AlNb ortho-alloys incorporating microalloying elements [20]. Nevertheless, the influence of copper on the processability of ortho-alloy production during SLM remains insufficiently explored [21].

In situ synthesis represents a relatively new approach that holds the potential to streamline fabrication processes and reduce production costs for new alloys and their associated products. The synthesis of required composition alloys from elemental powders has conventionally been achieved through powder metallurgy methods, including techniques like hot isostatic pressing (HIP) [22] and spark plasma sintering [23]. These methods have also found application in titanium-based alloys, notably in selective laser melting and other additive manufacturing technologies [21; 24; 25].

This article presents the outcomes of an *in situ* investigation involving the doped orthorhombic titanium alloy produced via selective laser melting. The study examines structure formation and alterations in phase composition resulting from the addition of copper in quantities ranging from 0 to 6 wt. %.

Experimental

For this research, a powder mixture was employed, derived from blending ortho-alloy powder Ti–22Al–23Nb–0.8Mo–0.3Si–0.4C–0.1B–0.2Y (at. %) (manufactured by AMC Powders Co. Ltd, China) and PMS-1 copper powder in varying proportions of 2, 4, and 6 wt. % (Fig. 1). The blending process involved a vertical mixer and lasted for 12 h. The copper powder, with a purity level of 99.5 %, was manufactured via the electrolyte method and characterized by dendritic particle morphology. The initial powder of the ortho-alloy consisted of spherical particles with an average size of d_{50} = 33 μm, produced through the gas atomization method.

Samples measuring 10×10×10 mm were manufactured for microstructure analysis from the prepared mixture using the SLM method on AconityMIDI unit (Aconity3D GmbH, Germany). fitted with a fiber laser with a wavelength of 1070 nm and a maximum power of 1000 W. The samples were fabricated in a protective argon atmosphere, and the substrate was preheated to temperatures of 300, 500, and 850 °C prior to the commencement of laser processing. The chosen range of substrate preheating temperatures aligned with the region of the eutectoid transformation of Ti_2Cu, as well as based on insights gleaned from previous studies on SLM processes involving orthorhombic alloys [26].

During the SLM method, samples were fabricated using a volumetric energy density level set at 49 J/mm^3. Selection of the primary process parameters for SLM was based on prior investigations into the SLM process for the ortho-alloy [20], ensuring conditions that would yield samples with a relative density exceeding 99 %. Samples with a diameter of 12 mm and a length of 70 mm were produced for the examination of mechanical properties. These samples were further machined to comply with the sizes specified by GOST 1497-84.

Microstructural and energy dispersive analyses (EDX) were conducted using a Mira 3 LMU scanning electron microscope (Tescan, Czech Republic). *X*-ray phase analysis (XPA) was performed employing a Bruker D8 Advance *X*-ray diffractometer (Bruker,

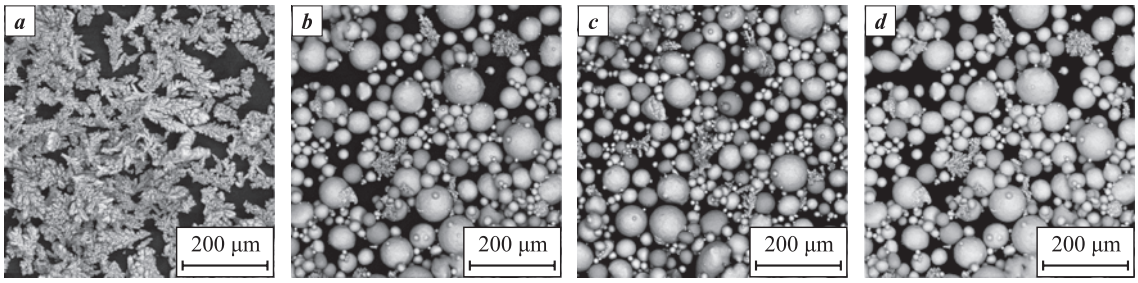

Fig. 1. SEM images of initial copper powder (***a***)
and powder mixture ortho-alloy + copper at various Cu contents (***b–d***)
Cu, wt. %: ***b*** – 2; ***c*** – 4; ***d*** – 6

Рис. 1. СЭМ-изображения исходного порошка меди (***a***)
и порошковой смеси орто-сплав + медь при различном содержании меди (***b–d***)
Cu, мас. %: ***b*** – 2; ***c*** – 4; ***d*** – 6

Bremen, Germany) using CuK_α radiation (λ = 1.5418 Å). Differential scanning calorimetry (DSC) was carried out using a STA409 Netzch/Pegasus analyzer (Netzch, Germany) employing a heating rate of 10 °C/min in an argon flow environment. Hardness measurements of the samples were taken using a Buehler VH1150 unit (Buehler, USA) under a 500 g load. Tensile tests were conducted on a Zwick/Roell Z100 testing machine (Zwick/Roell, Germany).

Results and discussion

Fig. 2 displays images showcasing microstructures of ortho-alloy with 6 wt. % copper, profuced using the SLM method at different substrate preheating temperatures. The microstructure and phase composition of the ortho-alloy, when combined with copper, exhibit considerable changes based on alterations in the substrate temperature during the SLM process. At a relatively low preheating temperature of 300 °C, the microstructure manifests as a single-phase structure comprising the B2/β phase with a bcc lattice (Fig. 2, *a*). Notably, thermal stress-induced cracks are observed on these samples. Elevating the preheating temperature to 500 °C induces the precipitation of the orthorhombic Ti_2AlNb-phase (dark gray color) along the boundaries of primary β-grains (Fig. 2, *b*). Further escalation of the temperature to 850 ºC initiates the thickening of ortho-phase precipitates along β-grain boundaries (Fig. 2, *c*). Additionally, finely dispersed needle-shaped ortho-phase precipitates (gray color) begin to form within the β-grains. Notably, regions with higher copper content were not detected through microstructural analysis. Energy dispersive analysis confirmed the homogeneous distribution of copper throughout the sample volume post-SLM of the powder mixture.

The observed transformations in microstructure and phase composition of the ortho-alloy, coupled with copper addition, as influenced by varying substrate preheating temperatures, align with previous research conducted on the ortho-alloy without copper [20]. However, the addition of copper notably facilitated the prominent formation of ortho-phase precipitates near boundaries and led to a reduction in the size of primary β-grains.

To mitigate crack defects in ortho-alloy samples combined with copper, it became evident that higher substrate preheating temperatures were necessary. At temperatures of t = 300 and 500 °C, the fabricated samples exhibited cracks due to substantial residual stresses, mirroring observations from previous studies on ortho-alloy without copper [20]. Consequently, further investigations were conducted using samples fabricated at a substrate preheating temperature of 850 °C.

In Fig. 3, microstructure images of ortho-alloy samples featuring varying copper content are presented. Irrespective of the quantity of copper incorporated into the alloy, the samples exhibit a two-phase B2/β + Ti_2AlNb microstructure, consistent with *X*-ray phase analysis findings (Fig. 4). Additionally, *X*-ray phase analysis indicates a minor presence of the α_2-Ti_3Al phase (white color), with its abundance increasing alongside the copper content in the alloy. However, specific Ti_2Cu intermetallic precipitates, typical in the Ti–Cu system, were not observed in the microstructure of the fabricated samples. This absence might be attributed to the high cooling rate inherent in the SLM process. A notable characteristic of the resulting microstructures is the influence of the melt bath outlines. The boundaries of the melt baths primarily exhibit small equiaxed grains, while elongated grains are predominantly observed in the center of the bath (Fig. 3, *c*). This distribution pattern mirrors the direction of heat dissipation, which largely coincides with the growth direction. For example, the article [27] refers to the formation of a composite microstructure featuring columnar and equiaxed crystallites, positioned differently along the laser movement direction based on scanning speed variations.

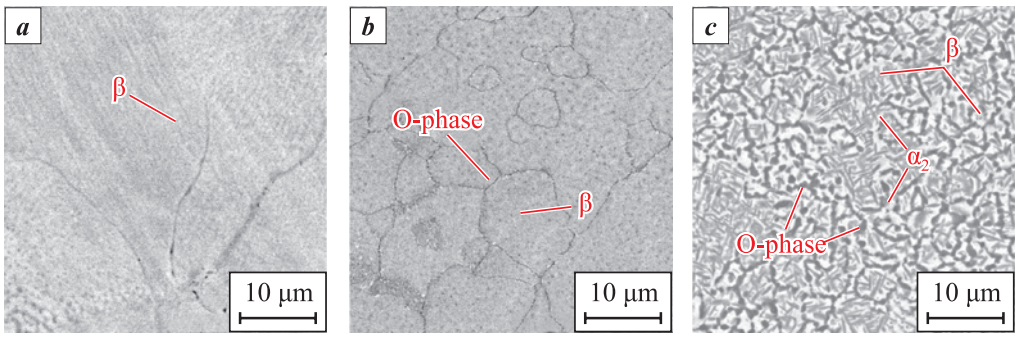

Fig. 2. Microstructure of ortho-alloy with 6 wt. % Cu substrate preheating at 300 °C (***a***), 500 °C (***b***) and 850 °C (***c***)

Рис. 2. Микроструктура орто-сплава с добавлением 6 мас. % меди, изготовленного при температурах подогрева подложки 300 °C (***a***), 500 °C (***b***) и 850 °C (***c***)

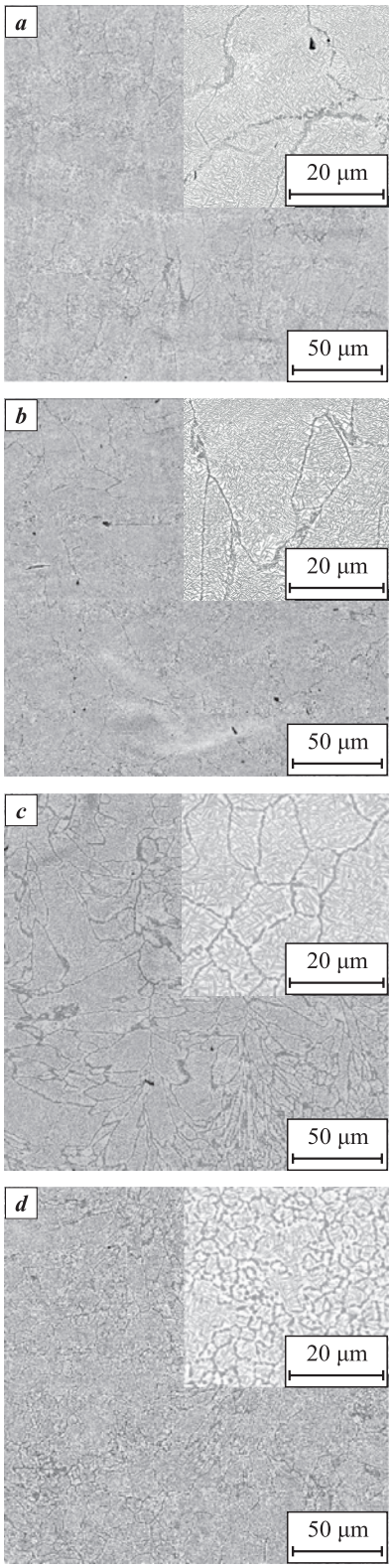

Fig. 3. Microstructure images of ortho-alloy samples produced by SLM, Cu content in the powder mixture

Cu, wt. %: ***a*** – 0; ***b*** – 2; ***c*** – 4; ***d*** – 6

Рис. 3. Изображения микроструктур образцов орто-сплава, изготовленных методом СЛП, при различном содержании меди в порошковой смеси

Cu, мас. %: ***a*** – 0; ***b*** – 2; ***c*** – 4; ***d*** – 6

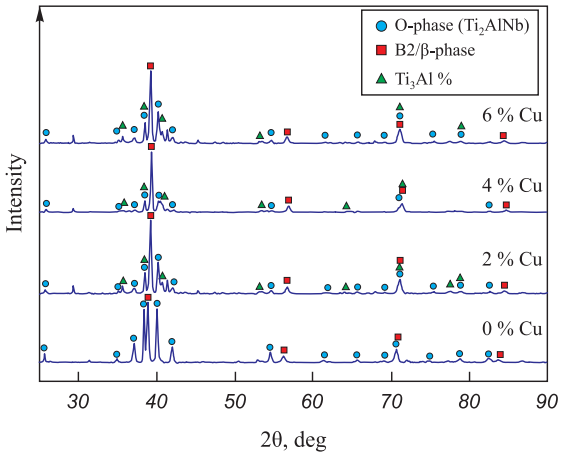

Fig. 4. *X*-ray phase analysis of ortho-alloy samples with copper content variation produced by SLM method at substrate preheating of 850 °C

Рис. 4. Результаты рентгенофазового анализа образцов орто-сплава с различным содержанием меди, изготовленных методом СЛП при температуре подогрева подложки 850 °C

Fig. 5 presents the results obtained from the differential scanning calorimetry (DSC) analysis conducted on $Ti_{22}Al_{25}Nb$ alloys, both with the inclusion of 6 wt. % copper and without it. In both cases, an exothermic transformation within the temperature range of $t = 631 \div 663$ °C is observed during preheating, linked to the precipitation of the orthorhombic phase. Furthermore, the curve exhibits an inflection towards the endothermic transformation within the B2/β + O zone, potentially correlated with the eutectoid decomposition of B2/β, leading to the formation of $\alpha + Ti_2Cu$. The DSC curve for the copper-doped alloy displays a noticeable shift in the peaks of phase transformations, expanding the regions associated with O-Ti_2AlNb and B2/β + O. Consequently, this narrows the region wherein the α_2-Ti_3Al intermetallic compound is formed. However, it's important to note that doping with copper did not significantly impact the temperature associated with the O + B2/β → B2 phase transition.

The incorporation of copper into the ortho-alloy via *in situ* doping during the SLM process, conducted under substrate preheating conditions at $t = 850$ °C, notably facilitated significant grain refinement. A clear trend toward grain size reduction is observed, commencing with the addition of 2 wt. % Cu, resulting in almost a halving of the β-phase grain size (Fig. 6). The average grain size in the ortho-alloy lacking copper addition measured 50.7 μm. Notably, the most substantial grain refinement, achieving an average size of 8.3 μm, was attained with the highest copper content of 6 wt. %. The enhanced thermal conductivity of copper compared to titanium ortho-alloy plays a crucial role in intensifying heat dissipation during melt crystallization in

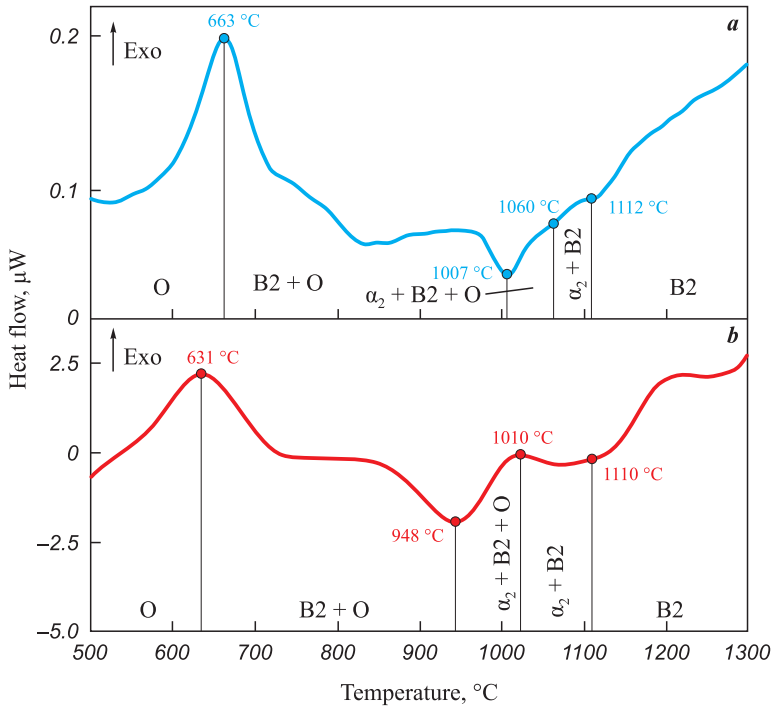

Fig. 5. Results of differential scanning calorimetry of ortho-alloy samples with 6 % copper (***a***) and without copper (***b***) produced by SLM at substrate preheating of 850 °C

Рис. 5. Результаты дифференциальной сканирующей калометрии образцов орто-сплава с содержанием меди 6 % (***a***) и без меди (***b***), изготовленных методом СЛП при температуре подогрева подложки 850 °C

the laser processing, consequently promoting the formation of a finer-grained microstructure [13]. Additionally, the presence of copper particles can induce the formation of secondary phases that effectively impede grain growth [10].

Fig. 7 illustrates the tensile curves of ortho-alloy samples containing varying copper content. The alteration in the mechanical properties of the alloy showcases a complex trend, where an increase in copper content initially results in heightened strength, particularly evident with 2 wt. % Cu. However, further escalation of copper content leads to a reduction in strength and eventual embrittlement of the alloy, despite the reduction in grain size. This embrittlement might be attributed to the formation and enlargement of brittle precipitates, particularly the intermetallic O-phase, located along the grain boundaries [16; 24]. It's worth noting that the tensile strength exhibited by the ortho-alloy containing 2 wt. % Cu in its initial state following SLM is compa-

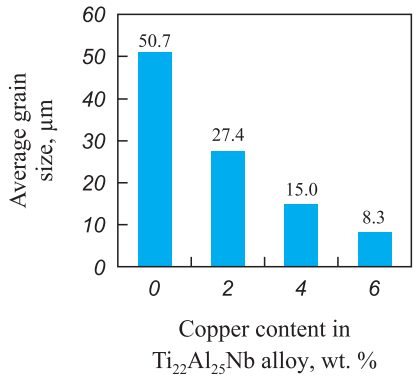

Fig. 6. Average grain size of ortho-alloy produced by SLM with different copper content

Рис. 6. Средний размер зерна орто-сплава, изготовленного методом СЛП, при различном содержании меди

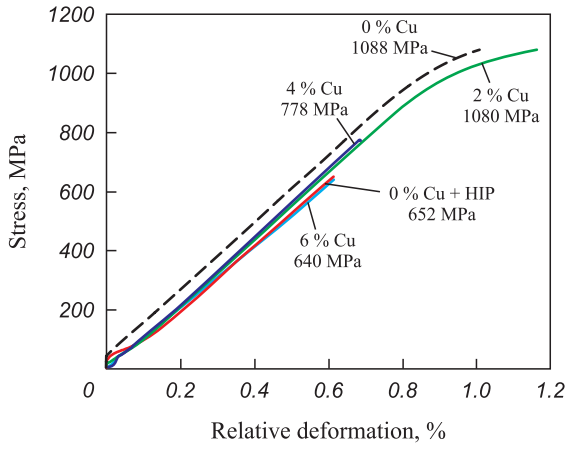

Fig. 7. Room temperature tensile test results for ortho-alloy samples with varying copper content

Рис. 7. Результаты испытаний на растяжение при комнатной температуре для образцов орто-сплава с различным содержанием меди

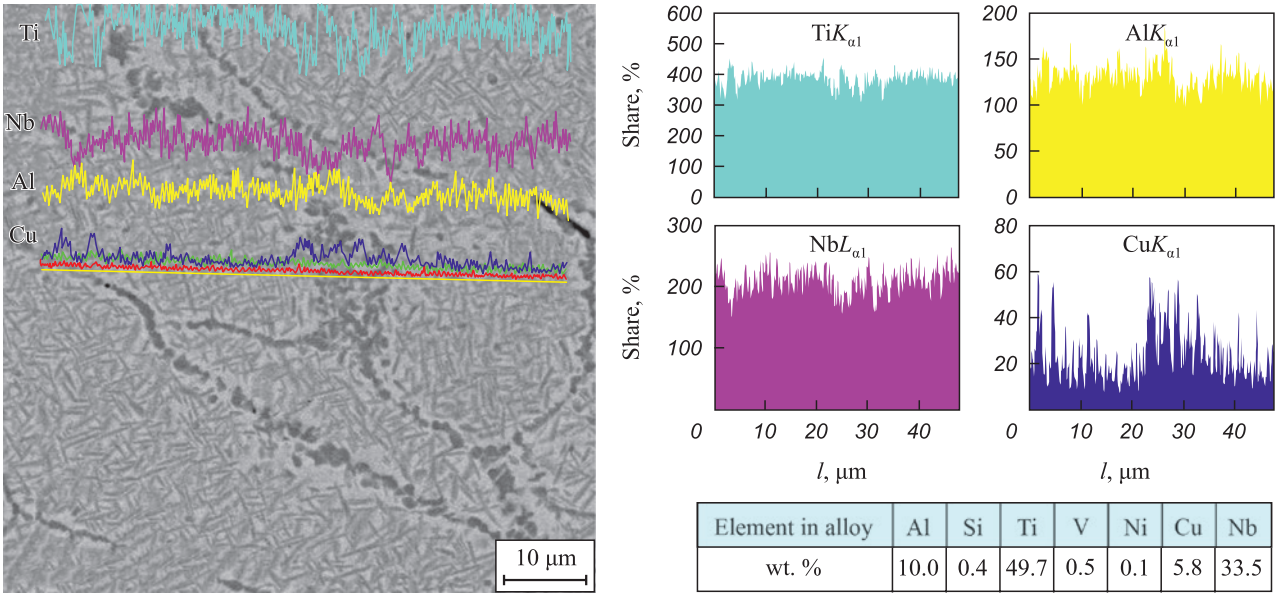

Element in alloy	Al	Si	Ti	V	Ni	Cu	Nb
wt. %	10.0	0.4	49.7	0.5	0.1	5.8	33.5

Fig. 8. Energy dispersive analysis of ortho-alloy sample with 6 wt. % Cu

Рис. 8. Результаты энергодисперсионного анализа образца орто-сплава с 6 мас. % меди

rable in value to the strength of the ortho-alloy lacking copper, obtained via the SLM method followed by hot isostatic pressing and subsequent heat treatment [17].

The hardness of ortho-alloy samples displays an uneven change with increasing copper content. Incorporating 2 wt. % Cu into the ortho-alloy resulted in a 5 % increase in hardness, measuring 388 $HV_{0.5}$ compared to the sample without copper. Subsequently, the highest microhardness values of 405 $HV_{0.5}$ were achieved with a copper content of 6 wt. %, corresponding to the smallest grain size and a higher quantity of the intermetallic phase. The initial hardness of the ortho-alloy lacking copper stood at 360 $HV_{0.5}$. Therefore, the addition of 6 wt. % Cu led to a 12 % increase in hardness. The observed higher hardness values are attributed to the refined grains brought about by the addition of copper, leading to a higher density of grain boundaries where the orthorhombic intermetallic phase precipitates form. Notably, an optimal ratio between α_2-Ti_3Al and the ortho-phase, found in the alloy containing 4 wt. % Cu, resulted in a hardness of 364 $HV_{0.5}$.

However, the addition of 4 wt. % Cu, despite grain refinement, led to the embrittlement of the alloy. This effect is observed in conditions of high concentration of grain boundaries where a fringe of a brittle intermetallic phase exists. EDX analysis (Fig. 8) indicated a higher concentration of titanium, aluminum, and copper on the grain boundaries compared to the main grain volume. To mitigate the quantity of embrittlement phases along the grain boundaries, additional heat treatment may be considered, which will be explored in future research articles.

Conclusions

This study investigates the impact of copper on the microstructure and mechanical properties of an orthorhombic titanium alloy manufactured through *in situ* doping during the selective laser melting process. The study's key conclusions are as follows:

1. Introduction of copper (0 to 6 wt. %) results in a significant microstructure refinement, yielding fine equiaxed grains. Within the studied copper content range, the phase composition of the ortho-alloy primarily consists of a two-phase B2/β + Ti_2AlNb microstructure, with a limited presence of α_2-Ti_3Al phase.

2. Variation in substrate preheating temperatures during the SLM process (ranging from 300 to 850 °C) leads to distinct alterations in the alloy's microstructure and phase composition. Starting with a singular B2/β-phase at 300 °C, the process progresses to the formation of the O-phase, accompanied by the precipitation of the Ti_3Al phase at a substrate preheating temperature of 850 °C. Notably, high-temperature substrate preheating serves as an effective method to prevent crack formation during the SLM process.

3. The addition of 6 wt. % Cu resulted in a 12 % increase in the hardness of the ortho-alloy compared to the alloy without copper. However, the inclusion of 4 wt. % Cu notably enhanced the alloy's strength, achieving a tensile strength of 1080 MPa, which is comparable to the strength of the copper-free ortho-alloy produced using SLM technology followed by hot isostatic pressing.

4. Embrittlement observed in the orthorhombic intermetallic alloy could be attributed to the suppres-

sion of the ortho phase, leading to its precipitation along grain boundaries and subsequent decay. This phenomenon is exacerbated by grain refinement induced by the presence of copper in the alloy.

References / Список литературы

1. Illarionov A.G., Stepanov S.I., Naschetnikova I.A., Popov A.A., Soundappan P., Thulasi Raman K.H., Suwas S. A review – additive manufacturing of intermetallic alloys based on orthorhombic titanium aluminide Ti_2AlNb. *Materials*. 2023;16(3):991. https://doi.org/10.3390/ma16030991
2. Zhang H., Yang M., Xu Y., Sun C., Chen G., Han F. Constitutive behavior and hot workability of a hot isostatic pressed Ti–22Al–25Nb alloy during hot compression. *Journal of Materials Engineering and Performance*. 2019;28(11):6816–6826. https://doi.org/10.1007/S11665-019-04453-W/FIGURES/12
3. Novak A.V., Alekseev E.B., Ivanov V.I., Dzunovich D.A. The study of the quenching parameters influence on structure and hardness of orthorhombic titanium aluminide alloy VTI-4. *Trudy VIAM*. 2018;2(62):5. (In Russ.).

   Новак А.В., Алексеев Е.Б., Иванов В.И., Дзунович Д.А. Изучение влияния параметров закалки на структуру и твердость интерметаллидного титанового орто-сплава ВТИ-4. *Труды ВИАМ*. 2018;2(62):5. https://doi.org/10.18577/2307-6046-2018-0-2-5-5
4. Yang J.L., Wang G.F., Zhang W.C., Chen W.Z., Jiao X.Y., Zhang K.F. Microstructure evolution and mechanical properties of P/M Ti–22Al–25Nb alloy during hot extrusion. *Materials Science and Engineering: A*. 2017;699:210–216. https://doi.org/10.1016/j.msea.2017.05.019
5. Raji S.A., Popoola A.P.I., Pityana S.L., Popoola O.M. Characteristic effects of alloying elements on β solidifying titanium aluminides: A review. *Heliyon*. 2020;6(7):e04463. https://doi.org/10.1016/j.heliyon.2020.e04463
6. Duan B., Yang Y., He S., Feng Q., Mao L., Zhang X., Jiao L., Lu X., Chen G., Li C. History and development of γ-TiAl alloys and the effect of alloying elements on their phase transformations. *Journal of Alloys and Compounds*. 2022;909:164811. https://doi.org/10.1016/J.JALLCOM.2022.164811
7. Hussain M.Z., Jiangtao X., Jinglong L., Siddique F., Zhang L.J., Zhou X.R. Effect of Ta microalloying on joint performance by tailoring the microstructure during laser beam welding of Ti–22Al–27Nb. *Materials Science and Engineering: A*. 2022;845:143157. https://doi.org/10.1016/j.msea.2022.143157
8. Yang X., Zhang B., Bai Q., Xie G. Correlation of microstructure and mechanical properties of Ti_2AlNb manufactured by SLM and heat treatment. *Intermetallics*. 2021;139:107367. https://doi.org/10.1016/J.INTERMET.2021.107367
9. Akbarpour M.R., Mirabad H.M., Hemmati A., Kim H.S. Processing and microstructure of Ti–Cu binary alloys: A comprehensive review. *Progress in Materials Science*. 2022;127:100933. https://doi.org/10.1016/j.pmatsci.2022.100933
10. Cardoso F.F., Cremasco A., Contieri R.J., Lopes E.S.N., Afonso C.R.M., Caram R. Hexagonal martensite decomposition and phase precipitation in Ti–Cu alloys. *Materials & Design*. 2011;32(8–9):4608–4613. https://doi.org/10.1016/j.matdes.2011.03.040
11. Zhang D., Qiu D., Gibson M.A., Zheng Y., Fraser H.L., StJohn D.H., Easton M.A. Additive manufacturing of ultrafine-grained high-strength titanium alloys. *Nature*. 2019;576(7785):91–95. https://doi.org/10.1038/s41586-019-1783-1
12. Donthula H., Vishwanadh B., Alam T., Borkar T., Contieri R.J., Caram R., Banerjee R., Tewari R., Dey G.K., Banerjee S. Morphological evolution of transformation products and eutectoid transformation(s) in a hyper-eutectoid Ti–12 at.% Cu alloy. *Acta Materialia*. 2019;168:63–75. https://doi.org/10.1016/j.actamat.2019.01.044
13. Popovich A.A., Sufiiarov V.S., Polozov I.A., Grigoriev A.V. Selective laser melting of the intermetallic titanium alloy. *Russian Journal of Non-Ferrous Metals*. 2019;60(2):186–193. https://doi.org/10.3103/S1067821219020081
14. Leder M.O., Kondrashov E.N., Rusakov K.A., Dolmato E.V., Maslov N.V., Shchetnikov N.V. Liquation defects in ortho-alloys VTI-4 and VIT1. In: *Modern achievements in the field of creating promising light alloys and coatings for aviation and space technology*: Collection of reports of the All-Russian scientific and technical conference (Moscow, 16 April 2021). Moscow: All-Russian Research Institute of Aviation Materials, 2021. P. 159–170. (In Russ.).

    Ледер М.О., Кондрашов Е.Н., Русаков К.А., Долмато Е.В., Маслов Н.В., Щетников Н.В. Ликвационные дефекты в орто-сплавах ВТИ-4 И ВИТ1. В сб.: *Современные достижения в области создания перспективных легких сплавов и покрытий для авиационной и космической техники*: Сборник докладов Всеросс. науч.-техн. конф. (Москва, 16 апр. 2021 г.). М.: Всероссийский научно-исследовательский институт авиационных материалов, 2021. С. 159–170.
15. Cobbinah P.V., Matizamhuka W.R. Solid-state processing route, mechanical behaviour, and oxidation resistance of TiAl alloys. *Advances in Materials Science and Engineering*. 2019;2019:ID4251953. https://doi.org/10.1155/2019/4251953
16. Zhang P., Zeng W., Zhang F., Ma H., Xu J., Liang X., Zhao Y. Fracture toughness of Ti_2AlNb alloy with different Al content: Intrinsic mechanism, extrinsic mechanism and prediction model. *Journal of Alloys and Compounds*. 2023;952:170068. https://doi.org/10.1016/j.jallcom.2023.170068
17. Wang J., Luo Q., Wang H., Wu Y., Cheng X., Tang H. Microstructure characteristics and failure mechanisms of Ti–48Al–2Nb–2Cr titanium aluminide intermetallic alloy fabricated by directed energy deposition technique. *Additive Manufacturing*. 2020;32:101007. https://doi.org/10.1016/j.addma.2019.101007
18. Li Z., Chang B., Cui Y., Zhang H., Liang Z., Liu C., Wang L., Du D., Chang S. Effect of twin-wire feeding methods on the in-situ synthesis of electron beam fabricated Ti–Al–Nb intermetallics. *Materials & Design*. 2022;215:110509. https://doi.org/10.1016/J.MATDES.2022.110509
19. Yang X., Zhang B., Bai Q., Xie G. Correlation of microstructure and mechanical properties of Ti_2AlNb manufactured by

SLM and heat treatment. *Intermetallics*. 2021;139: 107367. https://doi.org/10.1016/J.INTERMET.2021.107367

20. Polozov I., Gracheva A., Popovich A. Processing, microstructure, and mechanical properties of laser additive manufactured Ti_2AlNb-based alloy with carbon, boron, and yttrium microalloying. *Metals*. 2022;12(8):1304. https://doi.org/10.3390/met12081304

21. Wang Q., Zhang K., Niu W. Microstructural characteristic and mechanical properties of titanium-copper alloys *in-situ* fabricated by selective laser melting. *Journal of Alloys and Compounds*. 2021;885:161032. https://doi.org/10.1016/j.jallcom.2021.161032

22. Wang Guofeng, Yang Jianlei, Jiao Xueyan. Microstructure and mechanical properties of Ti–22Al–25Nb alloy fabricated by elemental powder metallurgy. *Materials Science and Engineering: A*. 2016;654:69–76. https://doi.org/10.1016/j.msea.2015.12.037

23. Sim Kyong Ho, Wang Guofeng, Kim Tae Jong, Ju Kyong Sik. Fabrication of a high strength and ductility Ti–22Al–25Nb alloy from high energy ball-milled powder by spark plasma sintering. *Journal of Alloys and Compounds*. 2018;741:1112–1120. https://doi.org/10.1016/J.JALLCOM.2018.01.279

24. Kanyane L.R., Popoola A.P., Pityana S., Tlotleng M. Heat-treatment effect on anti-corrosion behaviour and tribological properties of LENS *in-situ* synthesized titanium aluminide. *International Journal of Lightweight Materials and Manufacture*. 2022;5(2):153–161. https://doi.org/10.1016/J.IJLMM.2021.11.006

25. Vilardell A.M., Yadroitsev I., Yadroitsava I., Albu M., Takata N., Kobashi M., Krakhmalev P., Kouprianoff D., Kothleitner G., Plessis A.du. Manufacturing and characterization of *in-situ* alloyed Ti6Al4V(ELI)–3at.%Cu by laser powder bed fusion. *Additive Manufacturing*. 2020;36: 101436. https://doi.org/10.1016/j.addma.2020.101436

26. Polozov I., Sufiiarov V., Kantyukov A., Razumov N., Goncharov I., Makhmutov T., Silin A., Kim A., Starikov K., Shamshurin A. Microstructure, densification, and mechanical properties of titanium intermetallic alloy manufactured by laser powder bed fusion additive manufacturing with high-temperature preheating using gas atomized and mechanically alloyed plasma spheroidized powder. *Additive Manufacturing*. 2020;34:101374. https://doi.org/10.1016/J.ADDMA.2020.101374

27. Zhou Y.H., Li W.P., Zhang L., Zhou S.Y., Jia X., Wang D.W., Yan M. Selective laser melting of Ti–22Al–25Nb intermetallic: Significant effects of hatch distance on microstructural features and mechanical properties. *Journal of Materials Processing Technology*. 2020;276:116398. https://doi.org/10.1016/j.jmatprotec.2019.116398

Information about the Authors

Igor A. Polozov – Cand. Sci. (Eng.), Assistant Professor, Peter the Great St. Petersburg Polytechnic University (SPbPU)
ORCID: 0000-0002-5380-3072
E-mail: polozov_ia@spbstu.ru

Viktoria V. Sokolova – Engineer, Postgraduate Student, SPbPU
ORCID: 0009-0008-8279-2617
E-mail: sockolova.vero@ya.ru

Anna M. Gracheva – Engineer, Student, SPbPU
ORCID: 0009-0003-2567-3332
E-mail: gracheva.am@mail.ru

Anatoly A. Popovich – Dr. Sci. (Eng.), Professor, Director of the Institute of Machinery, Materials and Transport, SPbPU
ORCID: 0000-0002-5974-6654
E-mail: popovicha@mail.ru

Сведения об авторах

Игорь Анатольевич Полозов – к.т.н., доцент, Санкт-Петербургский политехнический университет Петра Великого (СПбПУ)
ORCID: 0000-0002-5380-3072
E-mail: polozov_ia@spbstu.ru

Виктория Владиславовна Соколова – инженер, аспирант СПбПУ
ORCID: 0009-0008-8279-2617
E-mail: sockolova.vero@ya.ru

Анна Максимовна Грачева – инженер, студент СПбПУ
ORCID: 0009-0003-2567-3332
E-mail: gracheva.am@mail.ru

Анатолий Анатольевич Попович – д.т.н., проф., директор Института машиностроения, материалов и транспорта СПбПУ
ORCID: 0000-0002-5974-6654
E-mail: popovicha@mail.ru

Contribution of the Authors

I. A. Polozov – determined the purpose of the work, conducted the experiments, and wrote the article.
V. V. Sokolova – wrote the article, participated in the discussion of the results.
A. M. Gracheva – prepared initial mixtures, conducted metallographic and *X*-ray phase analysis, took part in the discussion of the results.
A. A. Popovich – participated in the discussion of the results, determined the purpose of the work.

Вклад авторов

И. А. Полозов – определение цели работы, проведение экспериментов, написание статьи.
В. В. Соколова – написание статьи, участие в обсуждении результатов.
А. М. Грачева – подготовка исходных смесей, проведение металлографического и рентгенофазового анализов, участие в обсуждении результатов.
А. А. Попович – участие в обсуждении результатов, определение цели работы.

Received 23.06.2023
Revised 31.07.2023
Accepted 03.08.2023

Статья поступила 23.06.2023 г.
Доработана 31.07.2023 г.
Принята к публикации 03.08.2023 г.

Materials and Coatings Fabricated Using the Additive Manufacturing Technologies
Материалы и покрытия, получаемые методами аддитивных технологий

UDC 621.762.2

https://doi.org/10.17073/1997-308X-2024-1-40-51

Research article
Научная статья

Synthesis of $(TiTaNb)_xHf_yZr_zC$ high-entropy carbides resistant to high thermal oxidation by mechanical alloying and spark plasma sintering

A. E. Kim, N. E. Ozerskoi, N. G. Razumov, E. V. Volokitina, A. A. Popovich

Peter the Great St. Petersburg Polytechnic University
29 Polytekhnicheskaya Str., St. Petersburg 195251, Russian Federation

nikolaiozerskoi@yandex.ru

Abstract. This study presents the synthesis of (TiZrHfTaNb)C, $(TiTaNb)_{0.45}Hf_{0.275}Zr_{0.275}C$ and $(TiTaNb)_{0.3}Hf_{0.35}Zr_{0.35}C$ single-phase, high-entropy carbides through mechanical alloying and plasma sintering. High-entropy carbides hold promise for applications in jet engine components. We identified optimal mechanical alloying conditions to achieve powder homogeneity and minimize iron fouling. The microstructure, phase, and chemical compositions of the samples were investigated. At 1600 °C, a sample with a face-centered cubic (FCC) lattice and low content of zirconium and hafnium oxides was formed. Elevating the sintering temperature to 2000 °C facilitated oxide dissolution and the formation of single-phase, high-entropy carbides. The microhardness of the samples ranged from 1600 to 2000 HV, while the compressive strength varied between 600 and 800 MPa. Plasma heating tests demonstrated excellent resistance to thermal oxidation for $(TiTaNb)_{0.3}Hf_{0.35}Zr_{0.35}C$, withstanding temperatures up to 2250 °C.

Keywords: high-entropy alloys, high-entropy carbides, mechanical alloying, sparking plasma sintering, resistance to thermal oxidation

Acknowledgements: The study received financial support from the Ministry of Science and Higher Education of the Russian Federation under Grant Agreement No. 075-03-2023-004.

For citation: Kim A.E., Ozerskoi N.E., Razumov N.G., Volokitina E.V., Popovich A.A. Synthesis of $(TiTaNb)_xHf_yZr_zC$ high-entropy carbides resistant to high thermal oxidation by mechanical alloying and spark plasma sintering. *Powder Metallurgy and Functional Coatings*. 2024;18(1):40–51. https://doi.org/10.17073/1997-308X-2024-1-40-51

Синтез высокоэнтропийных карбидов $(TiTaNb)_xHf_yZr_zC$ с высокими термоокислительными свойствами путем механического легирования и искрового плазменного спекания

А. Э. Ким, Н. Е. Озерской, Н. Г. Разумов,

Е. В. Волокитина, А. А. Попович

Санкт-Петербургский политехнический университет Петра Великого
Россия, 195251, г. Санкт-Петербург, ул. Политехническая, 29

nikolaiozerskoi@yandex.ru

Аннотация. Представлен синтез однофазных высокоэнтропийных карбидов (TiZrHfTaNb)C, $(TiTaNb)_{0,45}Hf_{0,275}Zr_{0,275}C$ и $(TiTaNb)_{0,3}Hf_{0,35}Zr_{0,35}C$ механическим легированием и искровым плазменным спеканием. Высокоэнтропийные карбиды (ВЭК) перспективны в качестве материала для деталей реактивных двигателей. Получен режим механического легирования, при котором достигаются однородность порошка и низкий технический намол. Проведен анализ микроструктуры, фазового и химического составов полученных образцов. ВЭК с ГЦК-структурой и небольшим содержанием оксидов циркония и гафния образуется при температуре 1600 °С. Повышение температуры спекания до 2000 °С способствует растворению оксидов и формированию однофазного ВЭК. Микротвердость образцов колебалась от 1600 до 2000 HV. Прочность образцов на сжатие составляла от 600 до 800 МПа. Согласно результатам газодинамических испытаний, сплав $(TiTaNb)_{0,3}Hf_{0,35}Zr_{0,35}C$ показал отличную термоокислительную стойкость до температуры 2250 °С.

Ключевые слова: высокоэнтропийные сплавы, высокоэнтропийные карбиды, механическое легирование, искровое плазменное спекание, термоокислительные свойства

Благодарности: Исследование выполнено при финансовой поддержке Министерства науки и высшего образования Российской Федерации (Соглашение о предоставлении субсидии № 075-03-2023-004).

Для цитирования: Ким А.Э., Озерской Н.Е., Разумов Н.Г., Волокитина Е.В., Попович А.А. Синтез высокоэнтропийных карбидов $(TiTaNb)_xHf_yZr_zC$ с высокими термоокислительными свойствами путем механического легирования и искрового плазменного спекания. *Известия вузов. Порошковая металлургия и функциональные покрытия*. 2024;18(1):41–51.
https://doi.org/10.17073/1997-308X-2024-1-40-51

Introduction

High Entropy Ceramics (HEC) represent a novel class of materials that has garnered significant interest from the global scientific community. These multicomponent ceramics exhibit superior hardness, wear resistance, and oxidation resistance compared to pure metal carbides [1–9].

Most research focuses on high-entropy carbides containing metals from Group 4 (Ti, Zr, Hf) and Group 5 (V, Nb, Ta) of the Periodic Table. These compounds form monocarbides with a cubic NaCl-type structure, wherein the metals share a common cationic FCC (face-centered cubic) sublattice while carbon occupies the anionic sublattice [10].

To date, numerous high-entropy carbides have been synthesized and investigated. primarily utilizing powder-based methods. The significant distinction lies in the manufacturing processes of high-entropy carbides, with most studies commencing with wet milling and mixing of precursors [4–11].

Metal oxides undergo a carbothermal reaction followed by compaction, spark plasma sintering, or hot isostatic pressing at temperatures ranging from 1600 to 2200 °C. Through this process, $(Ti_{0.2}Zr_{0.2}Nb_{0.2}Ta_{0.2}W)C$ [4] and $(Ti_{0.2}Ta_{0.2}Nb_{0.2}Hf_{0.2}W)C$ [5] were synthesized, along with the high-entropy carbide (CrNbMoWV)C [12]. These powders may contain impurities such as oxides, amorphous carbon, and graphite, indicating potential incompleteness of the carbothermal reaction or variations in carbon content.

The following materials were derived from metal monocarbides: (TiZrNbHfTa)C [13], (HfTaZrNb)C [14], and $(Ta_{0.25}Zr_{0.25}Nb_{0.25}Ti_{0.25})C$ [10]. However, the resulting ceramic materials exhibit inconsistent phase and chemical compositions and contain inclusions similar to the initial carbides in terms of chemical composition.

In certain studies, elemental metal powders and carbon serve as initial components, following a process similar to the aforementioned works. The following materials were synthesized from elemental

powders of metals and carbon: $(TiZrHfNbV)C_5$ [15], $(Hf_{0.2}Ta_{0.2}Zr_{0.2}Nb_{0.2}Ti_{0.2})C$ and $(Hf_{0.2}Ta_{0.2}Ti_{0.2}Mo_{0.2}Nb)C$ [16], $(TiVZrHfNb)C_5$, $(TiVZrHfTa)C_5$, $(TiZrNbHfTa)C_5$, $(TiZrNbVTa)C_5$, $(TiHfNbVTa)C_5$, $(ZrHfNbVTa)C_5$ [17], $(Ti_{0.2}Zr_{0.2}Ta_{0.2}Nb_{0.2}W_{0.2})C$ [11], (VNbMoTaW)C [18]. However, this process also entails certain drawbacks. Carbides of different metals are formed sequentially, resulting in regions with varying contents of the original elements.

In our papers [19; 20], we demonstrated that spark plasma sintering of CrNbMoWV powder, obtained through mechanical alloying (MA) produces a single-phase coating approximately 100 μm thick on the surface. This coating exhibits enhanced corrosion and wear resistance, surpassing conventional materials in these properties. For instance, the wear rate difference between the carbide layers of a high entropy alloy (0.001 cm^3) and WC–8Ni carbide (0.003 cm^3) amounts to 300 % [19]. Subsequent research revealed that single-phase, chemically homogeneous high-entropy ceramics can be synthesized from a mixture of high-entropy alloy and carbon MA powders, with the high-entropy carbide (CrNbMoWV)C being the first product of this process [12].

The objective of this study is to explore the production of single-phase, high-entropy ceramic materials with high chemical homogeneity using mechanically alloyed powders of TiZrHfNbTa HEA system and to evaluate their properties.

Materials and methods

We used elemental powders of metals Ti, Nb, Hf, Zr, and Ta (99.5 % purity) as initial components for synthesizing TiZrHfNbTa. Three materials were synthesized: TiZrHfTaNb, $(TiTaNb)_{0.45}Hf_{0.275}Zr_{0.275}$ and $(TiTaNb)_{0.3}Hf_{0.35}Zr_{0.35}$, with their compositions listed in the table. MFG-7 graphite powder served as the carbon source, introduced alongside the elemental metal powders.

For mechanical alloying, we employed a Pulverisette 4 planetary mill (Fritsch, Germany) under an argon atmosphere. Mechanical alloying occurred over a duration of 5 to 10 h at drive/bowl rpm ranging from 200 to 400. The 500 ml grinding bowls and 12 mm diameter grinding balls were constructed from high-strength carbon steel. Each sample weighed 50 g, and the ball-to-powder weight ratio was maintained at 1:20.

We conducted particle size distribution analysis of the powders using an Analysette 22 NanoTec plus particle sizer (Fritsch, Germany), applying the Fraunhofer diffraction method for calculation.

For sintering, we employed an HPD 25 spark plasma sintering furnace (FCT Systeme GmbH, Germany) with a diameter 20 mm graphite mold, operating at temperatures of 1600, 1800 and 2000 °C, with a pressure of 50 MPa and a holding time of 5 min at the maximum temperature.

For a layer-by-layer examination of phase composition followed plasma heating tests, a SmartLab *X*-ray diffractometer (Rigaku Corp., Japan) was utilized, employing CuK_α radiation (λ = 1.5406 Å) and the CBO-μ Cross Beam Optics system for grazing incidence *X*-ray diffraction (ω = 10°). The incidence angle range was 20 to 80°, and the acquisition rate was set at 0.2 deg/min. Morphological and microstructural analysis of the powder particles was conducted using a Mira 3 scanning electron microscope (Tescan, Czech Republic). The chemical composition of the powder particles was determined through polished samples and *X*-ray microanalysis, employing an INCA Wave 500 microanalysis system (Oxford Instruments Analytical, UK) integrated with the scanning electron microscope.

We conducted microhardness measurements using a Buehler microhardness tester (USA) with loads of 300 and 500 g applied to ground and polished samples along the section parallel to the height of the cylindrical sample. Measurements were taken in a straight line with a 330 μm increment from the top to the bottom of the sample. Compressive strength testing was performed using a Zwick/Roell Z050 universal testing machine (Germany).

For plasma heating tests, we employed a UPIM-200 electric arc plasma generator (Composite, Korolev), with plasma generated in the air. Transient heat flow was measured using a cold copper barrier (calorimeter). Initially, the heat flux density was set

Initial alloy compositions after MA

Исходные композиции сплавов после МЛ

Alloy	Sample weight, g					
	Ti	Zr	Nb	Hf	Ta	Total
TiZrHfTaNb	4.450	7.710	7.855	15.090	15.295	50
$(TiTaNb)_{0.45}Hf_{0.275}Zr_{0.275}$	2.932	10.246	5.691	20.046	11.085	50
$(TiTaNb)_{0.3}Hf_{0.35}Zr_{0.35}$	1.891	12.613	3.670	24.678	7.148	50

at 3.1 Mw/m^2, and subsequently increased incrementally. The heat flux density increased by 0.4 MW/m^2 at each step. Throughout the test, we recorded the surface temperature of the sample using a pyrometer and monitored the surface temperature distribution using a thermal imaging camera.

Results and discussion

The dissolution of alloying elements in the early stages of mechanical alloying (MA) exhibits similarities across all systems studied. At the onset of MA, intense plastic deformation flattens the initial powder particles, leading to their fusion and the formation of a composite. After 5 h of MA, the composite particles develop a characteristic layered structure consisting of different combinations of the initial components. With further prolongation of MA duration up to 7.5 h, the primary processes involve homogenization of chemical composition and interaction between the initial components aimed at reducing the system's free energy (Fig. 1).

When the MA period extends to 10 h, the iron fouling content increases. Specifically, the average iron content in the powder rises from 0.12 % after 7.5 h of MA to 0.59 % after 10 h of MA. The measured particle size distribution (in micrometers, average values) is as follows: at τ_{MA} = 5 h – d_{10} = 19.3, d_{50} = 47.5, d_{90} = 87.9; τ_{MA} = 7.5 h – d_{10} = 8.2, d_{50} = 18.6, d_{90} = 33.8; τ_{MA} = 10 h – d_{10} = 17.1, d_{50} = 33.6, d_{90} = 59.3.

Fig. 2 depicts the XRD patterns of the initial powder mixture and the powder after mechanical alloying for 5, 7.5 and 10 h. The observed peak broadening after MA arises from a reduction in the size of coherent scattering regions and increased micro stresses. After 5 h of MA, titanium is entirely dissolved in the VCCL lattice of niobium and tantalum. This dissolution can be attributed to the similar atomic radii of these elements (Ti = 1.45 Å, Nb = 1.43 Å, Ta = 1.43 Å). However, after 10 h of MA, small peaks of zirconium and hafnium are still present due to the relatively large size of their atoms. The mass fraction of the hexagonal phase ($P6_3/mmc$) is 17 %, with a cubic lattice parameter (Im-$3m$) is 3.387 Å. The deviation from the cubic lattice

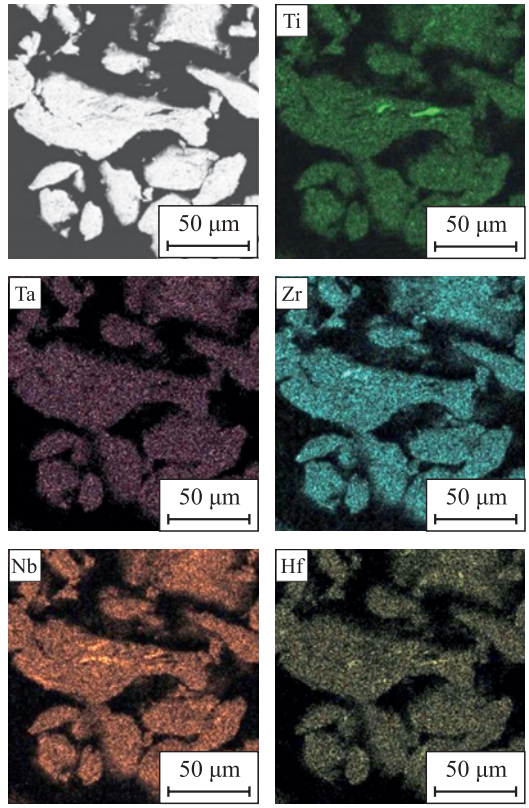

Fig. 1. Elemental distribution in TiZrHfTaNb alloy powder after τ_{MA} = 7.5 h

Рис. 1. Распределение элементов в порошке сплава TiZrHfTaNb после $\tau_{МЛ}$ = 7,5 ч

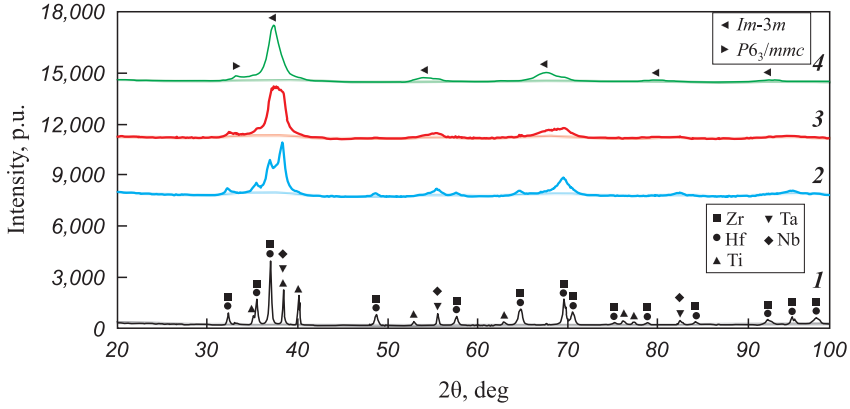

Fig. 2. Phase composition in TiZrHfTaNb powder during various MA stages

τ_{MA}, h: ***1*** – 0; ***2*** – 5; ***3*** – 7.5; ***4*** – 10

Рис. 2. Фазовый состав ВЭС-порошка TiZrHfTaNb на разных стадиях МЛ

$\tau_{МЛ}$, ч: ***1*** – 0; ***2*** – 5; ***3*** – 7,5; ***4*** – 10

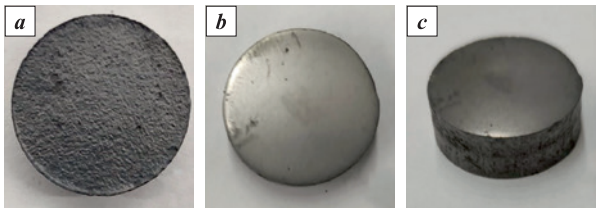

Fig. 3. Photos of (TiZrHfTaNb)C samples sintered at 2000 °C (20 mm in diameter)
a – after sandblasting; ***b–c*** – after grinding

Рис. 3. Фотографии образцов (TiZrHfTaNb)C диаметром 20 мм, спеченных при температуре 2000 °C
a – после пескоструйной обработки;
b–c – после шлифовки

parameter calculated by Vegard's law (a = 3.416 Å) for the equiatomic TiZrHfTaNb material can be attributed to the incomplete dissolution of Hf and Zr.

Based on the analysis of the microstructure, phase composition, elemental distributions, and particle size distributions of the MA samples obtained in the planetary mill, we selected τ_{MA} = 7.5 h, with a drive speed of 200 rpm and a bowl speed of 400 rpm, for the synthesis of high-entropy carbides.

High-entropy carbides were then produced from the MA powders using an FCT HPD 25 spark plasma sintering furnace. Fig. 3 displays photographs of 20 mm diameter (TiZrHfTaNb)C samples sintered at 2000 °C after undergoing sandblasting and grinding. Throughout the sintering process, we recorded various process variables including time, temperature, compression stroke, shrinkage rate, current, voltage, power, and compression force.

The experimental data obtained during the synthesis of (TiZrHfTaNb)C (Fig. 4) suggest that the process can be divided into four main stages: *1* – degassing and vacuumization; *2* – preheating; *3* – metal-carbon chemical reaction and carbide formation; *4* – compaction under 50 MPa pressure and homogenization for 5 min exposure time. These findings align with temperature profiles utilized in the solid-phase synthesis of TiC, ZrC, HfC, NbC, and TaC metal carbides [13], as well as with data obtained from spark plasma sintering of the (TiZrNbTaW)C alloy using various precursors [11].

The microstructure and phase composition of the (TiZrHfTaNb)C samples sintered at 1600 and 1800 °C reveal the presence of high-entropy HCC *Me*C carbide (*Me* = Ti, Zr, Hf, Ta, Nb), mixed zirconium-hafnium oxide, and a transition zone from the high-entropy carbide to oxide inclusions. Elevating the sintering temperature of (TiZrHfTaNb)C to 2000 °C results in increased crystal growth capacity (Fig. 5).

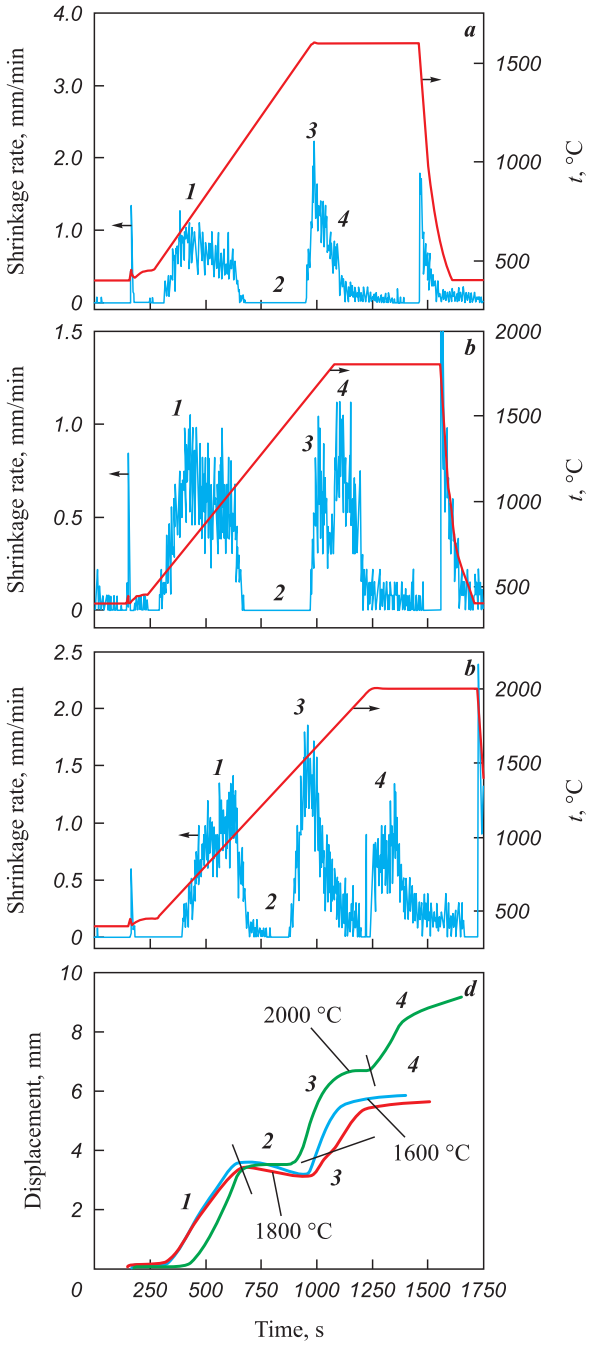

Fig. 4. Experimental curves for the synthesis of (TiZrHfTaNb)C
a–c – shrinkage rate vs. temperature and sintering time; ***d*** – compression stroke vs. time
t, °C – 1600 (***a***), 1800 (***b***), 2000 (***c***)
1–4 – synthesis stages: degassing and vacuumization (***1***), preheating (***2***), metal-carbon reaction and carbide formation (***3***), compaction under pressure (***4***)

Рис. 4. Экспериментальные кривые, полученные при синтезе ВЭК (TiZrHfTaNb)C
a–c – зависимости скорости усадки от температуры и времени спекания; ***d*** – перемещение пуансона как функция времени
t, °C – 1600 (***a***), 1800 (***b***), 2000 (***c***)
1–4 – стадии синтеза ВЭК: дегазация и вакуумирование (***1***), предварительный нагрев (***2***), химическое взаимодействие металл–углерод и образование карбида (***3***), уплотнение под воздействием давления (***4***)

The microstructure and elemental distribution of the sample sintered at t = 2000 °C (Fig. 6) indicate the formation of a homogeneous, single-phase, high-entropy carbide. The interface between zirconium-hafnium oxide and high-entropy carbide appears clear, without a zirconium-hafnium-depleted transition zone. The absence of this transition zone and the limited number of oxide inclusions, in comparison to samples sintered at lower temperatures, may suggest the completion of redox reactions and the formation of high-entropy carbides.

From the comparison of the phase composition, microstructure, and chemical homogeneity of the (TiZrHfTaNb)C samples with the thermomechanical data (Fig. 4) obtained during the synthesis, it can be inferred that the stage of chemical interaction and redox reactions (Fig. 4, stage *3*) is either completed or nearing completion when the temperature reaches 2000 °C. Stage *4* involves the densification and homogenization of the phase and chemical compositions. The formation of metal carbides is primarily driven by diffusion in the metal and carbon sublattices, with metal and carbon diffusion occurring independently [21; 22]. The diffusion rate of metals is several orders of magnitude lower than that of carbon [23]. As a result, metal diffusion significantly influences the formation of high entropy carbides and restricts the formation of secondary phases. Comparing our results with the synthesis of (TiZrNbTaW)C using a mixture of pure components and a mixture of pure carbides [11] confirms that when the starting material is a high entropy carbide, the kinetics of its formation is linear, resulting in the synthesis product being a single phase (TiZrHfTaNb)C high entropy carbide with high chemical homogeneity.

The microhardness measurements (Fig. 7) of the (TiZrHfTaNb)C samples sintered at different temperatures validate the findings from the phase composition and microstructure analysis. The samples sintered at t = 1600 and 1800 °C demonstrate high hardness levels attributed to microscopic stresses induced by the presence of non-equilibrium oxide, carbide, and transition phases. Upon increasing the sintering temperature to 2000 °C, a single-phase, high-entropy carbide is formed. The average hardness values of the samples are 1940, 1917 and 1653 HV, respectively.

We successfully synthesized $(TiTaNb)_{0.45}Hf_{0.275}Zr_{0.275}$ and $(TiTaNb)_{0.3}Hf_{0.35}Zr_{0.35}$ under the same sintering conditions as TiZrHfTaNb)C) (t = 2000 °C). These efforts resulted in obtaining single-phase $(TiTaNb)_{0,45}Hf_{0,275}Zr_{0,275}C$ and $(TiTaNb)_{0,3}Hf_{0,35}Zr_{0,35}C$ carbides.

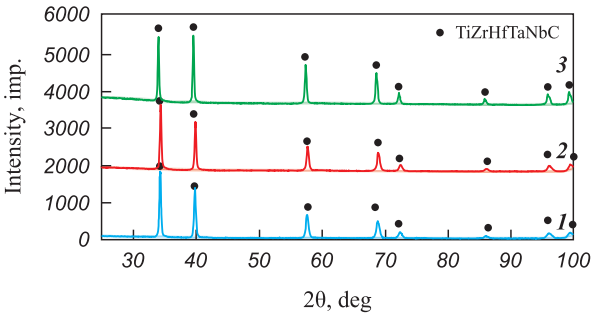

Fig. 5. Phase diagrams of (TiZrHfTaNb)C high-entropy carbides sintered at 1600 °C (*1*), 1800 °C (*2*), 2000 °C (*3*)

Рис. 5. Фазовые диаграммы высокоэнтропийных карбидов (TiZrHfTaNb)C, спеченных при температурах 1600 °C (*1*), 1800 °C (*2*), 2000 °C (*3*)

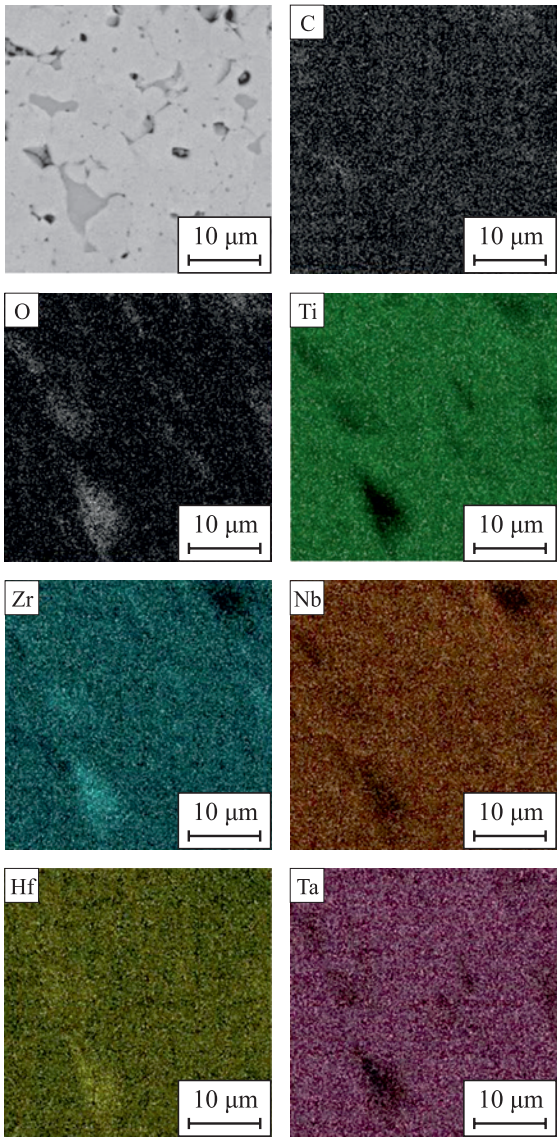

Fig. 6. Microstructure and elemental distribution of (TiZrHfTaNb)C sintered at 2000 °C

Рис. 6. Микроструктура и распределение элементов образца ВЭК (TiZrHfTaNb)C, спеченного при температуре 2000 °C

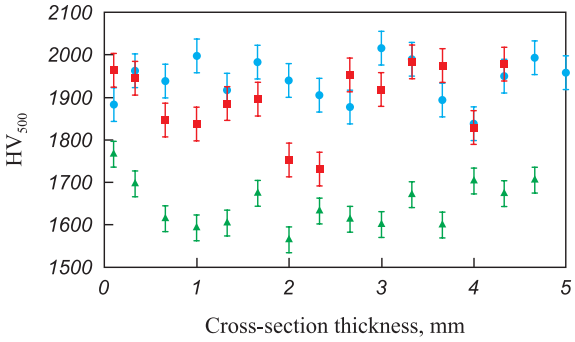

Fig. 7. Cross-sectional microhardness of the sintered (TiZrHfTaNb)C samples
t, °C: 1600 (●), 1800 (■), 2000 (▲)

Рис. 7. Микротвердость по сечению спеченных образцов (TiZrHfTaNb)C
t, °C: 1600 (●), 1800 (■), 2000 (▲)

Compression strength tests conducted on the synthesized ceramics (Fig. 8) revealed that the equiatomic (TiZrHfTaNb)C composition exhibited the highest ultimate strength of 795 MPa. As the content of Hf and Zr increased, the ultimate strength decreased to 690 for $(TiTaNb)_{0.45}Hf_{0.275}Zr_{0.275}C$ and 600 MPa for $(TiTaNb)_{0.3}Hf_{0.35}Zr_{0.35}C$, respectively.

The plasma heating tests conducted on the equiatomic (TiZrHfTaNb)C yielded unsatisfactory results (Fig. 9). Upon heating to $t = 1940$ °C, the substance melted with intense entrainment of the reaction products and base material.

The surface of the (TiZrHfTaNb)C sample following plasma heating tests exhibits regions with varying contents of the initial elements and oxygen (Fig. 10). There are three main types of elemental distribution observed: regions enriched in titanium, zirconium, and niobium; regions enriched in hafnium; and regions enriched in tantalum. The heterophase structure of the oxidation products is attributed to the differing free energies of metal oxide formation at various temperatures. During intense melting, oxidation, and entrainment of reaction products, metals with the lowest free energy of oxide formation are oxidized initially. Consequently, the resulting oxides possess different melting and evaporation temperatures, ultimately influencing the final phase composition of the reaction products.

The results of the phase composition analysis of the (TiZrHfTaNb)C sample surface after plasma heating tests (Fig. 11) validate the formation of three main phases identified through elemental distribution analysis. The hafnium-enriched phase corresponds to a mixed metal dioxide exhibiting a monoclinic lattice structure (HfO_2 prototype). The second phase, enriched in titanium, zirconium, and niobium, is characterized by the presence of mixed oxide $(TiNbZr)O_2$ with an orthorhombic lattice. This phase formation is attributed to high supercooling rates during the process, preventing the separation of the mixed oxide based on the higher niobium oxide Nb_2O_5. A similar appearance of this phase was observed during plasma heating tests of equiatomic high entropy carbide with a comparable composition. The third phase identified is the unstable TaO_2 oxide featuring a cubic lattice structure.

During testing, the $(TiTaNb)_{0.45}Hf_{0.275}Zr_{0.275}C$ and $(TiTaNb)_{0.3}Hf_{0.35}Zr_{0.35}C$ samples were subjected

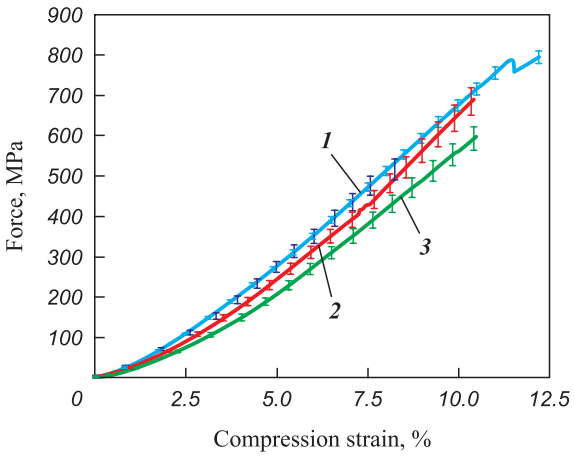

Fig. 8. Compressive strength of samples at room temperature
1 – (TiTaNbHfZr)C, ***2*** – $(TiTaNb)_{0.45}Hf_{0.275}Zr_{0.275}C$, ***3*** – $(TiTaNb)_{0.3}Hf_{0.35}Zr_{0.35}C$

Рис. 8. Прочность образцов на сжатие при комнатной температуре
1 – (TiTaNbHfZr)C, ***2*** – $(TiTaNb)_{0.45}Hf_{0.275}Zr_{0.275}C$, ***3*** – $(TiTaNb)_{0.3}Hf_{0.35}Zr_{0.35}C$

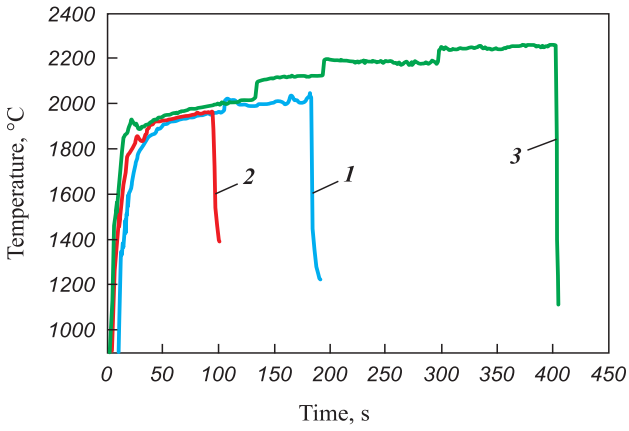

Fig. 9. Surface temperature vs. duration of plasma heating test
1 – (TiTaNbHfZr)C, ***2*** – $(TiTaNb)_{0.45}Hf_{0.275}Zr_{0.275}C$, ***3*** – $(TiTaNb)_{0.3}Hf_{0.35}Zr_{0.35}C$

Рис. 9. Зависимость температуры поверхности образцов ВЭК от длительности газодинамического испытания
1 – (TiTaNbHfZr)C, ***2*** – $(TiTaNb)_{0.45}Hf_{0.275}Zr_{0.275}C$, ***3*** – $(TiTaNb)_{0.3}Hf_{0.35}Zr_{0.35}C$

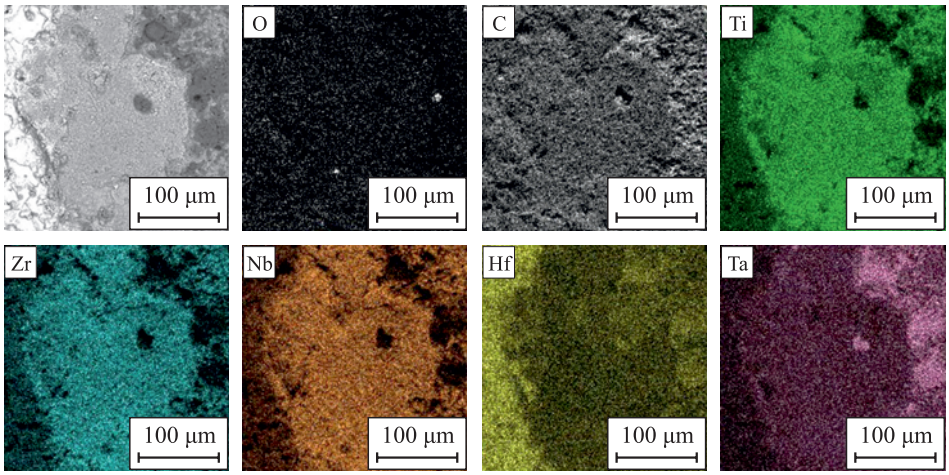

Fig. 10. Surface morphology and elemental distribution of (TiZrHfTaNb)C sample after plasma heating tests

Рис. 10. Морфология поверхности и распределение элементов образца (TiZrHfTaNb)C после газодинамических испытаний

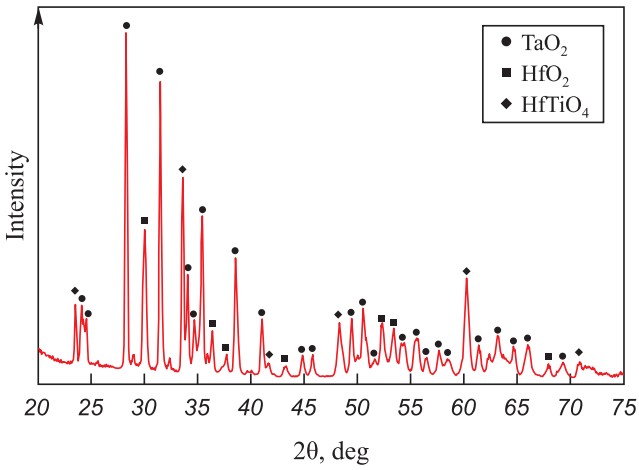

Fig. 11. XRD pattern of the oxidation products on the surface of (TiZrHfTaNb)C sample after plasma heating tests

Рис. 11. Дифрактограмма продуктов окисления на поверхности образца (TiZrHfTaNb)C после газодинамических испытаний

to an initial heat flux density of 3.1 MW/m^2, which was increased by 0.4 MW/m^2 at subsequent stages. The appearance of the samples before and after testing is illustrated in Figs. 12, *a* and 13, *a* respectively.

In the case of the $(TiTaNb)_{0.45}Hf_{0.275}Zr_{0.275}C$ sample, the transition to 3.9 MW/m^2 (τ = 170 s) resulted in burst boiling and subsequent destruction, as depicted in Fig. 12. The test was terminated after a cumulative time of 175 s, with the maximum temperature reached before sample failure being 2000 °C.

The $(TiTaNb)_{0.3}Hf_{0.35}Zr_{0.35}C$ sample underwent testing for 400 s. This demonstrated high resistance to thermal oxidation, with the surface temperature reaching 2250 °C. Subsequently, a liquid phase appeared (Fig. 13).

The layer-by-layer phase analysis of the oxidation products of the $(TiTaNb)_{0.45}Hf_{0.275}Zr_{0.275}C$ and $(TiTaNb)_{0.3}Hf_{0.35}Zr_{0.35}C$ samples revealed the segregation of layers based on the phase components (Figs. 14–16). On the surface, MeO_2 (a precursor of ZrO_2 with t_{melt} = 2715 °C); a high-melting mixed dioxide, was formed as the first layer. The second

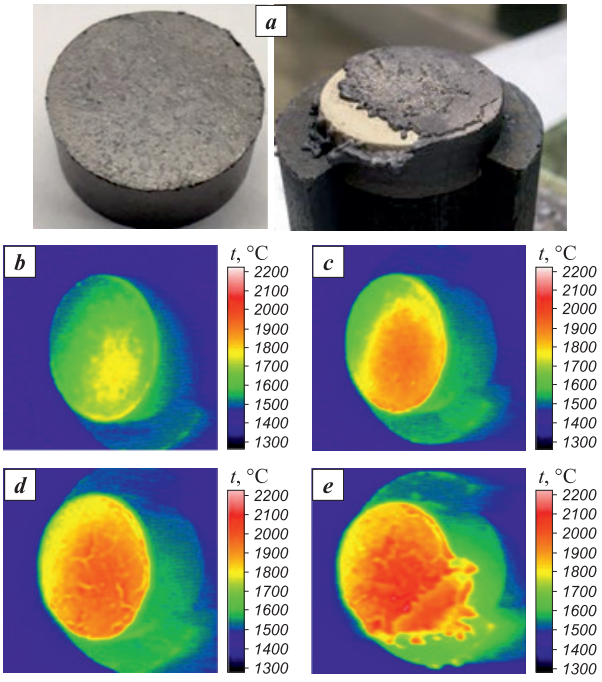

Fig. 12. $(TiTaNb)_{0.45}Hf_{0.275}Zr_{0.275}C$ sample before/after plasma heating tests (***a***) and thermal images (***b–e***)

τ, s: ***b*** – 30, ***c*** – 90, ***d*** – 150, ***e*** – 170

Рис. 12. Внешний вид образца $(TiTaNb)_{0,45}Hf_{0,275}Zr_{0,275}C$ до/после газодинамических испытаний (***a***) и термограммы испытания образца (***b–e***)

τ, с: ***b*** – 30, ***c*** – 90, ***d*** – 150, ***e*** – 170

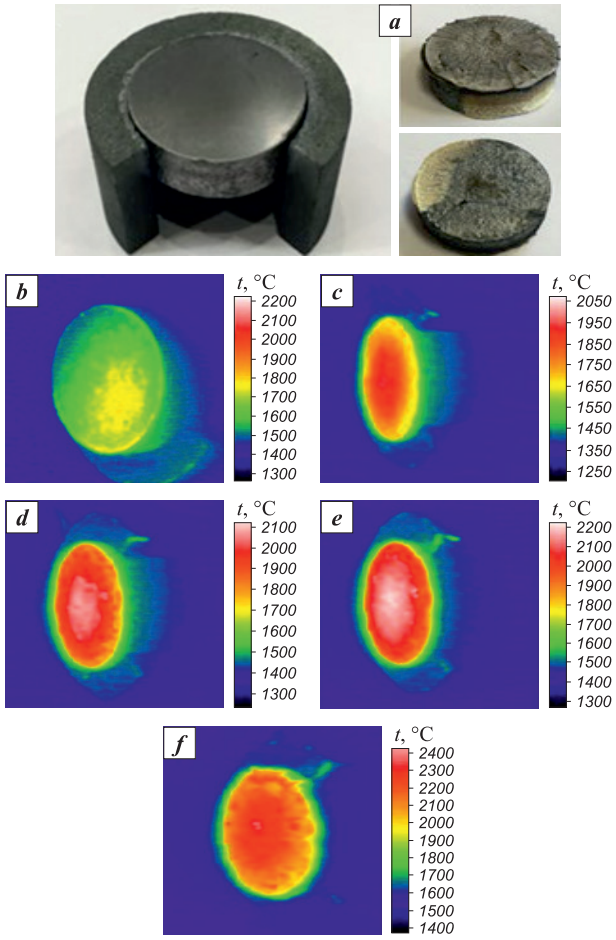

Fig. 13. $(TiTaNb)_{0.3}Hf_{0.35}Zr_{0.35}C$ sample before/after plasma heating tests (***a***) and thermal images (***b–f***)

τ, s: ***b*** – *8* (crack), ***c*** – 100, ***d*** – 150, ***e*** – 250, ***f*** – 350

Рис. 13. Внешний вид образца $(TiTaNb)_{0,3}Hf_{0,35}Zr_{0,35}C$ до/после газодинамических испытаний (***a***) и термограммы испытания образца (***b–f***)

τ, с: ***b*** – *8* (трещина), ***c*** – 100, ***d*** – 150, ***e*** – 250, ***f*** – 350

layer predominantly consists of $Me_2Me_6O_{17}$ (a precursor of $Nb_2Zr_6O_{17}$ with t_{melt} = 1670 °C); a low-melting mixed oxide. The third layer comprises Me_2O_5 (a precursor of Nb_2O_5 with t_{melt} = 1512 °C), another low-melting mixed oxide. The analysis confirms the formation of layers enriched in Zr and Hf, as well as Nb and Ta.

It is noteworthy that the $(TiTaNb)_{0.3}Hf_{0.35}Zr_{0.35}C$ sample exhibited high resistance to thermal oxidation,

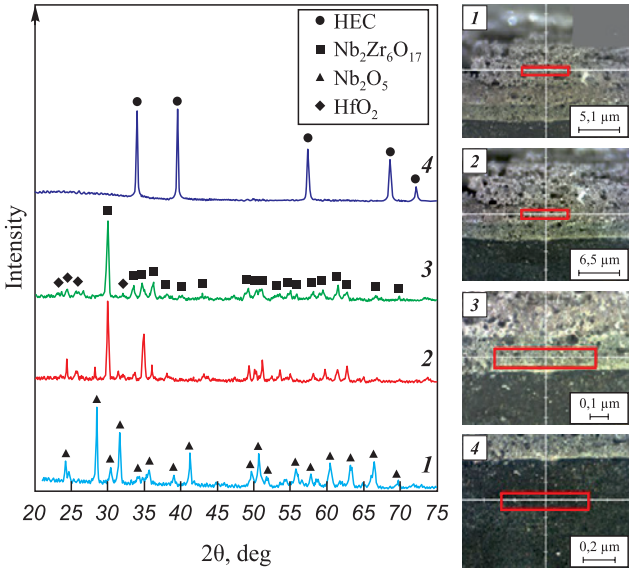

Fig. 14. Layer-by-layer phase composition analysis of $(TiTaNb)_{0.3}Hf_{0.35}Zr_{0.35}C$ sample cross-section

Areas ***1–4***: reaction products (***1***, ***2***), transition (***3***), and base material (***4***)

Рис. 14. Послойное исследование фазового состава в поперечном сечении образца $(TiTaNb)_{0,3}Hf_{0,35}Zr_{0,35}C$

1–4 – зоны: продуктов реакции (***1***, ***2***), переходной (***3***) и основного материала (***4***)

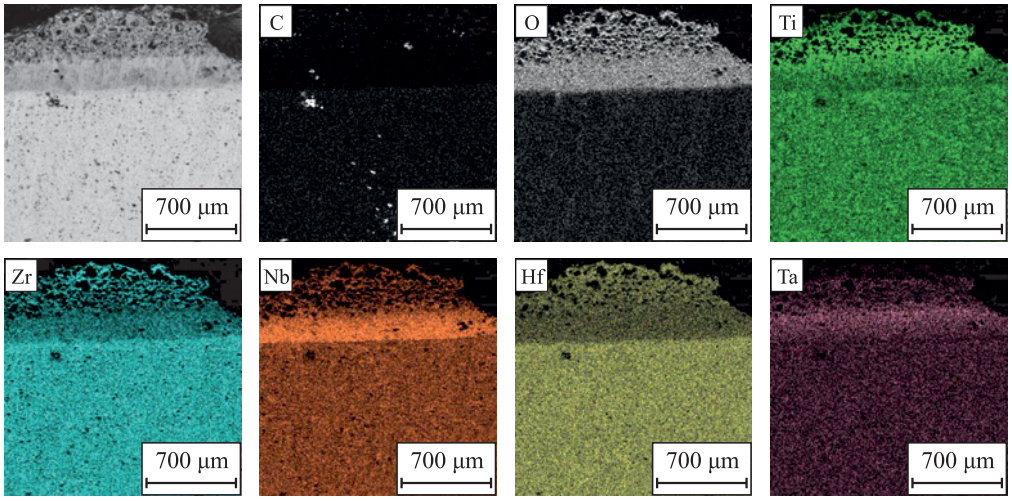

Fig. 15. Elemental distribution along the cross-section of $(TiTaNb)_{0.3}Hf_{0.35}Zr_{0.35}C$ sample

Рис. 15. Распределение элементов в поперечном сечении образца $(TiTaNb)_{0,3}Hf_{0,35}Zr_{0,35}$

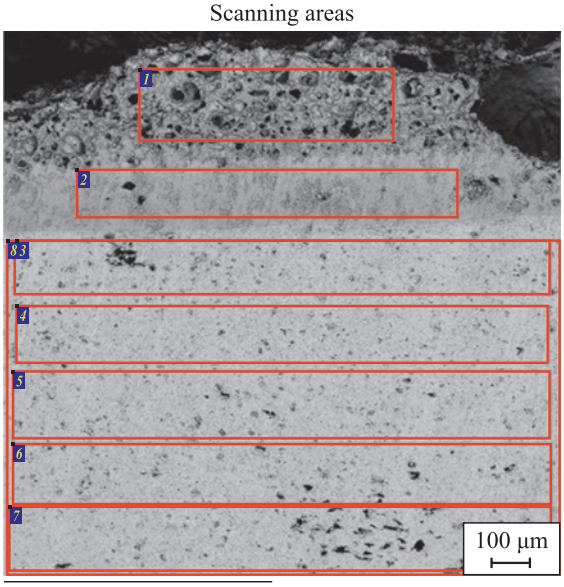

Scanning area	Elemental content, at %							
	C	O	Ti	Fe	Zr	Nb	Hf	Ta
1	22.54	56.38	3.64	0.13	5.11	1.96	7.54	2.71
2	18.79	58.23	2.41	0	4.36	6.83	4.70	4.69
3	62.69	9.56	2.71	0.23	8.38	3.11	10.61	2.70
4	58.45	9.08	3.10	0.17	10.07	3.65	12.41	3.09
5	59.83	8.44	3.14	0.53	9.66	3.50	11.88	3.03
6	62.81	8.38	2.74	0.59	8.77	3.17	10.80	2.74
7	68.22	7.37	2.34	0.41	7.26	2.66	9.38	2.36
8	62.93	8.39	2.71	0.41	8.77	3.17	10.85	2.76

Fig. 16. Elemental content in the reaction products (***1***), transition zone (***2***), and base material (***3***–***8***) in $(TiTaNb)_{0.3}Hf_{0.35}Zr_{0.35}C$ sample

Рис. 16. Содержание элементов в продуктах реакции (***1***), переходной зоне (***2***) и основном материале (***3***–***8***) образца $(TiTaNb)_{0,3}Hf_{0,35}Zr_{0,35}C$

which can be attributed to the formation of a high-melting oxide layer.

Conclusion

In summary, we have successfully synthesized single-phase, high-entropy (TiZrHfTaNb)C ceramic materials with high chemical homogeneity through mechanical alloying. This homogeneity results from the mixing of metals at the atomic level, leading to the formation of a single-phase solid solution.

Our investigation revealed that the optimal MA period is 10 h, irrespective of the initial composition. During MA, a solid solution with a face-centered cubic (FCC) lattice structure is formed, a process occurring in stages dependent on the atomic radii of the initial components. Specifically, elements with smaller atomic radii, such as Nb (0.145 nm), Ti (0.146 nm), and Ta (0.146 nm), dissolve first, followed by Hf (0.159 nm) and Zr (0.160 nm).

We have developed a process for obtaining single-phase, multicomponent ceramic materials from mechanically alloyed TiZrHfTaNb. Spark plasma sintering was utilized to investigate the physical and chemical properties of these materials. Through this process, we have successfully fabricated single-phase, equiatomic, and modified high-entropy carbides based on TiZrHfTaNb, which demonstrate resistance to high-temperature oxidation.

Furthermore, plasma heating tests revealed that resistance to thermal oxidation increases with higher Hf and Zr content. The equiatomic high-entropy carbide exhibited satisfactory results at 1900 °C. Additionally, the $(TiTaNb)_{0.3}Hf_{0.35}Zr_{0.35}C$ high-entropy ceramic material endured testing for 400 s at a surface temperature of 2250 °C.

Список литературы / References

1. Kan W.H., Zhang Y., Tang X., Lucey T., Proust G., Gan Y., Cairney J. Precipitation of (Ti, Zr, Nb, Ta, Hf)C high entropy carbides in a steel matrix. *Materialia*. 2019;1;100540. https://doi.org/10.1016/j.mtla.2019.100540
2. Braic V., Vladescu A., Balaceanu M., Luculescu C.R., Braic M. Nanostructured multi-element (TiZrNbHfTa)N and (TiZrNbHfTa)C hard coatings. *Surface Coatings Technology*. 2012;211:117–121. https://doi.org/10.1016/j.surfcoat.2011.09.033
3. Murty B.S., Yeh J.W., S. Ranganathan P.P.B. High-entropy alloys. *Advanced in Materials Science and Engineering*. 2015;1:1.
4. Zhang Y., Zhou Y.J., Lin J.P., Chen G.L., Liaw P.K. Solid-solution phase formation rules for multi-component alloys. *Advanced Engineering Materials*. 2008;10(6):534–538. https://doi.org/10.1016/j.mtla.2019.100540
5. Guo S., Ng C., Lu J., Liu C.T. Effect of valence electron concentration on stability of fcc or bcc phase in high entropy alloys. *Journal of Applied Physics*. 2011;109:103505. https://doi.org/10.1063/1.3587228
6. Zhang Y., Yang X., Liaw P.K. Alloy design and properties optimization of high-entropy alloys. *JOM*. 2012;64: 830–838. https://doi.org/10.1007/s11837-012-0366-5
7. Wang K., Chen L., Xu C., Zhang W., Liu Z., Wang Y., Zhou Y. Microstructure and mechanical properties of (TiZrNbTaMo)C high-entropy ceramic. *Journal of Materials Science and Technology*. 2020;39:99–105. https://doi.org/10.1016/j.jmst.2019.07.056
8. Yang Y., Wang W., Gan G.-Y., Shi X.-F., Tang B.-Y. Structural, mechanical and electronic properties of (TaNbHfTiZr)C high entropy carbide under pressure: Ab initio investigation. *Physica B: Condensed Matterials*. 2018;550:163–170. https://doi.org/10.1016/j.physb.2018.09.014
9. Zhang H., Hedman D., Feng P., Han G., Akhtar F. A high-entropy $B_4(HfMo_2TaTi)C$ and SiC ceramic composite. *Dalton Transactions*. 2019;48:5161–5167. https://doi.org/10.1039/c8dt04555k

10. Wang F., Yan X., Wang T., Wu Y., Shao L., Nastasi M., Cui B. Irradiation damage in $(Zr_{0.25}Ta_{0.25}Nb_{0.25}Ti_{0.25})C$ high-entropy carbide ceramics. *Acta Materialia*. 2020;195: 739–749. https://doi.org/10.1016/j.actamat.2020.06.011
11. Wei X.-F., Liu J.-X., Li F., Qin Y., Liang Y.-C., Zhang G.-J. High entropy carbide ceramics from different starting materials. *Journal of the European Ceramic Society*. 2019;39:2989–2994. https://doi.org/10.1016/j.jeurceramsoc.2019.04.006
12. Wei X.-F., Qin Y., Liu J.-X., Li F., Liang Y.-C., Zhang G.-J. Gradient microstructure development and grain growth inhibition in high-entropy carbide ceramics prepared by reactive spark plasma sintering. *Journal of the European Ceramic Society*. 2020;40:935–941. https://doi.org/10.1016/j.jeurceramsoc.2019.12.034
13. Zhou J., Zhang J., Zhang F., Niu B., Lei L., Wang W. High-entropy carbide: A novel class of multicomponent ceramics. *Ceramics International*. 2018;44:22014–22018. https://doi.org/10.1016/j.ceramint.2018.08.100
14. Csanádi T., Vojtko M., Dankházi Z., Reece M.J., Dusza J. Small scale fracture and strength of high-entropy carbide grains during microcantilever bending experiments. *Journal of the European Ceramic Society*. 2020;40:4774–4782. https://doi.org/10.1016/j.jeurceramsoc.2020.04.023
15. Chicardi E., García-Garrido C., Gotor F.J. Low temperature synthesis of an equiatomic $(TiZrHfVNb)C_5$ high entropy carbide by a mechanically-induced carbon diffusion route. *Ceramics International*. 2019;45(17):21858–21863. https://doi.org/10.1016/j.ceramint.2019.07.195
16. Moskovskikh D.O., Vorotilo S., Sedegov A.S., Kuskov K.V., Bardasova K.V., Kiryukhantsev-Korneev P.V., Mukasyan A.S. High-entropy (HfTaTiNbZr)C and (HfTaTiNbMo)C carbides fabricated through reactive high-energy ball milling and spark plasma sintering. *Ceramics International*. 2020;46:19008–19014. https://doi.org/10.1016/j.ceramint.2020.04.230
17. Chicardi E., García-Garrido C., Hernández-Saz J., Gotor F.J. Synthesis of all equiatomic five-transition metals high entropy carbides of the IVB (Ti, Zr, Hf) and VB (V, Nb, Ta) groups by a low temperature route. *Ceramics International*. 2020;46:21421–21430. https://doi.org/10.1016/j.ceramint.2020.05.240
18. Liu D., Zhang A., Jia J., Meng J., Su, B. Phase evolution and properties of (VNbTaMoW)C high entropy carbide prepared by reaction synthesis. *Journal of the European Ceramic Society*. 2020;40:2746–2751. https://doi.org/10.1016/j.jeurceramsoc.2020.03.020
19. Razumov N., Makhmutov T., Kim A., Shemyakinsky B., Shakhmatov A., Popovich V., Popovich A. Refractory crmonbwv high-entropy alloy manufactured by mechanical alloying and spark plasma sintering: Evolution of microstructure and properties. *Materials (Basel)*. 2021;14: 1–14. https://doi.org/10.3390/ma14030621
20. Makhmutov T., Razumov N., Popovich A. Synthesis of single-phase high-entropy carbides from a mixture of pre-mechanically alloyed CrNbMoWV HEA powders and carbon. *Materials Letters*. 2022;309:131363. https://doi.org/10.1016/j.matlet.2021.131363
21. Yut B.B. Nb G. of 14C in single crystals. *Crystals*. 1979;40:997–1006.
22. Zhang H., Akhtar F. Processing and characterization of refractory quaternary and quinary high-entropy carbide composite. *Entropy*. 2019;21(5):474. https://doi.org/10.3390/e21050474
23. Demaske B.J., Chernatynskiy A., Phillpot S.R. First-principles investigation of intrinsic defects and self-diffusion in ordered phases of V_2C. *Journal of Physics: Condensed Matterials*. 2017;29(24):245403. https://doi.org/10.1088/1361-648X/aa7031

Information about the Authors

Artem E. Kim – Engineer of the Laboratory "Synthesis of new materials and structures", Peter the Great St. Petersburg Polytechnic University (SPbPU)
ORCID: 0000-0002-2276-1359
E-mail: artem_7.kim@mail.ru

Nikolai E. Ozerskoi – Research Associate of the Scientific and Educational Centre "Additive Technologies", SPbPU
ORCID: 0000-0002-7371-558X
E-mail: nikolaiozerskoi@yandex.ru

Nilkolai G. Razumov – Cand. Sci. (Eng.), Head of Laboratory "Synthesis of new materials and structures", SPbPU
ORCID: 0000-0002-7147-6239
E-mail: n.razumov@onti.spbstu.ru

Ekaterina V. Volokitina – Engineer of the Russian-Chinese Research Laboratory "Functional Materials", SPbPU
ORCID: 0009-0002-5454-7733
E-mail: volokitina1606@gmail.com

Anatoly A. Popovich – Dr. Sci. (Eng.), Professor, Director of the Institute of Machinery, Materials and Transport, SPbPU
ORCID: 0000-0002-5974-6654
E-mail: popovicha@mail.ru

Сведения об авторах

Артем Эдуардович Ким – инженер лаборатории «Синтез новых материалов и конструкций» Санкт-Петербургского политехнического университета Петра Великого (СПбПУ)
ORCID: 0000-0002-2276-1359
E-mail: artem_7.kim@mail.ru

Николай Евгеньевич Озерской – научный сотрудник научно-образовательного центра «Аддитивные технологии» СПбПУ
ORCID: 0000-0002-7371-558X
E-mail: nikolaiozerskoi@yandex.ru

Николай Геннадьевич Разумов – к.т.н., заведующий лабораторией «Синтез новых материалов и конструкций» СПбПУ
ORCID: 0000-0002-7147-6239
E-mail: n.razumov@onti.spbstu.ru

Екатерина Владимировна Волокитина – инженер российско-китайской научно-исследовательской лаборатории «Функциональные материалы» СПбПУ
ORCID: 0009-0002-5454-7733
E-mail: volokitina1606@gmail.com

Анатолий Анатольевич Попович – д.т.н., проф., директор Института машиностроения, материалов и транспорта СПбПУ
ORCID: 0000-0002-5974-6654
E-mail: popovicha@mail.ru

Contribution of the Authors

A. E. Kim – planned the experiments, wrote the article, carried out the production of samples, participated in the discussion of the results.
N. E. Ozerskoi – conducted experiments, processed the obtained results, wrote the article, participated in the discussion of the results.

N. G. Razumov – critically analysed the literature, participated in the discussion of the results, formed the conclusions of the study.
E. V. Volokitina – conducted experiments, participated in the discussion of the results.
A. A. Popovich – conceptualised the idea, defined the aim of the work and its objectives, participated in the discussion of the results.

Вклад авторов

А. Э. Ким – планирование экспериментов, написание статьи, участие в обсуждении результатов.

Н. Е. Озерской – проведение экспериментов, обработка полученных результатов, написание статьи, участие в обсуждении результатов.
Н. Г. Разумов – критический анализ литературы, участие в обсуждении результатов, формирование выводов исследования.
Е. В. Волокитина – проведение экспериментов, участие в обсуждении результатов.
А. А. Попович – концептуализация идеи, определение цели работы и ее задач, участие в обсуждении результатов.

Received 28.06.2023
Revised 04.09.2023
Accepted 13.09.2023

Статья поступила 28.06.2023 г.
Доработана 04.09.2023 г.
Принята к публикации 13.09.2023 г.

Materials and Coatings Fabricated Using the Additive Manufacturing Technologies
Материалы и покрытия, получаемые методами аддитивных технологий

UDC 621.762

https://doi.org/10.17073/1997-308X-2024-1-52-61

Research article
Научная статья

Mechanical properties of the VZh159–CuCr1Zr alloy multi-material samples manufactured by selective laser melting

A. V. Repnin, E. V. Borisov, A. A. Popovich, N. A. Golubkov

Peter the Great St. Petersburg Polytechnic University
29 Polytekhnicheskaya Str., St. Petersburg 195251, Russian Federation

repnin_arseniy@mail.ru

Abstract. Selective laser melting (SLM) proves to be a suitable method for fabricating multi-material products, offering heightened performance. The objective of this study is to examine the mechanical properties of the VZh159–CuCr1Zr multi-material system produced through selective laser melting. We conducted tensile and compressive strength tests on these samples, followed by fractography, examination of polished sections, and a comparison of measured mechanical properties with existing data. Our findings are summarized as follows: the phase compositions in the regions of pure alloy denote solid solutions. *X*-ray diffraction (XRD) patterns of the interface zone reveal peaks corresponding to both alloys. The tensile strength of VZh159–CuCr1Zr multi-material samples, as measured in tensile tests, is $\sigma_u = 430 \pm 20$ MPa, with a relative elongation of $\varepsilon = 4.6 \pm 0.3$ %. Results from compressive strength tests show values of $\sigma_u = 822 \pm 23$ MPa, and relative compression $\varepsilon = 42.5 \pm 1.5$ %. Comparing these values with those of the pure CuCr1Zr alloy, the ultimate tensile strength is approximately 53 % higher (according to available data), while the conditional yield strength is about 80 % higher. Fractography of the VZh159–CuCr1Zr multi-material sample after tensile tests indicates that the interface zone exhibits both more ductile fracture features characteristic of the CuCr1Zr alloy (pits and a lack of a smooth surface) and less ductile features characteristic of the VZh159 alloy (microcracks). Examination of the polished section of a VZh159–CuCr1Zr multi-material sample after compressive strength tests reveals that the presence of a more ductile CuCr1Zr alloy in the interface zone contributes to arresting the crack, which propagates at a 45° angle to the direction of load application in the VZh159 alloy region.

Keywords: selective laser melting, multi-materials, mechanical properties, fractography, crack propagation, VZh159–CuCr1Zr

Acknowledgements: This study received support from Grant No. 23-79-30004 from the Russian Science Foundation, https://rscf.ru/project/23-79-30004/.

For citation: Repnin A.V., Borisov E.V., Popovich A.A., Golubkov N.A. Mechanical properties of the VZh159–CuCr1Zr alloy multi-material samples manufactured by selective laser melting. *Powder Metallurgy and Functional Coatings*. 2024;18(1):52–61. https://doi.org/10.17073/1997-308X-2024-1-52-61

Исследование механических свойств мультиматериальных образцов системы ВЖ159–БрХЦрТ, полученных методом селективного лазерного плавления

А. В. Репнин, Е. В. Борисов, А. А. Попович, Н. А. Голубков

Санкт-Петербургский политехнический университет Петра Великого
Россия, 195251, г. Санкт-Петербург, ул. Политехническая, 29

repnin_arseniy@mail.ru

Аннотация. Используя метод селективного лазерного плавления, можно успешно получать мультиматериальные изделия. Такие изделия будут обладать повышенными эксплуатационными характеристиками. Цель данной работы – изучение механических свойств мультиматериальной системы ВЖ159–БрХЦрТ В, полученной методом селективного лазерного плавления. Были проведены испытания ее образцов на растяжение и сжатие, после чего осуществлена их фрактография, исследованы шлифы после сжатия, выполнено сравнение полученных механических свойств с литературными данными. В результате сделаны следующие выводы: в зонах чистых сплавов фазовый состав представляет собой соответствующие твердые растворы, в переходной зоне наблюдаются пики, расположение которых соответствует пикам из обоих сплавов. При испытаниях на растяжение предел прочности мультиматериальных образцов системы ВЖ159–БрХЦрТ В составил $\sigma_в = 430 \pm 20$ МПа, относительное удлинение $\varepsilon = 4{,}6 \pm 0{,}3$ %, результаты на сжатие – $\sigma_в = 822 \pm 23$ МПа, относительное сжатие $\varepsilon = 42{,}5 \pm 1{,}5$ %. По сравнению с чистым сплавом БрХЦрТ В предел прочности мультиматериальных образцов системы ВЖ159–БрХЦрТ при испытаниях на растяжение выше на ~53 % (при сопоставлении с литературными данными), условный предел текучести в экспериментах на сжатие – на ~80 %. Фрактография мультиматериального образца системы ВЖ159–БрХЦрТ В после проведения испытаний на растяжение свидетельствует о том, что переходной зоне присущи признаки как более вязкого разрушения, характерного для сплава БрХЦрТ В (наличие ямок и отсутствие гладкого рельефа), так и менее вязкого, характерного для сплава ВЖ159 (наличие микротрещин). Исследование шлифа мультиматериального образца системы ВЖ159–БрХЦрТ В после испытаний на сжатие показало, что наличие в переходной зоне более вязкого сплава БрХЦрТ В способствует остановке развития трещины.

Ключевые слова: селективное лазерное плавление, мультиматериалы, механические свойства, фрактография, распространение трещины, ВЖ159–БрХЦрТ В

Благодарности: Исследование выполнено за счет гранта Российского научного фонда № 23-79-30004, https://rscf.ru/project/23-79-30004/.

Для цитирования: Репнин А.В., Борисов Е.В., Попович А.А., Голубков Н.А. Исследование механических свойств мультиматериальных образцов системы ВЖ159–БрХЦрТ, полученных методом селективного лазерного плавления. *Известия вузов. Порошковая металлургия и функциональные покрытия*. 2024;18(1):53–61. https://doi.org/10.17073/1997-308X-2024-1-52-61

Introduction

Additive manufacturing (AM) has become widely prevalent in high-tech industries such as petrochemicals, manufacturing, and power generation, among others [1]. One contributing factor is that AM processes can yield geometrically-complex products at a lower manufacturing cost compared to conventional methods [2]. To fabricate products from metals and alloys, diverse At can be employed. These include extrusion and deposition, laminated object manufacturing, binder jetting, direct deposition, and template-assisted synthesis. The latter involves building parts from 3D models by fusing thin layers of metal powder with an energy source [3–5].

Selective Laser Melting (SLM) is particularly notable for its ability to produce parts with variable chemical composition and enhanced performance [6]. Such products can be categorized into two groups: Functionally Graded Materials (FGM) and multi-materials [7]. Chen K. et al. [8] conducted a study on the 316L/CuSn10 multi-material system (316L being an austenitic stainless steel, and CuSn10 a tin bronze) using the SLM process. They successfully manufactured compact samples devoid of macrocracks in the interface zone. Their findings revealed a gradual decrease in Vickers microhardness from 330 HV in the 316L region to 173 HV in the CuSn10 region. The tensile and flexural strengths of the 316L/CuSn10 multi-material samples fell within the strength values for 316L and CuSn10, respectively. The shear stress of the 316L/CuSn10 sample measured 210 MPa, surpassing that of the same alloy manufactured by alternative processes.

Chen J. et al. [9] conducted a study on the same multi-material system and process. The Vickers microhardness perpendicular to the transition ranged from 230 HV in the 316L region to 155 HV in the CuSn10 region. The ultimate strength of the 316L/CuSn10 multi-material samples was measured at 420 MPa. Fracture curves indicated brittle fracture in the interface zone. SEM analysis revealed a width of approximately 550 μm for the interface zone, containing dendritic crack sources towards the steel interface.

Mei X. et al. [10] manufactured SLM samples and studied the 316L/IN718 system, where IN718 is an Inconel 718 heat-resistant nickel alloy. These samples exhibited an ultimate strength of 600 MPa and a relative elongation of 28 %. Optical microscopy, SEM, and energy-dispersive spectroscopy studies unveiled an interface zone width of approximately 100 μm, characterized by the occurrence of cracks and defects. It was suggested that to mitigate these defects, adjustments to 3D printing conditions should be made in the transition area for 316L/IN718 alloy multi-material samples.

Yusuf S. et al. [11] conducted similar studies, successfully producing compact samples with low porosity (~0.81 % on average). Metallographic analysis revealed dense dislocation networks in the interface zone, containing NbC and TiC carbides along with a small amount of Laves phases (<2 wt. %). The interfacial region exhibited equiaxed grains (average size – 45 μm), while columnar grains (average sizes – 55 and 85 μm) were observed in the pure IN718 and 316L alloy regions, respectively. Vickers microhardness (HV) measurements indicated that the hardness of the interface zone fell between the hardness values of the pure alloy regions.

Onuike B. et al. [12] investigated the IN718/GRCop-84 system (GRCop-84 being a heat-resistant bronze alloy) using a direct laser deposition process. Two approaches to producing multi-material samples were studied: direct deposition of GRCop-84 on IN718 and compositional gradation of the two alloys. The second approach yielded samples with fewer defects, while the first approach did not produce positive results. Metallographic studies revealed that the interface contained columnar grain structures and an accumulation of Cr_2Nb intermetallides. The thermal conductivity of the IN718/GRCop-84 multi-material samples was approximately 250 % higher compared to the pure IN718 alloy.

Marques A. et al. [13] made a sample representing a combustion chamber of a rocket engine, with cooling channels made of pure copper and the body constructed from the IN718 heat-resistant nickel alloy. The areas composed of pure IN718 alloy exhibited minimal defects, while defects were observed in the copper channels, distinguishable by their distinctive 200 μm width. The interface zone width was approximately 25 μm, and no intermetallic compounds were identified.

Ringel B. et al. [14] also produced a sample, a burner nozzle, using the IN718/CuCr1Zr multi-material system (CuCr1Zr being a heat-resistant bronze alloy). The cooling channels were made of CuCr1Zr, and the housing was composed of IN718. While the sample exhibited some defects, it demonstrated good processability. The width of the interface zone varied with its inclination relative to the build direction. The multi-material product structure contributed to enhanced heat transfer. The authors underscored the necessity for multi-material fabrication equipment.

Repnin A. et al. [15] investigated the impact of 3D printing parameters on the interface zone porosity in VZh159–CuCr1Zr multi-material samples, as well as the effects of heat treatment on microstructure, chemical composition, and phase compositions. The study revealed that a substantial increase in input energy was effective in reducing interface zone porosity in multi-material samples. However, common heat treatment processes applied to CuCr1Zr and VZh159 alloys did not significantly affect the microstructure, chemical composition, and phase compositions of the interface zones. The authors estimated the size of the interface zones at 300 μm when CuCr1Zr is deposited on VZh159. Unfortunately, the study did not include mechanical testing of the samples to identify the effects of a multi-material structure on material properties.

The literature review suggests that SLM can be employed to produce low-defect multi-material products, particularly in systems such as steel-bronze, steel-heat-resistant nickel alloy, and heat-resistant nickel alloy-heat-resistant bronze. However, the latter system remains poorly studied, lacking information on its mechanical properties at both room and elevated temperatures. Thus, the objective of this study is to investigate the mechanical properties of the heat-resistant nickel alloy-heat-resistant bronze system (VZh159–CuCr1Zr) obtained through SLM. To fulfill this objective, the following tasks were undertaken: conducting tensile and compressive strength tests on the multi-material samples, performing fractography after tensile tests, analyzing polished sections post-compression, and comparing the measured mechanical properties with available data.

Materials and methods

We used an SLM 280HL 3D printer (SLM Solutions, Germany) for the fabrication of multi-

material samples comprising VZh159–CuCr1Zr alloys, which were subsequently subjected to tensile and compressive strength tests. The samples were constructed using VZh159 and CuCr1Zr spherical powders (Fig. 1, Table 1), both of which were produced through atomization. Particle size distribution for the powders was determined employing the laser diffraction method with an Analysette 22 NanoTec plus system (Fritsch GmbH, Germany). The particle size distributions for the VZh159 and CuCr1Zr alloys are as follows (μm): d_{10} = 17, d_{50} = 32, d_{90} = 55 and d_{10} = 14, d_{50} = 29, d_{90} = 52.

The VZh159–CuCr1Zr multi-material samples were produced using SLM, involving 3D printing of the CuCr1Zr alloy onto the VZh159 alloy. To minimize defects in the interface zone (12 layers), the printing settings were adjusted from the standard settings for VZh159 [16] and CuCr1Zr alloys [17]. Table 2 details the SLM settings for the VZh159–CuCr1Zr multi-material sample printing. Fig. 2 illustrates the samples post-fabrication. For the tensile tests, the sample dimensions are as follows (mm): tested area width – 5, length – 20, thickness – 2 (1 mm each of VZh159 and CuCr1Zr alloys along the entire length of the sample), width of the grips – 8.2, length of the grips – 15. The dimensions for the compressive strength tests are as follows (mm): height – 7, width – 4.5, thickness – 6 (3 mm of VZh159–CuCr1Zr alloys along the entire height of the sample). The compressive test samples made of the CuCr1Zr alloy have the following dimensions (mm): height – 8.3; width and thickness – 3.

The heat treatment conditions for the VZh159–CuCr1Zr multi-material samples adhered to the standard VZh159 heat treatment procedures [18]. The heat treatment comprised five stages:

1) heating to 800 °C (10 °C/min heating rate);

2) holding for 8 h;

3) cooling to 700 °C in the furnace;

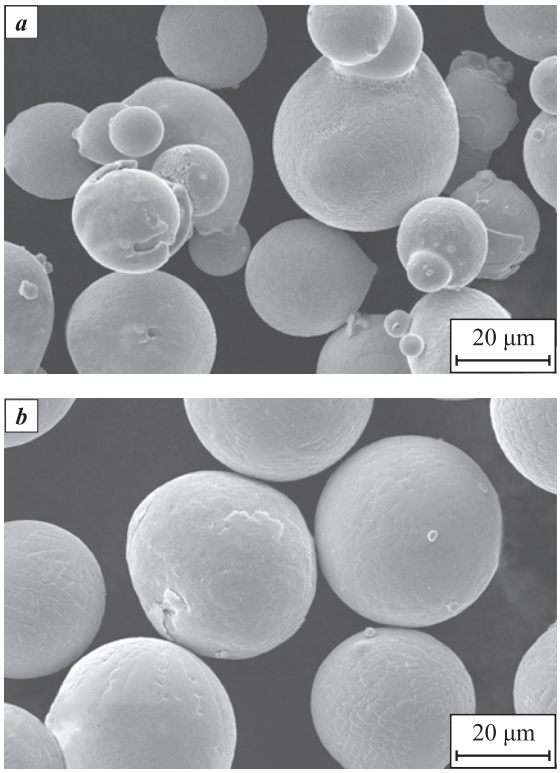

Fig. 1. Metal powder morphology
a – VZh159; ***b*** – CuCr1Zr

Рис. 1. Морфология металлического порошка
a – сплав ВЖ159, ***b*** – сплав БрХЦрТ В

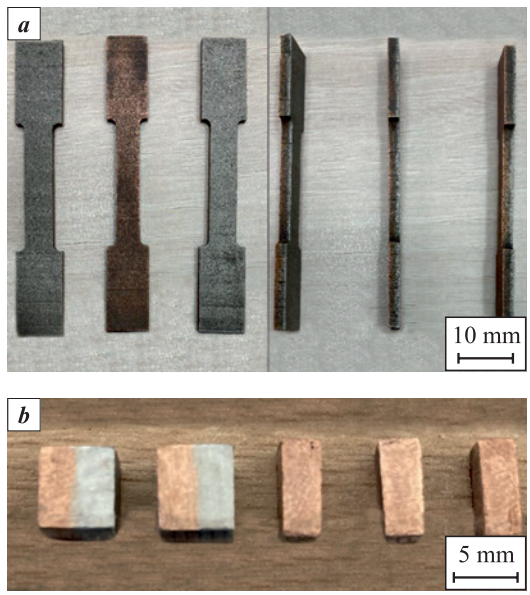

Fig. 2. VZh159–CuCr1Zr multi-material samples after SLM fabrication and machining
a – tensile test samples, ***b*** – compressive strength samples

Рис. 2. Мультиматериальные образцы системы ВЖ159–БрХЦрТ В после изготовления методом СЛП и механической обработки
a – образцы на растяжение, ***b*** – образцы на сжатие

Table 1. **Chemical composition, %, of VZh159 and CuCr1Zr powders**

Таблица 1. **Химический состав, %, порошков ВЖ159 и БрХЦрТ В**

Alloy	Cr	Ni	Al	Mo	Nb	Cu	Zr
VZh159	26–28	Base metal	1.25–1.55	7.0–7.8	2.7–3.4	–	–
CuCr1Zr	0.4–1.0	Up to 0.03	–	–	–	Base metal	0.03–0.08

Table 2. **SLM parameters for the manufacturing of VZh159–CuCr1Zr multi-material samples**

Таблица 2. **Параметры СЛП-процесса изготовления мультиматериальных образцов системы ВЖ159–БрХЦрТ В**

Alloy	Scanning speed, mm/s	Laser power, W	Hatch spacing, μm	Layer thickness, μm	Energy density, J/mm^3
VZh159	760	275	100	50	72
VZh159 + CuCr1Zr (12 layers)	160	400	150	50	325
CuCr1Zr	300	400	150	50	177

4) holding for 10 h;

5) air cooling.

It's noteworthy that conducting heat treatment to enhance the properties of both alloys is challenging due to the disparities in their structural and phase compositions. In the VZh159–CuCr1Zr system, the VZh159 alloy exhibits higher strength. Consequently, applying heat treatment to this alloy is more suitable. The standard heat treatment conditions for the VZh159 alloy do not alter the properties of the CuCr1Zr alloy or the interface zone between the alloys.

For mechanical testing, Zwick/Roell uniaxial floor-standing testing machines (Zwick Roell Group, Germany) were employed. Tensile tests were conducted on a Z050 machine (Zwick/Roell) at a 0.3 mm/min tensile rate, while compressive strength tests were performed on a Z100 machine (Zwick/Roell) at a 0.25 mm/min compression rate. Fractographic studies of the samples were carried out using a Mira 3 scanning electron microscope (Tescan, Czech Republic). The polished section with a crack that occurred after the compressive strength test was examined using a Leica DMi8 M optical microscope (Leica Microsystems, Germany). For phase composition analysis, a Rigaku SmartLab *X*-ray diffractometer (Rigaku Corporation, Japan) with a 100 μm pinhole was employed.

Results and discussion

Fig. 3 displays the *X*-ray diffraction patterns of the VZh159–CuCr1Zr multi-material sample in the pure alloy zones and the interface zone. The phase compositions in the pure alloy zones are characterized by solid solutions. In the XRDs of the interface zone, peaks are evident, indicating the presence of both alloys. The *X*-ray beam size was approximately 150 μm, fitting entirely within the interface zone (with a size of approximately 300 μm). The peaks in the interface zone overlap and cannot be distinctly separated, a phenomenon consistent with findings in other studies [12]. The XRD analysis did not reveal the presence of any additional phases.

Fig. 4 presents the results of tensile and compressive strength tests conducted on the VZh159–CuCr1Zr multi-material samples, along with pure CuCr1Zr alloy compressive strength tests. Table 3 provides a comparison of these test results with available data. The tensile strength of the VZh159–CuCr1Zr multi-material samples was $\sigma_u = 430 \pm 20$ MPa, and the relative elongation was $\varepsilon = 4.6 \pm 0.3$ % (see Table 3). The compressive test results were as follows: $\sigma_u = 822 \pm 23$ MPa, relative compression $\varepsilon = 42.5 \pm 1.5$ %.

Comparing the tensile test results with available data (Table 3) reveals an increase in ultimate strength by approximately 53 % relative to the pure CuCr1Zr alloy and a decrease by approximately 65 % relative to the pure VZh159 alloy. However, direct comparisons may lack precision due to variations in sample shapes and sizes among different researchers. Additionally, stress analysis considers the total cross-section containing both alloys, each comprising 50 % of the samples. Reassessing stress for the alloy with a greater impact on strength, the resulting tensile strength doubles to 860 MPa, reducing the relative difference to the pure VZh159 alloy to approximately 29 %. It's essential to note that available data [19] pertain to samples sub-

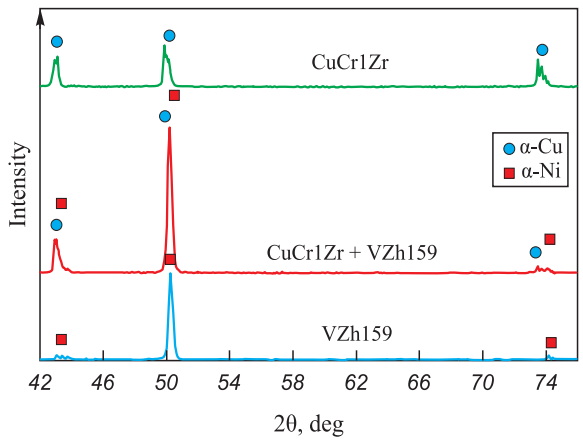

Fig. 3. Phase composition of the VZh159–CuCr1Zr multi-material samples

Рис. 3. Фазовый состав мультиматериальных образцов системы ВЖ159–БрХЦрТ В

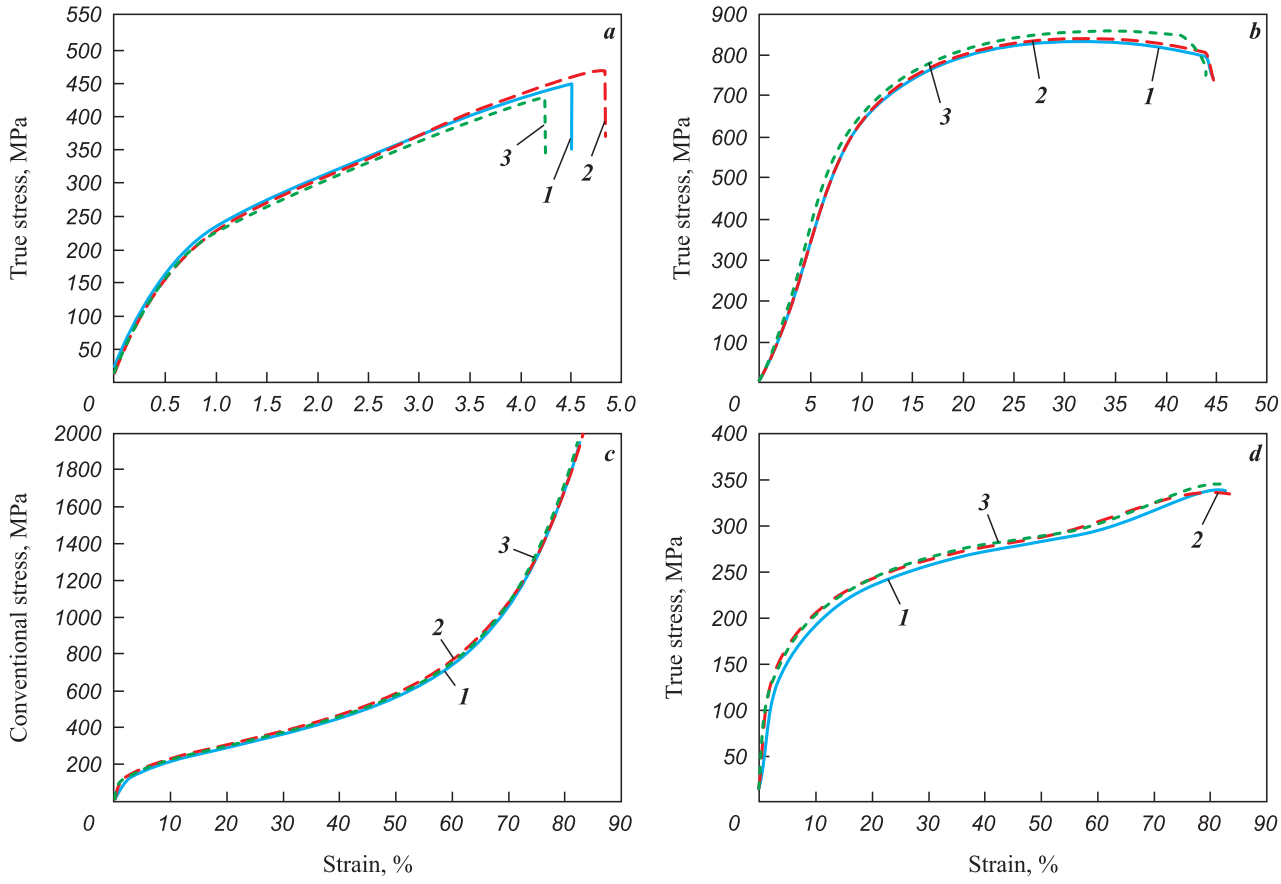

Fig. 4. Tensile (***a***) and compressive (***b***) stress-strain diagrams of the VZh159–CuCr1Zr system multi-material samples
Compressive stress-strain diagram of the pure CuCr1Zr alloy (***c*** and ***d***)

Рис. 4. Диаграмма деформирования при испытаниях на растяжение (***a***) и сжатие (***b***) мультиматериальных образцов системы ВЖ159–БрХЦрТ В, а также на сжатие чистого сплава БрХЦрТ В (***c*** и ***d***)

jected to hot isostatic pressing (HIP), a process enhancing mechanical properties, which was not conducted in this study.

The relative elongation of the VZh159–CuCr1Zr multi-material samples in the tensile tests, when compared to the pure CuCr1Zr and VZh159 alloys, reduces by 66 % and 83 %, respectively (see Table 3). This notable decrease can be attributed to the halving of the volume of the VZh159 alloy, which has a more pronounced effect on strength. Consequently, the size and number of defects in this alloy exert a greater influence on the reduction of its mechanical properties.

Comparing the results of the compressive strength test for the VZh159–CuCr1Zr multi-material samples with the available data (see Table 3) indicates a decrease in tensile strength by approximately 57 % (or 55 %) and a reduction in relative compression by 9 % (or 22 %) compared to Inconel 718 (analogous to VZh159). Similar to the analysis of tensile strength, it's important to note that stress analysis considered the entire

Table 3. **Comparison of mechanical testing results of the VZh159–CuCr1Zr multi-material samples with available data**

Таблица 3. **Сравнение результатов проведения механических испытаний мультиматериальных образцов системы ВЖ159–БрХЦрТ В с литературными данными**

Test	VZh159–CuCr1Zr multi-material samples (this study)		Alloy CuCr1Zr		Alloy VZh159		Inconel 718 alloy tests			
			[17]		[19]		[20]		[21]	
	σ_u, MPa	ε, %	σ_u, MPa	ε, %	σ_u, MPa	ε, %	σ_u, MPa	ε, %	σ_u, MPa	ε, %
Tension	430 ± 20	4.6 ± 0.3	203 ± 8	13.5 ± 2.5	1202 ± 13	26 ± 2.5	–	–	–	–
Compression	822 ± 23	42.5 ± 1.5	–	–	–	–	1900 ± 10	47 ± 2.5	1800 ± 50	55 ± 5

cross-section containing both alloys in a 1:1 ratio. After adjusting stresses for the alloy with a greater impact on strength, the reduction in ultimate strength in the specimens is 14 % and 9 %, respectively. Smith D. et al. [20] and Ghorbanpour S.et al. [21] present data for samples after HIP.

We also compared the compressive strength of the pure CuCr1Zr alloy (see Fig. 4, *c*) with available data. Our findings indicate that the properties of our samples are not inferior to those described in other studies. The offset yield strength ($\sigma_{0.2}$ true stress) of the VZh159–CuCr1Zr multi-material samples (Fig. 4, *b*) is approximately 80 % higher than that of the pure CuCr1Zr alloy (Fig. 4, *d*). Fig. 5 illustrates the VZh159–CuCr1Zr multi-material samples after the tensile and compressive strength tests.

Fig. 6 displays a fractography results of a VZh159–CuCr1Zr multi-material sample after the tensile test. In the CuCr1Zr alloy region, pits of various sizes and pores are evident, but microcracks are not present. The VZh159 alloy region exhibits a smooth fracture surface with some microcracks, suggesting that this region is more brittle compared to the CuCr1Zr region. In the interface zone, there are pits and an absence of a smooth surface, along with some microcracks. This observation implies that the interface zone exhibits both more ductile fracture features characteristic of the CuCr1Zr alloy (pits and no smooth surface) and less ductile fracture features characteristic of the VZh159 alloy (microcracks).

Fig. 7 shows a polished section of VZh159–CuCr1Zr multi-material samples after the compressive strength tests, along with an approximate crack pattern. The crack is oriented at 45° to the direction of load application in the VZh159 region. The crack ceases in the interface zone and does not propagate into the CuCr1Zr region. This observation suggests that the presence of a more

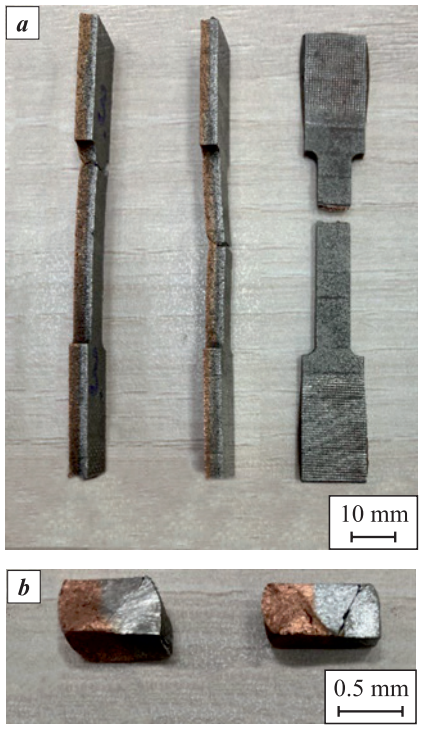

Fig. 5. VZh159–CuCr1Zr multi-material samples after tensile (***a***) and compressive strength (***b***) tests

Рис. 5. Мультиматериальные образцы системы ВЖ159–БрХЦрТ В после проведения испытаний на растяжение (***a***) и сжатие (***b***)

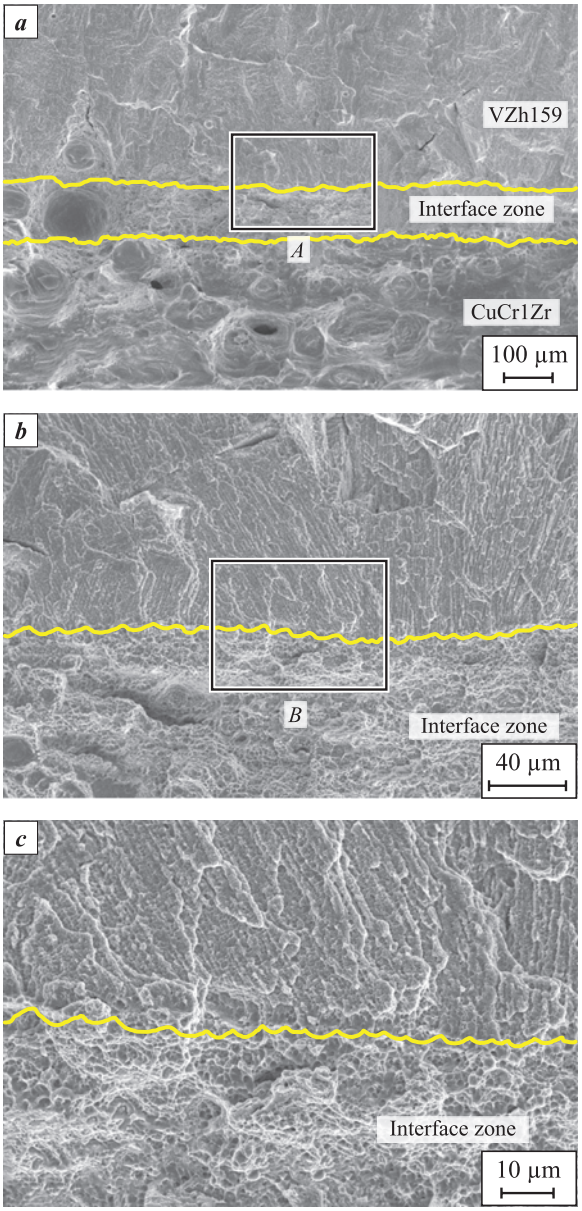

Fig. 6. Fractography of a VZh159–CuCr1Zr multi-material sample after tensile tests
a – general view, ***b*** – area *A*, ***c*** – area *B*

Рис. 6. Фрактография мультиматериального образца системы ВЖ159–БрХЦрТ В после проведения испытаний на растяжение
a – общий вид, ***b*** – область *A*, ***c*** – область *B*

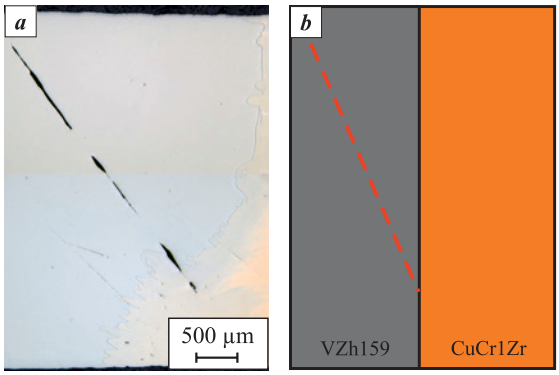

Fig. 7. Polished section of VZh159–CuCr1Zr multi-material samples after compressive strength tests (***a***) and approximate crack pattern (***b***)

Рис. 7. Шлиф мультиматериального образца системы ВЖ159–БрХЦрТ В после проведения испытаний на сжатие (***a***) и схематичное изображение распространения трещины (***b***)

ductile CuCr1Zr alloy in the interface zone contributes to the cessation of crack propagation.

Conclusions

In our investigation of the VZh159–CuCr1Zr multi-material system, we explored the phase composition of the interface zone and assessed mechanical properties, including ultimate strength, relative elongation, and relative compression through tensile and compressive strength tests. Additionally, we conducted fractography following tensile tests and analyzed crack propagation post-compressive strength tests. Our findings led to the following conclusions:

1. The phase compositions in the pure alloy zones are solid solutions. XRD patterns of the interface zone exhibit peaks corresponding to both alloys.

2. The tensile strength of the VZh159–CuCr1Zr multi-material samples, as determined by tensile tests, is $\sigma_u = 430 \pm 20$ MPa, with a relative elongation of $\varepsilon = 4.6 \pm 0.3$ %. The results of the compressive strength test were as follows: $\sigma_u = 822 \pm 23$ MPa, and relative compression $\varepsilon = 42.5 \pm 1.5$ %.

3. Tensile tests revealed that the ultimate strength of the VZh159–CuCr1Zr multi-material samples, when compared to the pure CuCr1Zr alloy, is approximately 53 % higher (according to available data), and the conditional yield strength increases by ~80 %.

4. The fractography of the VZh159–CuCr1Zr multi-material sample after tensile tests indicates that the interface zone displays both more ductile fracture features characteristic of the CuCr1Zr alloy (pits and no smooth surface) and less ductile features characteristic of the VZh159 alloy (microcracks).

5. Examination of the polished section of a VZh159–CuCr1Zr multi-material sample after compressive strength tests demonstrates that the presence of a more ductile CuCr1Zr alloy in the interface zone contributes to arresting the crack, which propagates at 45° to the direction of load application in the VZh159 alloy region.

References / Список литературы

1. Srivastava M., Rathee S., Patel V., Kumar A., Koppad P.G. A review of various materials for additive manufacturing: Recent trends and processing issues. *Journal of Materials Research and Technology*. 2022;21:2612–2641. https://doi.org/10.1016/j.jmrt.2022.10.015
2. Ngo T.D., Kashani A., Imbalzano G., Nguyen K.T.Q., Hui D. Additive manufacturing (3D printing): A review of materials, methods, applications and challenges. *Composites, Part B: Engineering*. 2018; 143:172–196. https://doi.org/10.1016/j.compositesb.2018.02.012
3. Gunasekaran J., Sevvel P., Solomon I.J. Metallic materials fabrication by selective laser melting: A review. *Materials Today: Proceedings*. 2021;37(2):252–256. https://doi.org/10.1016/j.matpr.2020.05.162
4. Negi S., Nambolan A.A., Kapil S., Joshi P.S., Karunakaran K.P., Bhargava P. Review on electron beam based additive manufacturing. *Rapid Prototyping Journal*. 2020;26(3):485–498. https://doi.org/10.1108/RPJ-07-2019-0182
5. Sefene E.M. State-of-the-art of selective laser melting process: A comprehensive review. *Journal of Manufacturing Systems*. 2022;63:250–274. https://doi.org/10.1016/j.jmsy.2022.04.002
6. Nandhakumar R., Venkatesan K. A process parameters review on selective laser melting-based additive manufacturing of single and multi-material: Microstructure, physical properties, tribological, and surface roughness. *Materials Today Communications*. 2023;35:105538. https://doi.org/10.1016/j.mtcomm.2023.105538
7. Nazir A., Gokcekaya O., Masum Billah K., Ertugrul O., Jiang J., Sun J., Hussain S. Multi-material additive manufacturing: A systematic review of design, properties, applications, challenges, and 3D printing of materials and cellular metamaterials. *Materials & Design*. 2023;226:111661. https://doi.org/10.1016/j.matdes.2023.111661
8. Chen K., Wang C., Hong Q., Wen S., Zhou Y., Yan C., Shi Y. Selective laser melting 316L/CuSn10 multi-materials: Processing optimization, interfacial characterization and mechanical property. *Journal of Materials Processing Technology*. 2020;283:116701. https://doi.org/10.1016/j.jmatprotec.2020.116701
9. Chen J., Yang Y., Song C., Zhang M., Wu S., Wang D. Interfacial microstructure and mechanical properties of 316L/CuSn10 multi-material bimetallic structure fabricated by selective laser melting. *Materials Science and Engineering: A*. 2019;752:75–85. https://doi.org/10.1016/j.msea.2019.02.097
10. Mei X., Wang X., Peng Y., Gu H., Zhong G., Yang S. Interfacial characterization and mechanical properties

of 316L stainless steel/Inconel 718 manufactured by selective laser melting. *Materials Science and Engineering: A*. 2019;758:185–91. https://doi.org/10.1016/j.msea.2019.05.011

11. Yusuf S., Mazlan N., Musa N.H., Zhao X., Chen Y., Yang S., Nordin N.A., Mazlan S.A., Gao N. Microstructures and hardening mechanisms of a 316L stainless steel/Inconel 718 interface additively manufactured by multi-material selective laser melting. *Metals*. 2023;13(2):400. https://doi.org/10.3390/met13020400
12. Onuike B., Heer B., Bandyopadhyay A. Additive manufacturing of Inconel 718 – Copper alloy bimetallic structure using laser engineered net shaping (LENSTM). *Additive Manufacturing*. 2018;21:133–140. https://doi.org/10.1016/j.addma.2018.02.007
13. Marques A., Cunha Â., Gasik M., Carvalho O., Silva F.S., Bartolomeu F. Inconel 718 – copper parts fabricated by 3D multi-material laser powder bed fusion: a novel technological and designing approach for rocket engine. *The International Journal of Advanced Manufacturing Technology*. 2022;122:2113–2123. https://doi.org/10.1007/s00170-022-10011-x
14. Ringel B., Zaepfel M., Herlan F., Horn M., Schmitt M., Seidel C. Advancing functional integration through multi-material additive manufacturing: Simulation and experimental validation of a burner nozzle. *Materials Today: Proceedings*. 2022;70:296–303. https://doi.org/10.1016/j.matpr.2022.09.241
15. Repnin A.V., Borisov E.V., Popovich A.A., Shamshurin A.I. Selective laser melting of multi-material VZh159–CuCr1Zr samples. *Global Energy*. 2023;29(2):175–188. (In Russ.). https://doi.org/10.18721/JEST.29212

    Репнин А.В.. Борисов Е.В., Попович А.А., Шамшурин А.И. Создание мульти-материальных образцов системы ВЖ159–БрХЦрТ методом селективного лазерного плавления. *Глобальная энергия*. 2023;29(2):175–188. https://doi.org/10.18721/JEST.29212
16. Popovich A.A., Sufiiarov V.S., Polozov I.A., Borisov E.V. Microstructure and mechanical properties of Inconel 718 produced by SLM and subsequent heat treatment. *Key Engineering Materials*. 2015;651–653:665–670.
17. Artemov A.L., Dyadchenko V.Yu., Lukyashko A.V., Novikov A.N., Popovich A.A., Rudskoy A.I., Svechkin V.P., Skoromnov V.I., Smolentsev A.A., Sokolov B.A., Solntsev V.L., Sufiyarov V.Sh., Shachnev S.Yu, Development of design and technology solutions for additive manufacturing of prototype inner lining for combustion chamber of multifunctional liquid-propellant rocket engine. *Space Technique and Technologies*. 2017;1(16):50–62. (In Russ.).

    Артемов А.Л., Дядченко В.Ю., Лукьяшко А.В., Новиков А.Н., Попович А.А., Рудской А.И., Свечкин В.П., Скоромнов В.И., Смоленцев А.А., Соколов Б.А., Солнцев В.Л., Суфияров В.Ш., Шачнев С.Ю. Отработка конструктивных и технологических решений для изготовления опытных образцов внутренней оболочки камеры сгорания многофункционального жидкостного ракетного двигателя с использованием аддитивных технологий. *Космическая техника и технологии*. 2017;1(16):50–62.
18. Khlybov A.A., Belyaev E.S., Ryabtsev A.D., Belyaeva S.S., Getmanovsky Y.A., Yavtushenko P.M., Ryabov D.A. Influence of the HIP technology on the structure and properties of nickel alloy VZH159. *Vestnik of Nosov Magnitogorsk State Technical University*. 2021;3:75–83. (In Russ.). https://doi.org/10.18503/1995-2732-2021-19-3-75-83

    Хлыбов А.А., Беляев Е.С., Рябцев А.Д., Беляева С.С., Гетмановский Ю.А., Явтушенко П.М., Рябов Д.А. Влияние технологии ГИП на структуру и свойства никелевого сплава ВЖ 159. *Вестник Магнитогорского государственного технического университета*. 2021;3:75–83. https://doi.org/10.18503/1995-2732-2021-19-3-75-83
19. Prager S.M., Solodova T.V., Tatarenko O.Y. Research of mechanical properties and microstructure of samples obtained by SLS from metal powder composition of VZh159 alloy. *Proceedings of VIAM*. 2017;11:1–11. (In Russ.). https://dx.doi.org/10.18577/2307-6046-2017-0-11-1-1

    Прагер С.М., Солодова Т.В., Татаренко О.Ю. Исследование механических свойств и структуры образцов, полученных методом селективного лазерного сплавления (СЛС) из сплава ВЖ159. *Труды ВИАМ*. 2017;11:1–11. https://dx.doi.org/10.18577/2307-6046-2017-0-11-1-1
20. Smith D.H., Bicknell J., Jorgensen L., Patterson B.M., Cordes N.L., Tsukrov I., Knezevic M. Microstructure and mechanical behavior of direct metal laser sintered Inconel alloy 718. *Materials Characterization*. 2016;113(1):1–9.
21. Ghorbanpour S., Alam M.E,. Ferreri N.C., Kumar A., McWilliams B.A., Vogel S.C., Bicknell J., Beyerlein I.J., Knezevic M. Experimental characterization and crystal plasticity modeling of anisotropy, tension-compression asymmetry, and texture evolution of additively manufactured Inconel 718 at room and elevated temperatures. *International Journal of Plasticity*. 2020;125:63–79. https://doi.org/10.1016/j.ijplas.2019.09.002
22. Bai Y., Zhao C., Zhang Y., Chen J., Wang H. Additively manufactured CuCrZr alloy: Microstructure, mechanical properties and machinability. *Materials Science and Engineering: A*. 2021;819:141528. https://doi.org/10.1016/j.msea.2021.141528

Information about the Authors

Arseniy V. Repnin – Engineer, Laboratory "Synthesis of new materials and structures", Peter the Great St. Petersburg Polytechnic University (SPbPU)
ORCID: 0009-0001-3157-3317
E-mail: repnin_arseniy@mail.ru

Сведения об авторах

Арсений Вячеславович Репнин – инженер лаборатории «Синтез новых материалов и конструкций» Санкт-Петербургского политехнического университета Петра Великого (СПбПУ)
ORCID: 0009-0001-3157-3317
E-mail: repnin_arseniy@mail.ru

Evgeny V. Borisov – Cand. Sci. (Eng.), Leading Researcher, Laboratory "Synthesis of new materials and structures", SPbPU
ORCID: 0000-0003-2464-6706
E-mail: evgenii.borisov@icloud.com

Anatoly A. Popovich – Dr. Sci. (Eng.), Professor, Director of the Institute of Machinery, Materials, and Transport, SPbPU
ORCID: 0000-0002-5974-6654
E-mail: popovicha@mail.ru

Nikita A. Golubkov – Lead Engineer, Laboratory "Synthesis of new materials and structures", SPbPU
ORCID: 0009-0009-6785-1444
E-mail: golubkovna@gmail.com

Евгений Владиславович Борисов – к.т.н., ведущий научный сотрудник лаборатории «Синтез новых материалов и конструкций» СПбПУ
ORCID: 0000-0003-2464-6706
E-mail: evgenii.borisov@icloud.com

Анатолий Анатольевич Попович – д.т.н., профессор, директор Института машиностроения, материалов и транспорта СПбПУ
ORCID: 0000-0002-5974-6654
E-mail: popovicha@mail.ru

Никита Александрович Голубков – ведущий инженер лаборатории «Синтез новых материалов и конструкций» СПбПУ
ORCID: 0009-0009-6785-1444
E-mail: golubkovna@gmail.com

Contribution of the Authors

A. V. Repnin – conducted experiments, processed the results, and wrote the initial draft manuscript.
E. V. Borisov – planned experiments, wrote the manuscript, and participated in discussions about the results.
A. A. Popovich – conceptualized the idea, determined the purpose of the work, and participated in discussions about the results.
N. A. Golubkov – carried out tensile and compression tests, and processed the results obtained.

Вклад авторов

А. В. Репнин – проведение экспериментов, обработка полученных результатов, написание черновика статьи.
Е. В. Борисов – планирование экспериментов, написание статьи, участие в обсуждении результатов.
А. А. Попович – концептуализация идеи, определение цели работы и ее задач, участие в обсуждении результатов.
Н. А. Голубков – проведение испытаний на растяжение и сжатие, обработка полученных результатов.

Received 27.06.2023
Revised 15.08.2023
Accepted 18.08.2023

Статья поступила 27.06.2023 г.
Доработана 15.08.2023 г.
Принята к публикации 18.08.2023 г.

Materials and Coatings Fabricated Using the Additive Manufacturing Technologies
Материалы и покрытия, получаемые методами аддитивных технологий

UDC 621.762

https://doi.org/10.17073/1997-308X-2024-1-62-72

Research article
Научная статья

Additive technology for forming multi-material samples of “stainless steel – high-entropy alloys” system

D. V. Masaylo ✉, A. V. Repnin, A. A. Popovich, N. G. Razumov, A. K. Mazeeva

Peter the Great St. Petersburg Polytechnic University
29 Polytekhnicheskaya Str., St. Petersburg 195251, Russian Federation

✉ dmasaylo@gmail.com

Abstract. The Metal Paste Deposition (MPD) method offers several advantages in producing multi-materials compared to other additive technologies. While there have been studies conducted on multi-material production using this method, they are limited. Hence, a significant objective is to expand the research scope concerning multi-materials produced through the MPD method. This study aimed to examine samples of multi-material systems comprising 316L steel with $CoCrFeMnNiW_{0.25}$ and 316L steel with CrMoNbWV obtained from metal paste. The investigation involved forming multi-material samples and analyzing the porosity, microstructure, phase composition, and hardness of the 316L steel metal paste after sintering. The findings lead to several conclusions: when forming multi-material samples of the 316L–$CoCrFeMnNiW_{0.25}$ system, there is no necessity to create a transition zone using mixed 316L steel and $CoCrFeMnNiW_{0.25}$ powders, as these alloys mix strongly within it. However, in the 316L–CrMoNbWV system, forming a transition zone of mixed powders is necessary to mitigate the effects of uneven shrinkage. Altering the sintering modes for multi-material samples of the 316L–$CoCrFeMnNiW_{0.25}$ system is recommended; the temperature should be reduced by 30–45 °C compared to the sintering modes for 316L steel. After sintering the metal paste derived from 316L steel, the resulting sample exhibits large and small spherical pores. To minimize these defects, degassing can be employed. Additionally, reducing porosity can be achieved through hot isostatic pressing post-sintering. The microstructure following the sintering of the metal paste from 316L steel consists of coarse austenite grains with minimal ferrite accumulation at the grain interface.

Keywords: additive technologies, metal paste deposition, multi-materials, high-entropy alloys, 316L steel

Acknowledgements: This research was funded by the Ministry of Science and Higher Education of the Russian Federation (State Assignment for basic research 075-03-2023-004).

For citation: Masaylo D.V., Repnin A.V., Popovich A.A., Razumov N.G., Mazeeva A.K. Additive technology for forming multi-material samples of “stainless steel – high-entropy alloys” system. *Powder Metallurgy and Functional Coatings*. 2024;18(1):62–72. https://doi.org/10.17073/1997-308X-2024-1-62-72

Аддитивная технология формирования мультиматериальных образцов системы «нержавеющая сталь – высокоэнтропийные сплавы»

Д. В. Масайло, А. В. Репнин, А. А. Попович, Н. Г. Разумов, А. К. Мазеева

Санкт-Петербургский политехнический университет Петра Великого
Россия, 195251, г. Санкт-Петербург, ул. Политехническая, 29

dmasaylo@gmail.com

Аннотация. Метод нанесения металлической пасты имеет ряд преимуществ при изготовлении мультиматериалов по сравнению с другими видами аддитивных технологий. Ведутся исследования получения мультиматериалов данным методом, но их количество не так велико. В связи с этим перспективной задачей является расширение исследовательской базы изучения мультиматериалов, получаемых методом нанесения металлической пасты. Целью данной работы являлось исследование образцов мультиматериальной системы сталь 316L–CoCrFeMnNiW$_{0,25}$ и сталь 316L–CrMoNbWV, полученных из металлической пасты. Проводились исследования формирования мультиматериальных образцов, а также анализ пористости, микроструктуры, фазового состава и твердости металлической пасты из стали 316L после спекания. В результате были сделаны следующие выводы: при формировании мультиматериальных образцов системы 316L–CoCrFeMnNiW$_{0,25}$ нет необходимости формирования переходной зоны из смеси порошков стали 316L и CoCrFeMnNiW$_{0,25}$, так как в ней происходит сильное смешивание двух сплавов. В системе 316L–CrMoNbWV имеется необходимость формирования переходной зоны из смеси порошков, так как это снизит влияние неравномерной усадки. Режимы спекания для мультиматериальных образцов системы 316L–CoCrFeMnNiW$_{0,25}$ должны быть изменены по сравнению с режимами для чистых сплавов – температура снижена на 30–45 °C по сравнению с режимами спекания стали 316L. Образец, полученный после спекания металлической пасты из стали 316L, имеет крупные и мелкие сферические поры. Для уменьшения количества подобного рода дефектов можно использовать дегазацию. Кроме того, снижение пористости может быть достигнуто за счет горячего изостатического прессования после спекания. После спекания металлической пасты из стали 316L микроструктура представляет собой очень крупные зерна аустенита с крайне небольшим количеством феррита, скапливающегося по границам зерен.

Ключевые слова: аддитивные технологии, нанесение металлической пасты, мультиматериалы, высокоэнтропийные сплавы, сталь 316L

Благодарности: Исследование выполнено при финансовой поддержке Министерства науки и высшего образования Российской Федерации (Соглашение о предоставлении субсидии № 075-03-2023-004).

Для цитирования: Масайло Д.В., Репнин А.В., Попович А.А., Разумов Н.Г., Мазеева А.К. Аддитивная технология формирования мультиматериальных образцов системы «нержавеющая сталь – высокоэнтропийные сплавы». *Известия вузов. Порошковая металлургия и функциональные покрытия*. 2024;18(1):63–72. https://doi.org/10.17073/1997-308X-2024-1-62-72

Introduction

The fabrication of products with 3D property alterations has been actively employed in manufacturing for many years [1; 2]. Such products demonstrate enhanced performance characteristics [3] and find applications across diverse industries like automotive, aerospace engineering, biomedicine, and defense [4; 5]. the fabrication of products featuring functional gradients (multimaterials) uses several production methods, including centrifugal casting, powder metallurgy, chemical vapor deposition, and additive technologies (AT) [6]. Notably, there's been a growing interest in research within the at recently [7].

In contrast to subtractive manufacturing methods involving machining, casting, and forging, at enables the creation of three-dimensional product geometries by incrementally adding material layer by layer, following a 3D model [8]. Additive technologies facilitate the utilization of various material types such as polymers, metals, ceramics, glasses, biomaterials, and composites [9]. These encompass techniques like stereolithography, selective laser melting, direct energy and material deposition, material extrusion, material inkjet deposition, among others.

Regarding the production of multi-materials from metals, notable at types include selective laser melting and direct supply of energy and material [10]. These methods entail melting metal powder layer by layer based on a specified 3D model, enabling the creation of geometrical complex metal products. However, the disadvantage of these procedures lies in the equipment's high cost and maintenance expenses, owing to their intricate design and expensive components [11]. Moreover, these processes require the melting and

acquisition of powder materials with specific shapes and a narrow particle size distribution (typically 20–63 μm for selective laser melting technology and 60–120 μm for direct energy and material supply technology). This limitation restricts the range of usable precursors and final multi-materials [12]. Mitigating these drawbacks in the production of multi-material products can be achieved through additive technologies that do not involve the melting of metal powders.

Alternative methods for producing multi-materials from metals and ceramics using at without directly melting metal powders include Binder Jetting, Material Jetting, Fused Deposition, and Metal Paste Deposition (MPD) [13]. Among these methods, MPD holds several advantages over others, such as lacking a complex polymer base in the binder and eliminating the need to produce filament, among other benefits [14]. A defining aspect of this technology is the absence of a requirement to burn out the binder, as it almost entirely evaporates during the printing process. This significantly accelerates manufacturing and reduces associated costs.

The core principle of the MPD method involves applying a paste comprising metal powder onto the substrate in necessary layers, as dictated by the 3D model, until the product is fully formed [15]. This paste consists of metal particles bonded by a mixture of water and a binder: 90 wt. % metal powder and 10 wt. % liquid. Throughout printing, the liquid evaporates, leaving a "green" part composed of metal particles with less than 1 % binder residue. an illustration of a 3D printer utilizing MPD technology and a diagram of the extruder can be observed in Fig. 1.

Currently, there are limited number of manufacturers producing 3D printers using MPD technology, such as Rapidia (Canada), Metallic 3D (US), and Mantle (US). It is worth noting that there are no off-the-shelf solutions available for manufacturing multi-material products using the MPD method [16]. However, devices employing this technology can be adapted for multi-material product fabrication by either swapping raw material cartridges during printing or utilizing multiple nozzles [17].

Numerous studies have investigated the production of multi-material products utilizing MPD technology and similar approaches. In a study by the authors of [18], samples derived from metal pastes composed of steel, copper, and alumina were prepared and analyzed. the investigation into dissimilar metal interactions revealed minimal differences in 3D shrinkage and increased porosity within the transition zone. Notably, the transition zone between steel and copper exhibited alloy mixing, resulting in a fourfold increase in electrical conductivity and a 34 % rise in Young's modulus compared to a pure steel sample. However, the multi-material system of steel with alumina displayed a 17 % lower Young's modulus compared to the pure steel sample, without any alloy mixing. In another study documented by the authors of [19], multi-material samples of the copper-chemically modified graphene system, produced via the MPD method, were examined. These samples were designed to simulate an electric battery. the resultant metal and graphene pastes demonstrated the potential for producing prototype electric batteries, suggesting that additive technologies could effectively fabricate electrodes and electric batteries with customized configurations.

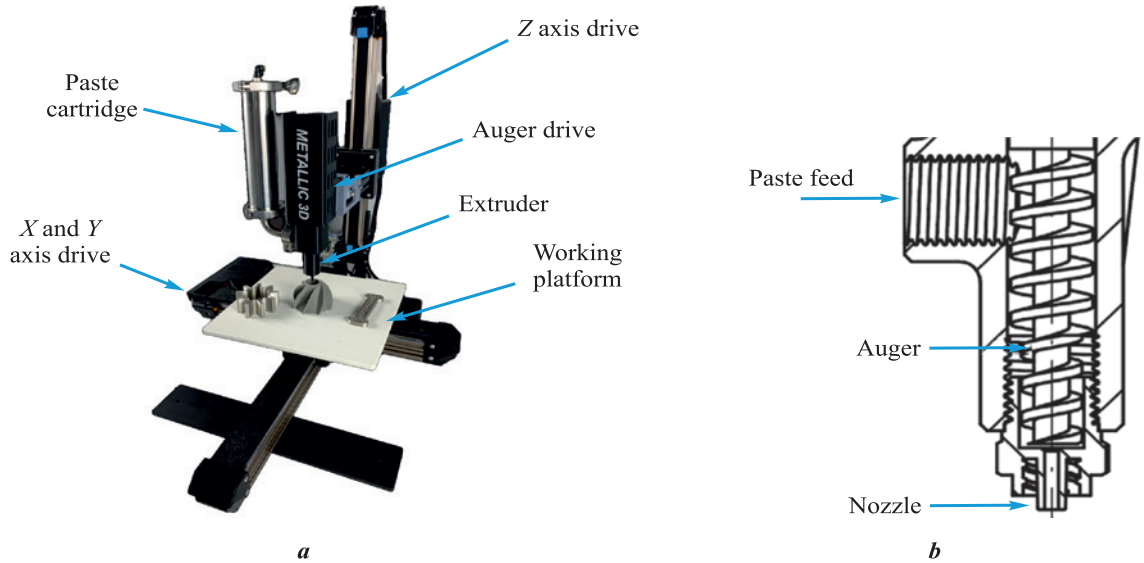

Fig. 1. MPD 3D printer (Metallic 3D, ***a***) and extruder diagram (***b***)

Рис. 1. Изображение 3D-принтера, работающего по технологии MPD (Metallic 3D, ***a***), и схема экструдера (***b***)

From the aforementioned literature review, it is evident that the metal paste deposition method for manufacturing multi-materials presents several advantages over other types of additive technologies. Although there have been studies conducted on multi-material production using this method, they remain relatively limited. Therefore, a promising area of focus involves expanding the research scope to further investigate multi-materials produced via the MPD method. For example, high-entropy alloys (HEAs) like CoCrFeMnNi exhibit superior impact strength, particularly in cryogenic conditions, and have a higher endurance limit compared to 304L and 316L steels. Furthermore, they demonstrate enhanced structural stability under ion irradiation compared to nickel alloys and possess commendable corrosion resistance, comparable to steel 304L. However, replacing traditional engineering alloys such as stainless steels or nickel-based superalloys with CoCrFeMnNi might escalate product costs. In this context, the concept of creating multi-materials within the CoCrFeMnNi–316L system could offer a promising solution to enhance performance characteristics without significantly inflating production expenses [20]. the addition of W to CoCrFeMnNi can elevate its melting point. HEAs like CrMoNbWV exhibit heightened corrosion strength, hardness, and wear resistance. This alloy type holds promise for applications in friction pairs and conditions involving severe abrasive wear within aggressive environments [21].

The objective of this study was to investigate samples of the multi-material systems comprising 316L steel with $CoCrFeMnNiW_{0.25}$ and 316L steel with CrMoNbWV obtained from metal paste. to achieve this goal, several key issues needed addressing: to analyze the impact of metal powder morphology and particle size distribution, along with the transitional layer comprising mixed powders, on the formation process of multi-material samples, and to examine the porosity, microstructure, phase composition, and hardness of the metal paste derived from 316L steel subsequent to sintering.

Materials and methods

To produce multi-material samples of the 316L–$CoCrFeMnNiW_{0.25}$ and 316L–CrMoNbWV systems, we used specific metal powders depicted in Fig. 2. Examination of the powders revealed that 316L steel and $CoCrFeMnNiW_{0.25}$ HEA powders consist predominantly of spherical particles exhibiting a smooth surface texture, with occasional irregularly shaped particles present. The 316L steel powder was manufactured through gas atomization by Sphere M LLC (Metlino Village, Chelyabinsk Region). the $CoCrFeMnNiW_{0.25}$

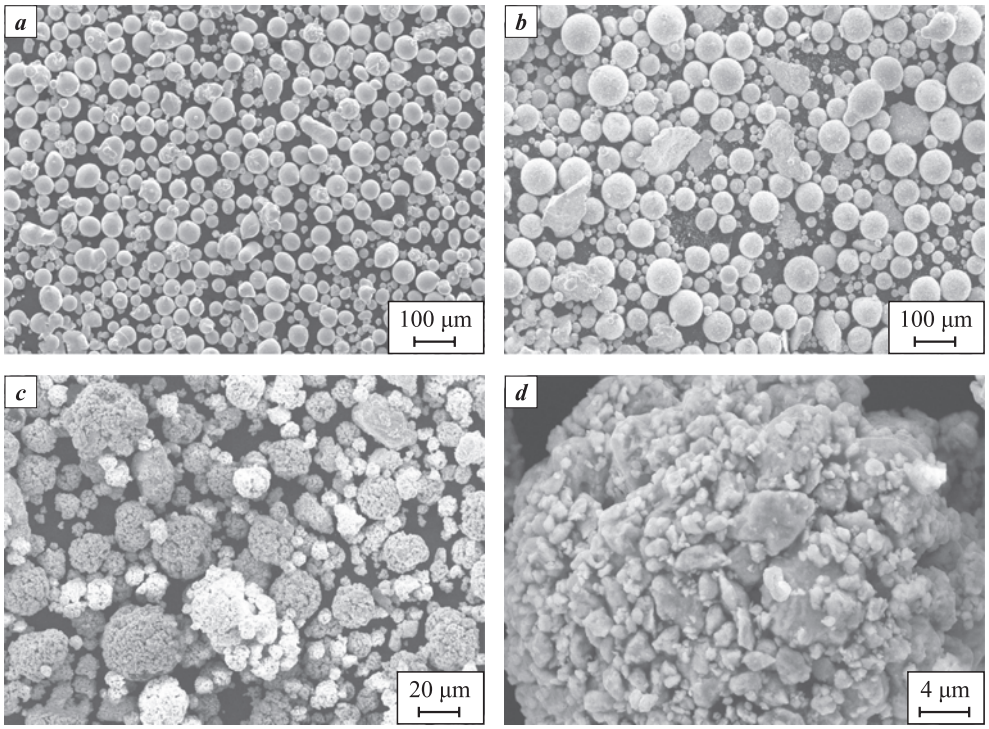

Fig. 2. Morphology of metal powders:
a – 316L steel; ***b*** – $CoCrFeMnNiW_{0.25}$ HEA; ***c***, ***d*** – CrMoNbWV HEA

Рис. 2. Морфология металлических порошков
a – сталь 316L; ***b*** – ВЭС $CoCrFeMnNiW_{0.25}$; ***c***, ***d*** – ВЭС CrMoNbWV

HEA powder was produced via mechanical alloying in a Fritsch Pulverisette 4 planetary mill (Fritsch GmbH, Germany) as follows: duration 5–20 h, main disk rotation speed 200–400 rpm, bowl rotation speed 400–800 rpm (rotation against the disk), grinding media of 10 mm steel balls with a ball-to-powder weight ratio of 20:1. Following mechanical alloying, the particles underwent spheroidization using a Tekna TEK-15 unit (Tekna, Canada) employing inductively coupled plasma with an Ar–H_2 gas mixture. the powder feed rate ranged from 20 to 25 g/min [22]. Similarly, the CrMoNbWV HEA powder was obtained through mechanical alloying using a Fritsch Pulverisette 4 planetary mill (Fritsch GmbH, Germany) as follows: duration 5 h, main disk/bowl rotation speed 350/700 rpm, grinding balls of high-strength steel with a diameter of 7–10 mm, maintaining a material-to-ball weight ratio 1:20 [21]. After mechanical alloying, the particles underwent agglomeration in a spray drying unit.

The particle size distribution of the powders was determined using laser diffraction analysis conducted with an Analysette 22 NanoTec Plus particle size analyze (Fritsch GmbH, Germany). the results of these measurements are detailed in Table 1.

Table 1 showcases distinct particle size distributions among the powders. These variations can potentially lead to uneven shrinkage during the fabrication of multi-material products. Additionally, it's important to note that the data acquired for the CrMoNbWV HEA pertain to the particles constituting the powder granules, as they disintegrated during analysis due to dissolution in water.

For the metal paste comprising 316L steel, $CoCrFeMnNiW_{0.25}$ HEA, and CrMoNbWV HEA, a 7 % polyvinyl alcohol solution in water served as the binder. This solution was prepared through continuous stirring at 80 °C until the polyvinyl alcohol crystals completely dissolved in water (~2 h).

The 316L steel metal paste was prepared for printing using a Tronxy Moore 1 Mini Clay 3D printer (Tronxy, China). While this printer typically employs ceramic paste extrusion technology, it was adapted to accommodate metal paste by adjusting the specific consistency required.

Sintering of the 316L steel paste was conducted in a vacuum furnace from Carbolite Gero GmbH & Co. KG, Germany. the sintering process followed these modes: heating to 600 °C at a rate of 5 °C/min, holding for 1 h; subsequent heating to 1380 °C at a rate of 5 °C/min, holding for 3 h, and cooling within the oven. the treatment occurred within a hydrogen atmosphere. the etching process to reveal the microstructure of 316L steel sample was performed using aqua regia.

Table 1. **Particle size distribution of metal powders**

Таблица 1. **Гранулометрический состав используемых порошков**

Fraction, vol. %	Particle size, μm		
	316L steel	$CoCrFeMnNiW_{0.25}$	CrMoNbWV
10	<20	<13	<2
50	<39	<50	<6
90	<70	<98	<18

For examining the macrostructure of the transition zone in the "green" bodies of the multi-material samples, a Leica M125 stereomicroscope (Leica Microsystems, Germany) was employed.

The melting point of the $CoCrFeMnNiW_{0.25}$ HEA powder was determined via differential scanning calorimetry (DSC) using a NETZSCH DSC 404 F3 Pegasus unit (NETZSCH GmbH, Germany) This analysis was conducted in a corundum crucible within a high-purity argon environment, employing a heating rate of 20 K/min in the temperature range of 1200 to 1600 °C. the DSC curve depicting the melting process exhibits an endothermic peak in the heat flow versus temperature relationship, delineating three distinct characteristic points: T_{onset}, T_{peak} and T_{end}. The peak onset point (T_{onset}) is identified as the intersection between the interpolated baseline and the tangent drawn to the deflection point of the ascending side of the peak. the peak point (T_{peak}) signifies the temperature corresponding to the maximum deviation between the DSC curve and the baseline. Finally, the peak end point (T_{end}) is recognized as the intersection between the interpolated baseline and the tangent drawn to the deflection point on the descending side of the peak.

The analysis of the microstructure in a 316L steel sample and the examination of the structure of the "green" bodies in multi-material samples were carried out using a Leica DMi8 M optical microscope (Leica Microsystems, Germany). the phase composition was determined through analysis performed with a Rigaku SmartLab *X*-ray diffractometer (Rigaku Corporation, Japan). Additionally, Vickers microhardness measurements were conducted using a MicroMet 5101 microhardness tester manufactured (Buehler Ltd, USA).

Results and discussion

Fig. 3 depicts multi-material samples ("green" bodies) from 316L–$CoCrFeMnNiW_{0.25}$ and 316L–CrMoNbWV systems after molding. the observations are as follows: the 316L–$CoCrFeMnNiW_{0.25}$ sample lacking a transition zone of mixed powders displays a predominantly smooth interface with a minor blending of the two alloys

(Fig. 3, *a*); the 316L–CoCrFeMnNiW$_{0.25}$ sample with a transition zone of mixed powders exhibits an uneven arc-shaped interface, characterized by substantial mixing of the two alloys (Fig. 3, *b*); the 316L–CrMoNbWV sample without a transition zone of mixed powders showcases a deep crack along the interface, stemming from uneven shrinkage due to varying particle size distributions of the two alloys (Fig. 3, *c*); the 316L–CrMoNbWV sample featuring a transition zone of mixed powders displays no deep cracks, presenting a smooth interface with a blending of the two alloys (Fig. 3, *d*).

Fig. 4 displays metallographic sections of multi-material samples, referred to as "green" bodies, obtained from the 316L–CoCrFeMnNiW$_{0.25}$ and 316L–CrMoNbWV systems.

Upon analyzing the metallographic sections, several observations regarding the interfaces in the multi-material samples of the 316L–CoCrFeMnNiW$_{0.25}$ and 316L–CrMoNbWV systems were noted: the interface between 316L and CoCrFeMnNiW$_{0.25}$ in the 316L–CoCrFeMnNiW$_{0.25}$ system displays a smooth transition without any breaks, discontinuities, or defects (Fig. 4, *a*). Similarly, the interface between 316L and a combination of CoCrFeMnNiW$_{0.25}$ and 316L exhibits no breaks, discontinuities, or defects, although it appears less distinct compared to the 316L and CoCrFeMnNiW$_{0.25}$ interface (Fig. 4, *b*). the interface between 316L and CrMoNbWV is clearly defined, attributed to the considerably smaller size of CrMoNbWV particles in contrast to those of the 316L alloy. This interface also lacks any breaks, discontinuities, or defects (Fig. 4, *c*). Likewise, the interface between 316L and a combination of CrMoNbWV and 316L presents a less distinct boundary but remains devoid of breaks, discontinuities, or defects (Fig. 4, *d*). the absence of breaks, discontinuities, and other defects at the interfaces within the multi-material samples from the 316L–CoCrFeMnNiW$_{0.25}$ and 316L–CrMoNbWV systems suggests a decreased likelihood of defect formation post the sintering process.

Based on the analysis of literature data concerning the manufacturing of multi-material products using AT, it has been highlighted that the transition zone, where dissimilar alloys are blended, necessitates specifically optimized printing parameters [23–25]. This is crucial because the properties of the alloy mixture differ from those of pure alloys, and utilizing printing parameters designed for pure alloys with the mixture can lead to an unstable synthesis process, potentially resulting in defects. In the MPD method, the primary interaction between dissimilar alloys occurs during the sintering phase. Given the limitation in separately influencing the zone of alloy differences during sintering, it becomes preferable to minimize the mixing zone between alloys

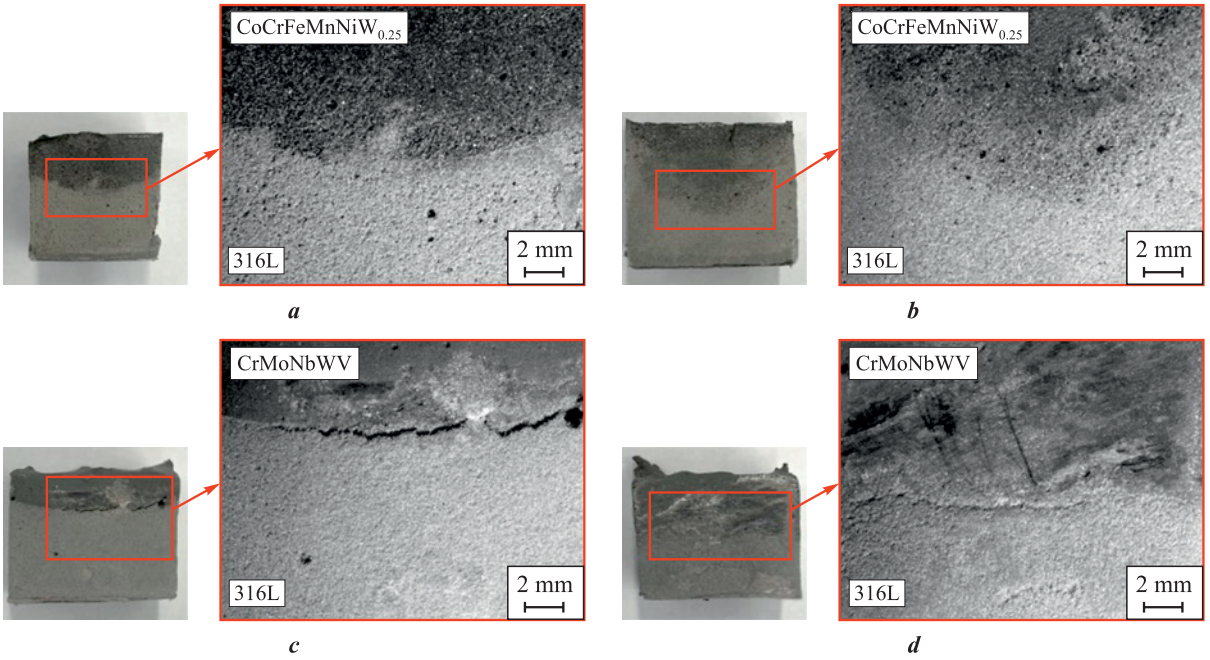

Fig. 3. Study of transition zones in multi-material samples ("green" bodies) of 316L–CoCrFeMnNiW$_{0.25}$ (***a***, ***b***) and 316L–CrMoNbWV (***c***, ***d***) systems

a, ***c*** – absence of a transition zone; ***b***, ***d*** – presence of a transition zone with mixed powders

Рис. 3. Исследование переходных зон мультиматериальных образцов («зеленые» детали) систем сталь 316L–CoCrFeMnNiW$_{0.25}$ (***a***, ***b***) и сталь 316L–CrMoNbWV (***c***, ***d***)

a, ***c*** – без переходной зоны; ***b***, ***d*** – с переходной зоной из смеси соответствующих порошков

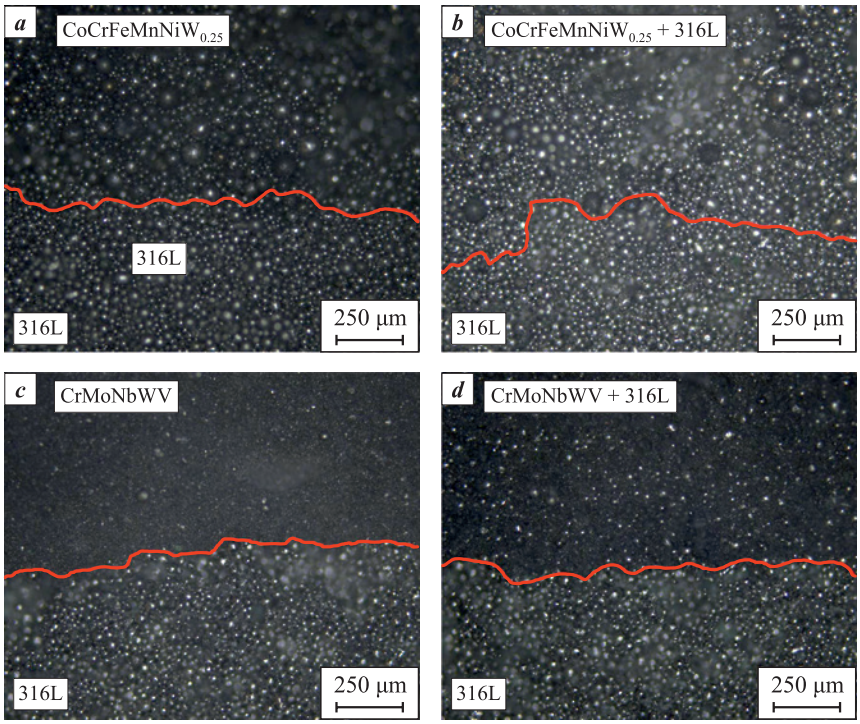

Fig. 4. Analysis of interfaces in multi-material samples ("green" bodies) from the 316L–$CoCrFeMnNiW_{0.25}$ (***a***, ***b***) and 316L–CrMoNbWV (***c***, ***d***) systems

a, ***c*** – absence of a transition zone; ***b***, ***d*** – presence of a transition zone with mixed powders
Red line indicates the interface between zones of different chemical composition

Рис. 4. Исследование границы раздела в мультиматериальных образцах («зеленые» детали) систем сталь 316L–$CoCrFeMnNiW_{0.25}$ (***a***, ***b***) и сталь 316L–CrMoNbWV (***c***, ***d***)

a, ***c*** – без переходной зоны; ***b***, ***d*** – с переходной зоной из смеси соответствующих порошков
Красная линия – граница раздела зон различного химического состава

to reduce the volume of material susceptible to unstable synthesis. From the observations in Figs. 3 and 4, it can be inferred that the absence of a transition zone between mixed 316L steel and $CoCrFeMnNiW_{0.25}$ powders is desirable due to significant mixing between two alloys occurs. For the 316L–CrMoNbWV system, having a transition zone of mixed powders is preferable. This choice aims to mitigate the impact of uneven shrinkage, thereby minimizing the occurrence of potential defects.

The sintering process for multi-material samples following the molding phase requires knowledge of the alloy's melting point to select appropriate sintering parameters. While sintering modes for 316L steel have been previously established, the melting point of $CoCrFeMnNiW_{0.25}$ HEA powder was determined via differential scanning calorimetry, as detailed in Table 2.

Table 2 indicates that the average melting point of $CoCrFeMnNiW_{0.25}$ ranges from 1373 ± 19 to 1403 ± 16 °C, while the melting point of 316L steel falls between 1402 ± 15 to 1435 ± 30 °C [26]. Consequently, the sintering parameters utilized for 316L steel may not be suitable for sintering multi-material samples within the 316L–$CoCrFeMnNiW_{0.25}$ system. Therefore, adjustments are necessary, suggesting a reduction in temperature by approximately 30–45 °C compared to the sintering modes established for 316L steel. Additionally, Table 2 highlights a trend of increasing temperature during measurement. This temperature rise might be attributed to the burnout of manganese, which possesses the lowest melting and

Table 2. **Investigation of $CoCrFeMnNiW_{0.25}$ powder melting temperature by differential scanning calorimetry**

Таблица 2. **Результаты определения температуры плавления порошка $CoCrFeMnNiW_{0,25}$ методом дифференциальной сканирующей калориметрии**

Run No.	Measuring range		
	Onset	Peak	End
1	1355	1386	1389
2	1362	1391	1394
3	1372	1398	1401
4	1383	1409	1412
5	1393	1418	1421
	Averages		
	1373	1400	1403

boiling points among all elements present in the HEA. Any alteration in the concentration of this less refractory element could contribute to an increase in temperature. Consequently, when determining sintering parameters, it is advisable to prioritize initial melting point measurements of $CoCrFeMnNiW_{0.25}$ and conducting further experimental studies.

Fig. 5 displays the outcomes of sintering a metal paste composed of 316L steel, revealing the presence of large (Fig. 5, *a*) and small (Fig. 5, *b*) spherical pores in the sintered 316L steel sample. It is plausible that these pores were formed due to the existence of gas bubbles generated during the preparation of the paste. to mitigate the occurrence of such defects, an additional step involving degassing can be implemented in the metal paste production process. Moreover, to address porosity concerns, another effective technique involves hot isostatic pressing (HIP) subsequent to sintering.

Fig. 6 depicts the microstructure of a sintered 316L steel sample, showcasing the presence of coarse austenite grains that are characteristic of austenitic stainless 316L steel [27]. This observation aligns with the results obtained from *X*-ray diffraction analysis (Fig. 7). the Axalit Metal software (Axalit SOFT LLC, Yekaterinburg) was used to determine an average grain area of 0.05 mm², derived from three Field-of-Views (FOVs) with approximately 25 grains in each. It's worth noting that the grain size in the sintered 316L steel metal paste sample is notably larger compared to samples produced by binder jetting or fused

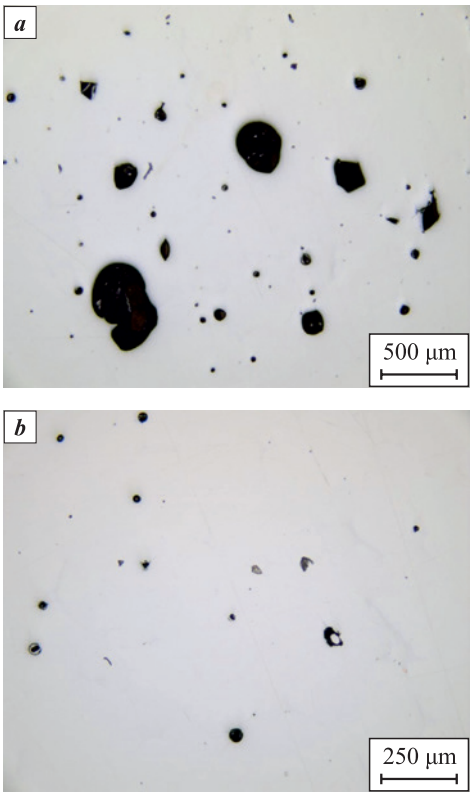

Fig. 5. Porosity of a 316L sintered specimen
a – area on the resurface with large spherical pores
b – area on the resurface with small spherical pores

Рис. 5. Металлографический шлиф спеченного образца из стали 316L
a – область на шлифе с крупными сферическими порами
b – область на шлифе с мелкими сферическими порами

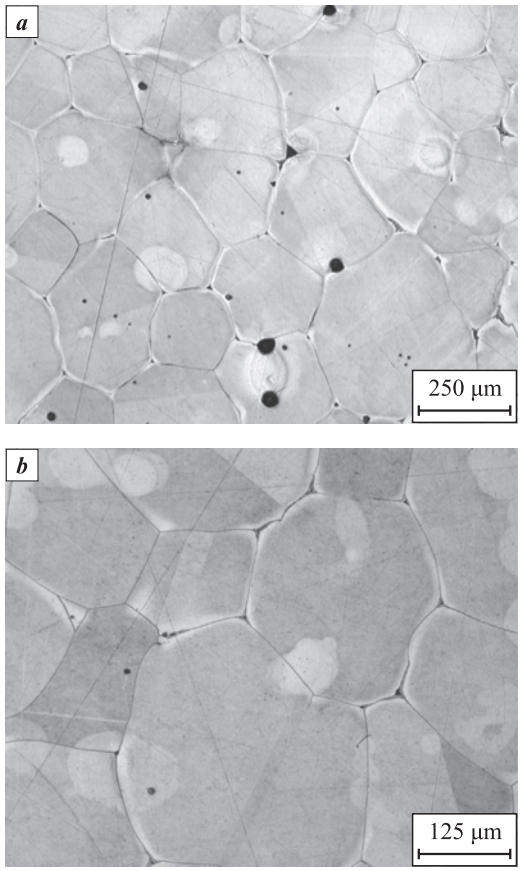

Fig. 6. Microstructure of metal 316L paste after sintering

Рис. 6. Микроструктура спеченного образца из стали 316L

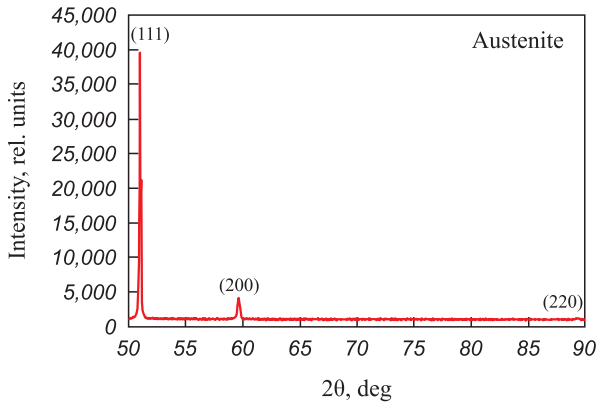

Fig. 7. *X*-ray diffraction patterns of metal 316L paste after sintering

Рис. 7. Фазовый состав спеченного образца из стали 316L

deposition methods [28; 29]. This disparity in grain size might be attributed to the larger particle size of the powder used to create the metal paste of 316L steel, consequently leading to larger original grains in the sintered product [30]. the microhardness values recorded were 132 ± 4 HV, indicating a lower hardness compared to samples sintered after binder jetting or fused deposition [31].

Conclusions

This study involved samples from the multi-material systems of 316L-CoCrFeMnNiW$_{0.25}$ and 316L–CrMoNbWV, which were prepared using a metal paste. Our investigation focused on understanding the impact of metal powder morphology, particle size distribution, and the presence of a transition layer composed of mixed powders on the development of multi-material samples. Additionally, we examined the porosity, microstructure, phase composition, and hardness of sintered 316L steel fabricated from the metal paste. the conclusions drawn from the results of this study are as follows:

1. For the molding of multi-material samples of the 316L–CoCrFeMnNiW$_{0.25}$ system, the creation of a transition zone comprising mixed 316L steel and CoCrFeMnNiW$_{0.25}$ powders is unnecessary due to the strong mixing observed between the two alloys. Conversely, in the 316L–CrMoNbWV system, forming a transition zone of mixed powders is essential to mitigate the impact of uneven shrinkage.

2. The sintering parameters for multi-material samples of the 316L–CoCrFeMnNiW$_{0.25}$ system need to be altered compared to those used for pure alloys. Specifically, it is recommended to reduce the sintering temperature by 30–45 °C relative to the sintering temperature employed for 316L steel.

3. The sintered 316L steel sample revealed the presence of large and small spherical pores, a microstructure characterized by sizable austenite grains (with an average grain area of approximately 0.05 mm^2), and a microhardness reading of 132 ± 4 HV.

References / Список литературы

1. Akshaya S.L., Prakash A., Bharati Raj J. Applications of functionally graded materials in structural engineering – A review. *Lecture Notes in Civil Engineering*. 2021;97:553–566. https://doi.org/10.1007/978-3-030-55115-5_51
2. Ghanavati R., Naffakh-Moosavy H. Additive manufacturing of functionally graded metallic materials: A review of experimental and numerical studies. *Journal of Materials Research and Technology*. 2021;13:1628–1664. https://doi.org/10.1016/j.jmrt.2021.05.022
3. Bandyopadhyay A., Zhang Y., Onuike B. Additive manufacturing of bimetallic structures. *SN Applied Sciences*. 2020;17(2):256–294. https://doi.org/10.1007/s42452-020-2918-6
4. Bandyopadhyay A., Traxel K.D., Lang M., Juhasz M., Eliaz N., Bose S. Alloy design via additive manufacturing: Advantages, challenges, applications and perspectives. *Materials Today*. 2022;52:207–224. https://doi.org/10.1016/j.mattod.2021.11.026
5. El-Galy I.M., Saleh B.I., Ahmed M.H. Functionally graded materials classifications and development trends from industrial point of view. *SN Applied Sciences*. 2019;1:1378. https://doi.org/10.1007/s42452-019-1413-4
6. Saleh B., Jiang J., Fathi R., Al-hababi T., Xu Q., Wang L., Song D., Ma A. 30 Years of functionally graded materials: an overview of manufacturing methods, applications and future challenges. *Composites. Part B: Engineering*. 2020;201:108376. https://doi.org/10.1016/j.compositesb.2020.108376
7. Liu G., Zhang X., Chen X., He Y., Cheng L., Huo M., Yin J., Hao F., Chen S., Wang P., Yi S., Wan L., Mao Z., Chen Z., Wang X., Cao Z., Lu J. Additive manufacturing of structural materials. *Materials Science and Engineering: R: Reports*. 2021 1;145:100596. https://doi.org/10.1016/j.mser.2020.100596
8. Zhai X., Jin L., Jiang J. A survey of additive manufacturing reviews. *Materials Science in Additive Manufacturing*. 2022;1(4):21. https://doi.org/10.18063/msam.v1i4.21
9. Srivastava M., Rathee S., Patel V., Kumar A., Koppad P.G. A review of various materials for additive manufacturing: Recent trends and processing issues. *Journal of Materials Research and Technology*. 2022;21:2612–2641. https://doi.org/10.1016/j.jmrt.2022.10.015
10. Zhang X., Liang E. Metal additive manufacturing in aircraft: Current application, opportunities and challenges. *IOP Conference Series: Materials Science and Engineering*. 2019;493(1):012032. https://doi.org/10.1088/1757-899X/493/1/012032
11. Gunasekaran J., Sevvel P., Solomon I.J. Metallic materials fabrication by selective laser melting: A review. *Materials Today Proceedings*. 2021;37(2):252–256. https://doi.org/10.1016/j.matpr.2020.05.162
12. Nandhakumar R., Venkatesan K. A process parameters review on selective laser melting-based additive manufacturing of single and multi-material: Microstructure, physical properties, tribological, and surface roughness. *Materials Today Communications*. 2023;35:105538. https://doi.org/10.1016/j.mtcomm.2023.105538
13. Camargo I.L., Fortulan C.A., Colorado H.A. A review on the ceramic additive manufacturing technologies and availability of equipment and materials. *Cerâmica*. 2022;68:329–347. https://doi.org/10.1590/0366-69132022683873331
14. Saadi M., Maguire A., Pottackal N.T., Thakur M., Ikram M., Hart A.J., Ajayan P., Rahman M. Direct Ink Writing: A 3D printing technology for diverse materials. *Advanced Materials*. 2022;34(28): 2108855. https://doi.org/10.1002/adma.202108855
15. Agrawal R., Anantachaisilp F., Tirano J., Zea Ramirez H., Marquez Z., Luhrs C. Paste-based 3D printing of metallic

materials: effect of binders and precursor sizes. *Materials Research Express*. 2019;6(10):106561. https://doi.org/10.1088/2053-1591/ab3996

16. Rocha V.G., Saiz E., Tirichenko I.S., García-Tuñón E. Direct ink writing advances in multi-material structures for a sustainable future. *Journal of Materials Chemistry A*. 2020;8(31):15646–15657. https://doi.org/10.1039/D0TA04181E
17. Liu W., Zhang Y.S., Heinrich M.A., Ferrari F., Jang H.L., Bakht S.M., Alvarez M.M., Yang J., Li Y.-C., Santiago G. Trujillo-de, Miri A.K., Zhu K., Khoshakhlagh P., Prakash G., Cheng H., Guan X., Zhong Z., Ju J., Zhu G.H., Jin X., Shin S.R., Dokmeci M.R., Khademhosseini A. Rapid continuous multimaterial extrusion bioprinting. *Advanced Materials*. 2017;29(3):1604630. https://doi.org/10.1002/adma.201604630
18. Xu C., Quinn B., Lebel L.L., Therriault D., L'espérance G. Multi-material Direct Ink Writing (DIW) for complex 3D metallic structures with removable supports. *ACS Applied Materials & Interfaces*. 2019;11(8):8499–8506. https://doi.org/10.1021/acsami.8b19986
19. Rocha V.G., García-Tuñón E., Botas C., Markoulidis F., Feilden E., D'Elia E., Ni N., Shaffer M., Eduardo Saiz E. Multimaterial 3D printing of graphene-based electrodes for electrochemical energy storage using thermoresponsive inks. *ACS Applied Materials & Interfaces*. 2017;9(42):37136–37145. https://doi.org/10.1021/acsami.7b10285
20. Sokkalingam R., Chao Z., Sivaprasad K., Muthupandi V., Jayaraj J., Ramasamy P., Eckert J., Prashanth K.G. Additive manufacturing of CoCrFeMnNi high-entropy alloy/AISI 316L stainless steel bimetallic structures. *Advanced Engineering Materials*. 2022;25(7):2200341. https://doi.org/10.1002/adem.202200341
21. Razumov N., Makhmutov T., Kim A., Shemyakinsky B., Shakhmatov A., Popovich V., Popovich A. Refractory CrMoNbWV high-entropy alloy manufactured by mechanical alloying and spark plasma sintering: Evolution of microstructure and properties. *Materials*. 2021;14(3):621. https://doi.org/10.3390/ma14030621
22. Makhmutov T., Razumov N., Kim A., Ozerskoy N., Mazeeva A., Popovich A. Synthesis of $CoCrFeNiMnW_{0.25}$ high-entropy alloy powders by mechanical alloying and plasma spheroidization processes for additive manufacturing. *Metals and Materials International*. 2021;27(1):50–54. https://doi.org/10.1007/s12540-020-00747-0
23. Wits W.W., Amsterdam E. Graded structures by multi-material mixing in laser powder bed fusion. *CIRP Annals*. 2021;70(1):159–162. https://doi.org/10.1016/j.cirp.2021.03.005
24. Chen K., Wang C., Hong Q., Wen S., Zhou Y., Yan C., Shi Y. Selective laser melting 316L/CuSn10 multi-materials: Processing optimization, interfacial characterization and mechanical property. *Journal of Materials Processing Technology*. 2020;283:116701. https://doi.org/10.1016/j.jmatprotec.2020.116701
25. Wei C., Li L. Recent progress and scientific challenges in multi-material additive manufacturing via laser-based powder bed fusion. *Virtual and Physical Prototyping*. 2021;16(3):347–371.
26. Pichler P., Simonds B.J., Sowards J.W., Pottlacher G. Measurements of thermophysical properties of solid and liquid NIST SRM 316L stainless steel. *Journal of Materials Science*. 2020;55(9):4081–4093. https://doi.org/10.1007/s10853-019-04261-6
27. Santamaria R., Salasi M., Bakhtiari S., Leadbeater G., Iannuzzi M., Quadir M.Z. Microstructure and mechanical behaviour of 316L stainless steel produced using sinter-based extrusion additive manufacturing. *Journal of Materials Science*. 2022;57(21):9646–9662. https://doi.org/10.1007/s10853-021-06828-8
28. Cabo Rios A., Hryha E., Olevsky E., Harlin P. Sintering anisotropy of binder jetted 316L stainless steel: part II – microstructure evolution during sintering. *Powder Metallurgy*. 2022;65(4):283–295. https://doi.org/10.1080/00325899.2021.2020486
29. Sadaf M., Bragaglia M., Nanni F. A simple route for additive manufacturing of 316L stainless steel via Fused Filament Fabrication. *Journal of Manufacturing Processes*. 2021;67:141–150. https://doi.org/10.1016/j.jmapro.2021.04.055
30. Park D.Y., Lee S.W., Park S.J., Kwon Y-S., Otsuka I. Effects of particle sizes on sintering behavior of 316L stainless steel powder. *Metallurgical and Materials Transactions A*. 2013;44: 1508–1518. https://doi.org/10.1007/s11661-012-1477-x
31. Krakhmalev P., Fredriksson G., Svensson K., Yadroitsev I., Yadroitsava I., Thuvander M., Thuvander M., Peng R. Microstructure, solidification texture, and thermal stability of 316L stainless steel manufactured by laser powder bed fusion. *Metals*. 2018;8(8):643. https://doi.org/10.3390/met8080643

Information about the Authors

Dmitry V. Masaylo – Cand. Sci. (Eng.), Deputy Head of the Laboratory "Synthesis of new materials and structures", Peter the Great St. Petersburg Polytechnic University (SPbPU)
ORCID: 0000-0001-5516-9848
E-mail: dmasaylo@gmail.com

Arseniy V. Repnin – Engineer of the Laboratory "Synthesis of new materials and structures", SPbPU
ORCID: 0009-0001-3157-3317
E-mail: repnin_arseniy@mail.ru

Сведения об авторах

Дмитрий Валерьевич Масайло – к.т.н., заместитель заведующего лабораторией «Синтез новых материалов и конструкций» Санкт-Петербургского политехнического университета Петра Великого (СПбПУ)
ORCID: 0000-0001-5516-9848
E-mail: dmasaylo@gmail.com

Арсений Вячеславович Репнин – инженер лаборатории «Синтез новых материалов и конструкций» СПбПУ
ORCID: 0009-0001-3157-3317
E-mail: repnin_arseniy@mail.ru

Anatoly A. Popovich – Dr. Sci. (Eng.), Professor, Director of the Institute of Machinery, Materials, and Transport, SPbPU
ORCID: 0000-0002-5974-6654
E-mail: popovicha@mail.ru

Nikolai G. Razumov – Cand. Sci. (Eng.), Head of the Laboratory "Synthesis of new materials and structures", SPbPU
ORCID: 0000-0002-7147-6239
E-mail: n.razumov@onti.spbstu.ru

Alina K. Mazeeva – Cand. Sci. (Eng.), Leading Researcher of the Laboratory "Synthesis of new materials and structures", SPbPU
ORCID: 0000-0002-8980-0869
E-mail: mazeevaalina@gmail.com

Анатолий Анатольевич Попович – д.т.н., профессор, директор Института машиностроения, материалов и транспорта СПбПУ
ORCID: 0000-0002-5974-6654
E-mail: popovicha@mail.ru

Николай Геннадьевич Разумов – к.т.н., заведующий лабораторией «Синтез новых материалов и конструкций» СПбПУ
ORCID: 0000-0002-7147-6239
E-mail: n.razumov@onti.spbstu.ru

Алина Константиновна Мазеева – к.т.н., ведущий научный сотрудник лаборатории «Синтез новых материалов и конструкций» СПбПУ
ORCID: 0000-0002-8980-0869
E-mail: mazeevaalina@gmail.com

Contribution of the Authors

D. V. Masaylo – designed the experiments, wrote the manuscript, participated in the discussion of the results.
A.V. Repnin – conducted the experiments, processed the results, drafted the manuscript.
A. A. Popovich – developed the main conceptual ideas and outline the proof, defined the purpose of the study, participated in the discussion of the results.
N. G. Razumov – critically analyzed the existing literature, participated in the discussion of the results, contributed to drawing conclusions based on the study findings.
A. K. Mazeeva – conducted research using differential scanning calorimetry and *X*-ray diffraction analysis, processed and analyzed the results.

Вклад авторов

Д. В. Масайло – планирование экспериментов, написание статьи, участие в обсуждении результатов.
А. В. Репнин – проведение экспериментов, обработка полученных результатов, написание статьи.
А. А. Попович – концептуализация идеи, определение цели работы и ее задачи, участие в обсуждении результатов.

Н. Г. Разумов – критический анализ литературы, участие в обсуждении результатов, формирование выводов исследования.

А. К. Мазеева – проведение исследований методом дифференциальной сканирующей калориметрии и рентгеноструктурного анализа, обработка и анализ полученных результатов.

Received 27.06.2023
Revised 02.10.2023
Accepted 04.10.2023

Статья поступила 27.06.2023 г.
Доработана 02.10.2023 г.
Принята к публикации 04.10.2023 г.

Materials and Coatings Fabricated Using the Additive Manufacturing Technologies
Материалы и покрытия, получаемые методами аддитивных технологий

UDC 621.762

https://doi.org/10.17073/1997-308X-2024-1-73-80

Research article
Научная статья

Simulating multi-material specimen manufacturing from VZh159 and CuCr1Zr alloys via SLM method: Computational modeling and experimental findings

A. V. Orlov, A. V. Repnin, E. M. Farber, E. V. Borisov, A. A. Popovich

Peter the Great St. Petersburg Polytechnic University
29 Polytekhnicheskaya Str., St. Petersburg 195251, Russian Federation

orlov_alexey88@mail.ru

Abstract. Manufacturing of multi-material products through layer-by-layer synthesis poses various challenges encompassing process parameter optimization, equipment calibration, and the mitigation of warping and internal stresses within the manufactured parts. The article investigates the feasibility of simulating the selective laser melting (SLM) process for manufacturing multi-material components, exemplified through specimens composed of the VZh159 nickel alloy and CuCr1Zr copper alloy. The study entails numerical simulations of the printing process, which were then validated against real specimens produced through SLM. Each test specimen was vertically divided into three parts: the top and bottom sections consisted of the VZh159 alloy, while the central part was composed of the CuCr1Zr alloy. Simulations involved using identical process parameters as employed in the printing process. Thermal and mechanical analyses for each part of the multi-material specimen were sequentially addressed, transferring the outcomes of the preceding analysis as initial conditions for subsequent calculations. The study concludes that while the obtained simulation results are indicative, they do not precisely capture the deformation observed in the specimens manufactured via the SLM method. The numerical values of deformations derived from simulation results slightly underestimate the actual deformations, attributed to limitations in the chosen calculation algorithms. For future utilization of numerical computer simulation in the SLM manufacturing of multi-material specimens, the study suggests the necessity of implementing a seamless, continuous simulation process without transitions between different parts of the specimen. This entails considering the entire manufacturing process without segregating sections, ensuring a comprehensive account of continuous deformation and stress accumulation throughout fabrication.

Keywords: multi-material, thermal and mechanical analysis, simulation of the process, selective laser melting, VZh159, CuCr1Zr, deformation

Acknowledgements: The research was supported by the Russian Science Foundation grant No. 23-79-30004, https://rscf.ru/project/23-79-30004/.

For citation: Orlov A.V., Repnin A.V., Farber E.M., Borisov E.V., Popovich A.A. Simulating multi-material specimen manufacturing from VZh159 and CuCr1Zr alloys via SLM method: Computational modeling and experimental findings. *Powder Metallurgy and Functional Coatings*. 2024;18(1):73–80. https://doi.org/10.17073/1997-308X-2024-1-73-80

Изготовление мультиматериальных образцов из сплавов ВЖ159 и БрХЦрТ В методом СЛП: численное компьютерное моделирование и экспериментальные результаты

А. В. Орлов, А. В. Репнин, Э. М. Фарбер, Е. В. Борисов, А. А. Попович

Санкт-Петербургский политехнический университет Петра Великого
Россия, 195251, г. Санкт-Петербург, ул. Политехническая, 29

orlov_alexey88@mail.ru

Аннотация. Изготовление мультиматериальных изделий методом послойного синтеза кроет в себе множество вопросов, связанных как с технологическими параметрами и подготовкой оборудования, так и с короблениями и внутренними напряжениями получаемых деталей. В данной статье показана возможность моделирования процесса селективного лазерного плавления (СЛП) в части создания мультиматериальных деталей на примере образцов из никелевого сплава ВЖ159 и медного сплава БрХЦрТ В. Результаты численного моделирования процесса печати были верифицированы на основе изготовленных образцов. Исследуемый образец был разделен на 3 части по вертикали: нижняя и верхняя части изготавливались из сплава ВЖ159, центральная – из сплава БрХЦрТ В. Для проведения численного моделирования использовались такие же технологические параметры, как и для печати. Последовательно решались задачи термического и механического анализов для каждой из частей мультиматериалоного образца с передачей результатов расчета предшествующей задачи в начальные условия последующей задачи. В результате проведенного исследования установлено, что полученные результаты моделирования являются показательными, однако не совсем точно описывают деформацию образца, изготовленного методом СЛП. Численные значений деформаций, полученные по результатам моделирования, несколько меньше, чем реальные, что связано с несовершенством выбранных алгоритмов расчета. Для возможности дальнейшего использования численного компьютерного моделирования процесса выращивания мультиматериальных образцов методом СЛП необходимо реализовать непрерывный процесс моделирования, без перехода между частями образца, когда одна часть начинает рассматриваться системой как подложка. Необходим учет непрерывного изготовления образца и, соответственно, непрерывного деформирования и накопления напряжений.

Ключевые слова: мультиматериал, термический и механический анализ, моделирование процесса, селективное лазерное плавление, ВЖ159, БрХЦрТ В, деформация

Благодарности: Исследование выполнено за счет гранта Российского научного фонда № 23-79-30004, https://rscf.ru/project/23-79-30004/.

Для цитирования: Орлов А.В., Репнин А.В., Фарбер Э.М., Борисов Е.В., Попович А.А. Изготовление мультиматериальных образцов из сплавов ВЖ159 и БрХЦрТ В методом СЛП: численное компьютерное моделирование и экспериментальные результаты. *Известия вузов. Порошковая металлургия и функциональные покрытия*. 2024;18(1):74–80. https://doi.org/10.17073/1997-308X-2024-1-73-80

Introduction

Today, numerous high-tech engineering challenges necessitate the use of products crafted from metals and alloys possessing enhanced and distinct properties that cannot be attained through a singular material composition [1]. Multi-material approaches prove invaluable in addressing such issues – encompassing the incorporation of multiple materials or alloys into a product's composition. This method enables the amalgamation of their properties or facilitates precise distribution of these attributes, thereby achieving desired qualities like localized wear resistance, elevated thermal conductivity, thermal insulation, resistance to chemical corrosion, among others, at specific points within a product or component [2].

The classification of multi-materials includes compositions like polymer–metal, metal–metal (bimetal), metal–ceramic, among others [3]. Bimetallic products are combinations of two metals or alloys achieved by welding or soldering, effectively mitigating their respective drawbacks while preserving the desired properties of each [4]. For example, copper-based alloys such as GRCop-84 exhibit remarkably high thermal conductivity, facilitating rapid cooling, elevated temperature strength with minimal thermal expansion, and substantial resistance to oxidation. This makes them suitable for applications in combustion chambers, jet sleeves of regenerative-cooled rocket engines (jet linings), and areas exposed to high-temperature gas flows [5; 6]. Conversely, nickel-based alloys like Inconel 718 are renowned for their resistance to high-temperature cor-

rosion, making them prevalent in aerospace applications, especially in gas-turbine and rocket engines due to their impressive tensile and tear strength, coupled with oxidation resistance at elevated temperatures. Nonetheless, these alloys have low thermal conductivity [7; 8]. Consequently, employing copper alloys atop nickel alloys (like Inconel 718 or similar) can enhance the thermal conductivity of products while upholding their strength characteristics [5].

To fabricate these products, both conventional technologies and additive manufacturing techniques are viable, enabling the production of items with intricate, sophisticated geometries [1; 3]. Presently, scientific literature exists detailing the characteristics of bimetallic and functional-gradient products falling under the "nickel alloy – copper alloy" classification (In718–Cu; In718–GRCop-84). These studies employ various methods, including direct energy and material supply processes [5; 6; 9], as well as synthesis processes on substrates, such as selective laser melting (SLM) [10; 11]. The SLM process involves numerous parameters that significantly impact the resultant properties, internal stresses, and potential defects in the manufactured materials and products [12–14]. Fine-tuning these process parameters is a crucial and indispensable aspect of the product development process [15]. Using numerical computer simulations proves pivotal in reducing the duration of parameter refinement and minimizing the cost of potential errors, particularly when fabricating products with intricate geometries [16–18].

Up to this point, simulations of the SLM process have been extensively documented [14; 16; 17; 19]. However, these studies have not addressed the simulation challenges associated with manufacturing products from multi-material compositions, particularly bimetallic products. Therefore, advancing the effective application of additive technologies in producing bimetallic products/parts for diverse purposes necessitates exploring the feasibility of simulating the SLM process for such products.

The objective of this study is to conduct numerical computer simulations of the SLM manufacturing process for multi-material specimens composed of the VZh159 nickel alloy and CuCr1Zr copper alloy. Subsequently, the obtained simulation results will be validated based on the specimens manufactured in the real-world setting.

Materials and methods

The numerical computer simulation of the multi-material specimen growth via the SLM method was conducted using the finite-element analysis package "ANSYS Workbench 2019 R2" with the utilization of the "Transient Thermal" and "Static Structural" modules [20]. Fig. 1 illustrates the model of the specimen, delineating the material composition of its three distinct parts: top, middle, and bottom. The simulation process involved a sequential resolution of the thermomechanical problem for each segment of the specimen. Initially, the thermal aspect was addressed using the "Transient Thermal" module, followed by the mechanical problem tackled through the "Static Structural" module. Fig. 2 provides a block diagram outlining the steps involved in the numerical computer simulation.

The simulation process for the product growth via the SLM method utilized specific parameters: for the VZh159 alloy – laser power of 275 W, scanning rate at 760 mm/s, distance between laser passes set at 0.1 mm, and a layer thickness of 0.05 mm; for the CuCr1Zr alloy – laser power of 400 W, scanning rate at 300 mm/s, distance between laser passes at 0.15 mm, and a layer thickness of 0.05 mm. Detailed physical and mechanical properties of the alloys employed in the simulation process are provided within a referenced Table.

Spherical powders of the VZh159 alloy (with distribution quantiles d_{10} = 17 μm, d_{50} = 32 μm, d_{90} = 55 μm) and CuCr1Zr alloy (with d_{10} = 14 μm, d_{50} = 29 μm, d_{90} = 52 μm) were used to create bimetallic material specimens. Fig. 3 displays SEM images depicting the particles of these powders.

The manufacturing process occurred within an inert gas atmosphere employing the SLM280HL machine (SLM Solutions GmbH, Germany). This machine is equipped with an ytterbium fiber laser possessing a wavelength of 1070 nm, a maximum power output of 400 W, a minimum laser beam diameter of 80 μm, and a maximum scanning rate of 15 m/s. The produced specimens were constructed with the upper and lower parts comprised of VZh159 alloy, while the middle sections were fashioned from CuCr1Zr alloy.

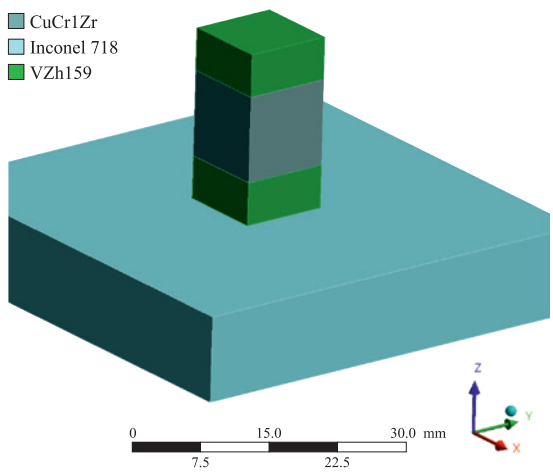

Fig. 1. Initial design of the multi-material specimen

Рис. 1. Исходная модель мультиматериального образца

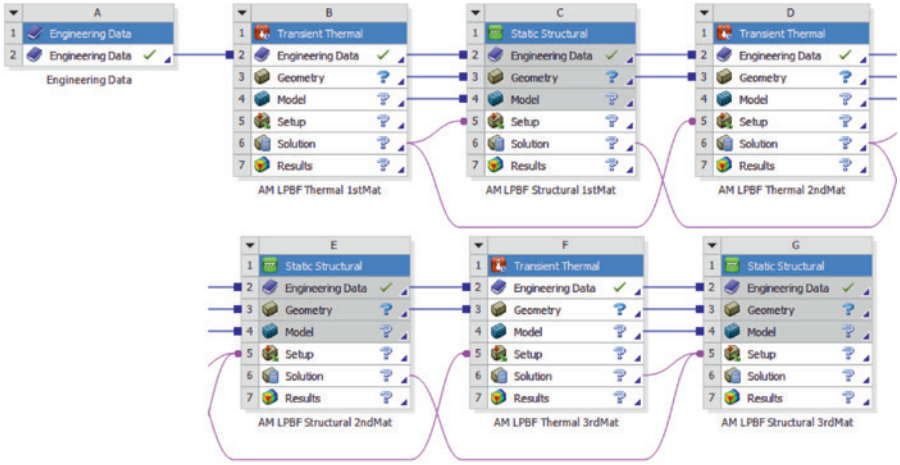

Fig. 2. Block diagram of computer simulation for manufacturing multi-material specimens

Рис. 2. Блок-схема численного компьютерного моделирования изготовления мультиматериальных образцов

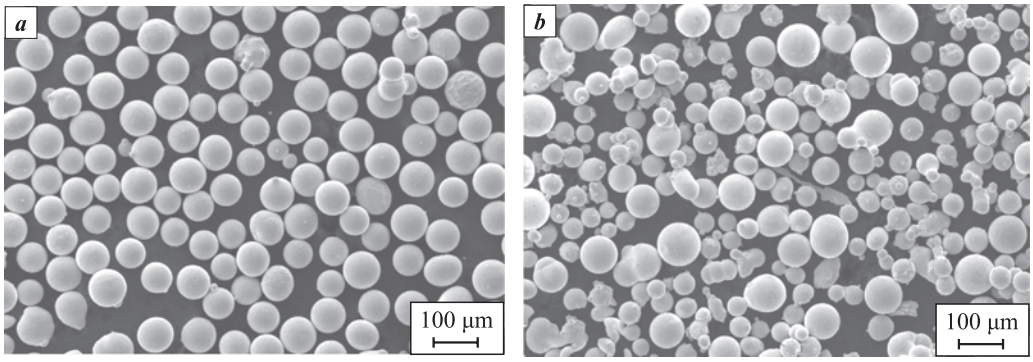

Fig. 3. SEM image of CuCr1Zr (***a***) and VZh159 (***b***) alloy powders used in the study

Рис. 3. СЭМ-изображения используемых в исследовании порошков сплавов БрХЦрТ В (***a***) и ВЖ159 (***b***)

Physical and mechanical properties of modeled alloys

Физико-механические свойства моделируемых сплавов

Alloy	Temperature, °C	Density, kg·m^3	Thermal-expansion coefficient, 10^{-5} °C^{-1}	Thermal conductivity, W/(m·°C)	Specific heat capacity, J/(kg·°C)	Elasticity	
						Young's modulus, GPa	Poisson ratio
VZh159	25	8.43	11.47	11.01	0.39	213.18	0.31270
	100	8.41	11.82	12.19	0.41	208.37	0.31473
	500	8.27	13.85	18.38	0.47	180.35	0.32554
	1000	8.04	16.41	26.03	0.56	139.68	0.33905
	1100	7.99	16.92	27.55	0.71	130.79	0.34175
	1350	7.65	25.68	27.67	0.69	–	–
	2000	7.09	31.97	35.97	0.76	–	–
CuCr1Zr	25	8.93	16.34	92.97	0.01	129.53	0.34903
	100	89.00	16.59	101.86	0.01	125.96	0.35319
	500	8.71	18.15	134.91	0.01	101.42	0.37662
	1000	8.43	20.40	162.42	0.01	57.78	0.40650
	1100	8.10	35.51	160.79	5.17	–	–
	1350	7.76	38.22	167.71	0.50	–	–
	2000	7.18	41.26	180.12	0.50	–	–

The examination of the acquired specimens was conducted using a light optical microscope called "Leica DMI 5000" (Leica Microsystems, Germany). To facilitate the examination process, the specimens were sectioned using the electroerosion method.

Results and discussion

Fig. 4 illustrates the outcomes of simulating the SLM manufacturing process for multi-material specimens, showcasing the deformation fields along the *Y*-axis. Notably, inward deformation of the specimen's sides is evident, reaching a maximum deformation of 83 μm.

Particularly, the middle section of the specimen made of CuCr1Zr experiences the most significant deformation. Additionally, the top part composed of VZh159 displays considerable deformation, especially at the interfaces between materials.

In Fig. 5, the simulation results portray the stress fields following the production of multi-material specimens via the SLM method. The highest stress values, approximately 900 MPa, are observed at the corners of the specimen at the material interfaces. Elevated stress, ranging from 400 to 500 MPa, is noticeable in the upper part of the specimen fabricated from VZh159. Comparatively, the lowest stress values do not exceed 100 MPa.

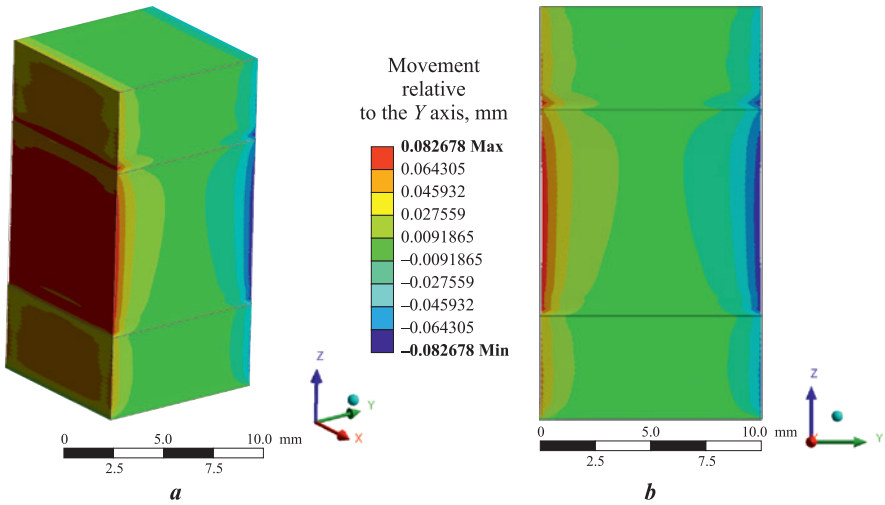

Fig. 4. Results of simulating of multi-material specimen manufacturing – specimen deformation along the *Y* axis
a – general view, ***b*** – view in the *X* plane

Рис. 4. Результаты моделирования процесса изготовления мультиматериального образца – его деформации по оси *Y*
a – общий вид, ***b*** – вид в плоскости *X*

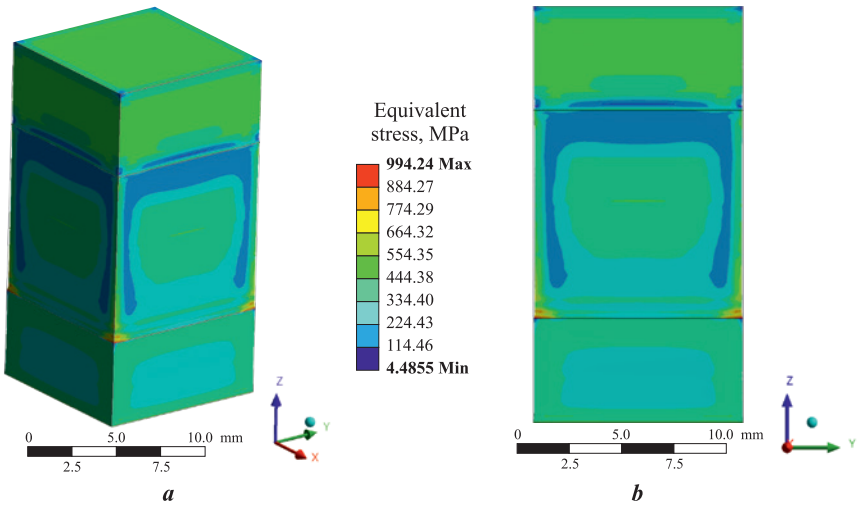

Fig. 5. Results of simulating of multi-material specimen manufacturing – specimen stress
a – general view, ***b*** – view in the *X* plane

Рис. 5. Результаты моделирования процесса изготовления мультиматериального образца – напряжения образца
a – общий вид, ***b*** – вид в плоскости *X*

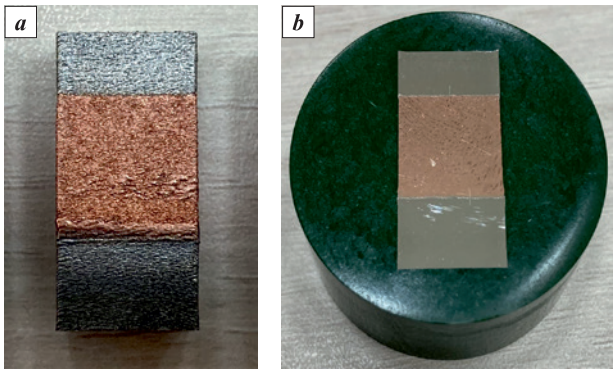

Fig. 6. Manufactured multi-material specimen (***a***) and thin section prepared from the specimen (***b***)

Рис. 6. Изготовленный мультиматериальный образец (***a***) и подготовленный шлиф образца (***b***)

Fig. 6 displays the multi-material specimens made using the SLM method. Visual examination indicates the absence of significant deformations or visible defects such as fractures or failures.

In Fig. 7, the verification of the deformation simulation for the specimen produced via the SLM method is presented, specifically at the interface between its top part (constructed from VZh159) and the middle part (constructed from CuCr1Zr).

The simulations depicted in Fig. 7, *a*, revealed deformations ranging from 64 to 83 μm at the interface between the top and middle sections of the specimen, illustrating distinct inward bending occurring separately in both the top and middle parts. Upon experimental examination of the SLM-manufactured specimen (Fig. 7, *b*), the deformation at the interface measured approximately 100 μm, slightly exceeding the simulated values (with the largest deviation being 36 μm). Inward bending with maximum deformation near the interface is predominantly observed in the middle part of the specimen constructed from CuCr1Zr.

The disparity between the simulation results and experimental data might be attributed to the inherent characteristics of the simulation process. As the simulation initiates the fabrication of the top part of the VZh159 specimen, its middle part ceases to influence stress and deformation calculations, being treated as part of the substrate. This leads to limitations in the acquired values of stresses and deformations. Consequently, the distinct nature of specimen deformation, observed when the simulated specimen deforms in two separate sections, is a direct consequence of this phenomenon. This limitation underscores the challenges in employing simulations for

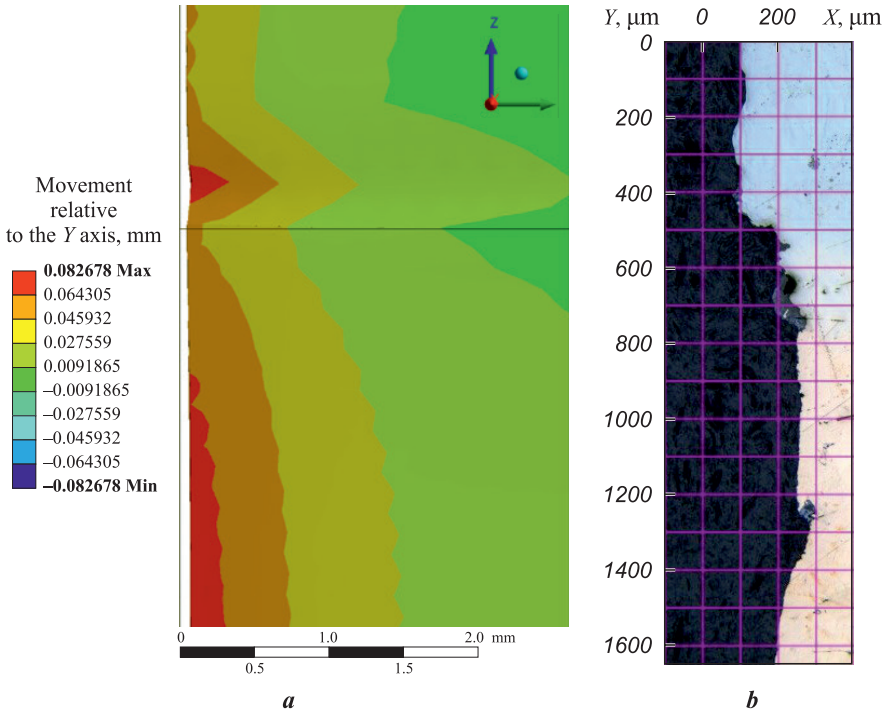

Fig. 7. Validation of deformation simulation at the interface between the top and middle parts of the VZh159 and CuCr1Zr alloys in the multi-material specimen produced by SLM

a – simulation results, ***b*** – experimental specimen

Рис. 7. Верификация моделирования деформации мультиматериального образца, изготовленного методом СЛП, на границе раздела между верхней и средней частями из сплавов соответственно ВЖ159 и БрХЦрТ В

a – результаты моделирования, ***b*** – экспериментально изготовленный образец

multi-material manufacturing processes using SLM method.

Nonetheless, the deformation values obtained through simulation generally present a representative approximation, closely aligning with the experimental values. However, for more intricate structures, optimizing the system becomes essential to achieve better alignment with real-world results.

Conclusion

Based on the completed research results, several conclusions have been drawn regarding the numerical computer simulation of the manufacturing process for multi-material specimens made from the VZh159 nickel alloy and CuCr1Zr copper alloy.

1. The simulation results, while indicative, do not precisely mirror the deformation observed in the specimen produced via the SLM method. The numerical values of deformations obtained from simulations (from 64 to 83 μm) slightly underestimate the actual deformations (approximately 100 μm). This discrepancy is attributed to the imperfections in the chosen calculation algorithms, particularly when the system stops considering the middle part of the specimen in the calculation and treats it solely as a substrate after initiating the calculation of the top part of the specimen manufacturing.

2. To enable the continued utilization of numerical computer simulation for the growth of multi-material specimens via the SLM method, it is imperative to implement a seamless simulation process without the discontinuity between different parts of the specimen. This involves accounting for the continuous manufacturing process of the specimen, thereby considering uninterrupted deformation and accumulation of stresses throughout the fabrication procedure.

References / Список литературы

1. Bandyopadhyay A., Zhang Y., Onuike B. Additive manufacturing of bimetallic structures. *Virtual and Physical Prototyping*. 2022;17(2):256–294. https://doi.org/10.1080/17452759.2022.2040738
2. Wang D., Liu L., Deng G., Deng C., Bai Y., Yang Y., Wu W., Chen J., Liu Y., Wang Y., Lin X., Han C. Recent progress on additive manufacturing of multi-material structures with laser powder bed fusion. *Virtual and Physical Prototyping*. 2022;17(2):329–365. https://doi.org/10.1080/17452759.2022.2028343
3. Nazir A., Gokcekaya O., Md Masum Billah K., Ertugrul O., Jiang J., Sun J., Hussain S. Multi-material additive manufacturing: A systematic review of design, properties, applications, challenges, and 3D printing of materials and cellular metamaterials. *Materials & Design*. 2023;226: 111661. https://doi.org/10.1016/j.matdes.2023.111661
4. Hasanov S., Alkunte S., Rajeshirke M., Gupta A., Huseynov O., Fidan I., Alifui-Segbaya F., Rennie A. Review on additive manufacturing of multi-material parts: progress and challenges. *Journal of Manufacturing and Materials Processing*. 2022;6(1):4. https://doi.org/10.3390/jmmp6010004
5. Onuike B., Heer B., Bandyopadhyay A. Additive manufacturing of Inconel 718–Copper alloy bimetallic structure using laser engineered net shaping (LENS™). *Additive Manufacturing*. 2018;21:133–140. https://doi.org/10.1016/j.addma.2018.02.007
6. Balkan M.E., Aydoğan E., Işık M., Derin B., Koç B. Directed energy deposition process development for functionally gradient Copper–Inconel 718 materials. *Journal of Additive Manufacturing Technologies*. 2021;1(3):581–581. https://doi.org/10.18416/JAMTECH.2111581
7. Ghorbanpour S., Alam M.E., Ferreri N.C., Kumar A., McWilliams B.A., Vogel S.C., Bicknell J., Beyerlein I.J., Knezevic M. Experimental characterization and crystal plasticity modeling of anisotropy, tension-compression asymmetry, and texture evolution of additively manufactured Inconel 718 at room and elevated temperatures. *International Journal of Plasticity*. 2020;125:63–79. https://doi.org/10.1016/j.ijplas.2019.09.002
8. Popovich A.A., Sufiiarov V.S., Polozov I.A., Borisov E.V. Microstructure and mechanical properties of Inconel 718 produced by SLM and subsequent heat treatment. *Key Engineering Materials*. 2015;651–653:665–670. https://doi.org/10.4028/www.scientific.net/KEM.651-653.665
9. Onuike B., Bandyopadhyay A. Bond strength measurement for additively manufactured Inconel 718–GRCop84 copper alloy bimetallic joints. *Additive Manufacturing*. 2019; 27:576–585. https://doi.org/10.1016/j.addma.2019.04.003
10. Marques A., Cunha Â., Gasik M., Carvalho O., Silva F.S., Bartolomeu F. Inconel 718–copper parts fabricated by 3D multi-material laser powder bed fusion: a novel technological and designing approach for rocket engine. *International Journal of Advanced Manufacturing Technology*. 2022;122(3-4):2113–2123. https://doi.org/10.1007/s00170-022-10011-x
11. Walker J., Middendorf J.R., Lesko C.C.C., Gockel J. Multi-material laser powder bed fusion additive manufacturing in 3-dimensions. *Manufacturing Letters*. 2022;31:74–77. https://doi.org/10.1016/j.mfglet.2021.07.011
12. Papazoglou E.L., Karkalos N.E., Karmiris-Obratański P., Markopoulos A.P. On the modeling and simulation of SLM and SLS for metal and polymer powders: A review. *Archives of Computational Methods in Engineering*. 2022; 29:941–973. https://doi.org/10.1007/s11831-021-09601-x
13. Wei C., Zhang Z., Cheng D., Sun Z., Zhu M., Li L. An overview of laser-based multiple metallic material additive manufacturing: from macro- to micro-scales. *International Journal of Extreme Manufacturing*. 2021;3(1):012003. https://doi.org/10.1088/2631-7990/abce04
14. Song X., Feih S., Zhai W., Sun C.N., Li F., Maiti R., Wei J., Yang Y., Oancea V., Romano Brandt L., Korsunsky A.M. Advances in additive manufacturing process simulation: Residual stresses and distortion predictions in complex metallic components. *Materials & Design*. 2020;193: 108779. https://doi.org/10.1016/j.matdes.2020.108779
15. Nandhakumar R., Venkatesan K. A process parameters review on selective laser melting-based additive manufacturing of single and multi-material: Microstructure, physi-

cal properties, tribological, and surface roughness. *Materials Today Communications*. 2023;35:105538. https://doi.org/10.1016/j.mtcomm.2023.105538

16. Gh Ghanbari P., Mazza E., Hosseini E. Adaptive local-global multiscale approach for thermal simulation of the selective laser melting process. *Additive Manufacturing*. 2020; 36:101518. https://doi.org/10.1016/j.addma.2020.101518
17. Zhou R., Liu H., Wang H. Modeling and simulation of metal selective laser melting process: a critical review. *International Journal of Advanced Manufacturing Technology*. 2022;121(9-10):5693–5706. https://doi.org/10.1007/s00170-022-09721-z
18. Bouabbou A., Vaudreuil S. Understanding laser-metal interaction in selective laser melting additive manufacturing through numerical modelling and simulation: A review. *Virtual and Physical Prototyping*. 2022;17(3):543–562. https://doi.org/10.1080/17452759.2022.2052488
19. Laakso P., Riipinen T., Laukkanen A., Andersson T., Jokinen A., Revuelta A., Ruusuvuori K. Optimization and simulation of SLM process for high density H13 tool steel parts. *Physics Procedia*. 2016;83:26–35. https://doi.org/10.1016/j.phpro.2016.08.004
20. Nagesha B.K., Anand Kumar S., Vinodh K., Pathania A., Barad S. A thermo-mechanical modelling approach on the residual stress prediction of SLM processed HPNGV aeroengine part. *Materials Today: Proceedings*. 2021;44: 4990–4996. https://doi.org/10.1016/j.matpr.2020.12.940

Information about the Authors

Aleksei V. Orlov – Researcher, Laboratory "Design of materials and additive manufacturing", Peter the Great St. Petersburg Polytechnic University (SPbPU)
ORCID: 0000-0002-0090-0442
E-mail: orlov_alexey88@mail.ru

Arseniy V. Repnin – Engineer, Laboratory "Synthesis of new materials and structures", SPbPU
ORCID: 0009-0001-3157-3317
E-mail: repnin_arseniy@mail.ru

Eduard M. Farber – Engineer, Laboratory "Synthesis of new materials and structures", SPbPU
ORCID: 0009-0007-8830-9887
E-mail: d.farber2010@yandex.ru

Evgeny V. Borisov – Cand. Sci. (Eng.), Leading Researcher, Laboratory "Synthesis of new materials and structures", SPbPU
ORCID: 0000-0003-2464-6706
E-mail: evgenii.borisov@icloud.com

Anatoly A. Popovich – Dr. Sci. (Eng.), Professor, Director of the Institute of Machinery, Materials, and Transport, SPbPU
ORCID: 0000-0002-5974-6654
E-mail: popovicha@mail.ru

Сведения об авторах

Алексей Валерьевич Орлов – научный сотрудник лаборатории «Дизайн материалов и аддитивного производства» Санкт-Петербургского политехнического университета Петра Великого (СПбПУ)
ORCID: 0000-0002-0090-0442
E-mail: orlov_alexey88@mail.ru

Арсений Вячеславович Репнин – инженер лаборатории «Синтез новых материалов и конструкций» СПбПУ
ORCID: 0009-0001-3157-3317
E-mail: repnin_arseniy@mail.ru

Эдуард Михайлович Фарбер – инженер лаборатории «Синтез новых материалов и конструкций» СПбПУ
ORCID: 0009-0007-8830-9887
E-mail: d.farber2010@yandex.ru

Евгений Владиславович Борисов – к.т.н., ведущий научный сотрудник лаборатории «Синтез новых материалов и конструкций» СПбПУ
ORCID: 0000-0003-2464-6706
E-mail: evgenii.borisov@icloud.com

Анатолий Анатольевич Попович – д.т.н., профессор, директор Института машиностроения, материалов и транспорта СПбПУ
ORCID: 0000-0002-5974-6654
E-mail: popovicha@mail.ru

Contribution of the Authors

A. V. Orlov – conducted experiments, processed experimental data, contributed to result analysis and discussion, drew conclusions from the study.
A. V. Repnin – conducted experiments, processed experimental data, authored the manuscript, contributed to result analysis and discussion.
E. M. Farber – conducted critical literature analysis, contributed to manuscript writing, participated in result analysis and discussion.
E. B. Borisov – planned and executed experiments, handled specimen manufacturing, contributed to result analysis and discussion.
A. A. Popovich – developed key conceptual ideas, outlined the study's objectives, contributed to result analysis and discussion.

Вклад авторов

А. В. Орлов – проведение экспериментов, обработка полученных результатов, участие в обсуждении результатов, формирование выводов исследования.
А. В. Репнин – проведение экспериментов, обработка полученных результатов, написание статьи, участие в обсуждении результатов.
Э. М. Фарбер – критический анализ литературы, написание статьи, участие в обсуждении результатов.
Е. В. Борисов – планирование экспериментов, изготовление образцов, участие в обсуждении результатов.
А. А. Попович – концептуализация идеи, определение цели работы и ее задач, участие в обсуждении результатов.

Received 28.06.2023
Revised 19.10.2023
Accepted 23.10.2023

Статья поступила 28.06.2023 г.
Доработана 19.10.2023 г.
Принята к публикации 23.10.2023 г.

Materials and Coatings Fabricated Using the Additive Manufacturing Technologies
Материалы и покрытия, получаемые методами аддитивных технологий

UDC 621.762.2
https://doi.org/10.17073/1997-308X-2024-1-81-94

Research article
Научная статья

Mechanical properties of high-nitrogen steel produced via selective laser melting using mechanically alloyed and spheroidized powders

N. E. Ozerskoi, N. G. Razumov, A. O. Silin, E. V. Borisov, A. A. Popovich

Peter the Great St. Petersburg Polytechnic University
29 Polytekhnicheskaya Str., St. Petersburg 195251, Russian Federation

nikolaiozerskoi@yandex.ru

Abstract. In recent years, the development of additive technologies has been one of the priority tasks in the sector. Primarily, additive technologies enable the effective implementation of various design and engineering ideas in high-tech industries, such as the aircraft industry, engine technology, and rocket engineering. The expanded range of standardized materials for additive technologies will facilitate their integration into large-scale production. Of significant interest is the potential use of nitrogen-containing heat-resistant powder alloys to produce complex-shaped aircraft parts using additive technologies. This paper describes the complete process of obtaining samples from powders of alloys with superequilibrium nitrogen content using the selective laser melting (SLM) method. Four different compositions of high-nitrogen steels were obtained through mechanical alloying. Subsequently, the powders of these steels underwent processing using the plasma spheroidization method to be utilized in the SLM process. The SLM method was also employed to produce samples for mechanical tests. Throughout each stage of the process, the powders were thoroughly analyzed. One of the most critical parameters was the nitrogen content in the resulting powders. At each subsequent production stage, its proportion decreased, yet it remained at the superequilibrium content level of 0.13–0.44 wt. %. The mechanical tests confirmed that the alloys fabricated by the SLM method are not inferior in terms of their properties compared to those obtained using classical metallurgical technologies.

Keywords: high-nitrogen steels, superequilibrium nitrogen content, plasma spheroidization, mechanical alloying, additive technologies, selective laser melting

For citation: Ozerskoi N.E., Razumov N.G., Silin A.O., Borisov E.V., Popovich A.A. Mechanical properties of high-nitrogen steel produced via selective laser melting using mechanically alloyed and spheroidized powders. *Powder Metallurgy and Functional Coatings*. 2024;18(1):81–94. https://doi.org/10.17073/1997-308X-2024-1-81-94

Механические свойства стали с высоким содержанием азота, полученной методом селективного лазерного плавления с использованием механически легированных сфероидизированных порошков

Н. Е. Озерской ✉, Н. Г. Разумов, А. О. Силин, Е. В. Борисов, А. А. Попович

Санкт-Петербургский политехнический университет Петра Великого
Россия, 195251, г. Санкт-Петербург, ул. Политехническая, 29

✉ nikolaiozerskoi@yandex.ru

Аннотация. В последние годы развитие аддитивных технологий является одной из приоритетных задач отраслей. Аддитивные технологии позволяют, прежде всего, эффективно реализовывать любые конструкторские и инженерные идеи в таких высокотехнологичных отраслях, как авиастроение, двигателестроение, ракетостроение. Расширение номенклатуры стандартизованных материалов для аддитивных технологий будет способствовать их внедрению в массовое производство. Значительный интерес представляет возможность использования азотсодержащих жаропрочных порошковых сплавов для изготовления деталей летательных аппаратов сложной формы с применением аддитивных технологий. В данной работе описан полный цикл получения образцов из порошков сплавов со сверхравновесным содержанием азота методом селективного лазерного плавления (СЛП). Механическим легированием были получены 4 различных состава высокоазотистых сталей. Затем порошки этих сталей были обработаны методом плазменной сфероидизации для использования в процессе СЛП. Также методом СЛП были изготовлены образцы для механических испытаний. На каждом этапе процесса порошки подвергались детальному исследованию. Одним из наиболее важных параметров было содержание азота в получаемых порошках. С каждым этапом производства его доля снижалась, но оставалась на уровне сверхравновесного содержания 0,13–0,44 мас. %. Механические испытания показали, что сплавы, полученные методом СЛП, не уступают по своим свойствам сплавам, изготовленным по классическим металлургическим технологиям.

Ключевые слова: высокоазотистые стали, сверхравновесное содержание азота, плазменная сфероидизация, механическое легирование, аддитивные технологии, селективное лазерное плавление

Для цитирования: Озерской Н.Е., Разумов Н.Г., Силин А.О., Борисов Е.В., Попович А.А. Механические свойства стали с высоким содержанием азота, полученной методом селективного лазерного плавления с использованием механически легированных сфероидизированных порошков. *Известия вузов. Порошковая металлургия и функциональные покрытия*. 2024;18(1): 82–94. https://doi.org/10.17073/1997-308X-2024-1-81-94

Introduction

Currently, nitrogen is extensively utilized as an alloying element alongside Cr, Ni, Mn, Mo, and others [1]. This usage enables the production of steels with a distinctive blend of strength, ductility, and corrosion resistance. Nitrogen possesses a critical advantage over other alloying elements due to its virtually unlimited availability. Obtaining nitrogen does not necessitate the destruction of the Earth's surface and subsoil, which is typically unavoidable during ore mining.

Presently, research on steels alloyed with nitrogen, focusing on structure formation and the interrelationships of steel properties with nitrogen, has generated significant results, leading to the proposal of new areas for their application [2–5]. Owing to their exceptional properties, nitrogen-containing steels have found widespread use in nuclear and thermal power engineering, the medical industry, aviation, the automotive industry, and more. Nitrogen alloying has the capability to confer special properties to steel and enhance its characteristics, thereby broadening its scope of applications. As of now, the full potential of nitrogen alloying remains unrealized, and research in this field continues.

The literature review reveals active scholarly investigations into the potential use of nitrogen-containing steels in various additive technologies (AT). Numerous studies have been published examining the testing of nitrogen-containing steels in selective laser melting (SLM) [6; 7], laser powder bed fusion (LPBF) [8–15], wire and arc additive manufacturing (WAAM) [16–19], and electron beam additive manufacturing (EBAM) [20–22]. Each technology possesses its distinct characteristics and features.

Studies [6; 7] emphasize that nitrogen emission occurs during the SLM of nitrogen-containing stainless steels. The emission levels correlate with the energy den-

sity, which is directly proportional to the laser power and inversely proportional to the scanning speed. Investigations [9–14] demonstrate the potential use of powders of nitrogen-containing steels in LPBF technology. They indicate that regardless of the process gas used to feed the powder into the melt pool, the nitrogen content decreases. Higher melt pool temperatures reduce nitrogen solubility in the melt, resulting in degassing and the formation of gas pores. Moreover, a study [15] illustrates that during LPBF, local changes in the geometry of the melt pool, influenced by energy density, can affect nitrogen emission. Elevated energy densities lead to prolonged melt pool lifetimes and higher maximum liquid phase temperatures. Assuming that nitrogen is primarily lost during the melting stage, increased maximum temperatures and extended lifetimes of the melt pool contribute to nitrogen loss. With increased energy density, the size of the melt pool – its depth and area – along with its temperature and lifetime also increase.

The paper [19] introduces a novel concept in wire and arc additive manufacturing aimed at achieving pure austenite with an exceptionally high nitrogen content. This technique involves the simultaneous introduction of nitrogen-containing steel welding wire and nitride alloy powder into the melt pool. As the nitride powder dissolves within the melt pool, it dissociates and is adsorbed to create steel with a superequilibrium nitrogen content. The authors highlight that during the wire and arc additive manufacturing process utilizing HNS6 wire (Fe–21.6Cr–16.8Mn–2.1Ni–1.2Mo–0.8N), there is a recorded nitrogen loss rate of up to 17.7 %. However, in hybrid wire and arc additive manufacturing, where nitride powder is introduced into the melt pool, the nitrogen content in the resultant material increases significantly, potentially reaching 1.07 wt. % based on the powder feed rate. Concurrently, there is a substantial reduction in ferrite content. As the feed rate reaches 0.33 g/min, the ferrite phase disappears entirely, resulting in a fully austenitic structure in the deposited metal. This transformation contributes to the enhancement of the material's mechanical properties.

The paper [20] details the successful application of the electron-beam additive method to produce high-nitrogen steel with the chemical composition: Fe–20.7Cr–22.2Mn–0.3Ni–0.6Si–0.15C–0.53N (wt. %), utilizing rods as the initial material. The authors demonstrate that during the manufacturing process, significant amounts of manganese and nitrogen undergo combustion. Consequently, the alloy obtained, with the composition Fe–22.9Cr–10.8Mn–0.1Ni–0.6Si–0.1C–0.48N, exhibits an increased proportion of ferrite, rising from 20 % in the initial rod to 40 % in the alloy produced via additive technologies (AT). Their findings indicate that alloys generated using both At and traditional methods possess comparable mechanical characteristics.

The primary method for producing nitrogen-containing steel powders is through gas atomization [6; 7; 9; 13; 14; 22–24]. The nitrogen content in these resultant powders typically does not surpass the equilibrium level and is contingent upon the specific alloy composition. Nevertheless, several researchers have explored the possibility of producing steel powders with nitrogen content surpassing equilibrium levels. In a study by the authors [25], the impact of various factors – such as atmosphere composition, chamber pressure, and gas jet pressure – during atomization on the nitrogen content in Cr17Mn11Mo3N alloy powder was investigated. The research demonstrated that the nitrogen proportion in atomized powders escalates as the pressure in the chamber increases during the melting and spraying process. Through the combined effect of chamber pressure during melting and spray pressure, the nitrogen content can reach up to 0.4 wt. % even in the absence of nitrogen-containing components added to the charge. The findings suggested that by regulating the spray pressure and/or pressure in the chamber, it is feasible to control both the powder particle size and the nitrogen content in the resultant powders.

The paper [26] presents findings from research involving the production of 17-4PH stainless steel powder using plasma wire atomization. The authors successfully produced powder with a nitrogen content of up to 0.15 wt. %, which was then utilized in the SLM technology.

In the paper [27], the production of high-nitrogen steel powders through plasma spraying of a rotating electrode is detailed. The resulting powder exhibited a notably high nitrogen content, surpassing levels achievable under normal conditions, and displayed an almost perfect spherical particle shape. Notably, in a nitrogen atmosphere during plasma spraying, the nitrogen content in the steel powders remained consistently at approximately 0.6 wt. % N, regardless of the nitrogen content in the plasma gas itself. It was observed that even when the nitrogen content in the plasma gas is 0 %, the steel becomes nitrogenized to 0.6 wt. % N. This occurrence is attributed to the interaction between the argon plasma and the surrounding nitrogen gas, which is sufficient for nitrogen sorption onto the steel particles.

The papers [28; 29] detail the process involving powders of AISI 316L and Fe17Cr11Mn3Mo alloys obtained through gas atomization and subsequently nitrogenized in a nitrogen atmosphere under pressure. The research demonstrates that, based on the nitrogenizing duration and powder composition, powders with nitrogen content up to 1.3 wt. % can be achieved.

Analysis indicates that this elevated nitrogen content is attained due to the formation of chromium nitride both on the surface and throughout the cross-section of the powder particles. However, this process is characterized as low-yielding, and there exists an issue concerning the homogeneity of nitrogen content across the particles.

The LPBF technology as described in paper [8], allows the utilization of non-spherical-shaped powder materials. High-nitrogen austenitic steel derived from powder synthesized by mechanical alloying (MA) is explored in this context. The study demonstrates that the alloy retains more than 71 % of the initial powder mixture's nitrogen content. Remarkably, this material surpasses 316L steel significantly in terms of mechanical properties.

Furthermore, in the additive technology (AT) process of welding steels with high nitrogen content, there's a tendency for nitrogen to be released in the melt pool, resulting in diminished mechanical characteristics of the final products. Researchers have been exploring various methods over the last few decades to increase nitrogen content in the solid solution in deposited material and reduce loss due to nitride or pore formation. These methods include optimizing the chemical composition to enhance nitrogen solubility [30–33], modifying shielding gas characteristics by increasing nitrogen partial pressure [34–37] or adding surfactants [38] or multicomponent gas mixtures [39] during welding, and using nitride flux-cored wire as feed material [40; 41]. While these approaches can reduce nitrogen loss during steel welding to some extent, the nitrogen content in the weld or deposited metal remains lower than that in the base or filler metal. Thus far, no solution has been presented to increase the nitrogen content in the deposited metal or weld beyond that of the filler or base metal.

Based on the outlined objectives, the following research is proposed: 1) establishing physical and chemical synthesis patterns of metallic nitrogen-containing heat-resistant powder alloys via MA and plasma spheroidization methods; 2) determining the influence of physical and chemical parameters within the SLM process on the nitrogen content of the alloy and evaluating the resulting material's mechanical properties.

This investigation will focus on studying a specific heat-resistant nitrogen-containing steel, Fe16Cr2.2Ni0.6Mn1.1Mo0.1N, with the following chemical composition, wt. %:

Fe	Base	Ni	2.0–2.5
Cr	15.0–16.5	C	0.12–0.18
Mo	0.9–1.3	Si	≤0.6
Mn	≤0.6	N	0.03–0.10

Materials and methods

In this research, powder materials of the composition Fe–16Cr–2.2Ni–0.6Mn–1.1Mo were synthesized using the MA method. Gaseous nitrogen, nitrogenized ferrochrome (FCr20), chromium nitride (Cr_2N), and nitrogenized ferromanganese (Mn87H6) were employed as nitrogen source during the synthesis. In order to investigate how the method of nitrogen introduction during MA affects the nitrogen content and distribution in the alloy, six compositions were examined: 1) Fe–Cr–Ni–Mn–Mo – mechanical alloying in the nitrogen atmosphere; 2) Fe–Cr–Ni–FeMnN–Mo – incorporating manganese in the form of nitrogenized ferromanganese; 3) Fe–Cr_2N–Ni–Mn–Mo – introducing chromium in the form of chromium nitride; 4) Fe–FeCrN–Ni–Mn–Mo – adding chromium in the form of nitrogenized ferrochromium; 5) Fe–(0.5Cr–0.5Cr_2N)–Ni-Mn–Mo and Fe–(0.5Cr–0.5FeCrN)–Ni–Mn–Mo – incorporating 50 % of the total chromium content in the form of chromium nitride or nitrogenized ferrochrome.

The calculation was conducted utilizing the CALPHAD method through ThermoCalc software for thermodynamic analysis employing the TCHEA4 data package.

Experimental investigations regarding powders plasma spheroidization were carried out using the TekSphero 15 unit (Tekna Plasma Systems Inc., Canada). This unit is equipped with a high-frequency generator reaching a maximum output of 15 kW, operating within a frequency range of 2 to 4 MHz. The experiments were conducted on compositions including Fe–(0.5Cr–0.5Cr_2N)–Ni–Mn–Mo, Fe–Cr_2N–Ni–Mn–Mo, Fe–(0.5Cr–0.5FeCrN)–Ni–Mn–Mo and Fe–FeCrN–Ni–Mn–Mo within both argon-hydrogen and argon-nitrogen plasma environments.

For studying powder morphology, the SEM Tescan Mira 3 scanning electron microscope (Tescan, Czech Republic) was utilized alongside the X-Flash 6/10 fluorescence detector (Bruker, USA), while the Leica DMI 5000 optical microscope (Leica Microsystems, Germany) aided in obtaining cross-sectional images to assess chemical makeup. The carbon content analysis was conducted using the absorption method via the CS-230 analyzer (LECO, USA, ISO 9556-1989). Determination of oxygen and nitrogen content was carried out by the reducing fusion method in an inert carrier flow (helium) using the TC-500 analyzer (LECO, USA, ISO 17053-2005 and ISO 15351-1999). The particle size distribution analysis of the acquired powder (ISO 8130-13) was performed using the Analysette 22 laser diffractometer (Fritsch GmbH, Germany). *X*-ray diffraction analysis was conducted using the Bruker D8

Advance *X*-ray diffractometer (USA) with CuK_α radiation (1.5406 Å) within the range 2θ = 30÷100°.

The samples were produced from nitrogen-containing steel powders using the SLM technology within a nitrogen atmosphere, employing the SLM280HL selective laser melting system (SLM Solutions GmbH, Lübeck, Germany). This system is equipped with the YLR laser featuring a wavelength of 1070 nm and focal length of ~80 μm.

Nitrogen-containing steel powders were compacted using the SLM technique. The experiments were conducted on compositions including Fe–(0.5Cr–0.5Cr_2N)–Ni–Mn–Mo, Fe–Cr_2N–Ni–Mn–Mo, Fe–(0.5Cr–0.5FeCrN)–Ni–Mn–Mo and Fe–FeCrN–Ni––Mn–Mo, synthesized in an argon-hydrogen plasma, influenced by oxygen content within the produced powder. To examine the influence of SLM parameters on the relative density and chemical composition of the resulting alloys, cubic samples with a side length of 10 mm were manufactured. This was achieved by varying laser power, scanning speed, and energy density. The powder layer applied was 0.05 mm thick, and the laser pass spacing was set at 0.12 mm. The specific SLM parameters utilized in these experiments are detailed in Table 1.

Results and discussion

The phase diagram calculation for the Fe–16Cr––2.2Ni–0.6Mn–1.1Mo–0.04C–N alloy, performed using the ThermoCalc software package for thermodynamic analysis, revealed that the nitrogen concentration limit during crystallization is 0.2 wt. %. When this limit is surpassed, nitrogen is emitted into the gas phase, potentially leading to the formation of bubbles and pores during crystallization. Throughout solidification, the composition of the liquid phase and the evolving solid phases continuously alter with changes in temperature and the amount of the liquid phase. Consequently, the solubility of nitrogen in δ-ferrite within the temperature range of 1470–1750 K does not exceed 0.07 wt. %, while in austenite, it reaches 0.6 wt. %.

Table 1. **SLM parameters for printing mode testing**

Таблица 1. **Параметры СЛП при отработке режимов печати**

No.	Laser power, W	Scanning rate, mm/s	*E*, J/mm^3
1	240	650	61.54
2	300	800	62.50
3	300	650	76.92
4	360	650	92.31
5	300	500	100.00
6	300	650	115.38

It has been observed that during the initial stages of MA, the dissolution of alloying elements in all investigated systems follows a general pattern. Due to significant plastic deformation, the particles from the initial powder undergo flattening and subsequent welding, resulting in the formation of a composite structure. Following a duration of MA for τ_{MA} = 5 h, the composite particles exhibit a characteristic layered structure comprising various combinations of the initial components.

With a prolonged duration of MA, the primary processes involve the homogenization of the composition concerning chemical makeup and the interaction between the initial components aimed at reducing the system's free energy. Analysis of the acquired diffractograms revealed that Ni is the initial alloying element to dissolve into the iron lattice (atomic radius r_a = 124 pm), followed by Mn (r_a = 127 pm), Cr (r_a = 130 pm), and Mo (r_a = 139 pm). This sequence is attributed to Ni, Mn, and Cr alloying elements forming substitutional solid solutions with iron, whereby the atomic radius of nickel is closest to that of iron (r_a = 126 pm), followed by manganese, chromium, and molybdenum, respectively. The dissolution of alloying elements leads to a modification of the α-Fe lattice parameter, ranging from 0.2866 to 0.2887 nm, contingent upon the system. Considering the proportions of the components, it is presumable that diffusion predominantly occurs along the crystal lattice defects during the MA process. In both the initial Fe–16Cr–2.2Ni–0.6Mn–1.1Mo composition and the one utilizing nitrogenized ferromanganese as the nitrogen source, the alloying elements exhibit nearly uniform distribution throughout the powder volume. They correspond to the chemical composition of the initial mixture after τ_{MA} = 10 h (Fig. 1, *a*). However, the dissolution of molybdenum is considerably impeded due to its atomic radius being significantly larger than that of the other composition elements. The MA process in these systems is similar owing to the fact that nitrogenized ferromanganese is primarily composed of manganese nitride – a compound easily degraded – with inclusions of iron and a small quantity of ferromanganese from the initial charge.

In systems where chromium nitride (Cr_2N) and nitrogenized ferrochrome (according to XRD results – 80 vol. % CrN + 20 vol. % Cr_2N) were utilized as nitrogen sources, the dissolution behavior of alloying elements differed from that in the initial composition. Following τ_{MA} = 10 h, alloying elements exhibited heterogeneous distribution across the volume. Upon reaching τ_{MA} = 15 h, chromium continued to remain non-uniformly distributed, residing inside the particles

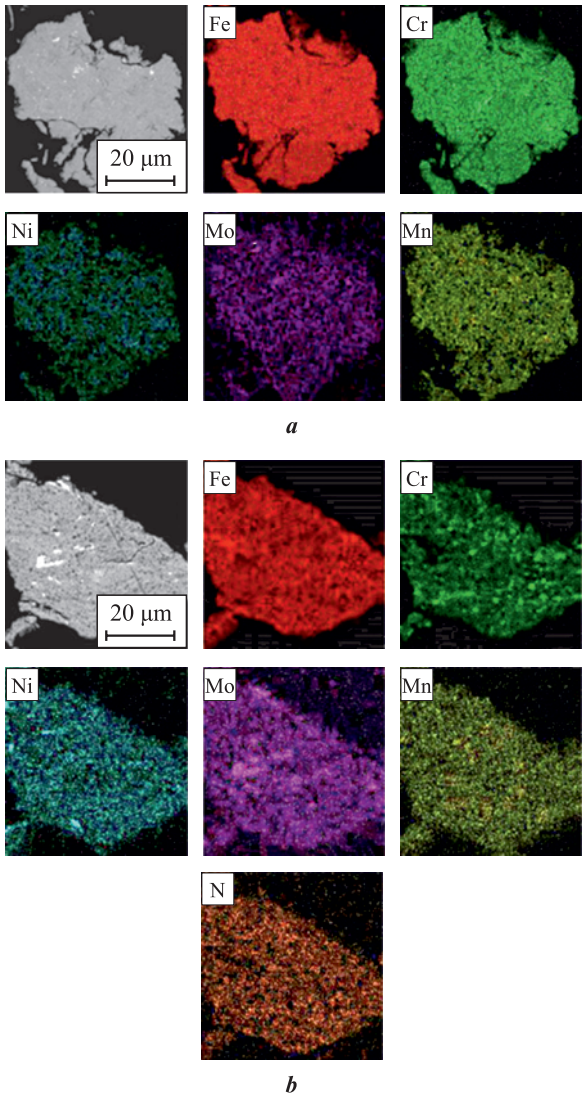

Fig. 1. Component distribution of the Fe–16Cr–2.2 Ni–0.6Mn–1.1Mo composition after MA
a – without nitrogen, τ_{MA} = 10 h
b – with nitrogenized ferrochromium, τ_{MA} = 15 h

Рис. 1. Распределение компонентов композиции Fe–16Cr–2,2Ni–0,6Mn–1,1Mo после МЛ
a – без азота, $\tau_{МЛ}$ = 10 ч
b – с азотированным феррохромом (ФХ20), $\tau_{МЛ}$ = 15 ч

in the form of submicron-sized inclusions evenly dispersed throughout the volume (Fig. 1, *b*). This pattern emerged because chromium was introduced in the form of chromium nitride – a relatively stable chemical compound – not in elemental powder form. Evidently, the energy imparted during the MA process might be insufficient for its breakdown and subsequent dissolution. Upon joint analysis of XRD results and the distribution of alloying elements within particle volumes, it is evident that the decline in Cr_2N peaks is likely attributed to its disintegration and distribution across the volume, rather than its dissolution into the iron lattice (Fig. 2). According to XRD results, a portion of Cr_2N remains undissolved even after 15 h of mechanical alloying. However, when materials such as chromium nitride or nitrogenized ferrochrome are incorporated at 50 % of the total chromium content, they demonstrate almost complete dissolution into the iron lattice, with only sporadic submicron-sized inclusions observed. This change in solubility may be attributed to the presence of pure chromium, which, due to its high affinity for nitrogen, attracts a portion of the nitrogen from the nitride, expediting its decomposition and facilitating nitrogen diffusion into the lattice.

The nitrogen content analysis in powder samples revealed that throughout the MA process, up to 2.5 wt. % nitrogen can be introduced into the Fe–16Cr–2.2Ni––0.6Mn–1.1Mo alloy, while the equilibrium content remains at 0.1 wt. % (Table 2). The samples employing nitrogenized ferrochrome or chromium nitride as the nitrogen source exhibited the highest nitrogen proportions. With this method of introduction, the nitrogen assimilation rate reached approximately 90 %. According to XRD and SEM results, a major portion of the nitrogen is dissolved within the Fe lattice. However, some nitrogen remains in nitrides, uniformly dispersed throughout the particle volume in the form of submicron-sized inclusions.

The analysis of the particle size distribution in the obtained powders indicates a correlation between higher nitrogen content in the alloy and an increased presence of powder particles smaller than 45 μm. This reduction in particle size is attributed to undissolved submicron nitride inclusions, inducing significant distortions within the crystal lattice and acting as stress concentrators. Under intensive mechanical forces

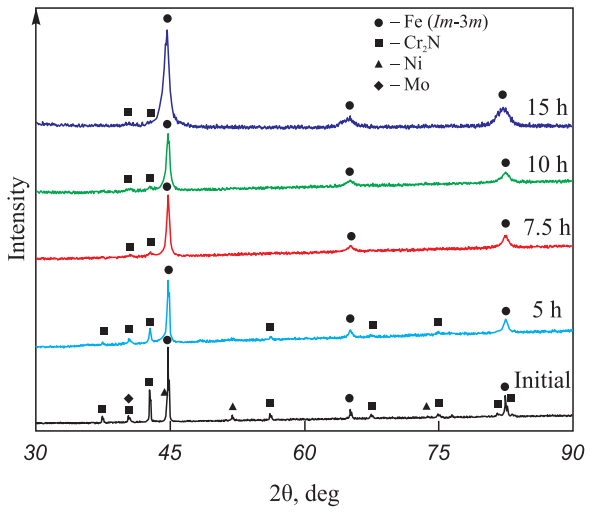

Fig. 2. Evolution of phase constitution with MA duration in Fe–Cr_2N–Ni–Mn–Mo composition

Рис. 2. Изменение фазового состава в зависимости от продолжительности МЛ композиции Fe–Cr_2N–Ni–Mn–Mo

Table 2. **Chemical composition of MA-powder for Fe–16Cr–2.2Ni–0.6Mn–1.1Mo alloy**

Таблица 2. **Химический состав МЛ-порошка сплава Fe–16Cr–2,2Ni–0,6Mn–1,1Mo**

Composition	Element content, wt. %						
	Fe	Cr	Ni	Mn	Mo	N	C
Fe–Cr–Ni–Mn–Mo	Basic	16.28	2.10	0.64	1.24	0.02	0.05
Fe–Cr–Ni–FeMnN–Mo	Basic	15.63	2.44	0.83	1.05	0.04	0.19
Fe–Cr_2N–Ni–Mn–Mo	Basic	15.92	2.26	0.59	1.29	1.90	0.15
Fe–FeCrN–Ni–Mn–Mo	Basic	15.59	2.37	0.65	1.13	2.48	0.28
Fe–(0.5Cr–0.5Cr_2N)–Ni–Mn–Mo	Basic	16.15	2.11	0.82	1.11	1.06	0.14
Fe–(0.5Cr–0.5FeCrN)–Ni–Mn–Mo	Basic	16.23	2.35	0.69	1.02	1.32	0.22

during the MA process, the existence of such stress concentrators tends to prompt crack formation, subsequently leading to material disintegration.

Several research studies [42–44] have highlighted that spherical powders of nitrogen-containing alloy Fe–16Cr–2.2Ni–0.6Mn–1.1Mo with a high degree of sphericity can be produced using thermal argon-hydrogen and argon-nitrogen plasma generated in a high-frequency plasmatron (Fig. 3). Investigation into powder particle morphology indicated that the proportion of spheroidized particles in the resulting powders ranges between 70–96 %. It was observed that, at the same powder feed rate, the occurrence of non-spherical particles after spheroidization in argon-nitrogen plasma is higher due to differing physical and chemical properties of the plasma-forming gas mixtures. Hydrogen dissociates by 90 % at T = 4700 K, while nitrogen does so at T = 9000 K, significantly affecting the plasma's heat content (enthalpy). To achieve powders with an equivalent proportion of spheroidized particles, the powder feed rate in argon-nitrogen plasma needs to be reduced by 10–15 %.

The analysis of SEM images and particle size distribution in the obtained powders has revealed distinct characteristics. Powders with low nitrogen content (Fe–Cr–Ni–Mn–Mo, Fe–Cr–Ni–FeMnN–Mo compositions) exhibited a differential curve in the particle size distribution after plasma spheroidization. The peak of this curve lies within the range of 30 to 125 μm, indicating a slight shift towards smaller sizes compared to the initial material (which ranged from 45 to 125 μm). Conversely, in powders with high nitrogen content, a considerable proportion (about 30–50 %) of particles emerged with sizes below 30 μm, despite the initial powder size range being 45 to 125 μm. These variations suggest the presence of elevated mechanical stresses and microcracks within the powder particles, likely a consequence of the intense mechanical impact during the MA process. The initial plasma temperature significantly surpasses the material's boiling point, not merely its melting point. Consequently, the powder particles experience rapid melting. During this swift heating and melting process, nitrogen might be swiftly released from the solution, transforming into the gaseous phase at a high rate. This phenomenon contributes to the wedging

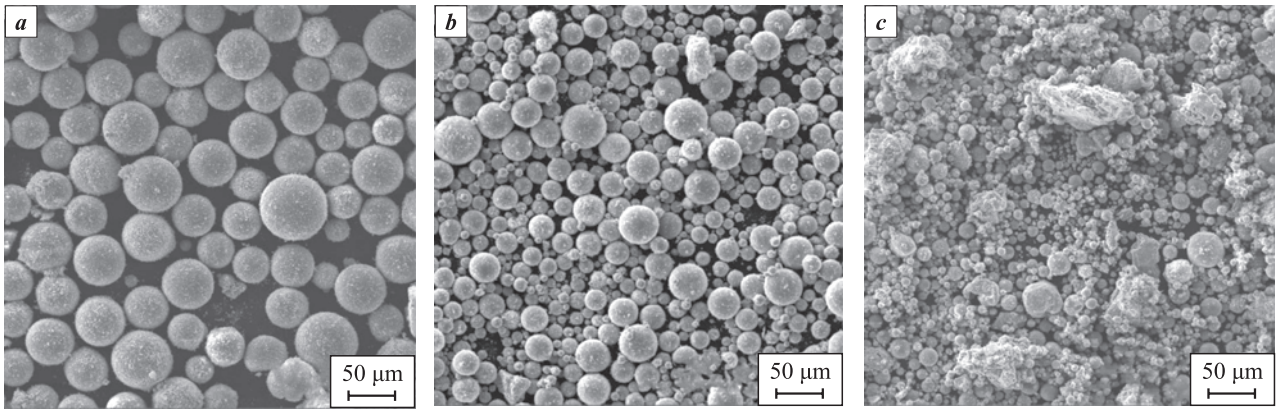

Fig. 3. Powder morphology after plasma spheroidization

a – Fe–Cr–Ni–Mn–Mo; ***b*** – Fe–(0.5Cr–0.5Cr_2N)–Ni–Mn–Mo; ***c*** – Fe–Cr_2N–Ni–Mn–Mo

Рис. 3. Морфология порошка после плазменной сфероидизации

a – Fe–Cr–Ni–Mn–Mo; ***b*** – Fe–(0,5Cr–0,5Cr_2N)–Ni–Mn–Mo; ***c*** – Fe–Cr_2N–Ni–Mn–Mo

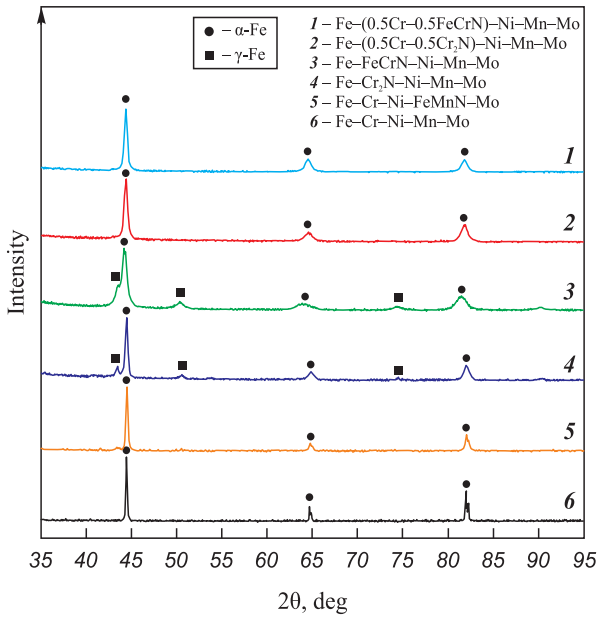

Fig. 4. Phase composition of Fe–Cr–Ni–Mn–Mo alloy powders after spheroidization in argon-hydrogen plasma

Рис. 4. Фазовый состав порошков сплава Fe–Cr–Ni–Mn–Mo после сфероидизации в аргоноводородной плазме

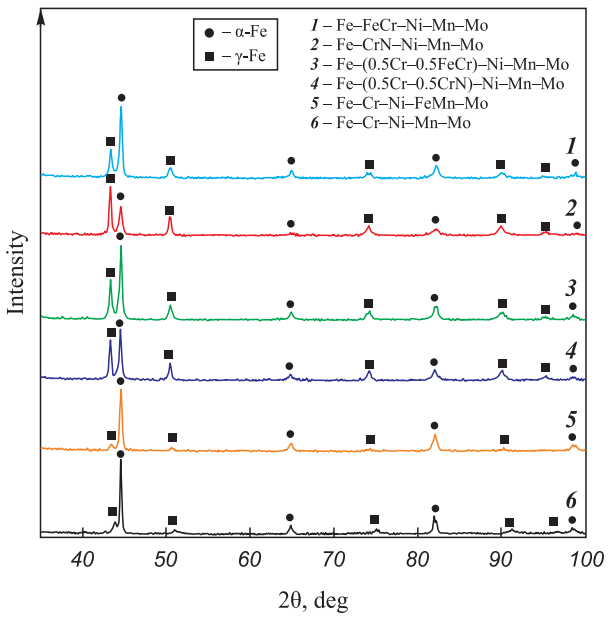

Fig. 5. Phase composition of Fe–Cr–Ni–Mn–Mo alloy powders after spheroidization in argon-nitrogen plasma

Рис. 5. Фазовый состав порошков сплава Fe–Cr–Ni–Mn–Mo после сфероидизации в аргоноазотной плазме

of microcracks and the destruction of particles before melting occurs, or during the intensive boiling and disintegration of already-melted particles. Some powders were found to contain individual hollow spheres, primarily exhibiting a cracked shell structure.

The *X*-ray phase analysis conducted on the powders post-spheroidization revealed the existence of α- and γ-Fe peaks (Fig. 4, 5). Nitrogen, being an element conducive to austenite formation, results in a marginal increase in the proportion of γ-Fe as the nitrogen content

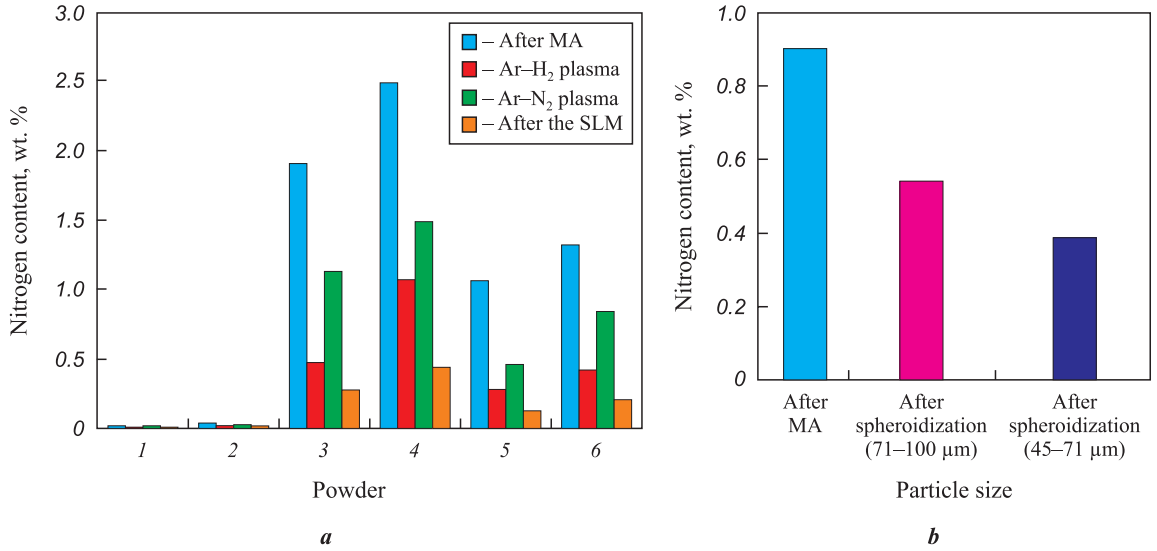

Fig. 6. Nitrogen content in powders post plasma flow treatment (***a***) and particle size-dependent nitrogen content variation (***b***)

1 – Fe–Cr–Ni–Mn–Mo; *2* – Fe–Cr–Ni–FeMnN–Mo; *3* – Fe–Cr_2N–Ni–Mn–Mo; *4* – Fe–FeCrN–Ni–Mn–Mo; *5* – Fe–(0.5Cr–0.5Cr_2N)–Ni–Mn–Mo; *6* – Fe–(0.5Cr–0.5FeCrN)–Ni–Mn–Mo

Рис. 6. Содержание азота в порошках после обработки в потоке плазмы (***a***) и зависимость содержания азота от размера частиц (***b***)

1 – Fe–Cr–Ni–Mn–Mo; *2* – Fe–Cr–Ni–FeMnN–Mo; *3* – Fe–Cr_2N–Ni–Mn–Mo; *4* – Fe–FeCrN–Ni–Mn–Mo; *5* – Fe–(0,5Cr–0,5Cr_2N)–Ni–Mn–Mo; *6* – Fe–(0,5Cr–0,5FeCrN)–Ni–Mn–Mo

in the alloy elevates. The phase composition of the powders subsequent to plasma spheroidization aligns with the results derived from the calculated state diagrams, indicating that the powders are in a quenched state.

The investigation revealed that a portion of nitrogen is lost from the alloy during spheroidization in plasma. Post-spheroidization, in argon-hydrogen plasma, the nitrogen content ranges between 0.01 to 1.0 wt. %, showcasing a decrease by 50–75 % (Fig. 6, *a*). Conversely, in argon-nitrogen plasma, the nitrogen content experiences a maximum reduction of 40 %. The use of argon-nitrogen plasma leads to the chamber atmosphere becoming saturated with molecular (N_2^+) and atomic (N^+) nitrogen ions. This occurrence arises from the excitation of electronic states within molecules by oscillating electrons in the flow of high-temperature argon plasma, followed by the subsequent decomposition of excited molecules. Consequently, this saturation contributes to an increased limit concentration of nitrogen within the melt during crystallization. Additionally, it slows down the release of nitrogen from the melt and aids in plasma-chemical nitriding processes. The variance in nitrogen content concerning the fractional composition of the powder mixture can be attributed to diffusion processes. Specifically, it involves the differential distance of nitrogen diffusion from the powder particle to its surface during spheroidization when the powder transforms into metal droplets. Furthermore, differences in the temperature of molten metal droplets play a role in this variation. Therefore, particles with smaller diameters tend to exhibit a lower mass fraction of nitrogen compared to particles with larger diameters. Regarding residual nitrogen amounts, the investigation found 0.54 wt. % in the powder fraction of 71–100 μm and 0.39 wt. % in the powder ranging from 45–71 μm. This is in contrast to the initial alloy's nitrogen content, which was approximately ~0.9 wt. % (Fig. 6, *b*).

In the process of spheroidization, when hydrogen is introduced into the plasma-forming gas, oxides are reduced, resulting in a decrease in the oxygen content to levels lower than 0.1 wt. % across all compositions. Conversely, during spheroidization in argon-nitrogen plasma, the reduction in oxygen content occurs primarily due to the evaporation of the oxide phase from the surface of molten particles, followed by subsequent condensation into submicron particles. Chemical analysis revealed that the oxygen content in the powders produced via spheroidization in argon-nitrogen plasma ranges between 0.2 and 0.3 wt. %.

The testing of the obtained powders in the SLM unit resulted in the formation of compact alloys showcasing a minimum porosity of 0.8 % (as depicted in Fig. 7). Notably, an increase in the initial powder's nitrogen content correlates with a rise in the minimum alloy porosity, reaching up to 11.5 %. During the SLM process, the nitrogen content in the alloy ranges from 0.13 to 0.44 wt. %, exceeding the nitrogen concentration limit during crystallization by twofold. This excess in nitrogen concentration prompts a challenge in steel solidification, where nitrogen release occurs into the gas phase, leading to the formation of nitrogen bubbles and subsequent porosity within the material. Throughout solidification, there's a continual alteration in the composition of the liquid and solid phases, contingent upon variations in temperature and the quantity of the liquid phase. Moreover, the local solubility of nitrogen in the residual liquid phase experiences changes, depending on the type of crystallization (austenitic, ferritic, or mixed) and the proportion of phase quantities. Ensuring compliance with a specific condition throughout the entire solidification duration is crucial for obtaining a dense ingot [45]:

$$[N]_{L,\,T} < [N]_{L,\,\text{eq. } P_{tot}},$$

where $[N]_{L,\,T}$ is the nitrogen content in the residual liquid at temperature T; $[N]_{L,\,\text{eq. } P_{tot}}$ is the equilibrium nitrogen content in the liquid metal at the same temperature T and under the total pressure in the system.

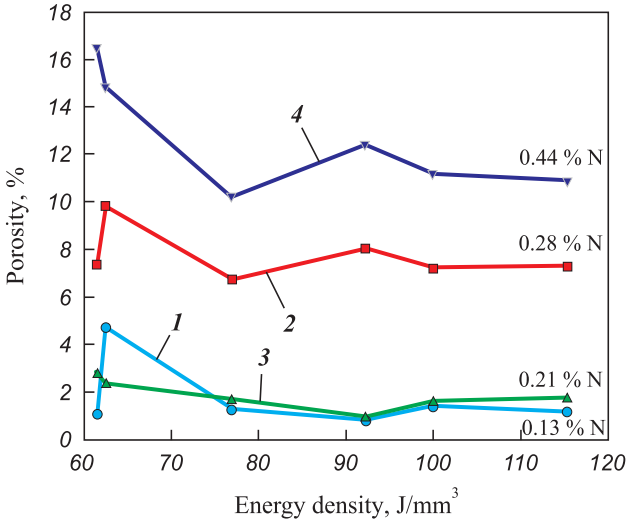

Fig. 7. Relative porosity of alloys fabricated via selective laser melting at various energy density levels
1 – Fe–(0.5Cr–0.5Cr_2N)–Ni–Mn–Mo
2 – Fe–Cr_2N–Ni–Mn–Mo
3 – Fe–(0.5Cr–0.5FeCrN)–Ni–Mn–Mo
4 – Fe–FeCrN–Ni–Mn–Mo

Рис. 7. Относительная пористость сплавов, полученных методом селективного лазерного плавления с разной плотностью энергии
1 – Fe–(0,5Cr–0,5Cr_2N)–Ni–Mn–Mo
2 – Fe–Cr_2N–Ni–Mn–Mo
3 – Fe–(0,5Cr–0,5FeCrN)–Ni–Mn–Mo
4 – Fe–FeCrN–Ni–Mn–Mo

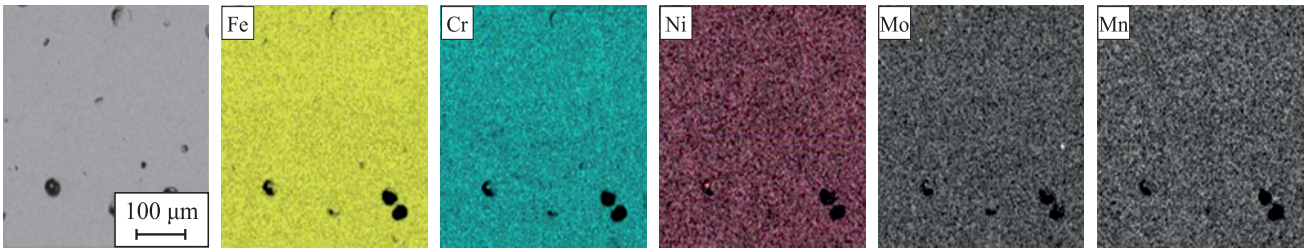

Fig. 8. Component distribution in Fe–FeCrN–Ni–Mn–Mo composition after SLM

Рис. 8. Распределение компонентов в композиции Fe–FeCrN–Ni–Mn–Mo после СЛП

As noted above, the limit concentration of nitrogen during crystallization of the studied alloy does not exceed 0.2 wt. %. The actual nitrogen content in the liquid phase during printing is greater than its equilibrium solubility, the pressure in the chamber being 1 atm, so nitrogen is released in the gaseous state. It is worth noting that the porosity of alloys obtained from powders in which nitrogenized ferrochrome was used as the source of nitrogen is higher than that of alloys with chromium nitride, which is due to the higher decomposition tem-

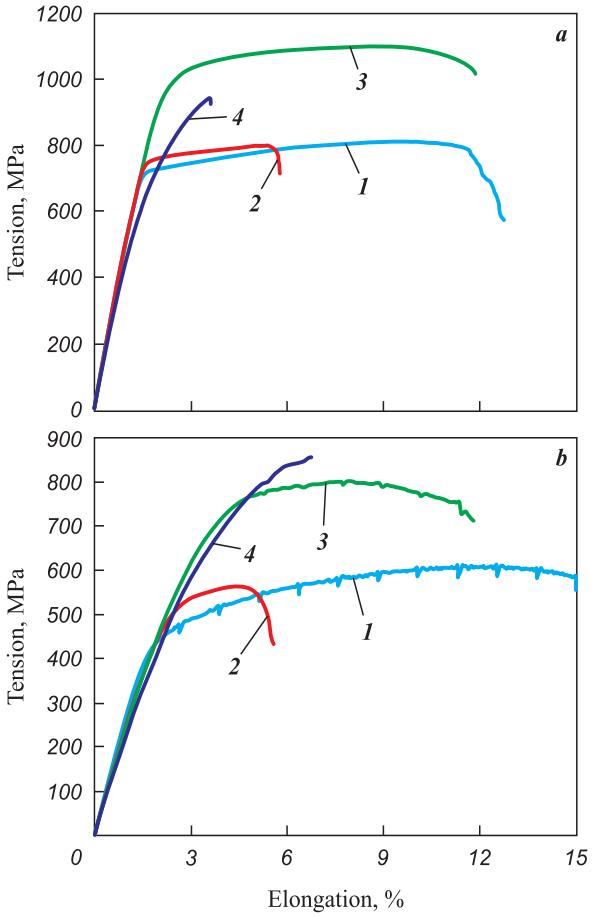

Fig. 9. Stretching diagram of alloys fabricated via SLM method

Test temperature: ***a*** – 20 °C; ***b*** – 500 °C
1 – Fe–(0.5Cr–0.5Cr_2N)–Ni–Mn–Mo; *2* – Fe–Cr_2N–Ni–Mn–Mo
3 – Fe–(0.5Cr–0.5FeCrN)–Ni–Mn–Mo; *4* – Fe–FeCrN–Ni–Mn–Mo

Рис. 9. Диаграмма растяжения сплавов, полученных методом СЛП

Температура испытаний: ***a*** – 20 °C; ***b*** – 500 °C
1 – Fe–(0,5Cr–0,5Cr_2N)–Ni–Mn–Mo; *2* – Fe–Cr_2N–Ni–Mn–Mo
3 – Fe–(0,5Cr–0,5FeCrN)–Ni–Mn–Mo; *4* – Fe–FeCrN–Ni–Mn–Mo

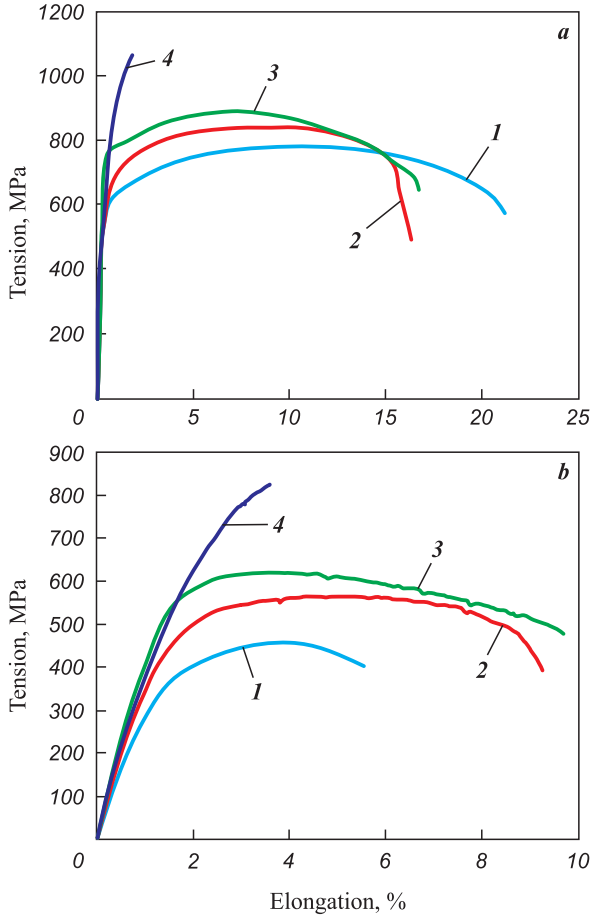

Fig. 10. Stretching diagram of alloys fabricated via SLM method followed by HIP

Test temperature: ***a*** – 20 °C; ***б*** – 500 °C
1 – Fe–(0.5Cr–0.5Cr_2N)–Ni–Mn–Mo; *2* – Fe–Cr_2N–Ni–Mn–Mo
3 – Fe–(0.5Cr–0.5FeCrN)–Ni–Mn–Mo; *4* – Fe–FeCrN–Ni–Mn–Mo

Рис. 10. Диаграмма растяжения сплавов, полученных методом СЛП с последующим ГИП

Температура испытаний: ***a*** – 20 °C; ***б*** – 500 °C
1 – Fe–(0,5Cr–0,5Cr_2N)–Ni–Mn–Mo; *2* – Fe–Cr_2N–Ni–Mn–Mo
3 – Fe–(0,5Cr–0,5FeCrN)–Ni–Mn–Mo; *4* – Fe–FeCrN–Ni–Mn–Mo

***Table 3.* Mechanical properties of alloys fabricated via SLM method**

***Таблица 3.* Механические свойства сплавов, полученных методом СЛП**

Composition	SLM						SLM and HIP					
	20 °C			500 °C			20 °C			500 °C		
	$\sigma_{0.2}$, MPa	σ_u, MPa	δ, %	$\sigma_{0.2}$, MPa	σ_u, MPa	δ, %	$\sigma_{0.2}$, MPa	σ_u, MPa	δ, %	$\sigma_{0.2}$, MPa	σ_u, MPa	δ, %
Fe–Cr_2N–Ni–Mn–Mo	730	780	5.5	480	560	5	620	840	16.0	400	560	8.2
Fe–FeCrN–Ni–Mn–Mo	–	980	–	600	820	4	800	1070	1.2	600	830	1.4
Fe–(0.5Cr–0.5Cr_2N)–Ni–Mn–Mo	700	790	12.0	430	610	10	610	780	21.0	370	460	4.0
Fe–(0.5Cr–0.5FeCrN)–Ni–Mn–Mo	960	1100	10.5	560	800	9	770	890	16.0	530	620	8.5
15X16H2AM (According to TS14-1-1431-75)	740	935	14.0	540	640	–	740	935	14.0	540	640	–

perature of the latter. Further investigation into the distribution of elements revealed that the alloying elements exhibit an even distribution across the cross-sections of the alloys (Fig. 8).

The obtained alloys underwent heat treatment following this procedure: quenching from a temperature of 1040 ± 10 °C in oil, followed by tempering within the range of 640 to 680 °C for 2 h. Mechanical tests conducted at room temperature and at 500 °C revealed (Fig. 9 and Table 3) that the alloys produced via the SLM technology did not meet the specifications' requirements for the Fe16Cr2.2Ni0.6Mn1.1Mo0.1N alloy due to excessive porosity, resulting in inadequate relative elongation. In order to mitigate the porosity issue, the alloys underwent hot isostatic pressing (HIP) at 1160 °C and a pressure of 150 MPa for 3 h. Following HIP treatment, the porosity in the alloys was successfully reduced to not exceeding 0.2 %, consequently enhancing the material's ductility at room temperature (Fig. 10, Table 3).

The heat treatment applied to the SLM alloys followed the standard mode specified in the TS for Fe16Cr2.2Ni0.6Mn1.1Mo0.1N steel. However, due to variations in carbon content between the synthesized alloy and the Fe16Cr2.2Ni0.6Mn1.1Mo0.1N steel composition (TS14-1-1431-75), the heat treatment methods as outlined in TS do not yield the most optimal properties for the synthesized alloy. Consequently, adjustments in the heat treatment modes are required, which will be the focus of future research.

Conclusion

The study revealed that during the initial stages of the MA process, regardless of the method of nitrogen introduction, the dissolution of alloying elements in all investigated systems follows a general pattern, forming a layered composite structure. When nitrogen is introduced as chromium nitride (Cr_2N), it is not fully dissolved in the iron lattice; instead, it distributes evenly throughout the volume as submicron inclusions. The stability of chromium nitride as a chemical compound might prevent its complete decomposition and dissolution due to the insufficient energy flow during the MA process.

By employing various nitrogen-containing initial components in the MA process, nitrogen up to 2.5 wt. % can be introduced, whereas the crystallization limit concentration remains ≤0.2 wt. %. Consequently, the degree of nitrogen assimilation reaches approximately 90 %. The increase in nitrogen content in the alloy correlates with a higher proportion of powder particles ≤45 μm in size. This is attributed to significant distortions in the crystal lattice caused by submicron nitride inclusions, resulting in crack formation and subsequent material disintegration.

During spheroidization in argon-hydrogen plasma, there is a reduction in nitrogen content by 50–75 % from its initial levels, while spheroidization in argon-nitrogen plasma leads to a decrease in nitrogen content by no more than 40 %. Synthesis of powders with a spherical shape and nitrogen content up to 1.2 wt. % was demonstrated, depending on the method of nitrogen introduction in the MA process and the composition of the plasma-forming gas.

The investigation delved into the impact of SLM process parameters on nitrogen content in alloys, their porosity, and mechanical properties. As the nitrogen amount in the alloy increases, the minimum porosity escalates to 11.5 %. Nitrogen content in the alloy obtained by SLM ranges from 0.13 to 0.44 wt. %, which surpasses the nitrogen concentration limit during crystallization twice. Mechanical tests affirmed that the alloys produced via selective laser melting exhibit comparable characteristics to those obtained using traditional metallurgical methods.

References / Список литературы

1. Svyazhin A.G., Kaputkina L.M. Nitrogen steels and high nitrogen steels. Industrial technologies and properties. *Izvestiya. Ferrous Metallurgy*. 2019;62(3):173–187. (In Russ.). https://doi.org/10.17073/0368-0797-2019-3-173-187

   Свяжин А.Г., Капуткина Л.М. Азотистые и высокоазотистые стали. Промышленные технологии и свойства. *Известия высших учебных заведений. Черная металлургия*. 2019;62(3):173–187. https://doi.org/10.17073/0368-0797-2019-3-173-187
2. Stein G., Hucklenbroich I. Manufacturing and applications of high nitrogen steels. *Materials and Manufacturing Processes*. 2004;19(1):7–17. https://doi.org/10.1081/AMP-120027494
3. Foct J., Domain C., Becquart C.S. High nitrogen steel and interstitial alloying. *Material Science Forum*. 2003; 426–432:161–170.
4. Qi-zeng L. Rapidly growing stainless steel industry in China. *Ironmaking Steelmaking*. 2006;10(1):112.
5. Speidel M.O. Nitrogen containing austenitic stainless steels. *Materialwissenschaft und Werkstofftechnik*. 2006; 37(10):875–880. https://doi.org/10.1002/mawe.200600068
6. Sun X., Ren J., Wang Y., Zhao D., Wang S., Xiong X., Rao J.H. Nitriding behaviour and microstructure of high-nitrogen stainless steel during selective laser melting. *Materials*. 2023;16(6):2505. https://doi.org/10.3390/ma16062505
7. Zheng Z., Wang L., Jia M., Cheng L., Yan B. Microstructure and mechanical properties of stainless steel/calcium silicate composites manufactured by selective laser melting. *Materials Science and Engineering: C*. 2017;71:1099–1105. https://doi.org/10.1016/j.msec.2016.11.032
8. Cheng B. Ambient pressure fabrication of Ni-free high nitrogen austenitic stainless steel using laser powder bed fusion method. *Additive Manufacturing*. 2022;55:102810. https://doi.org/10.1016/j.addma.2022.102810
9. Boes J., Röttger A., Theisen W., Cui C., Uhlenwinkel V., Schulz A., Walther F. Gas atomization and laser additive manufacturing of nitrogen-alloyed martensitic stainless steel. *Additive Manufacturing*. 2020;34:101379. https://doi.org/10.1016/j.addma.2020.101379
10. Yang K., Wang Z.D., Chen M.Z., Lan H.F., Sun G.F., Ni Z.H. Effect of pulse frequency on the morphology, microstructure, and corrosion resistance of high-nitrogen steel prepared by laser directed energy deposition. *Surface Coatings Technologies*. 2021;421:127450. https://doi.org/10.1016/j.surfcoat.2021.127450
11. Springer H., Baron C., Szczepaniak A., Jägle E.A., Wilms M.B., Weisheit A., Raabe D. Efficient additive manufacturing production of oxide- and nitride-dispersion-strengthened materials through atmospheric reactions in liquid metal deposition. *Materials and Design*. 2016;111:60–69. https://doi.org/10.1016/j.matdes.2016.08.084
12. Pauzon C., Hryha E., Forêt P., Nyborg L. Effect of argon and nitrogen atmospheres on the properties of stainless steel 316 L parts produced by laser-powder bed fusion. *Material and Design*. 2019;179:107873. https://doi.org/10.1016/j.matdes.2019.107873
13. Boes J., Röttger A., Theisen W. Microstructure and properties of high-strength C + N austenitic stainless steel processed by laser powder bed fusion. *Additive Manufacturing*. 2020;32:101081. https://doi.org/10.1016/j.addma.2020.101081
14. Becker L., Röttger A., Boes J., Weber S., Theisen W. Processing of a newly developed nitrogen-alloyed ferritic-austenitic stainless steel by laser powder bed fusion – microstructure and properties. *Additive Manufacturing*. 2021;46:102185. https://doi.org/10.1016/j.addma.2021.102185
15. Arabi-Hashemi A., Maeder X., Figi R., Schreiner C., Griffiths S., Leinenbach C. 3D magnetic patterning in additive manufacturing via site-specific in-situ alloy modification. *Applied Materials Today*. 2020;18:100512. https://doi.org/10.1016/j.apmt.2019.100512
16. Zhang X., Zhou Q., Wang K., Peng Y., Ding J., Kong J., Williams S. Study on microstructure and tensile properties of high nitrogen Cr–Mn steel processed by CMT wire and arc additive manufacturing. *Materials and Design*. 2019;166:107611. https://doi.org/10.1016/j.matdes.2019.107611
17. Zhang X., Zhou Q., Wang K., Peng Y., Ding J., Kong J., Williams S. Precipitation characteristics and tensile properties of high-nitrogen chromium-manganese steel fabricated by wire and arc additive manufacturing with isothermal post-heat treatment. *Material and Design*. 2023;225: 111536. https://doi.org/10.1016/j.matdes.2022.111536
18. A Hosseini V., Högström M., Hurtig K., Valiente Bermejo M.A., Stridh L.-E., Karlsson L. Wire-arc additive manufacturing of a duplex stainless steel: thermal cycle analysis and microstructure characterization. *Welding in the World*. 2019;63(4):975–987. https://doi.org/10.1007/s40194-019-00735-y
19. Wu T., Liu J., Wang K., Wang L., Zhang X. Microstructure and mechanical properties of wire-powder hybrid additive manufacturing for high nitrogen steel. *Journal of Manufacturing Processes*. 2021;70:248–258. https://doi.org/10.1016/j.jmapro.2021.08.029
20. Astafurov S., Astafurova E., Reunova K., Melnikov E., Panchenko M., Moskvina V., Kolubaev E. Electron-beam additive manufacturing of high-nitrogen steel: Microstructure and tensile properties. *Material Science and Engineering: A*. 2021;826:141951. https://doi.org/10.1016/j.msea.2021.141951
21. Reunova K.A., Astafurova E.G., Astafurov S.V., Melnikov E.V., Panchenko M.Y., Moskvina V.A., Kolubaev E.A. Microstructure and phase composition of vanadium-alloyed high-nitrogen steel fabricated by additive manufacturing. *AIP Conference Proceedings*. 2020;2310(1):020276. https://doi.org/10.1063/5.0034265
22. Panin V.E., Narkevich N.A., Durakov V.G., Shulepov I.A. Control of the structure and wear resistance of a carbon-nitrogen austenitic steel coating produced by electron beam cladding. *Physical Mesomechanics*. 2021;24(1):53–60. https://doi.org/10.1134/S1029959921010082
23. Cui C., Uhlenwinkel V., Schulz A., Zoch H.-W. Austenitic stainless steel powders with increased nitrogen content for

laser additive manufacturing. *Metals*. 2019;10(1):61. https://doi.org/10.3390/met10010061

24. Kuznetsov P.A., Shakirov I.V., Bobyr' V.V., Zhukov A.S., Klimov V.N. Features of melt gas atomization and selective laser melting of high-strength austenitic nitrogen-containing steel powders. *Metal Science and Heat Treatment*. 2020;62(1):76–80. https://doi.org/10.1007/s11041-020-00515-2

25. Ni G., Wang S., Li Q., Zhao D., Song C., Li C. Preparation of Cr17Mn11Mo3N powders by high-pressure gas atomization and the nitrogen increasing mechanism. *Powder Technology*. 2021;385:490–500. https://doi.org/10.1016/j.powtec.2021.03.025

26. Chen D., Daoud H., Scherm F., Klötzer B., Hauck C., Glatzel U. Stainless steel powder produced by a novel arc spray process. *Journal of Materials Research Technology*. 2020;9(4):8314–8322. https://doi.org/10.1016/j.jmrt.2020.05.076

27. Gammal T.E., Abdel-Karim R., Walter M.T., Wosch E., Feldhaus S. High nitrogen steels. High nitrogen steel powder for the production of near net shape parts. *ISIJ International*. 1996;36(7):915–921. https://doi.org/10.2355/isijinternational.36.915

28. Shen H., Zou J., Li Y., Li D., Yu Y., Wang X. Effects of nitrogen on predominant sintering mechanism during the initial stage of high nitrogen nickel-free stainless steel powder. *Journal of Alloys and Compounds*. 2023;945:169230. https://doi.org/10.1016/j.jallcom.2023.169230

29. Boes J., Röttger A., Becker L., Theisen W. Processing of gas-nitrided AISI 316L steel powder by laser powder bed fusion – Microstructure and properties. *Additive Manufacturing*. 2019;30:100836. https://doi.org/10.1016/j.addma.2019.100836

30. Mohammed R., Reddy G.M., Rao K.S. Effect of filler wire composition on microstructure and pitting corrosion of nickel free high nitrogen stainless steel GTA welds. *Transactions of the Indian Institute of Metals*. 2016;69(10):1919–1927. https://doi.org/10.1007/s12666-016-0851-6

31. Gawlik J., Schmidt J., Nowak T., Wójcicki Z., Zagórski A. Nitrogen as an alloying element improving material properties of the high carbon cast steel for ball mill liner plates. *Archives of Civil Mechanical Engineering*. 2017;17(4):926–934. https://doi.org/10.1016/j.acme.2017.04.007

32. Wendler M., Weiß A., Krüger L., Mola J., Franke A., Kovalev A., Wolf S. Effect of manganese on microstructure and mechanical properties of cast high alloyed CrMnNi–N steels. *Advanced Engineering Materials*. 2013;15(7):558–565. https://doi.org/10.1002/adem.201200318

33. Liu Z., Fan C., Chen C., Ming Z., Yang C., Lin S., Wang L. Design and evaluation of nitrogen-rich welding wires for high nitrogen stainless steel. *Journal of Materials Processing Technology*. 2021;288:116885. https://doi.org/10.1016/j.jmatprotec.2020.116885

34. Kikuchi Y., Matsuda F., Okabe T., Ohta M. Nitrogen content of 316L weld metal and its fine particle by means of high-pressure MIG arc welding. *ISIJ International*. 1996;36(7):977–982. https://doi.org/10.2355/isijinternational.36.977

35. Zhao L., Tian Z., Peng Y. Porosity and nitrogen content of weld metal in laser welding of high nitrogen austenitic stainless steel. *ISIJ International*. 2007;47(12):1772–1775. https://doi.org/10.2355/isijinternational.47.1772

36. Qiang W., Wang K. Shielding gas effects on double-sided synchronous autogenous GTA weldability of high nitrogen austenitic stainless steel. *Journal of Materials Processing Technology*. 2017;(250):169–181. https://doi.org/10.1016/j.jmatprotec.2017.07.021

37. Liu Z., Fan C., Ming Z., Chen C., Liu A., Yang C., Wang L. Gas metal arc welding of high nitrogen stainless steel with Ar–N_2–O_2 ternary shielding gas. *Defence Technology*. 2021;17(3):923–931. https://doi.org/10.1016/j.dt.2020.05.021

38. Du Toit M., Pistorius P.C. The influence of oxygen on the nitrogen content of autogenous stainless steel arc welds. *American Welding Society*. 2007;86(8);222S–230S.

39. Yang D., Huang Y., Fan J., Jin M., Peng Y., Wang K. Effect of N_2 content in shielding gas on formation quality and microstructure of high nitrogen austenitic stainless steel fabricated by wire and arc additive manufacturing. *Journal of Manufacturing Process*. 2021;(61)261–269. https://doi.org/10.1016/j.jmapro.2020.11.020

40. Liu Z., Fan C., Chen C., Ming Z., Liu A., Yang C., Wang L. Optimization of the microstructure and mechanical properties of the high nitrogen stainless steel weld by adding nitrides to the molten pool. *Journal of Manufacturing Processes*. 2020;49:355–364. https://doi.org/10.1016/j.jmapro.2019.12.017

41. Du Toit M., Pistorius P.C. Nitrogen control during the autogenous arc welding of stainless steel. Part 2: A kinetic model for nitrogen absorption and desorption. *American Welding Society*. 2003;82(9):231S–237S. https://doi.org/10.1007/BF03266398

42. Razumov N.G., Popovich A.A., Wang Q.S. Thermal plasma spheroidization of high-nitrogen stainless steel powder alloys synthesized by mechanical alloying. *Metals and Materials International*. 2018;24(2):363–370. https://doi.org/10.1007/s12540-018-0040-8

43. Popovich A.A., Razumov N.G. A study of the process of mechanical alloying of iron with austenite-forming elements. *Metal Science and Heat Treatment*. 2015;56(9–10):570–576. https://doi.org/10.1007/s11041-015-9801-X

44. Popovich A.A., Razumov N.G. Dissolution of alloying elements and phase formation in powder materials Fe–18Cr–8Ni–12Mn–xN during mechanical alloying. *Advanced Materials Letters*. 2014;5(12):683–687. https://doi.org/10.5185/amlett.2014.6585

45. Makhmutov T., Razumov N., Kim A., Ganin S., Shamshurin A., Popovich A., Popovich V. Microstructure and mechanical properties of high-nitrogen 16Cr–2Ni–Mn–Mo–xN stainless steel obtained by powder metallurgy techniques. *Materials Today: Proceedings*. 2020; 30(3): 768–772. https://doi.org/10.1016/j.matpr.2020.01.564

Information about the Authors

Nikolai E. Ozerskoi – Research Associate of the Research and Educational Center "Additive technologies", Peter the Great St. Petersburg Polytechnic University (SPbPU)
ORCID: 0000-0002-7371-558X
E-mail: nikolaiozerskoi@yandex.ru

Nikolai G. Razumov – Cand. Sci. (Eng.), Head of the Laboratory "Synthesis of new materials and structures", SPbPU
ORCID: 0000-0002-7147-6239
E-mail: n.razumov@onti.spbstu.ru

Aleksey O. Silin – Leading Engineer of the Research and Educational Center "Structural and functional materials", SPbPU
E-mail: silin_ao@spbstu.ru

Evgenii V. Borisov – Cand. Sci. (Eng.), Leading Researcher of the Laboratory "Synthesis of new materials and structures", SPbPU
ORCID: 0000-0003-2464-6706
E-mail: evgenii.borisov@icloud.com

Anatoly A. Popovich – Dr. Sci. (Eng.), Professor, Director of the Institute of Machinery, Materials and Transport, SPbPU
ORCID: 0000-0002-5974-6654
E-mail: popovicha@mail.ru

Сведения об авторах

Николай Евгеньевич Озерской – научный сотрудник научно-образовательного центра «Аддитивные технологии» Санкт-Петербургского политехнического университета Петра Великого (СПбПУ)
ORCID: 0000-0002-7371-558X
E-mail: nikolaiozerskoi@yandex.ru

Николай Геннадьевич Разумов – к.т.н., заведующий лабораторией «Синтез новых материалов и конструкций» СПбПУ
ORCID: 0000-0002-7147-6239
E-mail: n.razumov@onti.spbstu.ru

Алексей Олегович Силин – ведущий инженер научно-образовательного центра «Конструкционные и функциональные материалы» СПбПУ
E-mail: silin_ao@spbstu.ru

Евгений Владиславович Борисов – к.т.н., ведущий научный сотрудник лаборатории «Синтез новых материалов и конструкций» СПбПУ
ORCID: 0000-0003-2464-6706
E-mail: evgenii.borisov@icloud.com

Анатолий Анатольевич Попович – д.т.н., профессор, директор Института машиностроения, материалов и транспорта СПбПУ
ORCID: 0000-0002-5974-6654
E-mail: popovicha@mail.ru

Contribution of the Authors

N. E. Ozerskoi – conducted experiments, processed obtained results, authored the article, participated in result discussions.

N. G. Razumov – conducted critical literature analysis, contributed to result discussions, drew study conclusions.
A. O. Silin – conducted experiments, participated in result discussions.
E. V. Borisov – planned experiments, fabricated samples, participated in result discussions.
A. A. Popovich – conceptualized the idea, defined the work's purpose and objectives, participated in result discussions.

Вклад авторов

Н. Е. Озерской – проведение экспериментов, обработка полученных результатов, написание статьи, участие в обсуждении результатов.
Н. Г. Разумов – критический анализ литературы, участие в обсуждении результатов, формирование выводов исследования.
А. О. Силин – проведение экспериментов, участие в обсуждении результатов.
Е. В. Борисов – планирование экспериментов, изготовление образцов, участие в обсуждении результатов.
А. А. Попович – концептуализация идеи, определение цели работы и ее задач, участие в обсуждении результатов.

Received 03.07.2023
Revised 13.09.2023
Accepted 18.09.2023

Статья поступила 03.07.2023 г.
Доработана 13.09.2023 г.
Принята к публикации 18.09.2023 г.

Зарегистрирован Федеральной службой по надзору
в сфере связи, информационных технологий
и массовых коммуникаций.
Свидетельство о регистрации ПИ № ФС77-79230

Журнал распространяется агентством «Урал-Пресс»
Подписной индекс: 80752 (печатная версия)
05108 (электронная версия)